Harnessing Glycofluoroforms for Electrochemical Detection of Galectin-3

Alice Rose Hewson

Doctor of Philosophy

University of York
Chemistry

September 2025

Abstract

Despite underpinning biological communication, sugars have limited applications as biorecognition elements in biosensors, caused by promiscuity between sugar probes and protein binding partners. Here, site-specific fluorination was harnessed to introduce protein-sugar selectivity to specifically target galectin-3, a valuable diagnostic biomarker. Electrochemical detection methods were employed due to their speed, sensitivity, and affordability.

For the first time, electrochemical biosensing of galectin-3 was achieved by exploiting its enhanced binding affinity to glycofluoroforms (fluorinated analogues of native binding sugars). Polymer tethers were used to provide a passivated surface and the resulting biosensing platforms selectively bound galectin-3 compared to control glycans and proteins. Initially, the thiol functionality of the polymer, linked to the glycofluoroform via strain-promoted azide-alkyne cycloaddition, was used to immobilise the conjugate onto a gold electrode. Electrochemical impedance spectroscopy analysis quantified the increase in charge transfer resistance between the gold electrode surface and solution-phase potassium ferricyanide observed on galectin-3 binding. Titration experiments revealed an apparent K_d of 240 nM. However, a high level of irreproducibility was observed between sensors, and the electrochemical instability of the gold-thiol bond prevented the use of further electrochemical measurement techniques.

Subsequently, triazabutadienes were used as masked diazonium ions for covalent immobilisation of polymer-sugar conjugates onto carbon electrodes. Compared to gold-thiol self-assembly, electrografting yielded a higher coverage of glycofluoroform (5.201 pmol compared to 0.350 pmol) and conferred an apparent K_d of 13 nM. The higher affinity of this sensing platform and the wide range of detectable galectin-3 concentrations (1 ng mL^{-1} to 10 μg mL^{-1}) is more suited to the expected biological galectin-3 levels. Furthermore, the increased stability of the modified surface due to the covalent carbon-electrode bond allowed for more complex voltammetry methods to be explored. Extraction of faradaic current from Fourier transformed alternating current voltammetry experiments demonstrated a simpler analysis of galectin-3 binding.

Table of Contents

List of Abbreviations

A or CS	acceptor monosaccharide or control sugar
AC	alternating current
ACV	alternating current voltammetry
Ae. aegypti	*Aedes aegypti*
AFP	α-fetoprotein
B. anthracis	*Bacillus anthracis*
BCA	bicinchoninic acid
BRE	biorecognition element
BSA	bovine serum albumin
CE	counter (auxiliary) electrode
CEA	carcino embryonic antigen
CMA-ES	Covariance matrix adaptation evolution strategy
COPD	chronic obstructive pulmonary disease
CPE	constant phase element
CRD	carbohydrate recogition domain
CV	cyclic voltammetry
DAST	diethylaminosulfur trifluoride
DBCO	dibenzocyclooctyne
DC	direct current
DCV	direct current voltammetry
DPV	differential pulse voltammetry
E. coli.	*Escherichia coli*
EDC	1-ethyl-3-(3-dimethylaminopropyl)carbodiimide
EIS	electrochemical impedance spectroscopy
ELISA	enzyme-linked immunosorbent assay
ESI	electrospray ionisation
FAD	flavin adenine dinucleotide
FRET	fluorescence resonance energy transfer
FT	Fourier transform
FTV	Fourier transformed alternating current voltammetry
Gal	galactose
GC	glassy carbon
GFF	glycofluoroform
GlcNAc	N-Acetylglucosamine
GO_x	glucose oxidase
HIV	human immunodeficiency virus
HR-MS	high resolution mass spectrometry
HRP	horseradish peroxidase
IBD	inflammatory bowel disease

IPTG	isopropyl-β-D-1-thiogalactopyranoside
ITO	indium tin oxide
LB	Luria Broth
LC-MS	liquid chromatography-mass spectrometry
MCMC	Markov chain Monte Carlo
MDA-MB-231	M D Anderson - Metastatic Breast - 231
MS	mass spectrometry
NHS	N-hydroxysuccinimide
NMR	nuclear magnetic resonance spectroscopy
PDB	protein data bank
PSV	purely sinusoidal voltammetry
QCM(-D)	quartz crystal microbalance (with dissipation monitoring)
R_{ct}	resistance to charge transfer
RE	reference electrode
RNA	Ribonucleic acid
R_s	solution resistance
SARS-COV-2	severe acute respiratory syndrome coronavirus 2
SAW	surface acoustic wave
SDS-PAGE	sodium dodecyl sulfate-polyacrylamide gel electrophoresis
SH3	SRC Homology 3 domains
SHIRT	*Streptococcus* High Identity Repeat Tandem
SPAAC	strain-promoted azide-alkyne cycloaddition
SPE	screen-printed electrode
SPR	surface plasmon resonance
(ss)DNA	(single stranded) deoxyribonucleic acid
TABD	triazabutadiene
TLC	thin layer chromatography
WE	working electrode
Z_W	Warburg impedance

List of Figures

List of Schemes

List of Tables

Acknowledgements

The completion, and perhaps more significantly my enjoyment, of this project would not have been possible without so many people. To start with my supervisors Alison, Martin, and Nathalie and my IPM Anne. Thank you all for your thoughtful advice and encouragement. Martin and Nathalie, your incredible knowledge regarding the complex world of glycoscience and all things biology have been incredibly helpful in guiding this project. Alison, you have been a constant source of support, and I am so thankful to have been able to work under your supervision for so many years. Your ability to both fill me with enthusiasm and ideas for the work and help me to temper my sometimes-ridiculous list of goals has undoubtably saved me from madness. To all of chemical biology it has been a pleasure to work with all of you over the past few years. There is simply too many of us to name everyone but a shout out must go to all of those I have shared an office with for an extended period of time: Abby, Alex, Eva, Greg, Josh, Lloyd, Lydia, Matt(s), Morgan, Reuben, and Tom. It's been an experience – I'm glad to have share it with you all and that there was more laughter than there were tears. To Tash, Tess, and Saeed thank you for your support in all things biology. To the two phenomenal lab managers that have graced chemical biology with their presence during my PhD and kept things running smoothly against all odds, thank you Julia and Helen.

To the Parkin group: Alister, Beth, Connor, Ella, Henry, Jamie, Lucy G, Lucy H, Matt, Nat, Niamh, Nick G, Nick Y, and Oscar. I am glad I have had you all by my side to celebrate and commiserate all the electrochemical wins and losses. Henry, thank you for all your explanations, fixing my code when I break it, and your unique encouragements – hopefully my code skills have improved but if not, at least I've gained a friend. Nat, you introduced me to the world of EIS and were the best Australia travel partner a girl could ask for, I am glad you were my original Parkin Girlie. Nick, you have always been there with your advice, synthetic superpowers, and (sometimes terrible) jokes, but more importantly you always know exactly which one is needed. To all the people that have contributed to this work, from all our external collaborators, the students I've been lucky enough to supervise, and all those who have kindly donated molecules to keep me away from the fumehood (a very scary place for me) – thank you.

The Department of Chemistry at York has been a wonderful place to spend eight (!!!) years. To everyone that has provided support, from Rachel to keeping everything running, to Steve and Mike for always making me smile and having patience when I forgot to order/collect something, to all the technicians and the workshop team. Thank you to Abby, Chris, and Stu for fixing anything that broke and helping me solve problems, and in electrochemistry there's a lot of both. Outside of the lab, the department has introduced me to so many people I have enjoyed spending time with so thank you to my b block babes, fulford friends, everyone at Friday Football, my fellow regular Brew York patrons, and my OG reUNIon crew.

To my York friends AKA the reason I've made it to this point in the PhD with a smile on my face. To my fulford friends, Ella, Lucy, Morgan, and Beth (and Connor, you count!). Ella, the Kermit to my Elmo, the Mary-Kate to my Ashley, you have been the emotional co-author of this work, thanks for all the late night hugs, sitting on my floor to provide me with my required daily social interaction, and for trying to teach me how to use commas. Lucy, Morgan, and Beth (and Ella), our girls nights, shared meals, and having a place of such uplifting positivity has been so meaningful to me in these past few years. Connor, thank you for always making me laugh and keeping me company in all the office late nights. Lloyd and Nat, thank you for wearing matching Christmas jumpers with me, putting on your brightest clothes for my birthday, and being such wonderful friends. Lloyd, you've ~~told~~ taught me so much about myself and supported me in the highs and the lows. Nat, your resilience has inspired me so much, thank you for brightening up my days and always being ready for a hug. Lukas from frantically making crystals in undergrad (you – succeeding, me – failing), to nervous reintroductions at PhD induction, to countless incredibly joyful hours spent in various cafes around York. I am so glad we got each other through this journey. A final York-related acknowledgement to someone I didn't meet in York but am so thankful this PhD introduced me to. Thom, you inspire me in science and in life, thank you for all the encouragement you have provided, I'm looking forward to being back in the same timezone as you.

Perhaps one of the most frequently said sentences during my PhD in response to the many questions about my accent was "I'm from a small town in South Cumbria, Barrow-in-Furness, well technically Walney Island". Obviously, I am biased but I think everyone should be lucky to know about Barrow because it's full of so many amazing people (with fantastic accents).

Siân and Zara, my OG girls you have been a constant during this experience. Siân, to have had you as a friend for so long is a blessing. Zara you are maybe my biggest cheerleader and have picked me up so many times. To all of my family (the Atkinsons, Brooks, Caldwells, Ducies, Hewsons, McAlindens, Parrishs, and Welshs) thank you for all the support, for trying to understand what I do, and not minding when I miss things. To my Crigg family – especially Amy, Bridget, and Paul – our annual reunions have been such a source of joy throughout this whole PhD. Dad, thank you for showing me the value of hard work and for believing I could do it. Mum, thank you always giving me a safe place to come home to and for making sure I knew that it was always there. Lauren, thank you for showing me how important it is to always follow your dreams whatever they are. Nana, I am so excited to see your face when I tell you that I've done it! To everyone I love, thank you for loving me back.

It feels surreal to be coming to the end of this journey and while all the important 'thank you's are done there is some additional smaller things I could not have survived writing without: my favourite writing beverage trio (a fizzy can of Diet coke, vanilla lattes, and water – all iced!!) and countless episodes of procedural dramas. So my final words will not be my own and instead something from ones of my favourite shows which provided the soundtrack to this writing experience:

"Understanding, compassion, kindness, and love
are the only true revolutionary ideas."
Bones S3E2

Declaration

I, Alice Rose Hewson, declare that this thesis is a presentation of original work and I am the sole author. This work has not previously been presented for a degree or other qualification at this University or elsewhere. All sources are acknowledged as references. Contributions to this work by other researchers are explicitly indicated where relevant in the main text, figure captions, or materials and methods section.

Chapter 2 includes content from a previous publication where I am the first author, other contributions are discussed at the start of this chapter:

Hewson, A. R., Lloyd-Laney, H. O, Keenan, T., Richards, S-J., Gibson, M. I., Linclau, B., Signoret, N., Fascione, M.A, and Parkin, A., Harnessing glycofluoroforms for impedimetric biosensing, ***Chem. Sci.***, 2024, **15**, 16086-16095.

I acknowledge that I received assistance from Professor Alison Parkin (supervisor) and Ella Reid (friend/fellow Parkin group researcher) to proofread this thesis in line with the *Policy on Transparency in Authorship in PGR Programmes*.

Chapter One: Sugars in sensing – Targeting galectin-3 with glycofluoroforms

A biosensor is a self-contained integral device which is capable of detecting the presence of a specific analyte via the transduction of an analyte-bioreceptor binding event (**Figure 1.1**).[1,2] Generally, biosensing devices are aimed at determining the concentration of an analyte in solution and have applications in medical, environmental, food, pharmaceutical, and biotechnological industries.[3] Biosensing is utilised on a variety of scales: population diagnostics (regular measurements of large samples often applied in food and agriculture), point-of-care (fast measurements of individual samples often applied in medicine and security), and single-cell diagnostics (monitors biological phenomena at a cell level, applied in molecular biology).[4] This thesis explores the potential of developing a new biosensor for galectin-3, a reported biomarker for several diseases. The longer-term application of such work would be in point-of-care diagnostics. With an aging population, emerging novel diseases, and increasing antibiotic resistance, progression in diagnostics is clearly crucial. The global point-of-care market was estimated at £35.4 billion in 2024 and is expected to reach £50.7 billion by 2030;[5] advancements in this area clearly have immense potential in terms of patients and profits. This introduction seeks to present the common biorecognition elements observed in the literature, contextualise the biological background of sugars and galectins, and establish the reason galectin-3 and glycofluoroforms are a valuable target analyte and biorecognition element for the development of biosensors.

1.1. Biorecognition elements

In the literature, the biorecognition elements (BREs) encountered include antibodies, ssDNA/aptamers, enzymes, phages, cells and nanomaterials. Antibodies, DNA and enzymes are the most common,[6] whereas nanomaterials are considered a 'new' BRE.[1,7] Antibodies are affinity-based biorecognition elements relying on the strong interactions between antigens and antibodies. These sensors are often called immunosensors. They can be label-free where the formation of antigen-antibody complex is directly observed, typically for large analytes like cells and proteins,[8] or an unnatural label, e.g. a dye or fluorophore, can be introduced to the antibody to allow for observation of binding.[1] Advantages of using antibodies are the high specificity and high affinity of the antibody to the antigen on the analyte.[9] Disadvantages include that they must be biologically produced which requires intensive purification and results in batch-to-batch variations, and the fact that antibodies are

susceptible to denature due to high sensitivity to environmental conditions including ionic strength and temperature.[1,6]

Aptamers are single-stranded nucleic acids.[1] They can be designed to be the complementary strand of a nucleic acid analyte, capturing the analyte via hybridisation, or designed for non-nucleic acid targets where the presence of the analyte stabilises a specific folded conformation of the aptamer.[10] Aptamers are stable over a wide range of temperatures and storage conditions, able to be synthesised chemically, less expensive than antibodies, and suited to a wide range of analytes.[1,6,9] However, aptamers are influenced by environmental conditions such as temperature and pH, prone to degradation in biological fluids, and aptamers are discovered through the screening of random libraries, so optimal aptamers may not actually be found depending on what initial aptamers are generated in the library.[9,11]

Enzymes have multiple modes of action depending on the interaction between the enzyme and the analyte. This can be monitoring: (i) the consumption of analyte by the enzyme's catalytic action, (ii) the inhibition of the enzyme by the analyte, or (iii) alteration of the enzyme's biophysical characteristics.[1] Enzymes are suited to many transducers due to the variety of products of enzyme-catalysed reactions which include protons, electrons, light, and heat.[6] They also have a strong binding capacity, work at mild physiological conditions, are reusable for multiple detection events, and are highly specific as they are biologically designed to catalyse a single reaction.[6,8,9] However, this innate specificity can be a drawback as the mutagenesis and assaying involved to alter the native target or improve the binding properties of the enzyme are expensive and complicated.[1] Other disadvantages include the cost and the low stability due to sensitivity to pH, temperature, and humidity.[6]

A wide range of organisms including bacteria, fungi, algae, protozoa, and viruses, are used as whole cell BREs by exploiting the innate recognition ability of these microbes.[1] Using a whole cell removes the need to extract and purify the recognition element.[1] However, they typically exhibit lower sensitivity than molecular-based sensors, there is reduced lifetime regarding storage due to cell viability, and batch-to-batch variation due to the heterogeneity of cells.[12]

Nanomaterials used as BREs exist in a range of geometries, from zero- to three-dimensional and spanning from dots and particles, to wires and rods, to layers.[1] Therefore, a range of binding modes of action exist. Due to the small size of nanomaterials, direct binding of a biomolecule generally influences the physical and chemical properties of the biorecognition element enabling detection. Additionally, nanomaterials can be used to in combination with more classical BREs. This is used to enhance sensitivity, either due to the catalytic effect of a nanomaterial on the reaction being studied or due to the increase of surface area and thus the increase in presentation of the selected BRE.[1] Advantages depend on the selected nanomaterials but include high surface area, high electrical and thermal conductivity, and high (BRE) carrier capacity. Uniquely, nanomaterials can act as both the recognition element and the transducer.[1] But, nanomaterials can be toxic and are surrounded by sustainability concerns.[1]

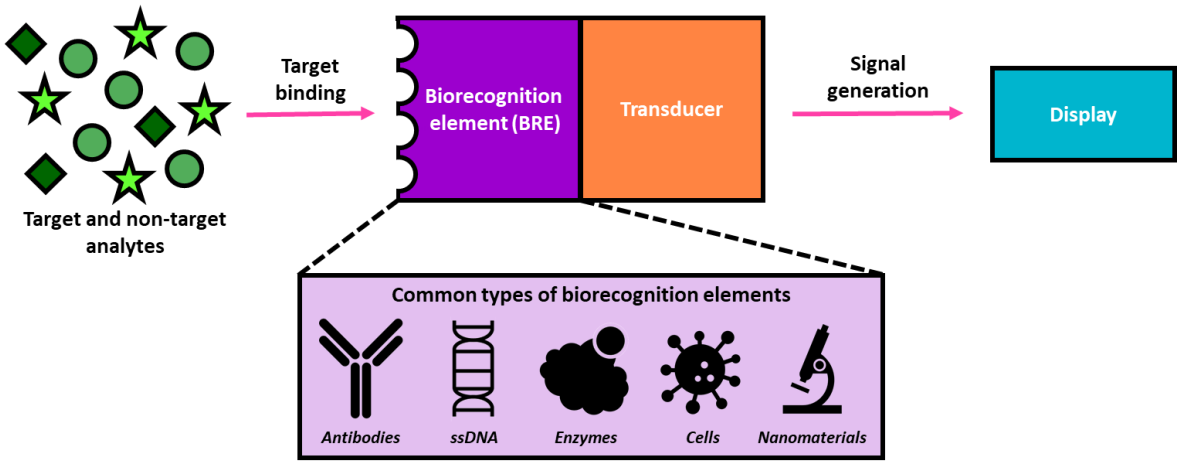

Figure 1.1. *Schematic diagram showing the varying components of a biosensor particularly highlighting types of biorecognition elements.*

Proteins, nucleic acids, sugars, and lipids are the four major classes of biological macromolecules. Therefore, the prevalence of proteins (in the form of enzymes and antibodies) and nucleic acids (e.g. aptamers) as bioreceptors is expected and lipids find use in biosensors immobilised on surfaces to capture receptors for sensing.[13–15] However, sugars are not widely harnessed as bioreceptors.[16] With sugars underpinning so much of cellular communication and possessing advantages over other biorecognition elements including greater chemical and thermal stability, scalability of chemical synthesis, and being the native ligand of many analytes,[17,18] they seem like an obvious choice for biorecognition elements.[19] The aim of this thesis will be to explore the utility of a sugar biorecognition element in an electrochemical biosensor.

1.2. The biological role of sugars and galectins

Sugars (also commonly referred to as saccharides, carbohydrates, or glycans) are the most common and structurally diverse of the molecules found in nature.[20] Monosaccharides, single sugar units, form oligo- and polysaccharides in linear and branched arrangements. These arrangements are often found incorporated into proteins and lipids to form glycoproteins and glycolipids. The arrangement of these conjugates vary between organisms, bringing complexity to studying this class of molecule.[21] Additionally, within an organism, glycan synthesis is influenced by proteins (mainly by lectins, glycosyltransferases, and glycoside hydrolases)[22] meaning there is spatiotemporal control over the expression of glycans. The complex nature and heterogeneity of glycans probably explains the historical absence of sugar biorecognition elements in the biosensor literature.[21]

However, glycoscience is a rapidly developing field due to the multifaceted roles sugars play in biology. In fact, glycans participate in almost every biological process.[23] They play a role in structure, energy generation and storage, metabolism, adhesion, infection, signalling, and recognition.[18] Several of these roles and interactions have been exploited in sensing, examples include detection of the SARS-COV-2 virus, pathogenic *E. coli.* strains, and a triple-negative breast cancer cell line.[24–26] For SARS-COV-2 one of the spike glycoproteins binds α,*N*-acetyl neuraminic acid, a common mammalian sugar. Immobilisation of this sugar forms the basis of a lateral flow test for the virus.[24] Often *E. coli.* attach to the host through FimH, a domain present on bacterial pili, which has high affinity for mannose.[25] MDA-MB-231 is a breast cancer cell line with overexpression of mannose receptors on their surface.[26] Therefore, mannose-based sensors can detect *E. coli.* and MDA-MB-231.[25,26]

This thesis is particularly focused on harnessing protein-sugar interactions which are involved in signalling, cell adhesion, agglutination, protein folding and the immune response.[27–29] The carbohydrate binding proteins integral to these interactions are known as lectins.[30] These exhibit reversible and non-covalent carbohydrate binding, both in solution and on surfaces, with substrates of varying complexity.[30,31] Lectins are sub-classified into large families primarily based on the structure of their carbohydrate recognition domain (CRD), and their carbohydrate binding specificity.[32] These cognate (native) ligands include glucose, mannose, galactose, *N*-acetyl-D-galactosamine, L-fucose, and sialic acids (**Figure 1.2**).[31] Binding at the CRD is mediated by hydrophobic interactions, van der Waals forces,

and hydrogen bonding networks.[33] Although lectins can bind oligosaccharides with high specificity, they often bind simpler mono- and disaccharides less discriminately. This indiscriminate binding can be because lectins possess multiple binding sites for different ligands or because a single binding site displays some 'off-target' lower affinity binding to a non-cognate ligand.[18] This innate non-selective small molecule binding,[34] combined with the fact that multiple lectins can also bind the same carbohydrate, is a significant barrier in the development of carbohydrate receptors for biosensor applications, with only a handful of examples of biosensor platforms using carbohydrate-based biorecognition elements in the literature.[17,35–43]

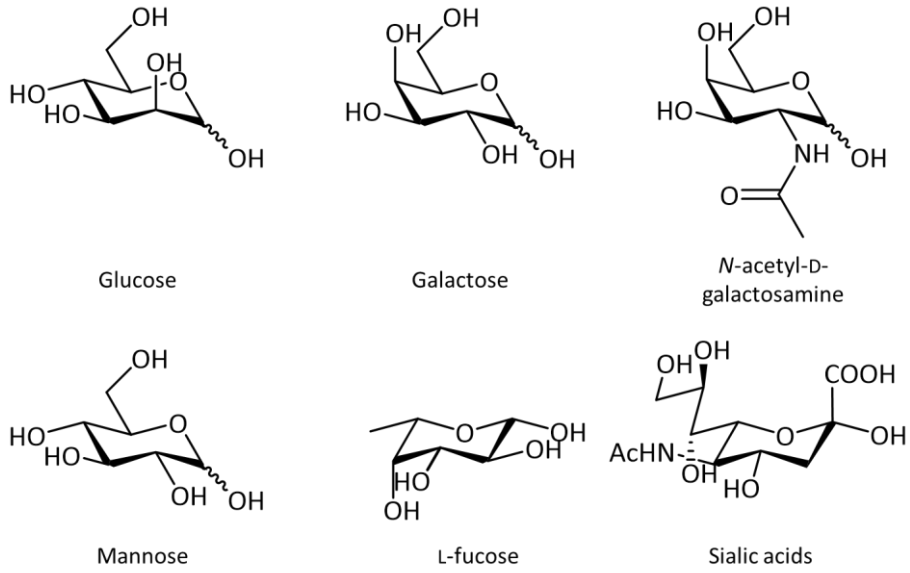

Figure 1.2. *Common cognate ligands of lectins.*

A sub-family that exemplifies these constraints are the galectin proteins. Galectins are a sub-group of the lectin family; there are 16 members with 12 being found in humans.[44] Despite the family's small size, the group has numerous native functions within organisms including adhesion, inflammation, and signalling, as well as being linked to several diseases.[45] These numerous disease links, some of which are presented in **Table 1.1**, highlight the potential of galectins as target analytes for sensor development. Galectins are synthesised in the cytosol and despite the lack of a signal sequence they are also found in the nucleus and outside the cell; this is suggestive of a nonclassical secretion pathway that does not involve the Golgi or endoplasmic reticulum.[46] This small group of proteins is characterised by a conserved β-galactoside binding site. β-galactosides are molecules with a galactose bound to another functionality via a glycosidic bond in the β arrangement, the most common is

lactose (**Figure 1.3**). This means galectin's primary binding partners include lactose, lactose derivatives (such as *N*-acetyllactosamine, LacNAc), and LacNAc epitopes of glycoproteins. These epitopes include several extracellular membrane proteins and are characterised by high levels of LacNAc at the glycoprotein surface. Galectins do exhibit some carbohydrate-independent binding via mechanisms that are not yet fully elucidated.[45]

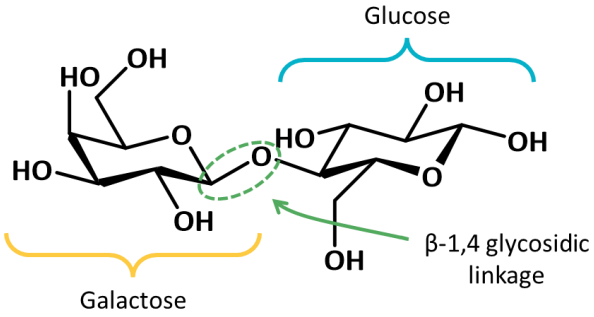

Figure 1.3. *Structural features of lactose, an example of a β-galactoside sugar.*

The CRD found in galectins contains around 130 amino acids residues and is made up of a sandwich of β-sheets.[47] There is a concentration of positive charge around the binding site (**Figure 1.4(a)**) and the key amino acids involved in binding are asparagine, histidine, arginine, tryptophan, and glutamic acid.[44] The 16 galectin proteins are classified into three sub-families (**Figure 1.4(b)**), based on the number and organisation of their CRDs: prototypes which have one CRD and exist as monomers or dimers; tandems which have two CRDs connected by a short peptide sequence; and chimeric which have multiple CRDs due to oligomer formation.[48] Galectin-3 is the only chimeric galectin, its N-terminal non-lectin domain is high in proline and glycine which enable the oligomerisation.[44] As mentioned above and demonstrated in **Figure 1.4(c)** there is high structural similarity between the classes which is the main contribution to the non-selective small molecule carbohydrate binding observed within galectins.

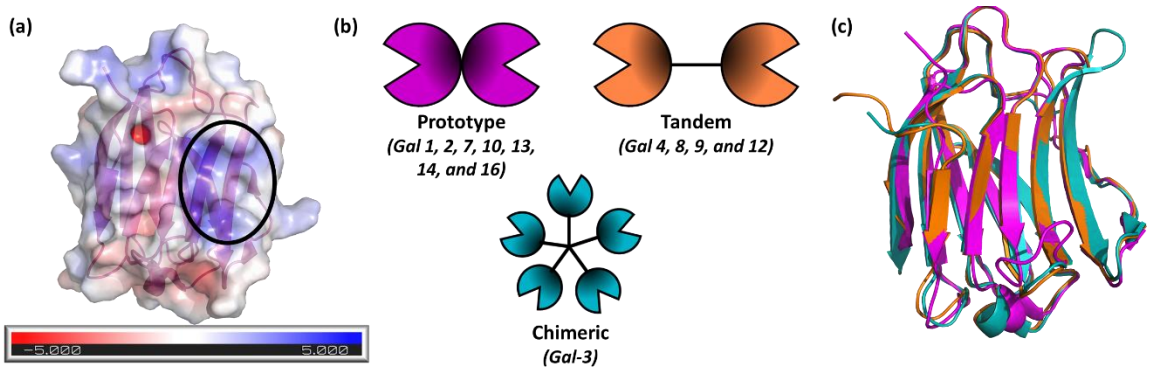

Figure 1.4.*(a) The charge surface of a galectin protein with the CRD domain circled in black, (b) schematic figures showing the three sub-families of galectin proteins, and (c) overlay of the CRDs of an archetypical prototype, tandem, and chimeric galectin protein. The same colour code is used in (b) and (c) – magenta for prototype, orange for tandem, and blue for chimeric. Protein structures are 5H9Q (a,c), 3NV1 (c), and 3ZSJ (c) in the PDB and correspond to a galectin-7, galectin-9, and galectin-3 structure.*[49–51]

Table 1.1. *Summary of the human galectins, their sub-classification regarding CRD, and the conditions where each galectin appears to play a role.*

Galectin	Type[52]	Associated Conditions	Ref.
1	Prototypic	Atherosclerosis, arthritis, cancers (breast, cervical, colorectal, head and neck, lung, lymphoma, melanoma, neurological, ovarian, and pancreatic), infection by HIV-1, inflammatory bowel disease (IBD), and pulmonary fibrosis.	32,44,53–55
2	Prototypic	Cancers (breast, colorectal, gastric, and thyroid) and coronary artery disease.	53,54,56
3	Chimeric	Alzheimer's disease, amyotrophic lateral sclerosis, atherosclerosis, cancers (bladder, breast, cervical, colorectal, endometrial, gastric, hepatocellular carcinoma, lung, lymphoma, melanoma, oesophageal, pancreatic, prostate, and thyroid), chronic obstructive pulmonary disease (COPD), cytokine release syndrome, diabetes, fibrosis (heart, kidney, liver, lung, nervous system, and skin), heart failure/cardiovascular disease, IBD, infection by HIV-1, inflammation, obesity, Parkinson's disease, pneumonia, rheumatoid arthritis, and sepsis.	32,44,54,55,57–59
4	Tandem	Cancers (breast, cervical, colorectal, gastric, head and neck, hepatocellular carcinoma, lung, pancreatic, prostate, and thyroid), diabetes, and IBD.	44,53–56
7	Prototypic	Cancers (bladder, breast, cervical, colorectal, endometrial, gastric, head and neck lymphoma, ovarian, neurological, prostate, and thyroid).	54

8	Tandem	Cancers (breast, cervical, colorectal, gastric, lung, melanoma, neurological, and prostate), inflammation, and thrombosis.	53–56
9	Tandem	Cancers (breast, cervical, colorectal, gastric, head and neck, hepatocellular carcinoma, lung, lymphoma, melanoma, neurological, and pancreatic), cytokine release syndrome, multiple sclerosis, myocarditis, and pulmonary fibrosis.	44,53,54,57
10	Prototypic	Asthma, esophagitis, periodontis, and various eosinophilic diseases.	44,60
12	Tandem	Cancer (pancreatic), diabetes, inflammation, and obesity.	32,54
13	Prototypic	Asthma and COPD.	61
14	Prototypic	Cancer (hepatocellular carcinoma).	54
16	Prototypic	Alzheimer's disease, cancers (breast, lymphomas, and myeloid leukemia), preeclampsia, and type 2 diabetes.	52

1.3. Galectin-3 in disease

As seen in **Table 1.1**, galectin-3 is the member of the galectin family which has been associated with the most diseases. This is possibly due to its unique chimeric form which enables biological functions exclusive to galectin-3; the formation of a chimeric structure in the extracellular space is vital for signal transduction within and between cells, and cell-matrix communication.[62] To-date, the diseases with the most focus on the link to galectin-3 are prostate cancer, thyroid cancer, and heart failure. Typically, enhanced levels of galectin-3 in the cytoplasm is indicative of disease progression, nuclear levels of galectin-3 do not show the same relationship, thus the localisation of galectin-3 is an important consideration when relating galectin-3 levels to disease.[46] Galectin-3 is secreted into biological fluids including serum, urine, and saliva; this secretion is increased by injured and inflamed cells.[44] This means there is the possibility of detecting galectin-3 in these fluids as a less-invasive means of diagnosis. In cancer, galectin-3 plays a multi-faceted role. As galectin-3 plays a role in cell-cell and cell-matrix adhesion, increased galectin-3 is indicative of cancer metastasis. Metastasis is the process of primary tumour cells detaching and aggregating elsewhere in the body where galectin-3 aids this adhesion. [46] Additionally, through a mechanism that isn't fully elucidated but is hypothesised to involve the phosphorylation of galectin-3 and the stabilisation of the mitochondria, increased galectin-

3 prevents cell apoptosis, reducing the efficacy of chemo- and radiotherapy.[63] Tumour growth is also aided by galectin-3 due to its role in angiogenesis (the development of new blood vessels).[62]

Prostate cancer is one of the most prevalent diagnosed cancers and the leading cause of deaths related to cancer in males.[64] In the UK, there are over 50,000 cases diagnosed per year and prostate cancer is responsible for around 12,000 deaths annually.[65] A study comparing galectin-3 levels in a control group and a group of prostate cancer patients showed a statistically significant increase in galectin-3 in patients' sera compared to the control group with an the average level of 0.29 ng mL^{-1} in cancer patients versus 0.01 ng mL^{-1} in non-cancer patients. Moreover, compared to prostate specific antigen (a common prostate cancer diagnostic biomarker) levels in the same subjects, galectin-3 more consistently distinguishes cancer and cancer-free patients.[66] However, in histological studies a decrease in galectin-3 was observed in cancerous tissues versus benign samples.[67] While further study is needed to fully elucidate the relationship between galectin-3 levels and prostate cancer, an alternative biomarker more reliable than prostate specific antigen, which struggles with accuracy providing both false-negatives and false-positives,[68] could enable national screening of this predominant disease.

In the UK, around 4000 people are diagnosed with thyroid cancer annually.[69] The exact role of galectin-3 in thyroid tumours is unknown but it is thought to be related to its role in regulating the cell cycle and its anti-apoptotic character.[70] Expression of galectin-3 is significantly higher in malignant thyroid tumours than in benign ones.[70] Many of these studies are histological, however one study examined serum galectin-3 levels which were found to be 3.04 ± 0.57 ng mL^{-1} for control patients and 10.22 ± 0.81 and 14.46 ± 0.3378 ng mL^{-1} for stage I and II thyroid cancer patients.[71] This suggests galectin-3 could be a valuable biomarker for thyroid cancer. A new, non-invasive diagnostic method for thyroid cancer would be an improvement on the current diagnostic method. Fine-needle aspiration biopsy, the current method, is painful to the patient causing bleeding and/or swelling and is not definitive in all cases.[72]

Heart failure affects over 60 million people worldwide and is challenging to diagnose as symptoms can be non-specific, physical examination is misleading, and more advanced diagnosis techniques are not available in all healthcare facilities.[73] Galectin-3 is released by

activated cardiac macrophages and initially prevents apoptosis of myocardial tissue, however prolonged inflammation, thus galectin-3 expression, results in deposits of collagen which form scar tissue in the cardiac ventricle.[74] A study looking at chronic heart failure found the level of galectin-3 in plasma to be 9.95 ± 2.8 ng mL^{-1} in patients with heart failure and 4.08 ± 1.3 ng mL^{-1} in the control population.[74] Another study suggests that a level of plasma galectin-3 above 17.8 ng mL^{-1} is associated with a higher chance of hospitalisation or death due to heart failure.[75] An aging population and lifestyle factors are likely to increase prevalence in what is already a disease associated with high mortality and costs.

Taken altogether, there is good evidence that it would be medically useful to develop a biosensor for detecting galectin-3.

1.4. Current approaches for targeting galectin-3

Outside of the sensor field, the traditional methods of detecting galectin-3 include the ELISA (enzyme-linked immunosorbent assay), immunohistochemical methods which use dye-labelled galectin-binding antibodies, a chemiluminescent immunoassay, and classic protein analytic methods including flow cytometry and western blotting.[46,76] The disadvantages of these methods are that they are time consuming, require sophisticated, expensive equipment, a skilled operator, and in some cases are only semi-quantitative.[46,76] These disadvantages preclude these types of detection methods in point-of-care applications. All these methods require antibodies in some way; therefore, it is not surprising that antibodies are established in the literature for targeting and sensing galectins. In an example by Primo *et al.*, anti-Gal3 antibodies were immobilised onto a gold substrate which had previously been modified with graphene oxide and 3-aminophenylboronic acid. The graphene oxide both immobilises the antibody and amplifies the response and the 3-aminophenylboronic acid orientates the immobilised antibody to increase recognition efficiency. Surface plasmon resonance detected the galectin-3 binding with a detection limit of 2 ng mL^{-1}.[73] Another example in work by Tang *et al.*, used anti-Gal3 antibodies in a sandwich-type electrochemical immunosensor. The capture antibodies were immobilised onto a modified glassy carbon electrode, and the detection antibodies were modified with methylene blue. Therefore, an electrochemical signal is generated when the methylene blue-modified antibodies bind to the captured galectin-3 on the electrode surface; this immunosensor had a detection limit of 33.33 fg mL^{-1}.[76]

Biology establishes selectivity in lectin binding through inducing variations in local glycan concentration as well as the 3-D presentation and multivalency of the binders.[77] Although the field of galectin-3 biosensors is still developing,[44] these, and other, factors have been exploited in a variety of sugar-based binders. Park *et al.* exploited nanomaterials which, as discussed above, enhance the affinity of a ligand due to improving binding geometry and increasing the number of binding sites; they showed increased binding sensitivity of galectin-3 to galactose when the sugar was conjugated to single-walled carbon nanotubes, with the binding range improving to 0.156 – 0.3125 ug mL^{-1} from 5 – 10 ug mL^{-1}.[78] Dendritic molecules are a strategy to exploit multivalent presentation of glycans, similar to that observed in biology. Martos-Maldonado *et al.* synthesised dendritic lactose-ferrocene conjugates which enhanced the binding interactions between lactose and galectin-3 due to high lactose presentation, and the induced signal because there are multiple ferrocene units participating in electron transfer.[79] Strategies designed to increase the presentation of the sugar help to increase binding, however, native sugars can undergo enzymatic hydrolysis or be recognised by other receptors which complicates the binding response observed in complex, unpurified biological samples.[80] Unnatural sugars or glycomimetics can alleviate these issues. One unnatural sugar used in the literature for galectin-3 sensing is β-D-galactopyranosyl-(1-1)-thio-β-D-galactopyranoside where the oxygen in the glycosidic bond is replaced with a sulfur. This molecule retains affinity for galectin-3 binding while possessing enhanced stability and specificity.[80]

1.5. Glycofluoroforms

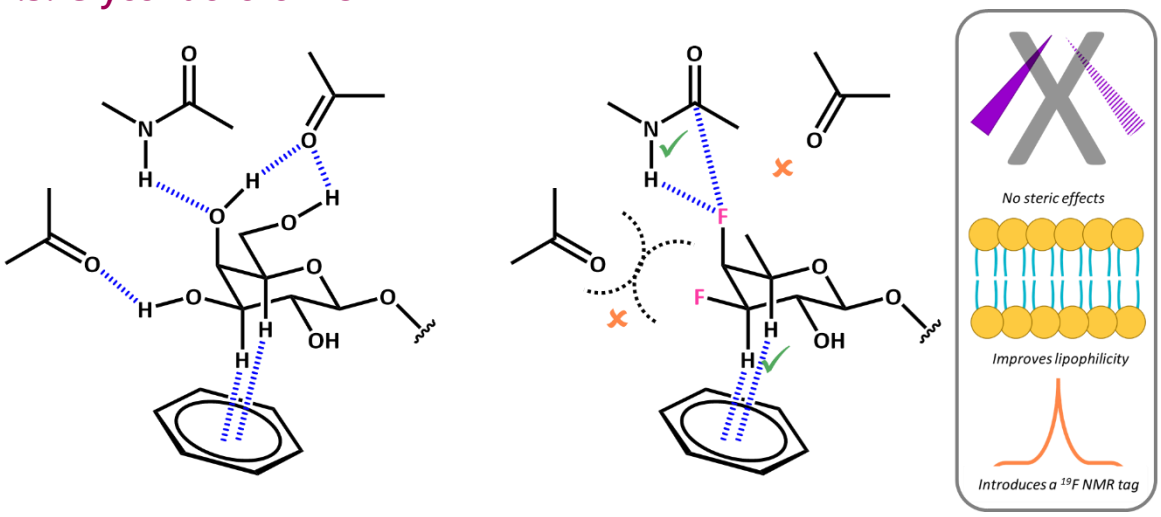

Figure 1.5. *Introducing fluorine modulates binding, has no steric effect, improves lipophilicity, and introduces an NMR tag. Binding modulation reproduced from [77].*

An emerging solution to the challenge of achieving selective galectin-binding to mono- and disaccharides is the use of glycofluoroforms (GFFs).[77] Glycofluoroforms are a type of unnatural glycomimetic where fluorine atoms are introduced into the carbohydrate scaffold. These modifications are generally deoxyfluorinations, the replacement of a hydroxy group with a fluorine, however sugar fluorination where a hydrogen is replaced with a fluorine is also common.[81] Typically mono, di, and tri- substitutions are observed. Generally, deoxygenation almost exclusively hinders binding. However, the replacement of a hydroxy group with a fluorine has a multitude of effects because the fluorine atom has hydrogen bond acceptor capability so only the donor ability is lost on this substitution (**Figure 1.5**).[81] Replacing the hydroxy group with a fluorine increases the hydrophobicity of that region of the molecule. This will also increase the lipophilicity of a molecule. Additionally, the resultant C-F bond is highly polarised as although oxygen and fluorine have similar electronegativities fluorine displays a unidirectional effect on the only the carbon atom, whereas the oxygen atom displays a bidirectional effect on both the carbon and the hydrogen atoms. Importantly, the atomic radii are similar, 1.47 Å for a fluorine versus 1.40 Å for a hydroxy group, which has been confirmed by 3-D studies.[82] This attractive combination of electronic modulation and minimal structural perturbation (a 'molecular editing' approach) has previously been applied in mechanistic and structure-activity relationship studies, as well as the construction of targeted probes and tools for structural biology, rational drug design and medicinal therapeutics.[81,83]

Table 1.2. *Library of lacto-N-biose derivatives and details (time, yield, enzyme quantities) of the enzymatic synthesis. A colour scale from yellow to pink showing low to high magnitudes of values is used.*

Cpd. #	Cpd. Structure	Time / h	Yield / %	m(enzyme added) / mg		Reaction volume / mL
				BiGalK	BiGalHexNAcP	
15	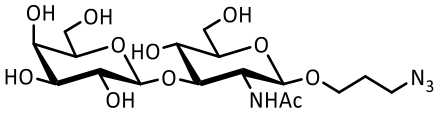	90	47	10.7	7.8	16.44
16	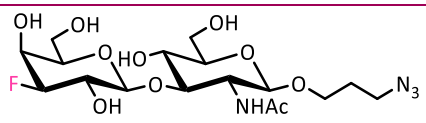	144	48	30.8	67.8	10.9

17	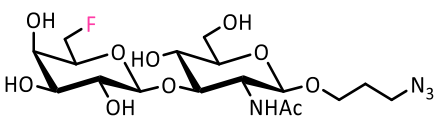	121	47	11	24.8	10.09
18	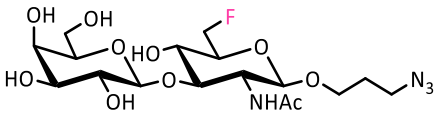	24	39	5	12	13
19	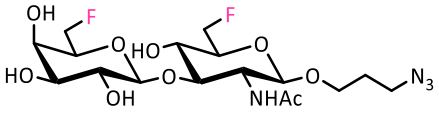	24	25	5	12	13
20	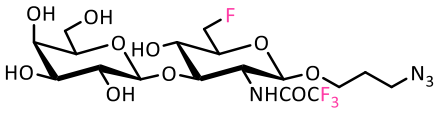	36	76	8	25	16.6
21	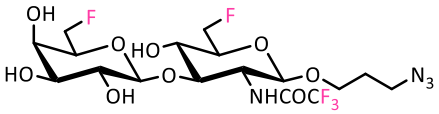	114	36	10	47.6	9.21
22	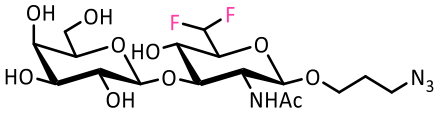	24	54	16.5	14.4	11.5
23	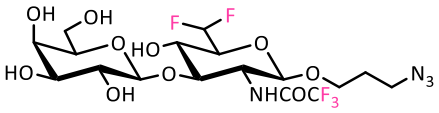	24	31	16.5	14.4	11

Recent work with the GFF class of glycomimetics involved the development of libraries of GFFs based on the same carbohydrate scaffold which are capable of selectively binding to different protein targets.[77,84,85] In particular, Richards *et al.* chemoenzymatically synthesised a library of nine fluorinated lacto-*N*-biose derivatives (**Table 1.2**) and studied the effect of fluorination on galectin binding.[84] The use of enzymatic synthesis to build the GFFs allows the incorporation of unnatural building blocks while maintaining the desired stereochemistry with relative ease over multi-step organic reactions. To produce GFFs, the enzymes must tolerate the addition of the fluorine at various points on the carbohydrate scaffold. BiGalK and BiGalHexNAcP have been identified as having high activity and appropriate promiscuity for these reactions.[86,87]

As well as incorporating the fluorine atoms into the carbohydrate scaffold, in the work by Richards *et al.*, an azido-propyl tether was also added for subsequent tethering. The native and fluorinated sugars were attached to a polymer containing both a strained alkyne handle for sugar tethering and a terminal thiol handle for gold nanoparticle attachment.[84] Gold nanoparticles are an established platform to assess glycan binding due to their unique optical properties and the fact that they require decreased quantities of glycans for binding

studies compared to techniques such as NMR or calorimetry.[88] The decorated nanoparticles (**Figure 1.6**) were used to study glycan-galectin interactions. This works as in the presence of galectin the nanoparticles aggregate due to the galectin-galectin interactions. This aggregation results in a red-blue colour shift observed in UV-Vis spectroscopy. For galectin-3, this analysis revealed compounds 16, 18, 22, and 23 showed higher affinity for galectin-3 than the native ligand (15). Compound 20 displayed lower affinity and the ligands with a fluorine at the 6-position on the galactose ring (compounds 17, 19 and 21) did not display any affinity for galectin-3. Kinetic examination of optical data revealed compound 16 also showed preferential binding kinetics. Further experiments using dynamic light scattering and biolayer interferometry confirmed these conclusions.

This therefore shows that compound 16, 3FGal-β(1,3)-GlcNAc, could be an attractive molecule to use as a BRE for a galectin-3 sensor. The selectivity of this ligand was evaluated by studying binding to galectin-7; an 8-fold decrease in binding affinity for observed. To quantify these differences apparent K_d values were calculated. When probing the binding between galectin-3 and the native ligand (15, Gal-β(1,3)-GlcNAc) and GFF 16, K_d was calculated to be 15.9±0.6 nM and 6.0±0.7 nM, respectively. Whereas, for galectin-7 the K_d for the glycofluoroform increased to 45.1±1.8 nM, showing a lower affinity for this ligand to galectin-7.[84] Therefore, a highly relevant clinical biomarker, galectin-3, and a suitable BRE, 3FGal-β(1,3)-GlcNAc, for this analyte have been identified and this thesis aims to explore these in electrochemical biosensing.

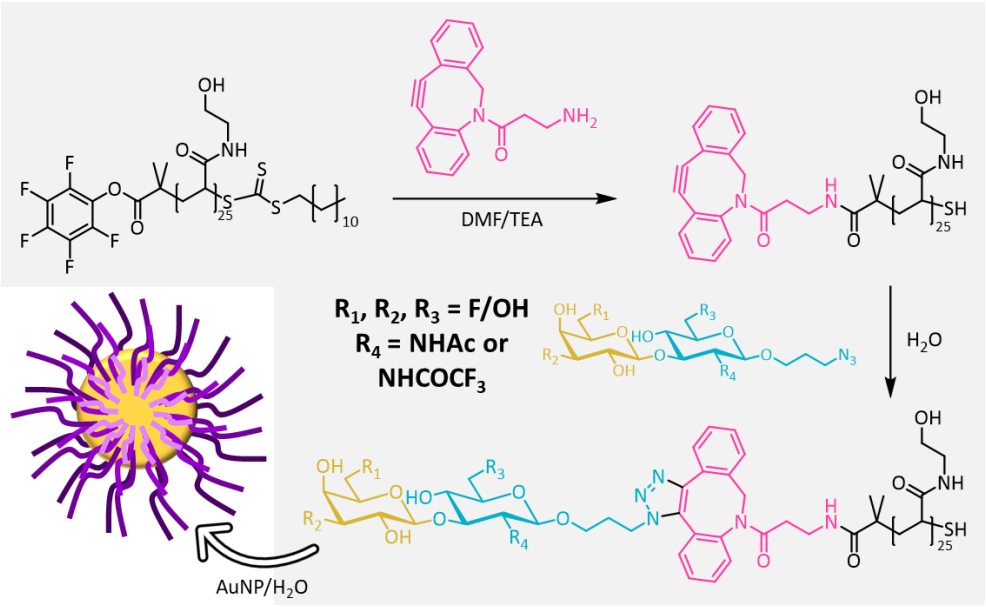

Figure 1.6. *Chemical scheme for the synthesis of the sugar-polymer conjugates and a schematic showing the modification of gold nanoparticles (AuNP).*

1.6. Thesis aims

The overall aim of this thesis is to develop electrochemical biosensors to detect galectin-3 binding to immobilised glycofluoroforms by examining how the electron transfer behaviour of solution-based potassium ferricyanide with the electrodes changes on analyte binding (**Figure 1.7**). 3FGal-β(1,3)-GlcNAc, a glycofluoroform previously identified to have increased affinity for galectin-3, will be immobilised onto an electrode to allow for the first examples of using this molecule as a biorecognition element in an electrochemical biosensor platform.

Chapter two aims to explore the possibility and optimisation of electrochemical characterisation and evaluation of the surface modification of screen-printed electrodes with polymer-glycofluoroform and the subsequent galectin-3 binding. The chemoenzymatically synthesised glycofluoroform will be conjugated to a thiol-terminated polymer via strain-promoted azide-alkyne cycloaddition. The resulting conjugate will be immobilised onto the electrode via spontaneously formed gold-thiol bonds. The modification and binding will be statistically assessed, and electrochemical impedance measurements will be used to characterise galectin-3 binding.

Chapter three will utilise triazabutadienes to explore covalently attaching the polymer-glycofluoroform to a carbon surface via diazonium electrografting; the covalent immobilisation strategy should provide improved sensor performance. The stability,

sensitivity, and electrode modification will be electrochemically interrogated and compared to the gold sensing platform.

Chapter four investigates if the triazabutadiene-mediated electrografting can expand the electrochemical transduction toolkit by enabling voltammetric study of galectin-3 binding. The ability of Fourier transformed alternating current voltammetry and purely sinusoidal voltammetry to produce a highly sensitive and rapid method of analysis suited for commercial applications will be tested.

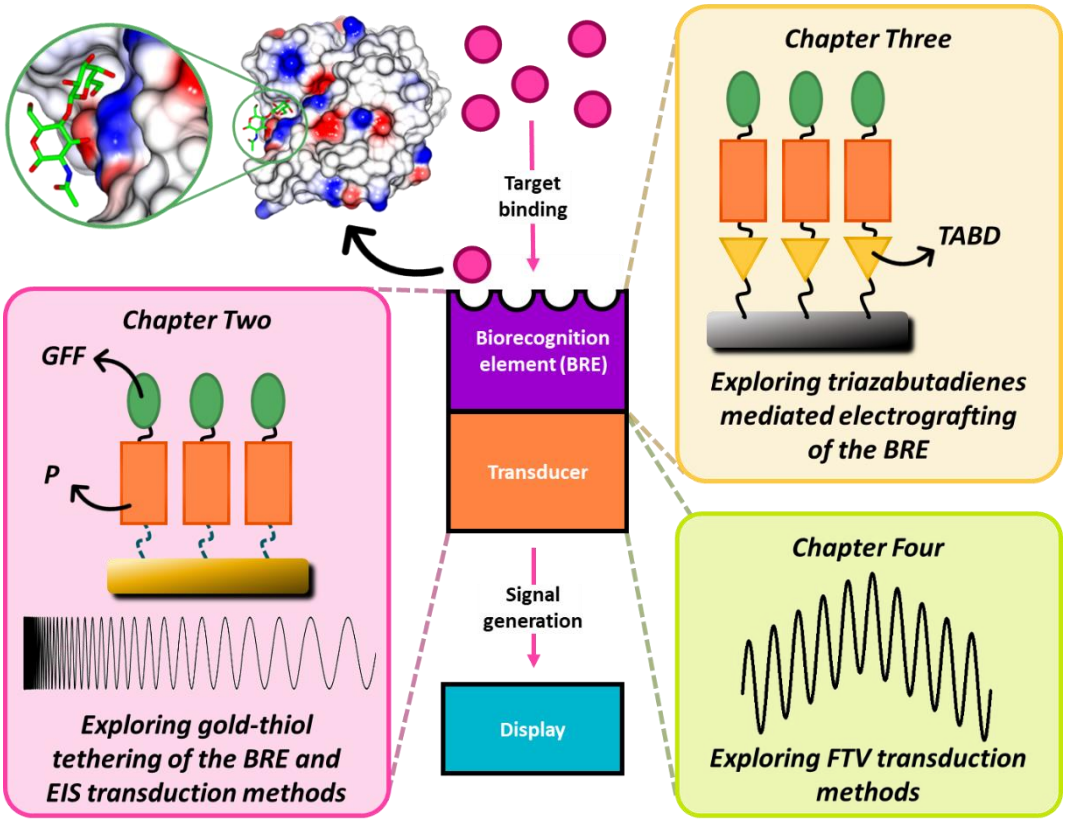

Figure 1.7. *Schematic overview of the biosensing platforms examined in this thesis highlighting each experimental chapter's focus regarding the biorecognition element and transducer of a biosensor. PBD showing galectin-3 ligand binding is 3ZSJ.*[51] *GFF = glycofluoroform, P = polymer, TABD = triazabutadiene, EIS = electrochemical impedance spectroscopy, and FTV = Fourier transformed alternating current voltammetry.*

NB: The non-sequential numbering of SPEs seen at points throughout this thesis is generally based on day-to-day experimental numbering. This was to allow the author to keep track of parallel experiments and the absence of numbers in a figure does not mean experiments have been omitted just that those SPEs would have corresponded to a different class of experiments.

Chapter Two: Development of a glycofluoroform-based galectin-3 electrochemical assay

This chapter describes the coupling of a glycofluoroform biosensor platform to an impedimetric electrochemical readout to detect the cancer-associated protein galectin-3. The introduction section provides background to electrochemical impedance spectroscopy, both the fundamentals of the techniques and its application to biosensing. The results show the first example of immobilisation of glycofluoroforms onto electrode surfaces, the development of novel and robust titration and impedimetric methods for galectin-3 detection, and the usage of Bayesian analysis to monitor experimental reproducibility and the uncertainty in applying an equivalent circuit to model the data.

This chapter is primarily based upon, and is an adaptation of, the paper 'Harnessing Glycofluoroforms for Impedimetric Biosensing' published in Chemical Science in September 2024. The author of this thesis, Alice R. Hewson, is the primary author and conducted all the novel in-lab research as well as writing the manuscript draft of the paper. The other author contributions to the manuscript were as follows: Henry O. Lloyd-Laney wrote the code used by the first author for the CMA-ES and MCMC analysis; Tessa Keenan synthesised, in addition to the first author, some components of the chemoenzymatic synthesis; Sarah-Jane Richards provided the polymer used in this and the following studies; Matthew I. Gibson and Bruno Linclau were (with Martin Fascione) PIs of BBSRC-funded 'Chemo-enzymatic Production of Specialty Glycans' project which underpins this work; and Nathalie Signoret, Martin A. Fascione, and Alison Parkin are the supervisors of Alice R. Hewson and thus provided project direction and manuscript edits and advice. Throughout this chapter, any collaborator contributions are clearly credited.

2.1. Introduction

As discussed in chapter one the fundamental components of a biosensor are its target, a biorecognition element (BRE), and the transducer. The target and BRE of the glycofluoroform galectin-3 detection system developed in this work were identified and discussed in chapter one. Therefore, this chapter introduction will focus on reviewing the benefits and drawbacks of electrochemical detection methods, with a specific focus on electrochemical impedance spectroscopy (EIS) as the transducer method. The fundamentals

underpinning EIS will be explained as well as analytical and implementation considerations and how it has been utilised in biosensing literature.

2.1.1. Electrochemical detection methods

In order to build a successful sensor, following target binding a signal must be generated to complete the sensing cascade. As shown in **Figure 2.1**, a wide variety of physical measurement methods including optical, electrochemical, mass-based, pyroelectric, piezoelectric, magnetic, and colorimetric have been implemented as transducers in biosensing,[89–91] with the three major types being optical, mass-based, and electrochemical.[9]

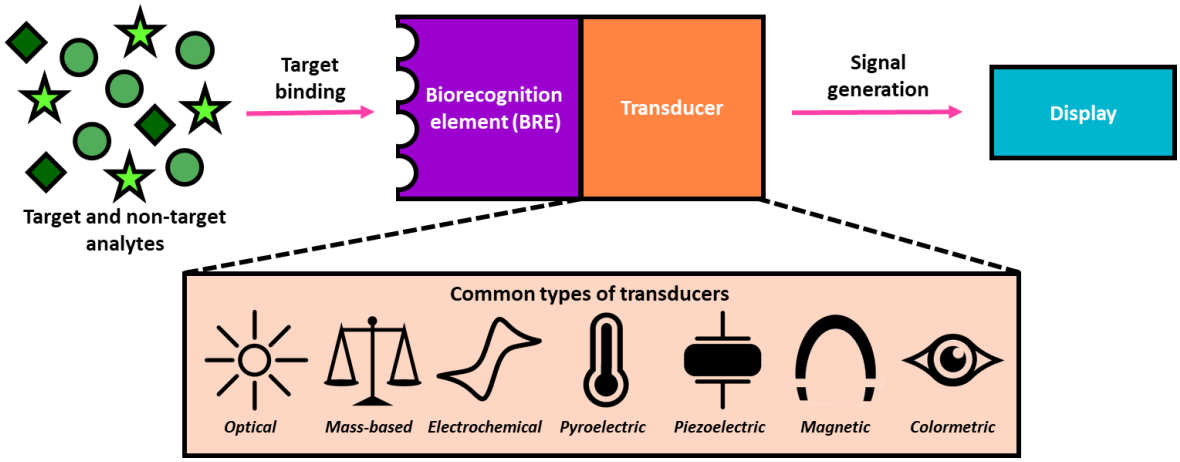

Figure 2.1. *Schematic diagram showing the varying components of a biosensor particularly highlighting types of transducers.*

Optical biosensors detect fluorescent, luminescent or refractive signals using techniques such as UV-Vis spectroscopy, surface plasmon resonance (SPR), and fluorescence resonance energy transfer (FRET).[92] They have high sensitivity, low noise levels, immunity to electromagnetic interference, and are easily operated remotely; however, they are both fragile and expensive.[93] Additionally, as the techniques rely on light-sensitive molecules they should be performed in controlled environments following training which precludes them from use in areas lacking sufficient healthcare infrastructure.[94] Mass-based techniques typically use piezoelectric crystals either in a quartz crystal microbalance or surface acoustic wave device (QCM or SAW), although sensors using mass spectrometry can also fall into this category. These techniques are highly sensitive to miniscule changes in mass and can be classed as a "label-free" detection method because they don't require any addition of photo- or redox-active additives for detection of an analyte. However, they are susceptible to mechanical instability and piezoelectric crystals have poor affordability. The drawbacks of using electrochemical techniques for sensor signal transduction are: (i) the signals are

susceptible to electromagnetic interference; (ii) the electrode surface can be vulnerable to fouling which can lead to a limited shelf life; (iii) devices will require an external energy input; and, (iv) depending on the precise electrochemical technique, in some cases a long detection time may be required.[95] However, the advantages of electrochemical biosensors are numerous including high sensitivity, low production cost, ease of use, simpler instrumentation requirements, fast responses, and that generally little-to-no chemical workup is required when testing.[3,94,96] All of these advantages make electrochemical biosensors suitable for point-of-care diagnostics and healthcare environments with less developed infrastructure. In fact, electrochemical biosensors are of particular interest because the opportunity exists to interface smart phone devices with very low cost electronic circuit boards and screen-printed electrodes (which are affordable and decrease required sample volumes)[94] to generate affordable potentiostats that can readily upload data into the cloud.[97–99] Indeed, modern diabetic glucose sensors essentially operate on this principal, uploading the data from enzyme-based electrochemical monitoring of glucose levels direct to a user's smart phone.[100]

As electrochemistry is a broad field with applications beyond sensing including mechanism determination, electroanalysis, bioelectrochemistry, battery technologies, and corrosion studies, a variety of signal measurement archetypes are present in the literature.[101,102] In general, sensors are either potentiometric, amperometric, voltammetric, conductometric, impedimetric or coulometric.[103] In the work described in this chapter, the chosen detection method is electrochemical impedance spectroscopy. This is because the application of a small amplitude sinusoid ensures no destructive effects within the measurement, there are rapid quantitative methods for data analysis, and it is a well-established method in biosensing literature.[104,105] In subsequent experimental chapters, a broader range of measurement techniques will be explored.

2.1.2. Electrochemical impedance spectroscopy (EIS)

Many electrochemical sensing measurements use a three-electrode cell, where the sensing process occurs at the working electrode, the potential of the working electrode (WE) is measured relative to that of a reference electrode (RE), and a counter/auxiliary electrode (CE) balances the current flow (**Figure 2.2(a)**). There are two main configurations used in electrochemical biosensing experiments, either (i) a 'non-faradaic' set-up, where there is no

formal electron transfer process, and instead just the charging of the electrode-electrolyte interface is probed (i.e. all current is so-called 'non-faradaic' current); or (ii) a 'faradaic' set-up, where the electron transfer to/from a redox-reactive reagent is probed, and therefore both non-faradaic and faradaic current contribute to the experimental measurements. A faradaic set-up is more commonly encountered, presumably because the theory around modelling faradaic electron transfer is highly developed,[102] and because non-faradaic electrochemical impedance biosensors require measurements at low frequencies and these are significantly impacted by high electrochemical impedance and resulting leakage currents.[106] Additionally, non-faradaic EIS typically has lower sensitivity as capacitance changes are small and often indistinguishable from non-specific binding interactions or from the changes due to molecules being trapped at the electrode surface during binding events.[107] Therefore, in this work only faradaic EIS is used.[108] The aim of this chapter is to use EIS to detect galectin-3 binding to a glycofluoroform; because both of these molecules are redox-inert, the experiments in this chapter are run by spiking the buffer solution with a chemical redox-active probe, as illustrated in **Figure 2.2(a)**. This is a common approach in the electrochemical biosensing literature.

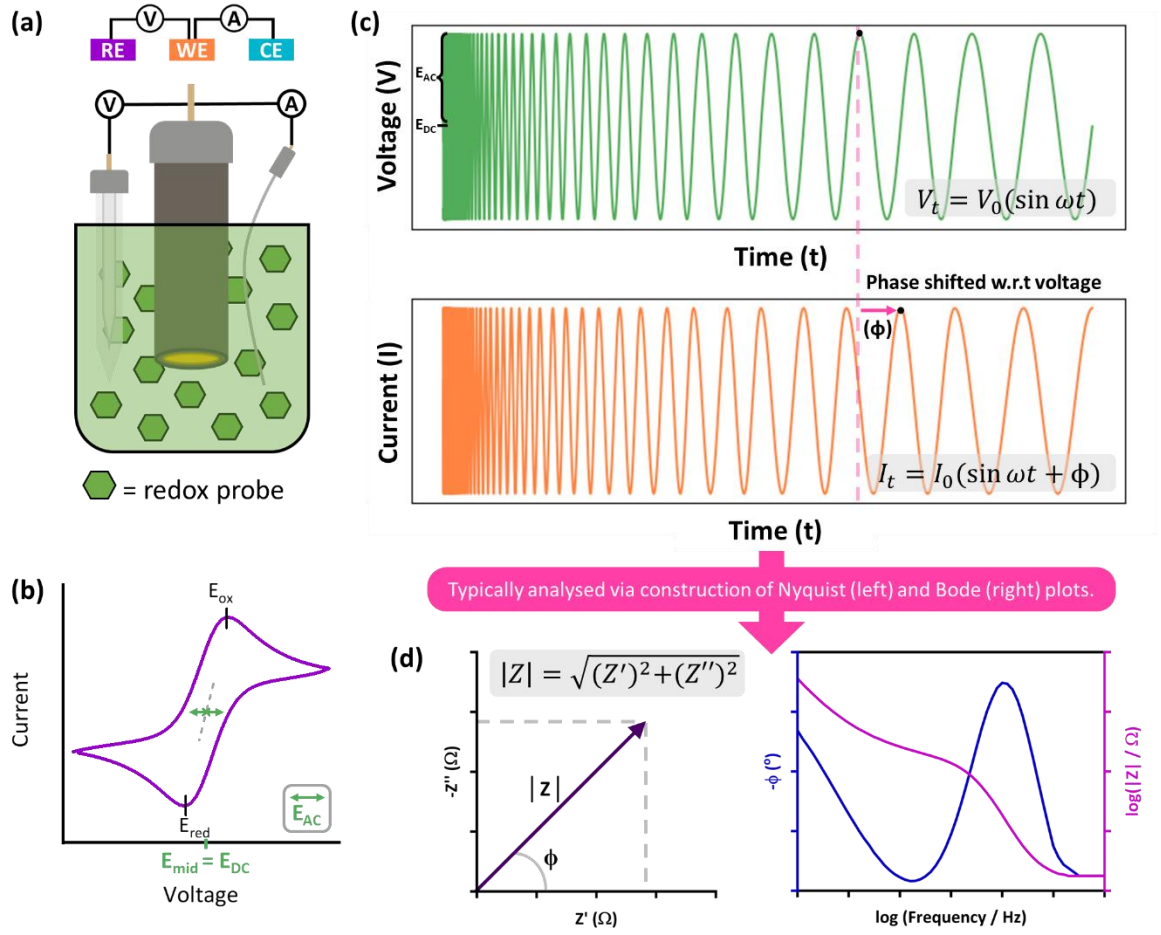

Figure 2.2. *(a) Illustration of an electrochemical cell in a 3-electrode configuration, (b) direct-current cyclic voltammogram of a soluble redox reagent, (c) the applied voltage-time and resultant current-time of an EIS experiment highlighting the phase shift, and (d) the common visualisation of EIS data: Nyquist (left) and Bode (right) plots. RE = reference electrode, WE = working electrode, CE = counter electrode, ω = angular frequency, ϕ = phase shift, and Z = impedance (': real, '': imaginary).*

Electrochemical impedance spectroscopy (EIS) is a highly sensitive and quantitative method that is used to measure and provide mechanistic insight into changes taking place on the electrode surface. The technique measures the opposition to current flow, i.e. the impedance, in the experimental system. The EIS experiment works via the application of a small amplitude sinusoidal voltage-oscillation (V_t) of changing frequency (ω) to the working electrode, with measurement of the resultant current (**Figure 2.2(c)**).[104] Practically, this involves selecting (i) the midpoint voltage of the sinusoidal oscillation, often defined as the dc-potential (E_{DC}, **Figure 2.2(b)**); (ii) the amplitude of the voltage oscillation (typically 10 mV), V_0 in Equation 2.1 but also referred to as the ac-potential (E_{AC}) within EIS instrument software; and, (iii) the frequency range of the experiment, which generally spans multiple orders of magnitude, with measurements taken at regular logarithmic intervals within this range.

$$V_t = V_0 \sin(\omega t), \text{ where } \omega = f(t) \qquad \textit{Equation 2.1}$$

$$I_t = I_0 \sin(\omega t + \phi) \qquad \textit{Equation 2.2}$$

where: V_t: voltage as a function of time (V); V_0: voltage amplitude (i.e E_{AC}) (V); ω: angular frequency (rad s^{-1}); I_t: current as a function of time (A); I_0: current amplitude (A); t: time (s); ϕ: phase shift between V-t and I-t functions (rad)

When EIS is being used to probe an electrochemical cell which contains a chemical redox-active probe capable of reversible electron transfer, setting E_{DC} to the midpoint potential determined by cyclic voltammetry (**Figure 2.2(b)**) and allowing an equilibration time ensures the system is being probed at equilibrium or steady state.[109] The use of a small amplitude in the voltage-time oscillation means the electrochemical cell response is assumed to be pseudo-linear, i.e., the current response (I_t) has the same frequency (ω) as the applied potential but with a phase shift (ϕ), Equation 2.2 (**Figure 2.2(c)(ii)**).[110] Compared to other electrochemical methods such as cyclic voltammetry (CV) and differential pulse voltammetry (DPV), EIS is less destructive to the surface-immobilised biological system because the measurement occurs within a narrower potential window.[111] Because the current at a given frequency is related to processes occurring at timescales of the inverse frequency (e.g., f = 10 Hz, t = 0.1 s), EIS measurements also enable facile differentiation between faradaic and non-faradaic processes which should enhance the sensitivity of the measurement.

2.1.2.1. Calculating impedance

The conventional mode of analysis in EIS is to assess the impedance response, where impedance (Z) is the ratio of voltage (V) and current (I).[112] Impedance can therefore be expressed in two key ways: using Euler's relationship (Equation 2.3), and in a manner analogous to Ohm's Law (Equation 2.4). The existence of these two equations leads to the two most common ways of plotting impedance data, the Nyquist plot and the Bode plot.

$$Z(\omega) = \frac{V(\omega)}{I(\omega)} = Z_0 \, exp(j\phi) = Z_0(\cos\phi + j\sin\phi) = Z_{Re} + jZ_{Im} \equiv Z' + jZ'' \qquad \textit{Equation 2.3}$$

$$Z_t = \frac{V_t}{I_t} = \frac{V_0}{I_0}\frac{(\sin\omega t)}{\sin(\omega t + \phi)} \qquad \textit{Equation 2.4}$$

$$|Z| = \sqrt{{Z_{Re}}^2 + {Z_{Im}}^2} \equiv \sqrt{Z'^2 + Z''^2} \qquad \textit{Equation 2.5}$$

2.1.2.2. Nyquist plot

As shown in Equation 2.3, by considering the ratio of voltage to current at each frequency an equation can be derived in which the total impedance, Z, is a complex quantity that is expressed in terms of a real component, Z_{Re}, and an imaginary component, Z_{Im}, where *j* is the imaginary number. The Nyquist plot is generated by graphing the real component (Z_{Re}, sometimes referred to as Z′) on the x-axis and the imaginary component on the y-axis ($-Z_{Im}$, sometimes referred to as -Z′′), where each point on a Nyquist plot is an impedance measurement at a single frequency.[110] The negative value of the imaginary impedance contribution is plotted to allow for easier visualisation as these contributions generally take a negative value. The shape of the Nyquist plot is characteristic of the behaviour of the electrochemical system under investigation and can be used to determine the contribution of individual processes to the total impedance. Due to the importance of the shape of the Nyquist plot and the fact impedance is dependent on ϕ, Nyquist plots are traditionally plotted on orthonormal axes, meaning the x- and y-axes use the same scale. This helps visual interpretation of the data and allows for the calculation of the impedance at a specific point on the curve (Equation 2.5).[113]

2.1.2.3. Bode plot

Alternatively, as shown in Equation 2.4, impedance can be expressed in terms of the magnitude of the impedance, Z_0; phase shift, ϕ; and frequency, ω. An analysis of EIS data based on this equation leads to Bode plot(s) which show the logarithm of the total impedance ($\log Z_0$) on one y-axis, the phase shift ($-\phi$) on a second y-axis, both plotted versus the logarithm of the frequency ($\log \omega$) either on a common x-axis, or two separate stacked x-y plots.[114] The Bode plot shows how the impedance, and therefore the behaviour of the system, changes with frequency.[105] In a Bode plot an ideal resistor would have a constant phase angle of 0^o, an ideal capacitor would have $\phi = -90^o$ and an ideal inductor would have $\phi = +90^o$. Thus, the values of the phase angle show what type of electrochemical behaviour dominates as a function of frequency. The concept of modelling an experiment as a sum of different circuit elements is described as "equivalent circuit fitting", as detailed in the following section.

2.1.2.4. Equivalent Circuit Fitting

Equivalent circuit fitting is a traditional way of analysing EIS data. It essentially breaks down the electrochemical reaction happening at the electrode-solution interface into individual

circuit components connected together to model the whole system.[105] Common circuit elements encountered in electrochemical impedance spectroscopy modelling along with their mathematical definition, the phase angle the component exhibits, and their frequency dependence are presented in **Table 2.1**. Using an appropriate equivalent circuit model allows a simple algebraic solution for Z′ and -Z′′ as a function of the applied frequency and avoids the numerical calculation methods required to simulate other types of electrochemical data. This rapid analysis method is another reason to favour using an impedimetric transducer technique over other electrochemical measurements in electrochemical biosensing devices.[115]

Table 2.1. *Common equivalent circuit fitting elements.*[102,104,116–118]

Circuit element	Symbol	Mathematical definition	-Phase angle / °	Frequency dependent?
Resistor	R	$Z_R = R$	0	✗
Inductor	L	$Z_L = j\omega L$	-90	✓
Capacitor	C	$Z_C = {}^{1}/_{j\omega C}$	90	✓
Constant phase element	CPE / Q	$Z_{CPE} = {}^{1}/_{A(j\omega)^{\alpha}}$	0 – 90	✓
Warburg element	W	$Z_W = {}^{\sigma}/_{\sqrt{\omega}}(1-j)$ $where\ \sigma = \frac{RT}{n^2F^2\sqrt{2}}\left(\frac{1}{\sqrt{D_O}c_O} + \frac{1}{\sqrt{D_R}c_R}\right)$	45	✓
Gerischer element	G	$Z_G = {}^{G}/\sqrt{k + j\omega}$	0 - 90	✓

where: R: resistance (Ω); L: inductance (H); C: capacitance (F ≡ C V^{-1}); j: imaginary unit; ω: angular frequency (rad s^{-1}); A: electroactive area (cm^2); α: dispersion coefficient; σ: Warburg coefficient (Ω s$^{1/2}$); R: gas constant (J K^{-1} mol^{-1}); T: temperature (K); n: nº of electrons; F: Faraday's constant (C mol^{-1}); D_O: diffusion coefficient of the oxidised species (cm^2 s^{-1}); c_O: concentration of the oxidised species (mol cm^{-3}); D_R: diffusion coefficient of the reduced species (cm^2 s^{-1}); c_R: concentration of the reduced species (mol cm^{-3}); G: Gerischer coefficient (Ω s$^{-1/2}$); k: reaction rate (s^{-1})

The first three circuit elements in **Table 2.1** are based on real circuit components whereas the following elements don't exist as single electronic components but have been developed as theoretical circuit elements commonly used in EIS simulations because they

mathematically describe more complex behaviours that are observed in real electrochemical systems.

Of the simple circuit elements, resistors are components that limit or regulate current flow and are used to describe electron transfer across interfaces. Inductors are components that resist changes in current and represent magnetic inductance. Capacitors are components that store charge and describe non-faradaic charging at an interface. Of the theoretical modelled circuit components, the constant phase element (CPE) is an imperfect capacitator, i.e. an element that shows a more complex relationship to frequency than an ideal capacitor, this is a more accurate description of capacitive behaviour observed in electrochemical experimental systems.[102,104,109,116–120] The Warburg element is a CPE where the phase angle is constricted to -45° and is used to model any processes where the redox species must be transported to an interface via diffusion. Often chemical changes accompany an electrochemical change and these chemical processes will alter the overall impedance; the Gerischer element is used in equivalent circuit models to account for the EIS response of such systems.

2.1.3. Impedimetric biosensing

The impedimetric biosensor field has grown rapidly in the 21st century until 2019, as shown by **Figure 2.3**. A 2014 review paper reported the use of different impedimetric biosensors to detect 147 target molecules.[121] Most impedimetric biosensors are defined as "affinity-based" sensors, meaning the EIS is used to detect surface-based changes to the working electrode.[122] Affinity-based impedimetric biosensors have been shown to be suited to a broad range of biological analytes ranging in size from small biomolecules, such as sugars and hormones, to large proteins, such as lectins, immunoglobins, and antibodies, to whole cells, and even whole organisms such as *E. coli*, *B. anthracis,* and SARS-CoV-2. [121,123–126]

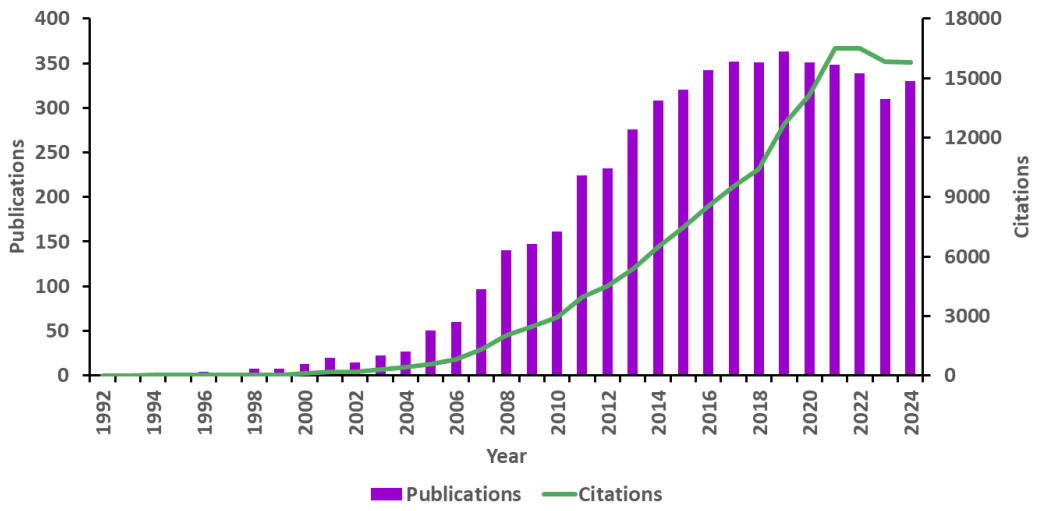

Figure 2.3. *Numbers of publications and citations relating to impedimetric biosensing over the past 20 years. The search was performed with the key words 'impedance spectroscopy' and 'biosensor' on Web of Science.*

For affinity-based impedimetric biosensors using a redox-active probe the Nyquist plot data is normally interpreted by reference to the Randles circuit (**Figure 2.4**). In the Randles circuit model, it is assumed that applying a potential between the reference and working electrodes leads to the movement of ions in solution, which is governed by a solution resistance, R_s, which is controlled by the solution conductivity and the distance between electrodes. The different ions in solution can then generate current via two distinct processes. Capacitive (or non-faradaic) current is caused by the charging and discharging of the electrochemical double layer at the working electrode-solution interface, i.e. the formation of a gradient in the concentration of ions moving away from the electrode surface, modelled in the Randles circuit by a CPE to reflect the non-idealities between the observed behavior of real electrochemical systems and a perfect capacitor. The second current contribution is faradaic current, the current which arises from an electron transfer process between the electrode and a redox active molecule changing oxidation state. Faradaic current is therefore limited by both (i) the rate of electron transfer, represented in the Randles circuit by the charge transfer resistance, R_{ct}, and (ii) the rate of diffusion of the solution phase redox active species to the electrode, represented by Z_W in the Randles circuit.[121]

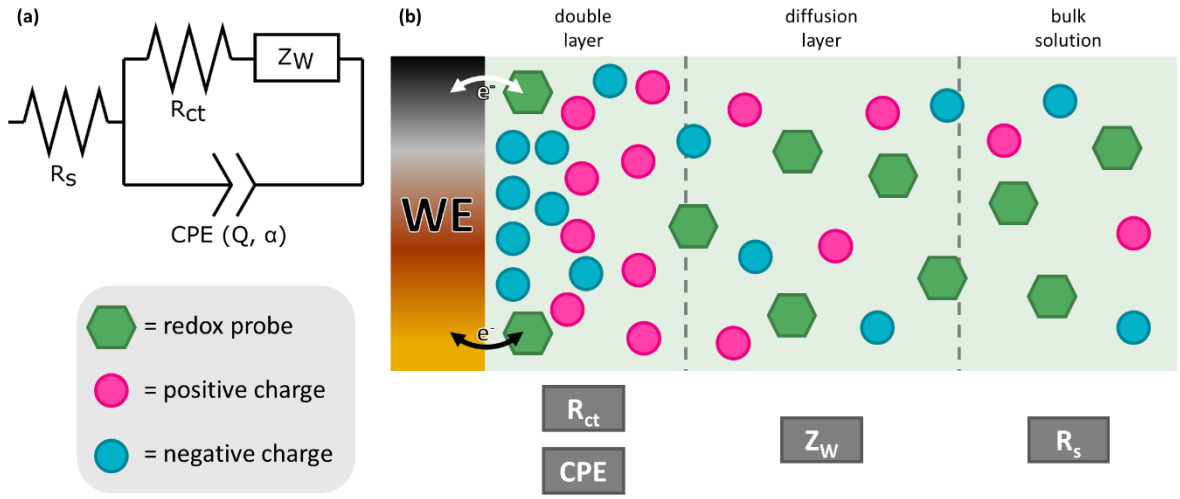

Figure 2.4. *(a) The Randles equivalent circuit model to model (b) double-layer arrangement typically of solution electrochemistry (simplified representation) where R_s is solution resistance, R_{ct} is resistance to charge transfer, Z_W is a Warburg element, CPE is a constant phase element, and WE is the working electrode.*[121]

Each of the physical and chemical processes which contribute towards current generation (diffusion of different ions, oxidation state change) occur on different timescales, and so different regions of the Nyquist and Bode plots (**Figure 2.5(a)** and **(b)**) report on different processes. In the low impedance region of the Nyquist plot (left-hand side) there is a semi-circle region which reports on processes limited by electron transfer. In the high impedance region, there is a linear portion which reports on diffusion limited processes.[105] Moreover, the diameter and height of this semi-circle region can be used to qualitatively compare the amount of resistance and capacitance in different systems, as seen in **Figure 2.5**. The Bode plot shows how the frequency and magnitude of impedance change with frequency (**Figure 2.5(b)**). At high frequencies (right-hand side of the plot) the plot is reporting on solution resistance so will have lower magnitude and a phase angle close to 0°. In the mid frequency region, the plot is reporting on capacitive behaviour with the magnitude of impedance increasing and the phase angle approaching 90°. At lower frequencies the data is reporting on the charge-transfer process(es), with a phase angle close to 0° reflecting the frequency range of the experiment that is dominated by the resistance to charge transfer and the frequency range with a phase angle close to 45° showing where the experimental process is under diffusion control. These two parts of the charge-transfer process are less distinguishable in the impedance magnitude part of the Bode plot but a slight difference in gradient can be observed. Warburg diffusion isn't always observed as it is not always possible to collect data at a sufficiently low frequency.[104,109,127,128] The phase portion of a

Bode plot is particularly useful in providing information about the surface modification of a working electrode. The maximum phase angle gives an indication of the quality of the modification; since $-\phi = 90^{o}$ reflects ideal capacitive behaviour and therefore is indicative of a well-ordered and well-packed monolayer. Additionally, shouldering is often most easily seen in this plot, this means there are multiple processes with different time constants that aren't fully resolved; the presence of many individual processes is suggestive of inconsistent electrode surface modification.

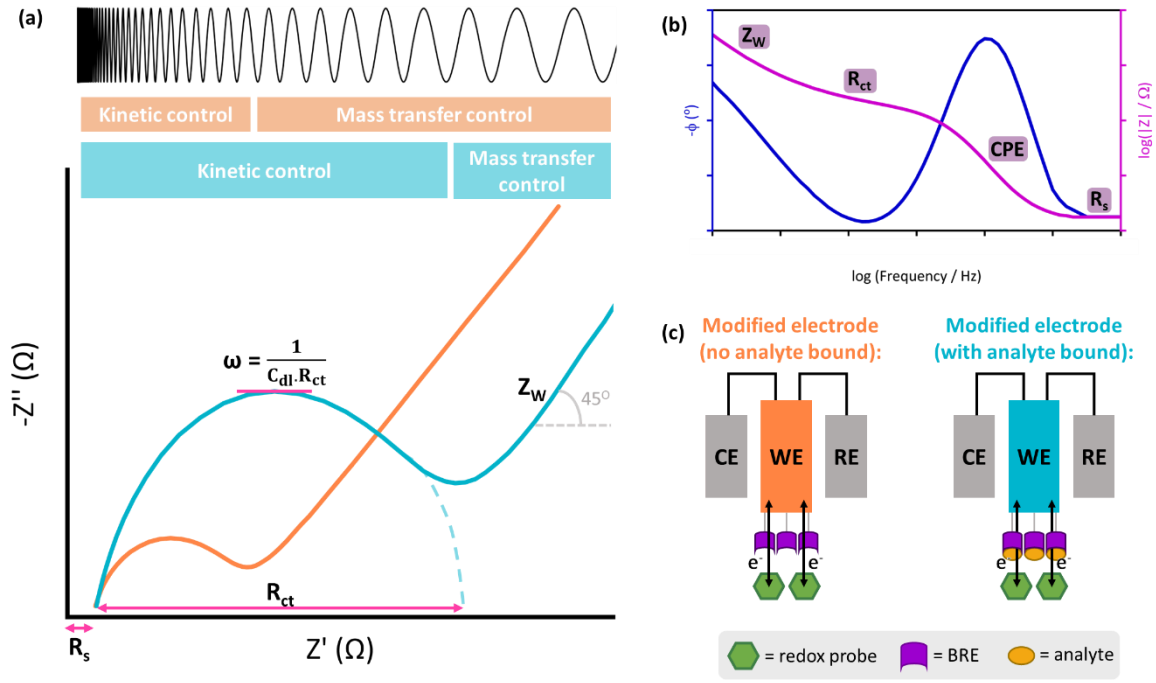

Figure 2.5. *Annotated (a) Nyquist and (b) Bode plots representative of the behaviour of the Randles circuit, highlighted are different regions of behaviour and how the values of the elements are calculated from the Nyquist plot. (c) Schematic diagrams showing the binding of the target analyte to the biorecognition element, the simplest response to this binding event is shown in (a) where the orange line is the response for no analyte bound and the blue line is the response for analyte bound. R_s = solution resistance, R_{ct} = resistance to charge transfer, ω = angular frequency, C_{dl} = double layer capacitance, Z_W = Warburg element, CPE = constant phase element, BRE = biorecognition element, and CE, WE, and RE are the counter, working, and reference electrodes respectively.*

Simplistically, it would be assumed that adsorption events on the surface of the working electrode increase R_{ct} (**Figure 2.5(a)** and **(c)**) (and vice versa desorption events decrease R_{ct}). Hypothesising that when the affinity complex between an analyte and a biorecognition element on the surface of the electrode is formed, the movement of the spiked solution redox probe to the electrode surface is hindered. This causes a corresponding decrease in electron transfer rate and results in an increase in electrochemical impedance which is quantitatively observed as an increase in R_{ct}.[129] However, depending on the redox probe and

the structure of the monolayer this may not be the case. For example, in electrochemical biosensors using single-strand DNA or RNA biorecognition elements, desorption of a short chain analyte molecule can lead to channels which facilitate electron transfer and decrease resistance, but desorption of a long and flexible analyte molecule could induce coils or helices that physically block the surface and increase resistance.[130] The nature of the redox probe and the working electrode surface is also important, with electrostatic interactions between the probe and the surface also playing a key role in determining the EIS response of a biosensor.[131] For example, detecting the presence of a cationic protein on an electrode surface with a anionic redox probe (e.g. sensing lysozyme with potassium ferricyanide as the redox probe) will result in an decrease in R_{ct} as a function of protein concentration because the electrostatic attraction between the redox probe and the electrode increases as more analyte binds to the working electrode. Therefore in biosensing EIS experiments the identity of the chosen redox probe (potassium ferricyanide is the most common)[132] can play a crucial role in determining the response of the sensor to analyte because it can interact with the monolayer in different ways depending on electron-transfer mechanism, electrostatics, and concentration.[130,133,134] This shows that while electrochemical impedance spectroscopy is a highly suitable detection method, care and consideration is needed when implementing the method and analysing the output.

2.2. Aims

The role of glycans in biological communication is unexplored in the biosensor field. This chapter aims to highlight the utility of glycofluoroforms, unnatural sugar molecules with enhanced galectin-3 selectivity, as biorecognition elements. This chapter aims to combine these molecules and electrochemical impedance spectroscopy studies in a novel sensing platform. To achieve this several objectives will be explored:

1. Exploration of the best methodologies for synthesising and determining the purity of the glycofluoroform and electrode types to develop the target sensor.
2. Usage of electrochemical methods to characterise both bare and modified electrode surfaces including monitoring reproducibility and parameter uncertainty by equivalent circuit, CMA-ES and MCMC fitting.
3. Optimisation of the best redox probes to use for titration experiments with regards to stability, sensitivity, and experimental ease.

4. Comprehensive galectin-3 binding analysis to investigate selectivity and specificity of analyte binding to electrode surfaces. Quantification of binding will be explored with two binding models to assess the affinity of the immobilised glycofluoroform to galectin-3.

2.3. Results and Discussion

2.3.1. Successful immobilisation of a galectin-3 detecting glycofluoroform onto screen-printed electrodes

Inspired by a previous study,[84] a galectin-3 EIS biosensor was assembled by immobilising the glycofluoroform 3F-Gal-β(1,3)-GlcNAc-N_3 (GFF) on a 'thiophilic' gold SPE (screen-printed electrode), using a thiol terminating poly(hydroxyethyl acrylamide) polymer as an intermediary platform to maximise display of the ligand on the surface. The polymer was supplied by Dr S-J Richards (University of Manchester) and a DBCO (dibenzocyclooctyne) strained alkyne incorporated within the polymer could be subjected to strain-promoted azide-alkyne cycloaddition (SPAAC)[135] to efficiently attach the azide containing GFF prior to surface immobilisation, with the polymer intermediary also potentially passivating the electrode and beneficially minimising non-specific interactions during detection of the analyte.[136] The first steps were to synthesise the glycofluoroform via chemoenzymatic synthesis, and determine the best electrodes to utilise for electrochemical studies.

2.3.1.1. Expression and purification of BiGalK and BiGalHexNAcP

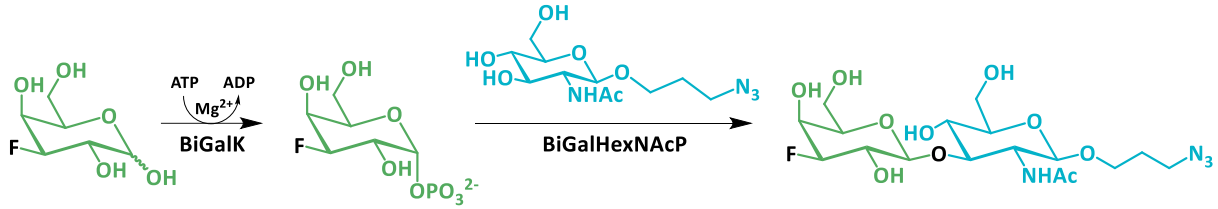

Scheme 2.1. *Reaction scheme for the chemoenzymatic synthesis of the fluorinated disaccharide, 3FGal-β(1,3)-GlcNAc-N_3 (GFF).*

The first stage of the enzymatic synthesis (**Scheme 2.1**) was the expression and purification of the two enzymes required: BiGalK and BiGalHexNAcP. BiGalK catalyses the phosphorylation of 3F-galactose, a commercially available unnatural (but tolerated) substrate. BiGalHexNAcP catalyses the transfer of phosphorylated galactose to a N-acetylglucosamine acceptor, provided by Dr N. Hatton and J. Fair from the Fascione group (University of York), by reverse phosphorylysis.[84] Although based on published procedures,[137,138] as the proteins were overexpressed from freshly transformed cells

expression tests were carried out to determine the efficacy and localisation of the expression. The plasmids were overexpressed in BL21 DE3 chemically competent cells and induced by addition of isopropyl-β-D-1-thiogalactopyranoside (IPTG) to a final concentration of 0.2 mM for BiGalK and 0.1 mM for BiGalHexNAcP. SDS-PAGE was carried out on both samples, shown in **Figure 2.6**. There is clear overexpression for BiGalK (m=45.8 kDa for the His-tagged protein)[139] in the induced soluble bands at around 45 kDa in **Figure 2.6(a)**. For BiGalHexNAcP (m=86.5 kDa for the His-tagged protein)[140], **Figure 2.6(b)**, it is less visible due to gel processing issues however there are bands between the 66.2 and 97.4 kDa in the soluble samples, highlighted by the grey dashed box. This shows the transformation has worked and therefore large-scale expression was performed.

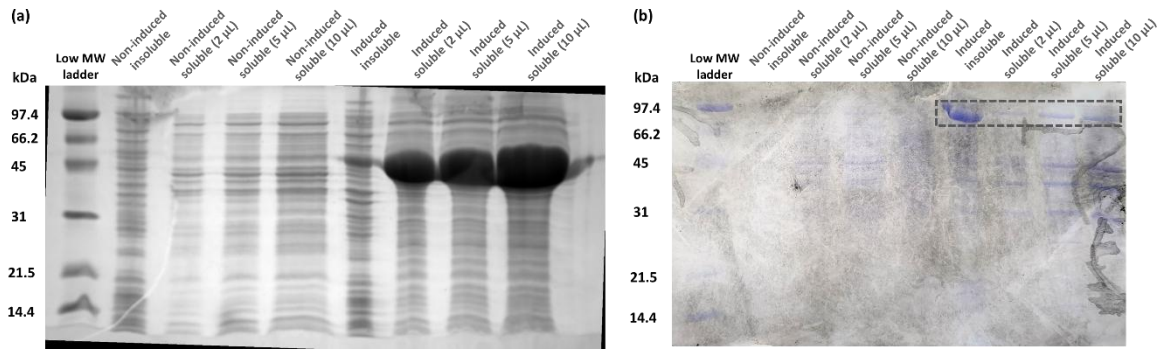

Figure 2.6. *12 % SDS page expression gels for (a) BiGalK and (b) BiGalHexNAcP.*

Both proteins were successfully purified by nickel affinity chromatography as evidenced by UV absorbance peaks at 280 nm in the chromatographs and gel bands corresponding to the correct molecular weights which are provided in appendix 7.1. Further purification via size exclusion chromatography was performed for BiGalHexNAcP, although enzymatic activity remains high without full purity. Based on both chromatograms and gels, protein-containing fractions were pooled, dialysed, and concentrated, the typical yields for both proteins were 38 mg L^{-1} determined by BCA assays. In subsequent syntheses BiGalHexNAcP was obtained from a commercial source (Prozomix) and was desalted and concentrated before use.

2.3.1.2. Synthesis and purification of glycofluoroform, 3FGal-β(1,3)-GlcNAc-Pr-N_3

Previously, when synthesising glycofluoroforms using these kinases and phosphorylases, a one-pot two enzyme synthetic strategy was employed.[84] However, for the target glycofluoroform the chemoenzymatic synthesis requires extremely forcing conditions. In the library of nine molecules synthesised in the paper investigating galectin binding,[84] four

molecules only required a 24-hour reaction time whereas the target GFF took 144 hours to reach a comparable yield. Additionally, it required significantly more of both enzymes: 30.8 and 67.8 mg of BiGalK and BiGalHexNAcP respectively when the average amounts for the other eight sugars were 10.3 and 19.75 mg. When examining the literature regarding the non-fluorinated version of the target sugar, the initial study using a one-pot two-enzyme strategy reports a 95% yield (with only a 48 h reaction),[87] however when replicated only a 47% yield was achieved and in another study, albeit with a different kinase, a 68% yield was achieved.[137,138] This variation shows there are complexities when using these enzymes in tandem. One reason is likely to be the difference in pH optima for the two enzymes. BiGalHexNAcP works maximally over a narrow pH range of 5.0 to 6.5, whereas BiGalK works well above 7.0, reasonably at 6.5, and poorly below 6.5.[87] The one pot reaction is carried out at pH 6.5 which will limit BiGalK's activity and thus the turnover of the reaction. Therefore, within the Fascione group the glycofluoroform is preferably synthesised in a two-pot two-enzyme reaction with each step at a different pH. The first step of the reaction had previously been performed on a large scale therefore the crude phosphorylated fluorinated galactose (3FGal-1P) was provided to the author by Dr T. Keenan (University of York). Additionally, unpublished work within the Fascione group hypothesised the limiting factor for turnover was the concentration of the enzymes used and suggested that increasing the reaction volume hindered turnover. Therefore, for the second step, two concentrations of the BiGalHexNAcP enzyme were tested (10 mg mL^{-1} and 21.15 mg mL^{-1}) and although the reaction was prepared in a single vessel it was aliquoted to circa. 500 µL for incubation to keep the reaction volume lower.

To elucidate if the concentration of BiGalHexNAcP plays a role in reaction turnover, and thus affects the yield of crude GFF, two reactions (split into aliquots as discussed above) were run simultaneously. Equivalent volumes of enzyme were added at each stage, but the first reaction used an enzyme stock of 10 mg mL^{-1} and the second reaction 21.15 mg mL^{-1}. The reactions were monitored by thin-layer chromatography (TLC) and liquid chromatography-mass spectrometry (LC-MS). TLC showed the emergence of a product spot over several days and LC-MS chromatographs show the amount of acceptor monosaccharide (peak at ca. 305 m/z) decreasing relative to the amount of GFF (peak at ca. 469 m/z) over the course of the reaction. To track this conversion and to allow the comparison of both reactions the ratio of

the peaks associated with the GFF and GlcNAc-Pr-N_3, known as the acceptor monosaccharide or "A" (because in phosphorylation the acceptor is the non-phosphorylated molecule), was plotted against the time of the reaction (**Figure 2.7**). Although MS is not fully quantitative (in the absence of internal standards) the conversion rate can be inferred based on the peak ratios. The reaction turnover seems to increase slightly with the 'high' [BiGalHexNAcP] although the error bars suggest this difference isn't significant. However, the reaction turnover is certainly quicker with the higher concentration enzyme. It did appear that there was increased precipitation throughout the reaction with the more concentrated BiGalHexNAcP which could explain why the turnover isn't increased further and could be due to low reaction volumes limiting solubility. The measure of conversion is the ratio of the $[M+H]^+$ peaks for the GFF and A, though the $[M+Na]^+$ peaks show a similar trend.

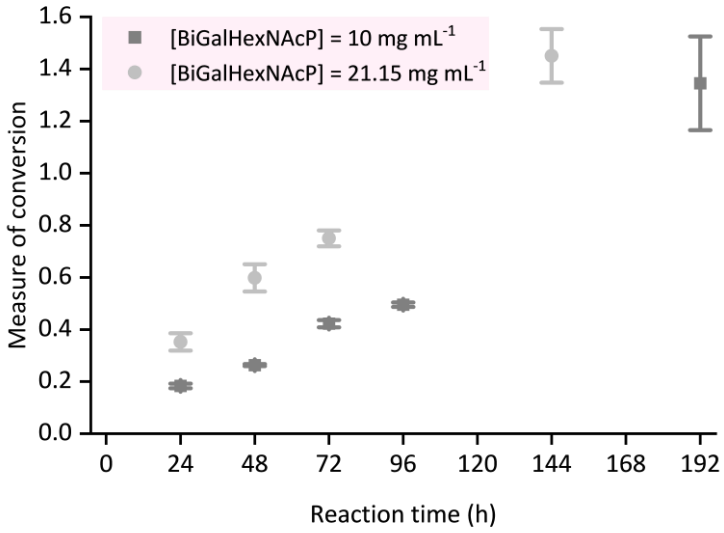

Figure 2.7. *Reaction progress monitored by positive-mode ESI-LCMS analysis of the enzymatic synthesis carried out with 'low' (dark grey squares) and 'high' (light grey circles) concentrations of BiGalHexNAcP. The measure of conversion was determined by taking the intensity of the $[GFF+H]^+$ peak and dividing by the intensity of the $[A+H]^+$ peak in the extracted ion chromatogram. The error bars represent standard error where n=3 for all datapoints except the 72h point of the 'low' [BiGalHexNAcP] dataset where n=2 due to an instrument error. The reactions were incubated at 37 °C and contained 100 mM Tris. HCl buffer (pH 6.5), 25 mM crude 3FGal1P, 10 mM GlcNAc-N_3, 15 mM $MgCl_2$ and BiGalHexNAcP.*

The synthesised disaccharide was purified in a two-step method. First, on a silica column eluted along an ethyl acetate-methanol gradient followed by gel filtration on a BioGel P2 column in distilled water. TLC data showed that some acceptor monosaccharide remained in the sample after the silica column. The fractions from the gel filtration column showed

reasonable separation of GFF and A with the purity varying slightly, earlier fractions contain just GFF with negligible A, **Figure 2.8(a)**, with the presence of A increasing in later fractions, **Figure 2.8(b)**, before A becomes the majority with some minor amounts of GFF, **Figure 2.8(c)**. Based off the MS data, fractions were combined in several batches to try to maximise yield without sacrificing purity. The purity of the isolated glycofluoroform was assessed via NMR analysis, the ^{19}F, ^{13}C, and ^{1}H NMR data is given in appendix 7.6, and is in line with literature data,[84] showing the purification of this batch of glycofluoroform was successful and so can be used for electrode modification.

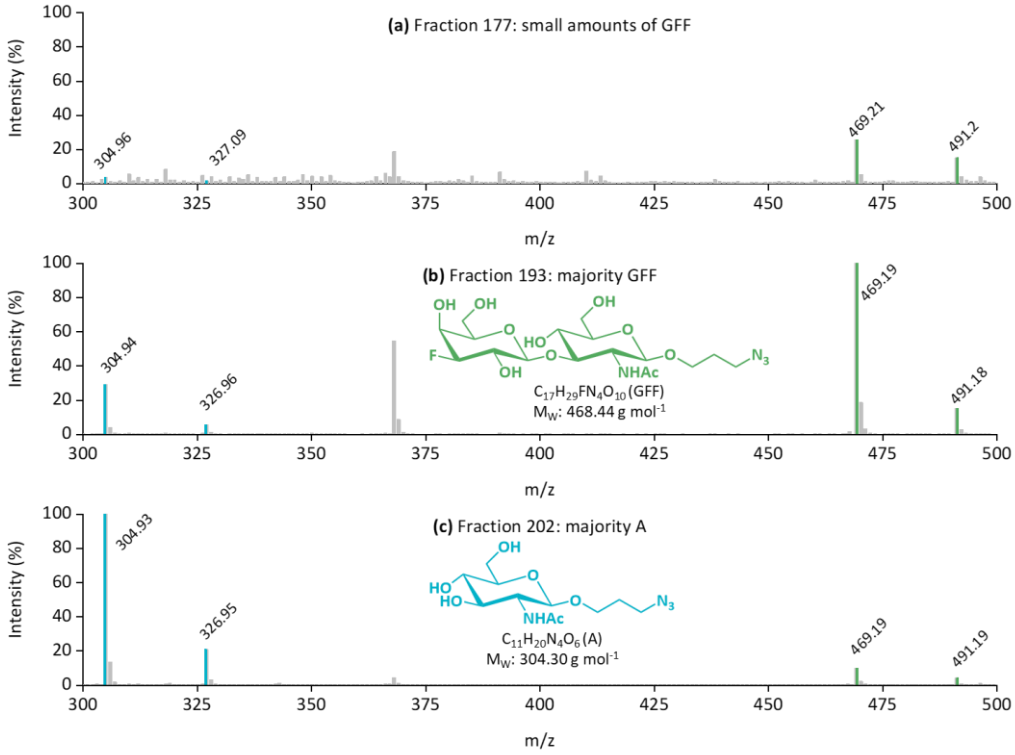

Figure 2.8. *Representative positive mode ESI-LCMS data showing the appearance of the glycofluoroform (GFF), 3FGal-β(1,3)-GlcNAc-Pr-N_3, shown by $[M+H]^+$ and $[M+Na]^+$ peaks at ca. 469 and 491 m/z (highlighted in green) and the later appearance of the acceptor monosaccharide (A), GlcNAc-Pr-N_3, shown by $[M+H]^+$and $[M+Na]^+$ peaks at ca. 305 and ca. 327 m/z peaks (highlighted in green).*

2.3.1.3. Development of a better measurement of fraction purity

The repurification of the remaining impure batches containing a mix of monosaccharide and glycofluoroform was attempted by running the BioGel P2 column again with fresh resin to see if this achieved better separation as the prior column ran slower than expected. Unfortunately, MS analysis showed monosaccharide contamination across all fractions, albeit in very small amounts in some fractions. The chromatogram shows a sharp peak at around 5 minutes for the purer fractions but as the monosaccharide becomes more dominant this peak broadens, shown in **Figure 2.9**.

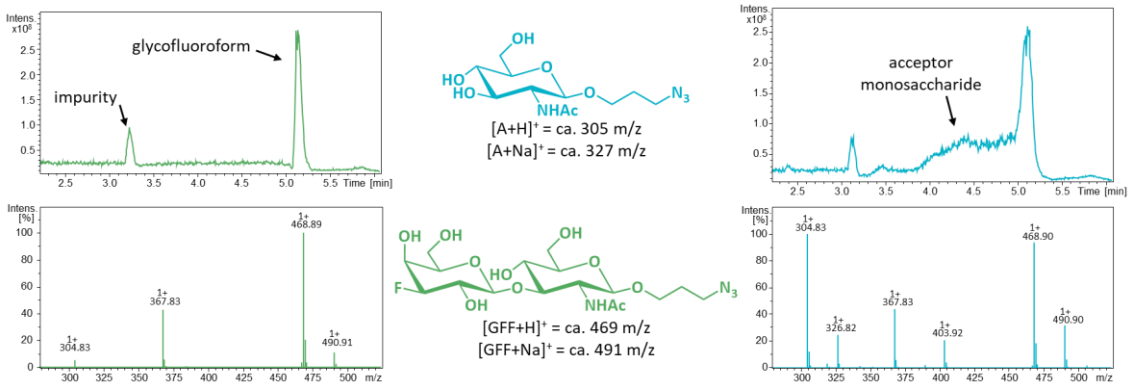

Figure 2.9. *Comparison of the chromatograms (top) and the extracted ion compound spectra (bottom) for fraction 162 (left) and 170 (right) showing the increased contamination by the monosaccharide in the right compared to the left.*

As the chemoenzymatic synthesis is a lengthy process requiring the expression and purification of two enzymes (both of which require multiday expression and purification) and post-purification the fractions are screened via time-intensive MS it is important to isolate as much glycofluoroform per synthesis as possible to make these intensive processes worthwhile. To try and salvage some glycofluoroform from these fractions a more quantitative measure of the ratio of the two sugars was needed. Glycans typically don't ionise or vaporise efficiently,[20] thus derivatisation with a charged substrate can be performed to improve MS quantification. In our experiments fraction 170, a fraction which appeared to have a roughly 1:1 ratio of both sugars (as seen by the similar intensities of the ca. 305 and ca. 469 m/z peaks in the bottom-right of **Figure 2.9**), was reacted with a reagent containing an imidazolium tag (iTag reagent). The iTag reagent is charged so easily ionises in MS and therefore conclusions made from comparing the peak intensity is more reliable when the sugars have been tagged.

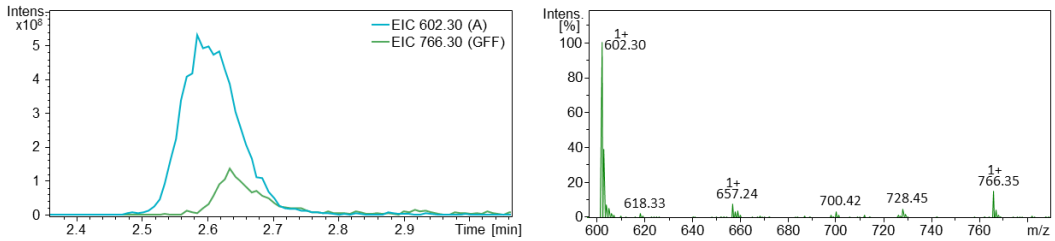

Figure 2.10. *Chromatograms (left) and extracted ion compound spectra (right) for the acceptor monosaccharide (A) and iTag reagent conjugate at 602.30 m/z and the glycofluoroform (GFF) and iTag reagent conjugate at 766.35 m/z.*

When examining the results from the i-Tagged fraction, **Figure 2.10**, the acceptor monosaccharide (appearing at 602.30 for the $[M]^+$ peak) is significantly more abundant than

the glycofluoroform (appearing at 766.30 for the $[M]^+$ peak). In fact, the peak intensities have a ratio of around 5:1 showing that the amount of glycofluoroform present is lower than what is indicated in the initial MS analysis. By comparing to the 1:1 ratio in the original fractions the untagged glycofluoroform ionises significantly better than the acceptor monosaccharide. Knowing that the tagged MS data is more quantitively reliable, further fractions were screened in this manner which allowed another 1.1 mg of glycofluoroform to be isolated with appropriate purity, as determined by NMR spectroscopy. This shows the advantages of using a more sophisticated fraction screening method. However, the isolation of the glycofluoroform is still challenging.

2.3.1.4. Evaluation of screen-printed electrodes

Previously, the glycofluoroform galectin-3 binding has been studied with the GFF-polymer immobilised onto gold nanoparticles and binding quantification via optical measurements, namely UV-Vis spectroscopy and dynamic light scattering.[84] However, due to the advantages of using electrochemical methods of detection discussed in section 2.1.1 this work seeks to examine the same binding relationship but with electrochemical measurements. To do this different electrode types and electrode preparation strategies and methodologies were evaluated to identify the optimal electrochemical system.

Commonly, both within literature and the research group, electrochemical studies are performed using a disc working electrode within a classic three-electrode electrochemical cell in a bulk volume of electrolyte solution.[102,141] Screen-printed electrodes (SPEs) are an alternative experimental set-up for electrochemical studies and comprise all three electrodes printed onto a support, typically made of ceramic or plastic composites.[142] With the long-term aim of industrial sensing applications, using SPEs confer certain advantages including disposability, high scale of economics, and reduced sample volume whilst the working electrode diameter remains a typical size ensuring signal intensity is maintained.[112] To compare a standard disc working electrode to SPEs CV measurements were taken. In a CV measurement the potential is first scanned in one direction, e.g. from positive to negative potential, and then at a turning point the potential is then swept in the opposite direction, i.e. from negative to positive potential. The current in response to this cycling potential is recorded. The peak potentials, the position on the x-axis where the current reaches either the oxidative or reductive maxima, inform on the thermodynamics of the redox reaction.

Additionally, as the voltage is scanned at a constant rate, kinetic information can also be extracted. Thus, comparing CV responses allows the evaluation of electrochemical activity and surface inhomogeneity of the studied electrodes.

A detailed CV study was performed to compare disc electrodes and screen-printed electrodes (SPEs). From the CVs on both electrodes with and without the solution redox probe, potassium ferricyanide ($K_3[Fe(CN)_6]$), several observations can be made:

- The disc electrodes have lower background redox activity than the SPE as seen by comparing the bare scans (dashed lines in **Figure 2.11**). This background redox activity is caused by the gold surface or impurities on the surface showing the disc electrode has a cleaner electrode surface. This is likely due to the extensive polishing protocol employed before making measurements on disc electrodes, as discussed later in this section.
- In the presence of potassium ferricyanide well-defined oxidative and reductive peaks are seen for both electrodes. The two sets of scans (absence and presence of $K_3[Fe(CN)_6]$) are on the same electrode but despite this, the original background electrode activity disappears when observing the redox probe. This is suggestive of passivation of the electrode surface by the redox probe and implies that measuring our system without a redox probe, i.e. via solely capacitance measurements, would be challenging. Therefore, electrochemical measurements will take place in buffer spiked with potassium ferricyanide.
- The $E_{mid,}$ the midpoint between the oxidative and reductive potentials, varies by 95 mV. The composition of the redox solution is the same for both measurements, so this discrepancy is likely due to the different reference electrodes used: Ag/AgCl (3M KCl) for the disc electrode and Ag covered in AgCl for the SPE. The minor difference in ΔE ($E_{oxidative} - E_{reductive}$), 10 mV, further supports the idea that the underlying redox chemistry isn't changing, only the reference electrode composition.
- Despite the same electrolyte composition (10 mM potassium ferricyanide in 100 mM sodium phosphate, 233 mM sodium chloride pH 7.0 buffer), the current is lower on the SPE, although it is not decreased to a degree that will hamper the sensitivity of thesensing measurements. One reason for the variation is that although the working electrode diameters were the same for both measurements the actual

electrochemical surface area for both will vary from the theoretical due to differences induced by polishing or printing. Also, the inks used in SPE manufacturing are likely to be less conductive than the solid materials used in disc electrodes due to additives essential for the printing process.[143] However, this reduced conductivity will be partially mediated by an SPE design that minimises the distance between electrodes.

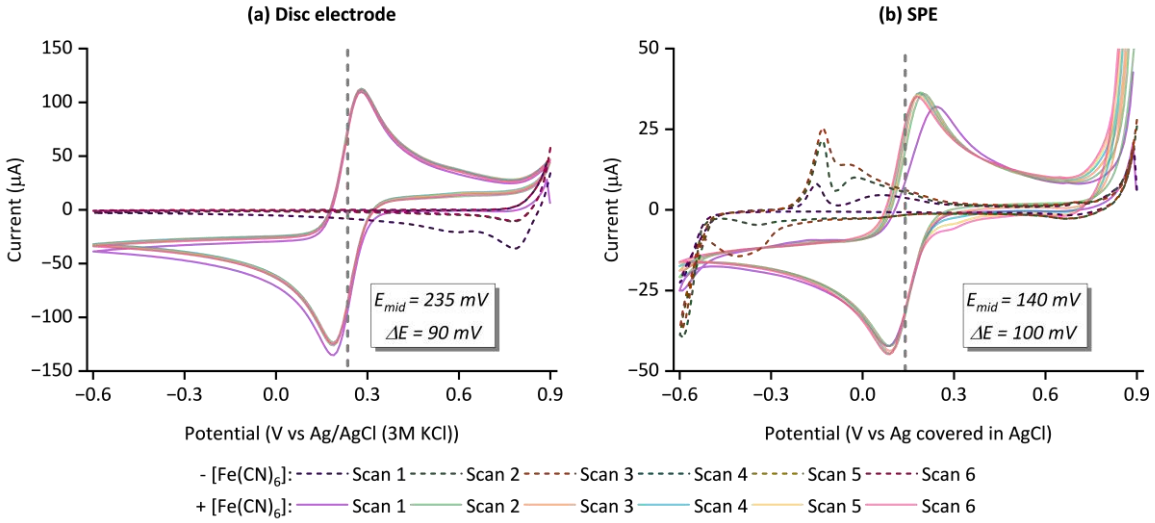

Figure 2.11. *Scans for both (a) disc and (b) SPE measurements in the absence (dashed lines) and presence (solid lines) of 10mM $K_3[Fe(CN)_6]$. The voltage was cycled between 0.9 and -0.6 V at 0.1 V s^{-1}, and the supporting electrolyte was pH 7 buffer (100 mM sodium phosphate, 233 mM sodium chloride). For (a) the cell was completed with a platinum counter electrode and a Ag/AgCl (3 M KCl) reference electrode. For (b) there is a gold counter and Ag covered in AgCl reference electrode on the SPE.*

Table 2.2. *Summary of extracted parameters from* ***Figure 2.11*** *for the two electrode types studied. *Reference is V vs Ag/AgCl (3M KCl) for the disc electrode and Ag covered in AgCl for the SPE.*

Electrode type	Potential / mV vs Ref*			
	$E_{oxidative}$	$E_{reductive}$	E_{mid}	ΔE
Disc	280	190	235	90
SPE	190	90	140	100

The lower background redox activity and higher conductivity of the disc electrode is attributed to the polished uniform gold surface. This is achieved through an intensive polishing protocol. The disc electrodes are first manually polished, then sonicated in water followed by ethanol, and finally electrochemically polished in both basic (0.5 M NaOH) and acidic (0.5 M H_2SO_4) solutions. This process takes approximately two hours per electrode thus hindering the number of electrodes that can be studied each day and, in some cases (likely due to the age and previous experimental history of the disc electrodes used), is

unsuccessful. An example of both a successful and unsuccessful polish is shown in **Figure 2.12**. A successful polish (**Figure 2.12(a)**) is established by observing single (or a single major) peak in the oxidative and reductive scans for both polishes, contrastingly for an unsuccessful polish multiple peaks, like those seen in the acid polish in **Figure 2.12(b)**, are observed signifying multiple gold environments. Other variations in the CVs recorded throughout polishing can be due to differences in electroactive surface area due to polishing discrepancies and changes in the distance between the working and reference electrodes, although the cell is designed to reduce this latter variation as much as possible. The electrochemical polishing protocol was employed on a gold SPE to determine the homogeneity of these surfaces and if polishing was viable. Following polishing, the surface of the SPE is clearly degraded, inset of **Figure 2.12**, and stable electrochemical connections were not possible proving SPEs are not compatible with electrochemical polishing. While this lack of polishing may result in more variation in bare gold SPE surfaces compared to gold disc electrode surfaces a polishing protocol could not realistically be employed in a commercial setting. Therefore, the incompatibility of SPEs with polishing is not an issue and examining these SPEs unpolished is a more realistic experimental system than highly polished gold surfaces.

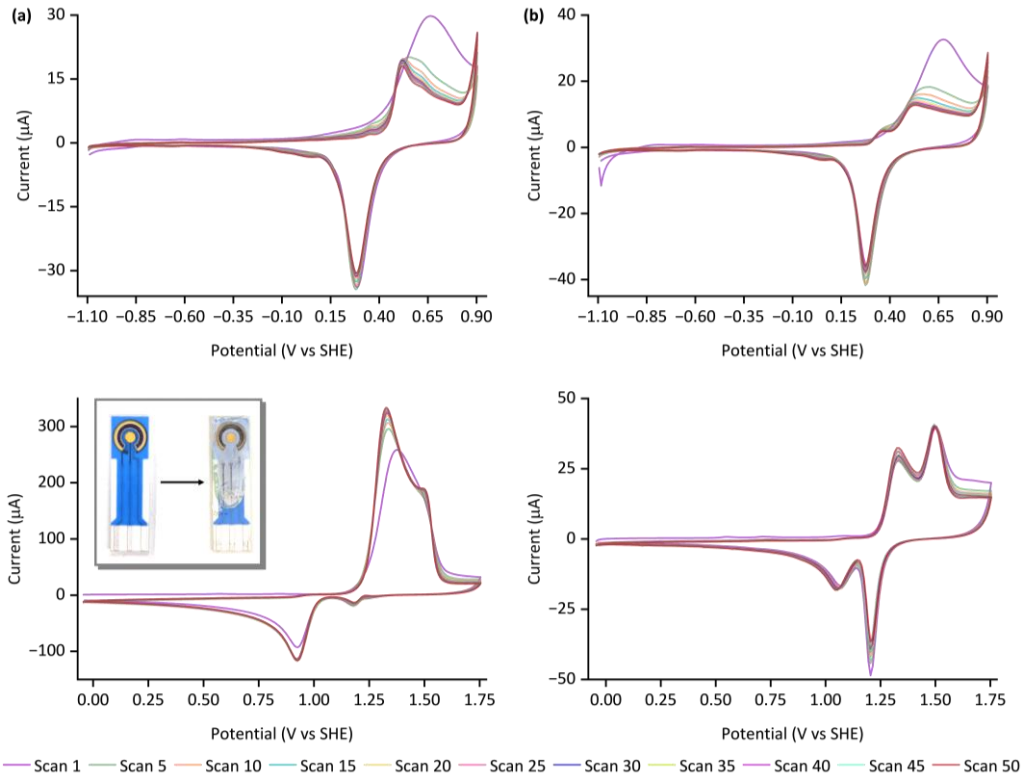

Figure 2.12. *Resultant CVs from electrochemical polishing in 0.5 M NaOH (top) and 0.5 M H_2SO_4 (bottom) solutions for both (a) successful and (b) unsuccessful gold disc electrode polishes. The*

voltage was cycled between -1.1 and 0.9 V vs SHE or -0.05 to 1.75 V vs SHE (for base and acid polishes respectively) at 0.1 V s^{-1} for 50 scans. For both the counter electrode was platinum wire. The data in (a) was collected with a saturated calomel electrode (3 M KCl) and a correction factor of +0.256 V was used to convert to V vs SHE. The data in (b) was collected with a Ag/AgCl (3 M KCl) and a correction factor of +0.208 V was used to convert to V vs SHE. ***Inset:*** *Visualisation of the SPE surface before and after polishing.*

Several repeats of the cyclic voltammetry experiments were performed with different bare Au-SPEs (i.e., new, from the packet electrodes) and disc electrodes (both different electrodes and the same electrodes polished freshly each time). To assess the variability of the electrochemical systems the midpoint potential (E_{mid}) and the current magnitude (ΔI calculated by subtracting I_{red} from I_{ox}) were extracted and compared, **Figure 2.13**. These two variables were chosen as E_{mid} relates to the thermodynamics and ΔI is related to electroactive surface area, with a larger electroactive surface area resulting in a higher current assuming all other factors are constant. For bare electrodes, i.e. the comparison of the bars with lighter grey backgrounds in (a) and (b), it can be seen that the bare electrodes have a slightly larger variation in E_{mid} for SPEs than disc electrodes and significantly larger variation in ΔI. This shows, as expected due to the lack of polishing the bare SPE surfaces display greater electrochemical variation than the highly polished disc electrodes. As the energetics displayed by the solution ferricyanide redox probe are consistent throughout the repeats this is primarily due to variation in the electroactive surface area. However, whilst the bare electrode surfaces should be considered, most of the studies are going to be performed on the modified electrode surfaces.

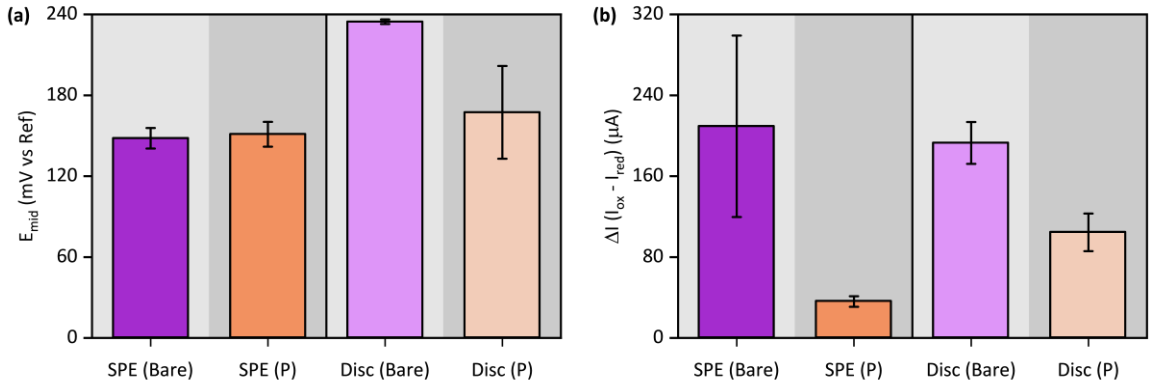

Figure 2.13. *Comparison of (a) E_{mid} and (b) ΔI for bare (purple bars on light grey background) and polymer-modified (P) (orange bars on darker grey background) SPE and disc electrodes. The SPEs are coloured a darker shade than the disc electrodes. For SPEs the reference electrode was Ag covered in AgCl and for disc the reference electrode was Ag/AgCl (3 M KCl).*

To examine the modified electrode surfaces bare electrodes (of both types) were immersed in either a 0.32 mM solution of the P (polymer) or P-GFF (polymer-glycofluoroform) and left

for 18 – 24 hours. The P-GFF solution is accessed by carrying out a SPAAC reaction, where P and GFF are mixed together in Milli-Q H_2O in a molar ratio of 1:1.1 and incubated at room temperature overnight, the reaction mixture is used as is for immobilisation studies. Both the P and P-GFF aliquots are stored in the freezer in between uses. This incubation allows for the formation of self-assembled monolayer of polymer on the gold surface (shown in the inset of **Figure 2.14**) due to spontaneous gold-thiol bond formation between the terminating thiol group on the polymer and the gold working electrode surface. The formation of the gold-thiol bind is confirmed by CV studies. It can be seen that the ΔE increases on modification, 120 mV for bare versus 472 mV for P-GFF, this along with the decreased current magnitude shows that the electron transfer rate decreases on modification. This is expected as the solution redox probe will exchange electrons with a bare electrode significantly easier than with a modified surface. This hinderance has several possible contributions: slower diffusion rate as the redox probe must diffuse through the P-GFF layer to the electrode, a greater electron transfer distance if the P-GFF holds the redox probe further from the electrode, and the P-GFF will make the electrode surface more insulating compared to the bare gold metal.

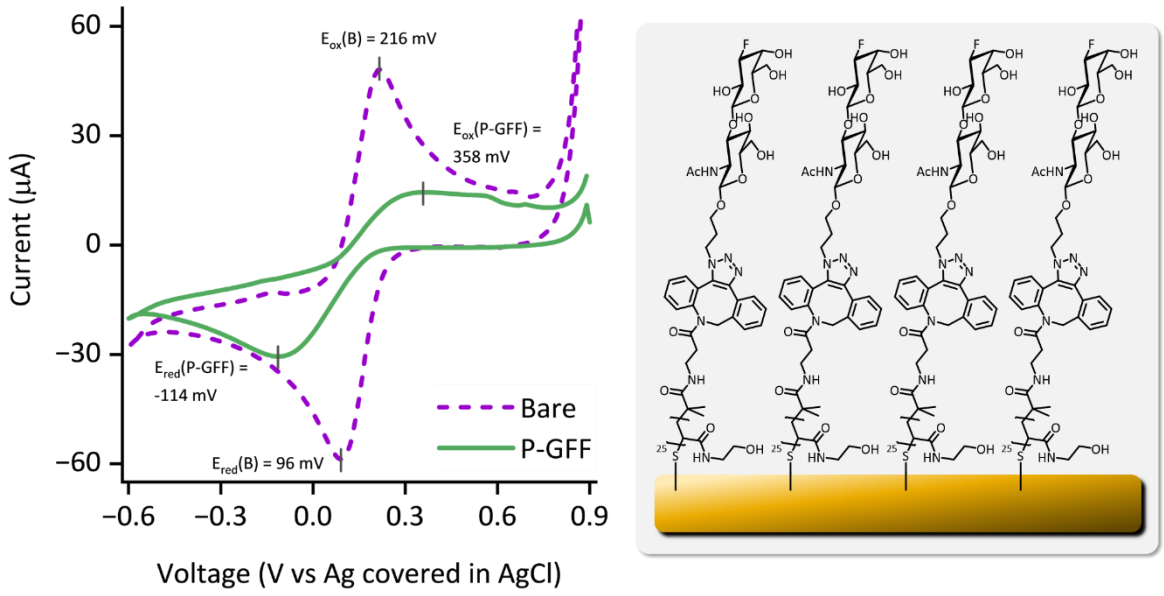

Figure 2.14. *Overlay of the first scan from CVs of a bare (purple dashed line) and a P-GFF modified (green solid line) gold SPE with E_{ox} and E_{red} annotated for both surfaces. The voltage was swept between 0.9 and -0.6 V vs Ag covered in AgCl at 0.1 V s^{-1} and the supporting electrolyte was 10 mM $K_3[Fe(CN)_6]$ in pH 7 buffer (100 mM sodium phosphate, 233 mM sodium chloride). Inset: Self-assembled monolayer of P-GFF on Au. B: bare, P-GFF: polymer-glycofluoroform.*

The variability of modified electrodes was also assessed via CV study. The polymer alone was used for these comparative studies to conserve the glycofluoroform which is only accessible in small amounts following a time-consuming synthesis, purification, and isolation. In contrast to bare electrodes, when studying the DCV behaviour of polymer-modified electrodes, i.e. the comparison of the bars with darker grey backgrounds in **Figure 2.13(a)** and **(b)**, the SPEs display less variation than the disc electrodes. This perhaps suggests that the modification is more consistent on the SPEs which could be due to the ability to modify two electrodes in the same aliquot of solution ensuring the environmental conditions are identical. Alternatively, it could be that the presence of the modification passivates the background redox activity of the electrode, which, as found earlier, is larger than that of the disc electrodes. This multi-electrode study confirms that usage of SPEs is an appropriate choice to study our electrochemical system.

Voltammetry techniques are often used as detection methods, either with a simple cyclic voltage ramp or a more complex pulse or square-wave ramp; for our system both ΔE and ΔI appear to be sensitive to modification and therefore are likely also to be responsive to changes in analyte concentration. This suggests DCV could be used as a detection method, however, an important observation was made that over continuous scans the current magnitude increases and the ΔE decreases. As shown in **Figure 2.15(a)** and **(b)**, for both P and P-GFF modified electrodes over subsequent scans E_{ox} and E_{red} move towards the average value for these parameters on bare SPEs. This indicates that the wide voltage sweep carried out in a DCV experiment cleaves the gold-thiol bond and thus the CV signal returns to that of a bare Au-SPE. This is substantiated by work in the literature which shows that applying a negative potential to a gold surface causes reduction of the thiol bonds, a process known as electrochemical desorption.[144] Further experimental evidence from our own studies supports this cleavage via comparison of the Bode plot before and after a 'stripping' experiment (**Figure 2.16**) indicates the removal of the immobilised substrate due to a large decrease in phase angle.

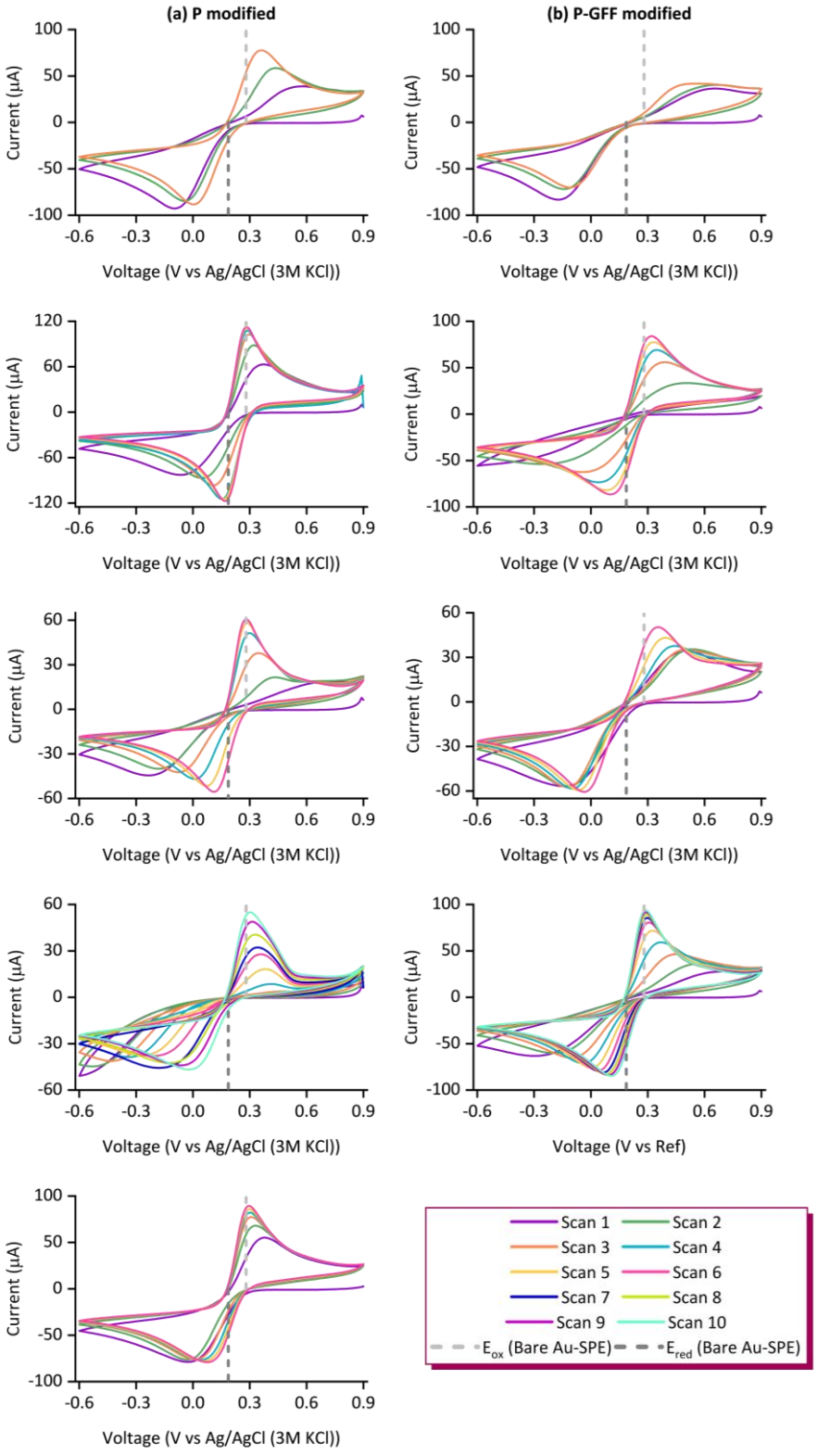

Figure 2.15. *100 mV s^{-1} DCV 'stripping' of (a)P and (b)P-GFF modified Au disc electrodes; changes in the voltammetric shape arise from electrochemically activated gold-thiol bond cleavage. The voltage was cycled from 0.9 to -0.6 V vs Ag/AgCl (3M KCl) at 0.1 V s^{-1} in a solution of 10 mM $K_3[Fe(CN)_6]$ in pH 7 aqueous buffer (100 mM sodium phosphate, 233 mM sodium chloride). The dashed lines represent the average oxidation (light grey) and reductive (dark grey) peak potentials.*

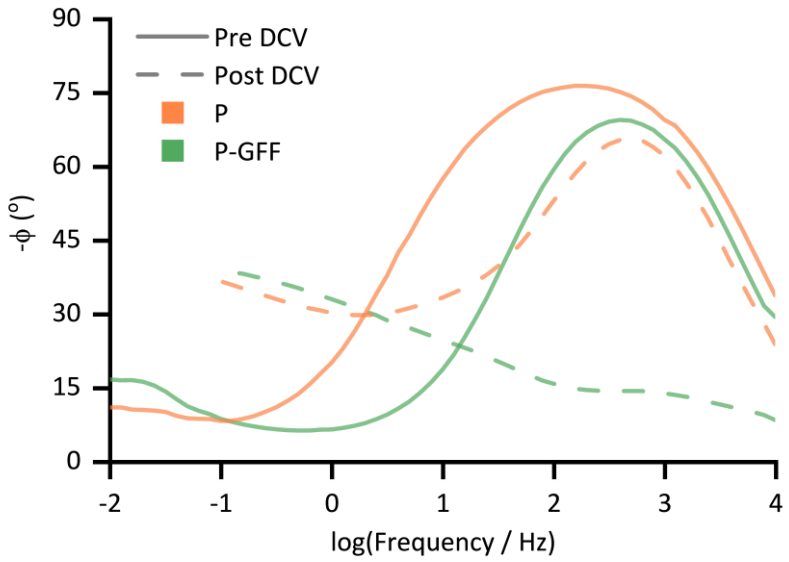

Figure 2.16. *Simplified Bode plots for P (orange) and P-GFF (green) modified Au-SPEs pre (solid lines) and post (dashed lines) DCV 'stripping'. For EIS experiments, E_{DC} = 0.23 V vs Ref, E_{AC} = 10 mV, $t_{equilibration}$ = 300 s, with a frequency range of 10 kHz – 0.01 Hz for pre-DCV measurements and 10 kHz – 0.1 Hz for post-DCV measurements. The supporting electrolyte was 10 mM $K_3[Fe(CN)_6]$ in pH 7 aqueous buffer (100 mM sodium phosphate, 233 mM sodium chloride). P: polymer, P-GFF: polymer-glycofluoroform.*

2.3.1.5. Electrochemical impedance spectroscopy is a sensitive yet non-destructive detection methodology

As described in the chapter introduction, electrochemical impedance spectroscopy (EIS) is an electrochemical method in which a sinusoidal voltage wave oscillating about a set voltage at a range of frequencies is applied to the electrochemical system. Crucially, the voltage window has a small amplitude, typically 10 mV, thus it will not have the same destabilising effect observed in CVs. EIS has two methods of visualisation: Bode and Nyquist plots. As shown above, Bode plots show how the phase (and magnitude) of the impedance response change with frequency, whereas Nyquist plots show the real and imaginary components of the impedance and each point represents a measurement at a singular oscillation frequency. Notably, a distinct difference can be observed between the bare Au-SPE and the P-GFF modified Au-SPE in these three plots (**Figure 2.17**). Often Bode plots are shown with a double y-axis but in this thesis, they are shown as separate plots for clarity due to the fact usually multiple sets of data are plotted on a single plot.

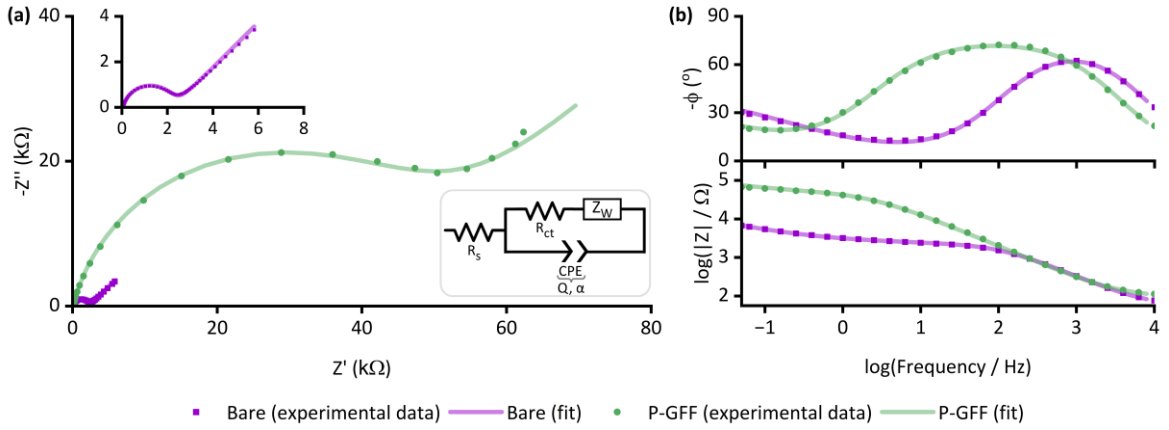

Figure 2.17. *(a) Nyquist and (b) Bode plots of experimental data (points) and the computational fitting (lines) to a modified Randles circuit for EIS measurements of a bare gold SPE (purple) and a P-GFF modified gold SPE (green). Inset: Magnified view of the Nyquist plot for the bare gold SPE and the modified Randles circuit used in the data analysis. EIS measurements were performed in the presence of 10 mM $K_3[Fe(CN)_6]$ in pH 7 aqueous buffer (100 mM sodium phosphate, 233 mM sodium chloride) with the following parameters: $t_{(equilibration)}$ = 180 s, E_{DC} = 0.16 V for bare 0.230 V for modified, E_{AC} = 10 mV, f = 0.05 Hz – 10 kHz. Every other experimental data point is shown. R_s = solution resistance, R_{ct} = resistance to charge transfer, Z_W = Warburg element, CPE = constant phase element.*

The larger magnitude of the Nyquist plot (**Figure 2.17(a)**) for the P-GFF modified Au-SPE relative to a bare Au-SPE indicated that incubation of a Au-SPE in SPAAC P-GFF reaction mixture resulted in gold-thiol bond formation, with the presence of the coating on the gold surface hindering electron transfer between solution potassium ferricyanide and the electrode surface. Numerically, this can be quantified as the change in the electron transfer rate, as discussed later.[145] As discussed in the introduction and later in this text the diameter of the semi-circle correlates to the resistance to charge transfer, in this example the P-GFF modified electrodes exhibits a ~20 times larger diameter (2.2 versus 48.2 kΩ). This magnitude of change is much larger than the differences observed in DCV, suggesting EIS is a more sensitive method for detecting the modification, and thus analyte binding, and is therefore a more suitable detection technique. In the Bode plots, the increase in phase angle from ca. 60° to 75° means the electrode is displaying greater capacitive behaviour due to the more insulating polymer layer formation. Additionally, the shift to the phase maxima occurring at a lower frequency means the dominant electrochemical process (in this case the charge transfer) is happening more slowly. In the magnitude plot the transition from low to high continues throughout the lower frequencies, showing that the charge transfer processes are happening over a longer timescale and flattening out at a higher magnitude, indicative of a higher resistance to charge transfer. The similar magnitude at the higher frequencies indicates similar solution resistance processes. These electrochemical

measurements which are carried out in the presence of solution-phase potassium ferricyanide showed the expected response for a solution EIS experiment in the Nyquist plot (**Figure 2.17**),[112] namely a semi-circle with a linear region at approximately 45°. This indicated that analysis using a modified Randles circuit (**Figure 2.17**, inset) was appropriate, with computational analysis generating a good fit to the experimental data.

Complementary control experiments replacing the glycofluoroform with a ferrocene derivative were carried out to determine the extent of modification and provide further evidence of gold-thiol bond formation. An azido-containing ferrocene derivative was synthesised and clicked to the thiol-containing polymer and immobilised onto the electrode in the same manner as the previous (glycofluoroform-)polymer studies (**Scheme 6.3**, R = P-FD-01). A reversible surface-confined ferrocene DCV signal was observed (**Figure 2.18(a)**) and analysed using a third-order polynomial baseline subtraction to isolate the faradaic current (**Figure 2.18(b)**). The faradaic current must be isolated in order to determine the number of ferrocene molecules that are responsible for the faradaic current generation and thus the number of molecules immobilised on the electrode. The background response was modelled as a third order polynomial.

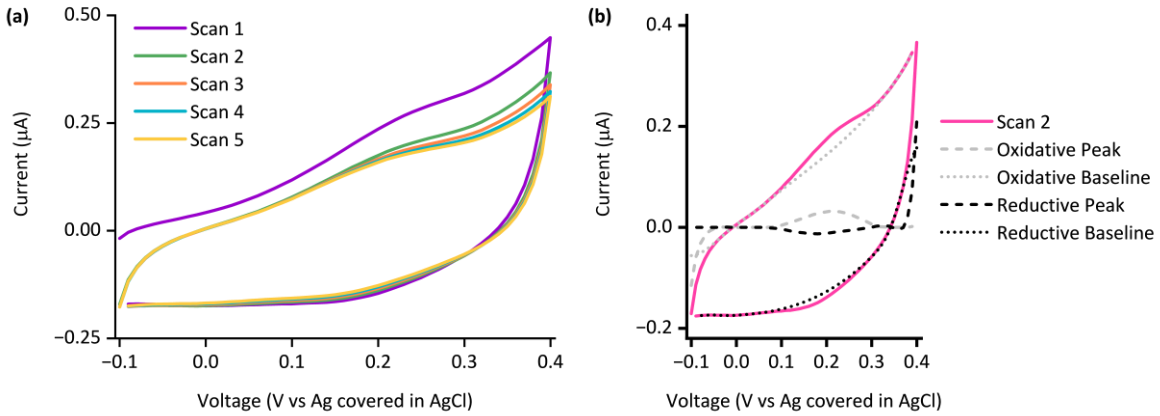

Figure 2.18. *(a) DCV scans for the immobilised P-FD-01 on a Au-SPE and (b) scan 2 with fitted polynomial baselines and extracted faradaic peak for both the oxidative and reductive scans shown. The voltage was cycled between -0.10 V to 0.40 V (vs Ag covered in AgCl) for 5 scans at a scan rate of 100 mV s^{-1}.*

Using a one-electron Nernst model, the surface coverage in this experiment was found to be 0.350 pmol which is approximately three-fold lower than the estimated monolayer coverage, 1.01 pmol. A Nernstian analysis is appropriate as the cyclic voltammetry was conducted at a suitably slow scan rate to ensure the electron transfer was under

thermodynamic control. It has to be acknowledged that as the peaks aren't equal in surface area it may be thought that the electron transfer isn't fully reversible, but the same asymmetry was observed at even slower scan rates. Therefore, this discrepancy is attributed to the simplified method of capacitance subtraction. The area under the extracted redox peaks was calculated via integration in the units A V, this is divided by the scan rate (0.1 V s^{-1}) to calculate the charge passed. This is converted to immobilised coverage by dividing by Avogadro's constant and into surface coverage by considering the area of the working electrode. This is detailed in **Table 2.3**. The areas for the oxidative and reductive scans were averaged to account for under or over-estimation of peak size due to the simplified background subtraction process. To compare this to a maximum coverage value the molecular footprint of the polymer was estimated based on Chimera modelling (Figure 2.19). If the polymer 'footprint' is considered to be circular the diameter of the polymer can be calculated as 24.38 Å by approximating the extreme points as an isosceles triangle. The geometric surface area of the working electrode is approximately 0.03 cm^2 so assuming hexagonal lattice packing (90.7%),[146] a monolayer polymer coverage can be estimated as 1.01 pmol, or 32.3 pmol cm^{-2}.

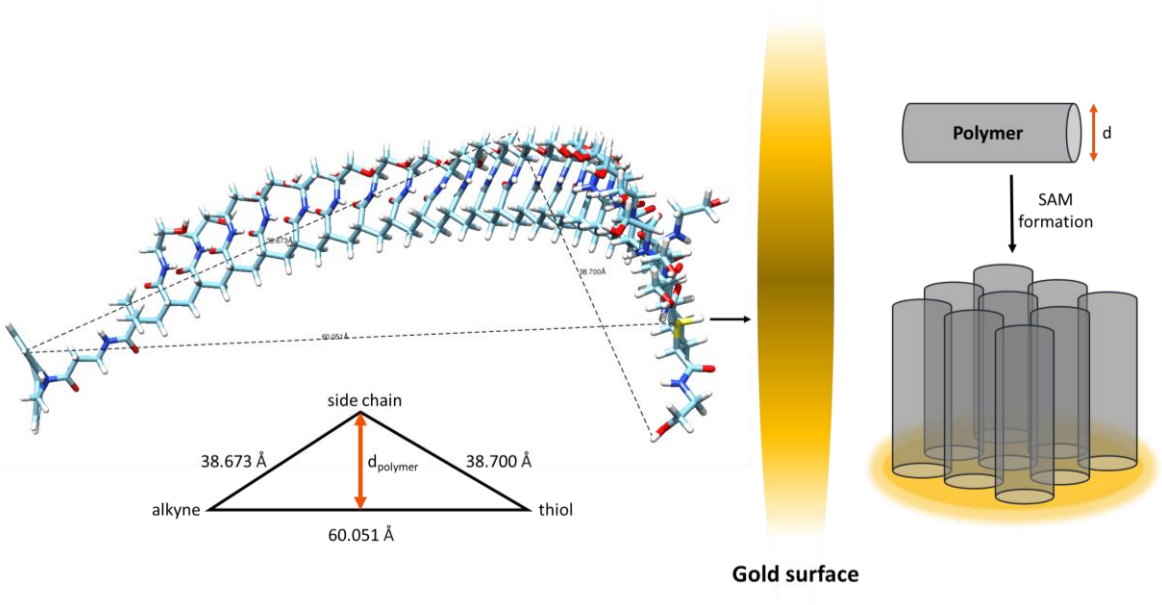

Figure 2.19. *Predicted 3-D polymer structure and calculated distances (from Chimera) and a schematic showing how an estimated diameter and packing efficiency can be used to calculate a maximum surface coverage estimate. SAM: self-assembled monolayer.*

Table 2.3. *Surface coverage extracted for immobilised FD-01 for oxidative and reductive scans.*

Parameter	Oxidative Scan	Reductive Scan
Extracted peak area / A V	4.42×10^{-9}	2.34×10^{-9}
Charge passed / C	4.42×10^{-8}	2.34×10^{-8}
Immobilised FD-01 / pmol	0.458	0.243
Surface coverage / pmol cm^{-2}	14.6	7.72
Average immobilised FD-01 / pmol	0.350	
Average surface coverage / pmol cm^{-2}	11.2	

Since the polymer structure is consistent, and the gold-thiol bond formation chemistry will be unchanged, we also interpret the ferrocene measurements as providing a proxy measurement of the coverage of GFF on the electrode surface. Other control experiments also indicate non-ideal, sub-monolayer formation.

2.3.2. Exploration of reproducibility with statistical methods reveals electrode-to-electrode variation

EIS experiments comparing bare and P-GFF modified electrodes were repeated extensively (**Figure 2.20**), the P modified electrodes were also studied but with fewer repeats (n = 5), the raw data and experimental fits are provided in appendix 7.2. The Nyquist plots showed substantive variation within the P-GFF dataset that is not present in the bare Au-SPE dataset. This variation could not be reduced by careful control of experimental conditions. Even construction of a specialised tank (3-D printed by A. Robertson, University of York) to enable the simultaneous immersion of eight SPEs in a single aliquot of SPAAC P-GFF reaction mixture (**Figure 2.20(c)**), with agitation to ensure solution homogeneity, identical temperature, concentration, and incubation time, still resulted in a large variation in Nyquist response (**Figure 2.20(a)**). From this data, we concluded electrode modification was inconsistent, which is unsurprising considering extensive pre-modification mechanical and electrochemical polishing is necessary to achieve highly consistent self-assembled Au-thiol monolayer formation on gold disc electrodes.[147] Such extensive cleaning of the gold surface is not possible when using Au-SPEs (as shown in **Figure 2.12(inset)**).

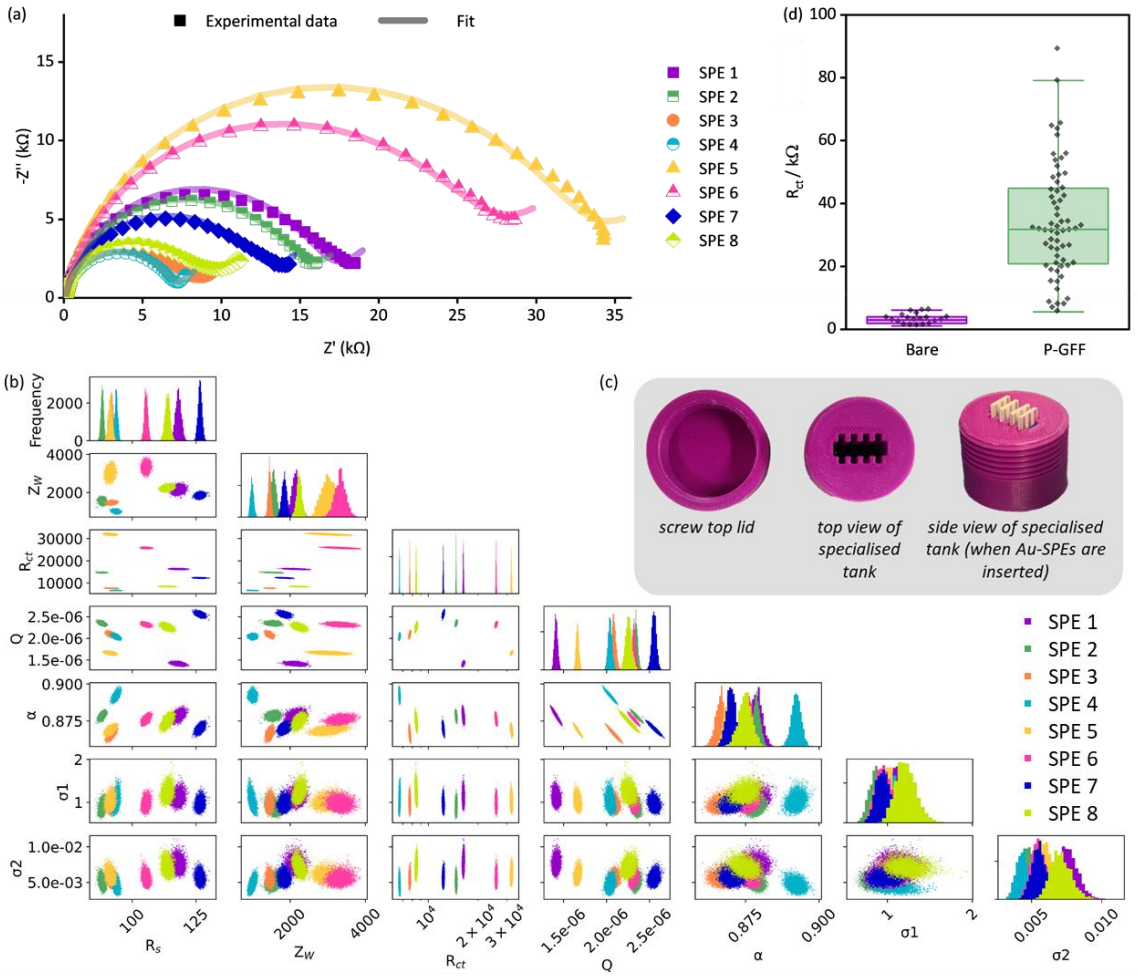

Figure 2.20. *(a) Nyquist plots of experimental data (dots) and the computational fitting to a modified Randles circuit (line) for EIS measurements of eight P-GFF Au-SPEs modified simultaneously. (b) MCMC analysis of the data in Figure 2.20(a). The same colour code is used to distinguish between the separate electrodes. The uppermost plots (along the top diagonal) comprise 1-D histograms (y-axis is frequency) for each parameter used in equivalent circuit fitting (see x-axis labels), showing the distribution of the best-fit values for multiple analysis runs for each individual SPE. The 2-D scatter plots show correlations between parameters. (c) Pictures of the tank used for simultaneous Au-SPE modification. (d) A box and whisker plot showing the variation in the extracted Rct parameters for experiments on different 'bare', i.e. unmodified, Au-SPE (purple, n = 20) and different 'P-GFF' modified Au-SPEs (green, n = 63) following equivalent circuit fitting to the large datasets shown in Figures S4 and S5.The limits of the solid box represent the 25th and 75th percentile (1.9 and 4.0 kΩ or 20.8 and 44.9 kΩ, for bare and P-GFF respectively), the central horizontal line in the box shows the position of the median (3.0 or 31.7 kΩ) and the upper and lower horizontal "whisker" lines represent the 5th and 95th percentiles (1.0 and 6.1 kΩ or 5.5 and 79.1 kΩ). EIS measurements were performed in the presence of 10 mM $K_3[Fe(CN)_6]$ in pH 7 aqueous buffer (100 mM sodium phosphate, 233 mM sodium chloride) with the following parameters: t(equilibration) = 300 s, E_{DC} = 0.160 V vs Ref, E_{AC} = 10 mV, f = 0.1 Hz – 10 kHz. R_s = solution resistance, R_{ct} = resistance to charge transfer, Z_W = Warburg element, Q and α are the parameters used to model a constant phase element, and σ1 and σ2 are noise parameters.*

The Nyquist plots of the dataset comprised of eight simultaneously modified Au-SPEs all exhibit significant variation from one another (**Figure 2.20(a)**) but could all be well modelled by the same modified Randles circuit. This suggests a single electron charge transfer environment is present on the electrode but to different extents. It is established that there

can be variability in electrode printing, contaminants present in the ink, and non-ideal surfaces formed in the screen-printing process.[148,149] As gold-thiol immobilisation is dependent on the gold surface oxidation and atomic arrangement,[150] the surface variation between SPEs means gold-thiol bond formation occurs to different extents resulting in the variations observed in EIS experiments. As established, there is no pre-treatment possible for these electrodes which could alleviate some of this variation (**Figure 2.12(inset)**). For the CMA-ES (covariance matrix adaptation-evolution strategy) fitting it was explored whether it was best to fit to the Nyquist or Bode portion of the data and if the Warburg element should be replaced with a second constant phase element (CPE). This is detailed in appendix 7.3, our studies found it's best to use a one CPE circuit and fit to the Bode portion of the data, thus we have used this throughout the work. To explore if there were any underlying trends in the best fit parameters, we conducted a MCMC (Markov chain Monte Carlo) analysis to generate posterior fitting distributions that represent the different equivalent circuit model parameters that can give a "best-fit" to the experimental data (**Figure 2.20(b)**). Within this, we observed the expected correlation between Q and α, the coupled parameters which together constitute the constant phase element (CPE) used to model double-layer capacitance (diagonal lines in the scatter plot with Q on the x-axis and α on the y-axis).[116] However, the plots showing the frequency distribution for each best fit parameter (the uppermost graphs within **Figure 2.20(b)**) reveal no clear trends in the electrode-to-electrode variation; i.e. the ordering of the best fit parameter values with respect to the SPE number (essentially the colour bar code) is different from one parameter frequency distribution to another, meaning there is no clear underlying synergistic trend in the way one parameter changes versus another. Alternatively, this lack of pairwise parameter compensation can also be seen by the fact that there is no clear trend in how one parameter value changes relative to another in the 2-D scatter plots where one equivalent circuit model parameter is on the x-axis, and another is on the y-axis. Thus, the R_{ct} value of a GFF-modified Au-SPE cannot be normalised with respect to another parameter to enable the trivial correction for variation in the dataset. This means it will be crucial to be able to measure multiple galectin-3 concentrations on the same modified electrode.

$$R_{ct} = \frac{RT}{nFI_0} \qquad \textit{Equation 2.6}$$

$$I_0 = nFAk_{et}[S] \qquad \textit{Equation 2.7}$$

where: R_{ct}: charge transfer resistance (Ω); R: gas constant (J K^{-1} mol^{-1}); T: temperature (K); n: number of electrons; F: Faraday constant (C mol^{-1}); I_0: equilibrium current (A); A: electrode surface area (cm^2); k_{app}: apparent electron transfer rate constant (cm s^{-1}); $[S]$: redox probe concentration (mol cm^{-3})

Since most EIS biosensors are assayed in a manner which correlates change in the charge transfer resistance (R_{ct}) with target analyte concentration,[13] the variation in the extracted R_{ct} parameters from all the unmodified and P-GFF modified Au-SPEs datasets (appendix 7.2) were compared (**Figure 2.20(d)**). The 11-fold increase in the average R_{ct} for the bare electrodes (3.1 kΩ) versus the P-GFF dataset (34.2 kΩ) is equivalent to a 11-fold decrease in the apparent ferricyanide electron transfer rate constant, k_{app}, of 2.7 μm s^{-1} versus 0.2 μm s^{-1}.[102,145] This is calculated as described in Equation 2.6 and Equation 2.7. First, charge transfer resistance is translated into equilibrium (exchange) current (the current flowing when an electrode reaches dynamic equilibrium in an electrolyte meaning no net redox processes are occurring) in Equation 2.6, which can be converted to an apparent electron transfer rate constant in Equation 2.7. The observed variation between P-GFF modified electrodes was substantive, and this means it is non-trivial to compare repeats across multiple electrodes in experiments described later.

However, it is notable that this variability does not change as a function of the age of the SPAAC P-GFF reaction mixture (**Figure 2.21(a)**), with no correlation between R_{ct} and the age (days post click reaction) of the SPAAC P-GFF reaction mixture. This dataset is comprised of extracted R_{ct} values from different Au-SPEs modified with the same aliquot of SPAAC P-GFF reaction mixture and demonstrates the remarkable stability of the P-GFF conjugate, which yields self-assembled monolayers over an approximate 10-month time scale despite multiple freeze-thaw cycles. In addition, the formation and stability of the P-GFF conjugate was confirmed by comparison with the EIS response for Au-SPE modified with thiol-polymer only (**Figure 7.7**). In these 'GFF-free' control experiments a significantly larger Nyquist response is observed for the 'polymer-only' dataset (average R_{ct} = 89.4 kΩ), showing the linkage formed between the P and GFF during the SPAAC reaction is stable. The difference between the two modifications is attributed to differences in the interactions of the solution-based ferricyanide with polymer versus polymer-glycofluoroform; the anionic

charge of the $Fe(CN)_6^{4-/3-}$ redox couple makes it highly sensitive to changes in electrode surface electrostatics.[151] The difference between the control experiment data and data from the modification of different Au-SPEs with a single P-GFF aliquot (**Figure 2.21(a)**) supports our assertion that the glycofluoroform modified polymer is stable over a prolonged timescale. To further assist in the visualisation of differences between datasets, **Figure 2.21(b)** presents an overlay of the distributions of R_{ct} values from repeat experiments analysing bare Au-SPEs, the full P-GFF dataset (both from **Figure 2.20(d)**), the subset of P-GFF experiments carried out across many different days using the same polymer-glycofluoroform solution to modify the electrode (**Figure 2.21(a)**), and polymer-only control experiments (**Figure 7.7**).

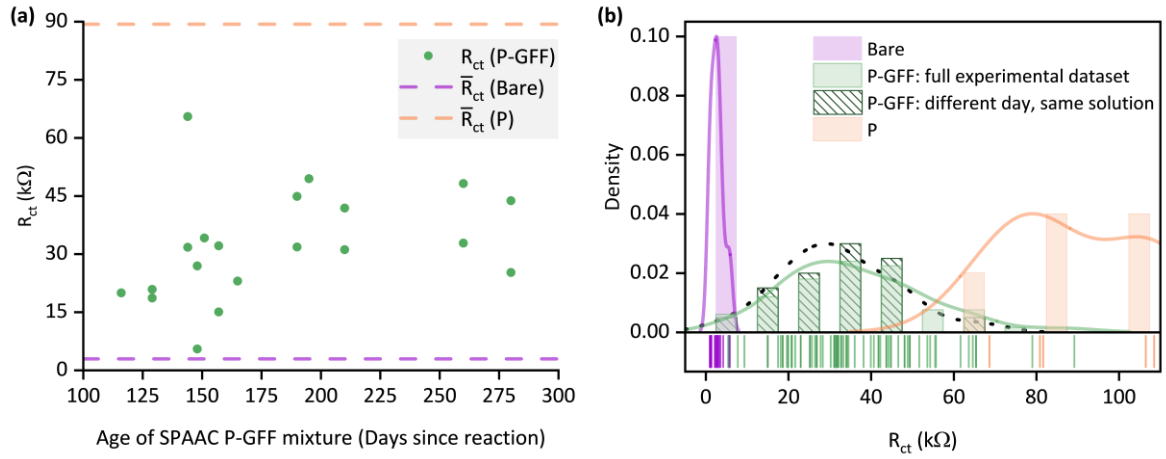

Figure 2.21. *(a) Extracted R_{ct} parameters (green dots) for individual P-GFF modified Au-SPEs plotted against the age of the P-GFF conjugate solution showing no correlation in R_{ct} over time. The mean R_{ct} values ($\bar{R}_{ct}$) for both bare (purple dashed line) and polymer only, "P", modified (orange dashed line) Au-SPEs are shown for comparison. (b) Distribution plots overlaying the datasets from* ***Figure 2.20****(d) (purple and green),* ***Figure 2.21****(a) (dark green with diagonal bars) and* ***Figure 7.7*** *(orange). Lines represent Kernel Smooth distributions and a 50% gap is used to separate the vertical bars. The lower portion of the plot is a "rug" representing the point values of the individual measurements.*

Complementary t-test analysis (see appendix 7.4 for details) supports the conclusion that there is a statistically significant difference between the bare Au-SPE electrodes and the combined P-GFF dataset, but the inter-day variability is insignificant when this sub-dataset (n = 20) is compared to the mean of the collated P-GFF dataset from all experiments (n = 63). We did not make comparison to the polymer-only dataset because as shown in **Figure 2.21(b)** we have insufficient data to resolve the skewed distribution in this relatively small (n = 5) set of control experiments, and polymer-only modifications are not the focus of this study.

Overall, the work in this section proves that electrochemical impedance spectroscopy successfully observes P-GFF (and P) SPE modification and proves variability within this modification. This variation is non-trivial to remove through environmental control. Importantly it isn't due to instability within the P-GFF conjugate, in fact this shows remarkable stability over a ten-month period. Based on this variation it will be essential to be able to carry out multiple measurements for galectin-3 binding studies.

2.3.3. Optimisation of redox probe and incubation methodology for galectin-3 binding studies

The next stage of work to determine the binding response of galectin-3 requires being able to take multiple measurements on a single SPE. A series of redox probes were assessed: potassium ferricyanide, hexaammineruthenium (III) chloride, 6-(ferrocenyl)hexanethiol and the ferrocene azide derivative FD-01 previously used to determine surface coverage, the structures of which are provided in **Figure 2.22**. The focus was selecting a redox probe that provided both sensitivity and stability and considering the aim of industrial applications all except the ferrocene azide derivative are commercially available (although the 6-(ferrocenyl)hexanethiol was previously synthesised in-house by Dr N. D. J. Yates and was kindly provided to the author for testing).

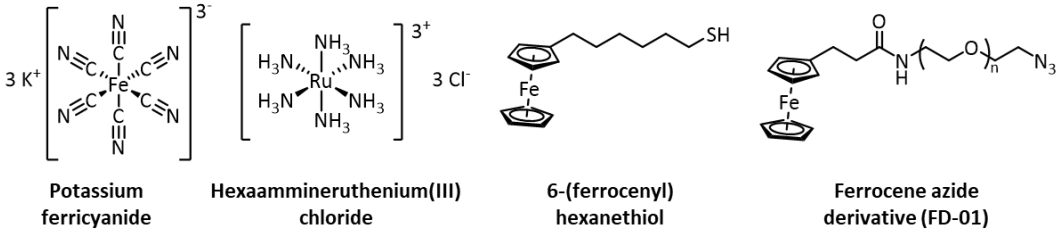

Figure 2.22. *The four redox probes that have been explored in this work.*

2.3.3.1. Using potassium ferricyanide

Potassium ferricyanide consists of iron(III) bound to six cyanide ligands in an octahedral geometry. The d-electrons are in the low-spin arrangement, and the iron is easily reduced to iron(II) to form the ferrocyanide ion. Potassium ferricyanide transfers electrons via an inner sphere electron transfer mechanism.[134] In a chemical reaction, inner sphere electron transfer occurs between complexes via a bridging ligand, at least one of the complexes needs to be labile to allow the bridge to form and bonds are broken and formed. The $[Fe(CN)_6]^{3-/4-}$ is a redox couple that is commonly used as an electrochemical standard or calibrant and as a redox probe in buffers, it has also been used to investigate various

electrodes, to determine the antioxidant capability of samples, and it is widely used in sensing, including impedimetric sensing.[152–155] Based on its well-characterised electrochemical behaviour, its commercial availability, its inorganic nature meaning it should not perturb protein or aptamer structure, and its prevalence in impedimetric biosensing potassium ferricyanide was the initial choice to study and characterise our biosensor system. This was successfully performed as described in section 2.3.2, however, issues with potassium ferricyanide were observed when repetitive measurements were attempted.

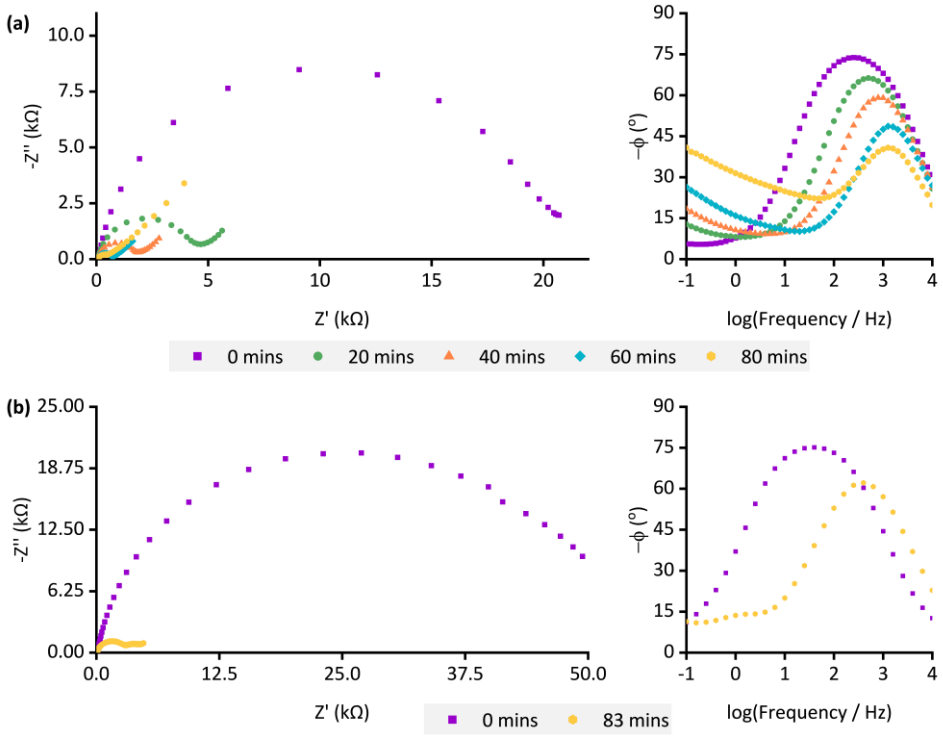

Figure 2.23. *Nyquist and Bode plots for (a) a P-GFF modified SPE and (b) a P modified SPE with constant exposure to $K_3[Fe(CN)_6]$. EIS measurements taken at 0.16 V (vs Ref) with an amplitude of 0.01 V from 10 kHz to 0.1 Hz with ten readings per decade in 10 mM $K_3[Fe(CN)_6]$ in pH 7 aqueous buffer (100 mM sodium phosphate, 233 mM sodium chloride).*

When multiple measurements were attempted on the same electrode, instability in both the Nyquist and Bode plots was observed. **Figure 2.23(a)** shows the results for five impedance measurements recorded over 80 minutes for a P-GFF modified SPE that was immersed in potassium ferricyanide continuously. In the Nyquist plot the semi-circle diameter decreases from approximately 20 kΩ to 0.5 kΩ and in the Bode plot -ϕ decreased from 75° to 40°, this shows significant monolayer destruction. To determine if the destruction was caused by potassium ferricyanide or multiple impedance measurements a P modified electrode was exposed to a 10 mM potassium ferricyanide solution for 83 minutes but only two EIS measurements were taken. **Figure 2.23(b)** shows that despite only two measurements

being recorded there is a similar level of decay showing potassium ferricyanide must be the cause. Repeat measurements at both stages (P and P-GFF) of modification were performed and proved the decay was independent of modification. On consulting the literature, it is found that ferricyanide has a destructive effect on gold surfaces and causes etching. Combined SPR/EIS and QCM-D/EIS measurements have shown damage to the gold surface during EIS measurement due to cyanide ions released from the ferri/ferrocyanide redox probe.[156] The redox couple can exchange a cyanide ligand with water leaving free cyanide ions in solution.[124] The gold surface is etched in the presence of free cyanide as a $Au(CN)_2^-$ complex forms via the Elsner reaction.[157] Mediation of this destructive effect was attempted by rinsing and storing the modified SPE in phosphate buffer in between measurements. Some electrochemical long-term stability was observed but these results were not reproducible. On reflection, a different buffer should have been considered as phosphate buffers can amplify the damage done by potassium ferricyanide;[158] however, in our studies there was no visible damage after long-term storage in phosphate buffer. In fact, in a repetitive EIS study of four buffers (**Figure 2.24**), phosphate, Mes, Tris, and HEPES, the phosphate buffer performed best regarding signal consistency, so experiments have continued with the current phosphate buffer.

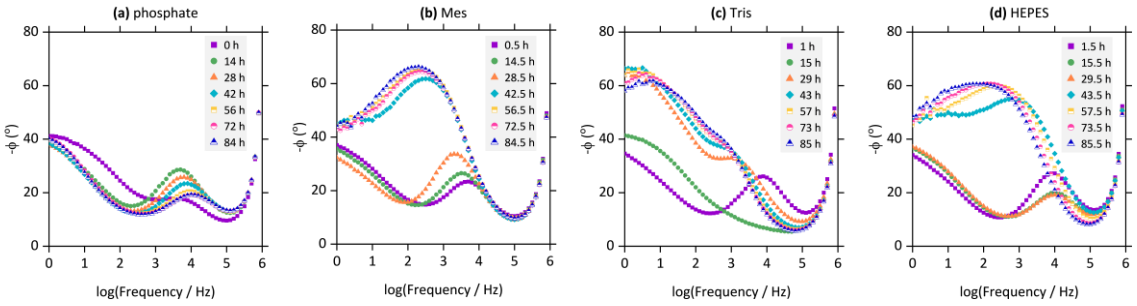

Figure 2.24. *Bode plots showing seven measurements over 84 hours for a bare Au-SPE incubated in a variety of buffers all containing 10 mM $K_3[Fe(CN)_6]$: (a) phosphate, (b) Mes, (c) Tris, and (d) HEPES.*

2.3.3.2. Using hexaammineruthenium(III) chloride

Hexaammineruthenium(III) chloride is a low-spin octahedral complex with ammonia ligands. The ruthenium atom undergoes reversible redox chemistry between the Ru(III) and Ru(II) oxidation states meaning the complex moves between a 3^+ and 2^+ charge. This is oppositely charged compared to potassium ferricyanide so the two redox probes will interact differently with the same system. Although the complex is only stable in the oxidized state a DC bias potential can be applied so the complex can be used as a probe for EIS.[124] Hexaammineruthenium(III) chloride has been used in a variety of ways: monolayer

characterization,[159] protein detection,[160] and in a functional human-IgG biosensor, where it exhibited a linear response from 11.3 ng mL^{-1} to 113 µg mL^{-1}.[124] Conversely to potassium ferricyanide a combined EIS/QCM-D study showed no mass change when using hexaammineruthenium(III) chloride to study gold surfaces via impedance which proves no surface etching occurs.[158] In addition, when used as a redox probe for repetitive cyclic voltammetry study of a modified SPE the CV signals were stable over the 70 minutes studied.[124] This increased stability can be attributed to the fact that hexaammineruthenium(III) chloride transfers electrons via an outer-sphere mechanism so it interfaces with the electrode in a different way to inner-sphere redox probes.[161] A potential drawback of using hexaammineruthenium(III) chloride over potassium ferricyanide is that SAM modification passivates the surface less when compared to ferricyanide. This means the recorded charge transfer resistance will be lower for hexaammineruthenium(III) chloride measuring the same system compared to when using potassium ferricyanide which may reduce sensitivity. For example, on a gold surface modified with p-aminothiophenol the charge transfer resistance was measured as 378 kΩ in $[Fe(CN)_6]^{3-/4-}$ and as 117 kΩ in $[Ru(NH_3)_6]^{2+/3+}$.[134]

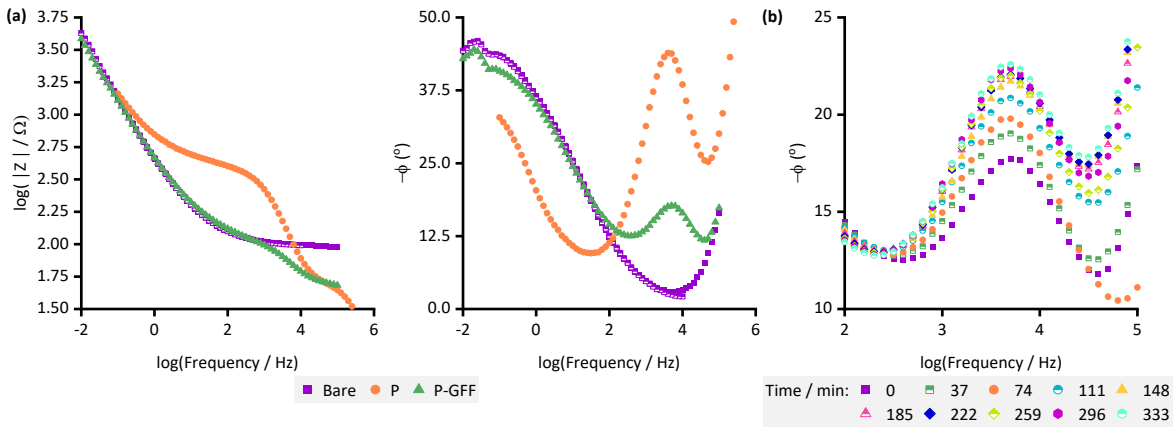

Figure 2.25. *(a) Bode plots for all stages of the modification of disc electrodes (bare, purple squares (two scans are shown to encompass full frequency range); P modified, orange circles; P-GFF modified, green triangles) and (b) Bode plots for a P-GFF modified disc electrode with constant exposure to $[Ru(NH_3)_6]Cl_3$. EIS measurements taken at -0.23 V (vs Ref) with an amplitude of 0.01 V over varying frequency ranges between 1 MHz and 0.01 Hz with ten readings per decade in 10 mM $[Ru(NH_3)_6]Cl_3$ in pH 7 aqueous buffer (100 mM sodium phosphate, 233 mM sodium chloride).*

Through determining the E_{DC} potential to be -0.23 V from CV analysis it can be seen that this voltage should not destabilise the gold-thiol bonds and thus is compatible with the system. Initial experiments (**Figure 2.25(a)**) show that the hexaammineruthenium(III) chloride does detect modification, particularly in differences in the phase angle (-ϕ). The

magnitudes of these phase angles are different compared to those seen with potassium ferricyanide which is attributed to the difference in the complexes charge. To explore stability, a P-GFF modified disc electrode was exposed to hexaammineruthenium(III) chloride for 5.5 hours with EIS data collected every 37 minutes (**Figure 2.25(b**)). While the signal isn't completely stable, with -ϕ increasing from 17.5° to 22.5°, the changes appear to stabilise at the three-hour mark and are significantly less drastic than those observed with potassium ferricyanide so could simply be due to the dynamic nature of the monolayer or the electrostatic interactions inducing more order in the monolayer throughout the experiment. This increased stability makes hexaammineruthenium(III) a promising candidate. The EIS parameter space was explored to determine the optimal conditions as an applied voltage of -0.2 V and a frequency range of 1 MHz to 1 Hz. Using these optimal parameters, a series of measurements of both bare and P-GFF modified electrodes were carried out (analogous to the data collected with potassium ferricyanide, **Figure 2.17** and **Figure 2.20(d)**). The two different groups are distinguishable, **Figure 2.26**, but when compared to the data collected using potassium ferricyanide there is lower sensitivity. This means that although hexaammineruthenium(III) chloride has higher stability, its sensitivity may not be compatible with the requirements for biosensing in our system.

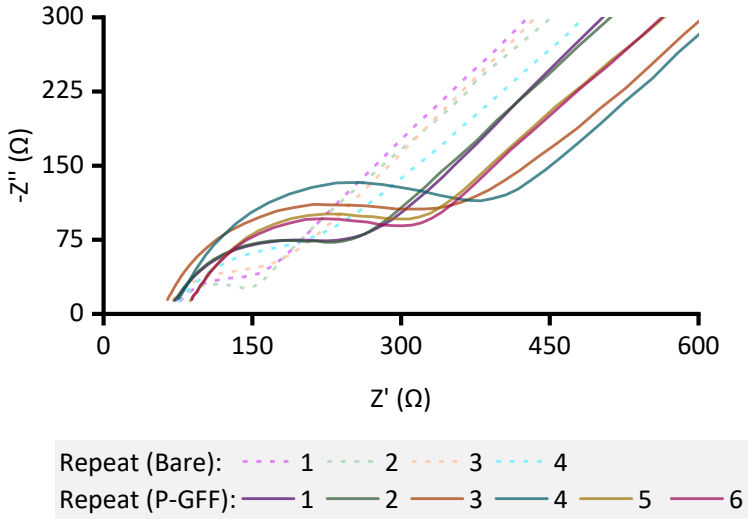

Figure 2.26. *Nyquist plot for a series of repeats of blank and polymer-sugar (P-GFF) modified SPEs studied in 10 mM $[Ru(NH_3)_6]Cl_3$ in pH 7 aqueous buffer (100 mM sodium phosphate, 233 mM sodium chloride). EIS measurements taken at -0.2 V (vs Ref) with an amplitude of 0.01 V from 1 MHz to 1 Hz with ten readings per decade.*

2.3.3.3. Using tethered ferrocene redox probes

Another strategy to consider would be to use an immobilised redox probe opposed to a probe dissolved in solution, this could remove some of the issues with the redox probe damaging the monolayer because it is anchored to the electrode so has limited mobility. Two molecules were studied: 6-(ferrocenyl)hexanethiol, which can be directly linked to the electrode via gold-thiol bond and SAM formation, and a ferrocene azide derivative (FD-01) which can be conjugated to the thiol-polymer via SPAAC and then immobilised onto the electrode. 6-(ferrocenyl)hexanethiol was immobilised onto gold in a 1:10 mixture with the polymer, CV analysis showed redox peaks indicating successful immobilisation centred at 0.5 V (**Figure 2.27(a)**). Probing the electrodes at this positive potential for the duration of an EIS measurement has the possibility to destabilise the gold-thiol bonds, thus this redox probe was deemed unsuitable. Solution CVs on the ferrocene azide derivative revealed a midpoint potential of 0.15 V showing this probe could be studied without destabilising the gold-thiol bonds. The clicked P-FD-01 was immobilised onto an SPE and CV analysis showed successful immobilisation based on observable peaks centred at around 0.19 V, **Figure 2.27(b)**. EIS experiments, carried out prior to CV analysis to ensure no CV destabilisation, shown in **Figure 2.27(c)** are different to what has previously been observed but are in-line with surface-confined redox processes. The experimental data is reasonably well-modelled by the Randles circuit without a Warburg element showing there's no diffusion processes as the probe is tethered. However, with tethered molecules results may be less sensitive as they may not provide a global view of the electrode as the molecules would be interspersed throughout the P-GFF layer. Additionally, the data profiles are less immediately conclusive based on purely visual analysis, thus incorrect conclusions may be made misinforming subsequent measurements during a series of experiments.

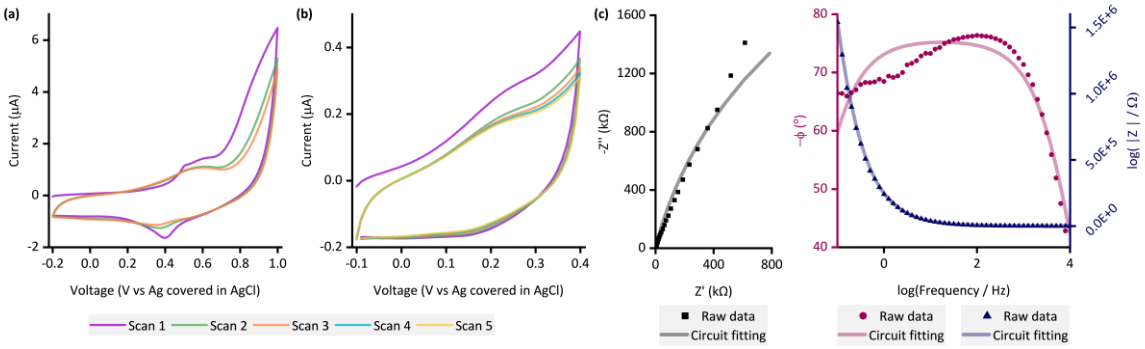

Figure 2.27. *(a) Cyclic voltammograms for a 1:10 mixture of 6FcSH and polymer (left for 24 hours for SAM formation) recorded from 1.0 to -0.2 V (vs Ref) at 100 mV s^{-1}, (b) Cyclic voltammograms for*

immobilised and clicked FD-01 recorded from -0.1 to 0.4 V at 100 mV s^{-1}, and (c) Nyquist and Bode plots for immobilised FD-01. EIS measurements taken at 0.19 V (vs Ref) with an amplitude of 0.01 V from 10 kHz to 0.1 Hz with ten readings per decade.

2.3.3.4. Optimisation of galectin-3 detection

As hexaammineruthenium(III) chloride was identified as a promising potential redox probe in the previous section it was used to carry out some galectin-3 incubation trials. There was a decrease in impedance response observed when we had expected to see an increase in resistance to charge transfer as the galectin-3 would hinder the electron transfer between the solution redox probe and the electrode surface. This may have been due to using too little galectin-3 (P-GFF modified SPEs were incubated in 0.5 mg mL^{-1} for 20 minutes) or due to the ruthenium complex being less sensitive due to its outer sphere mechanism. To examine this further bare Au-SPEs were incubated with BSA, a protein that is expected to display strong non-specific adsorption to surfaces, and interrogated via EIS with both redox probes. It seems that both redox probes do detect this adsorption, **Figure 2.28**. With the ruthenium probe, **Figure 2.28(a)**, the Bode plot appears more sensitive. For the iron probe, **Figure 2.28(b)**, the Bode plot shows a similar magnitude of change as **Figure 2.28(a)** but the Nyquist plot shows a much more obvious change. Importantly, an increase in signal following binding shows mediation of the previously observed degradation of the gold surface by potassium ferricyanide. It is apparent that despite the stability issues of potassium ferricyanide it has much higher sensitivity to binding events so will be prioritised in further studies. Considering the potential degradation of the gold surface by releasing cyanide ions, the experimental protocol has been optimised to reduce the EIS experiment length and ensure electrodes are rinsed thoroughly following contact with potassium ferricyanide.

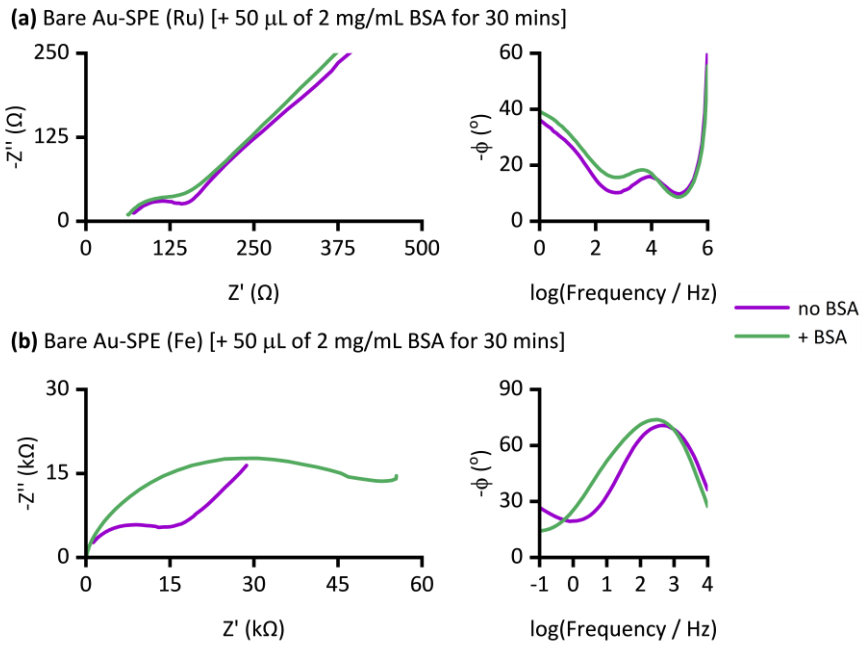

Figure 2.28. *Nyquist (left) and simplified Bode (right) plots for BSA incubation experiments on P-GFF modified SPEs probed with (a) $[Ru(NH_3)_6]Cl_3$ and (b) $K_3[Fe(CN)_6]$. EIS measurements were taken before and after BSA application at -0.2 V (vs Ref) between 1 MHz and 1 Hz for the ruthenium probe and at 0.23 V (vs Ref) between 10 kHz and 0.1 Hz for the iron probe. Solutions were 10 mM of the redox probe in pH 7 aqueous buffer (100 mM sodium phosphate, 233 mM sodium chloride).*

2.3.4. Titration experiments reveal selective and specific galectin-3 binding to the GFF-modified Au-SPEs

2.3.4.1. Studying galectin-3 binding

Galectin-3 titration experiments were performed using EIS analysis, with a 30-minute incubation time used for each protein concentration based on binding kinetics from previously published work.[84] A dataset and corresponding MCMC analysis for a single P-GFF modified Au-SPE (**Figure 2.29**) was generated, with fitting performed for each concentration of galectin-3 to find the best fit values for all seven parameters in the equivalent circuit model (five parameters constitute the modified Randles circuit plus two noise parameters for the phase and magnitude of the impedance). The data is well-modelled by this circuit as a semi-circle and diffusion region is observed, the diffusion region contributes to a lower portion of the experiment at higher concentrations but does remain showing there is still a diffusional contribution to electron transfer. Notably, we observed an increase in magnitude of R_{ct} with galectin-3 concentration and importantly, as shown in the R_{ct} histogram, the distribution of the fitted values of this parameter at different protein concentrations showed no overlap. This data therefore indicated the successful construction of an electrochemical impedimetric biosensor which is responsive to changing levels of

galectin-3. In contrast to earlier experiments comparing different electrodes (**Figure 2.20(b)**), there are smaller distributions in the non R_{ct} parameters, in particular the R_s and Z_W values overlap extensively, suggesting these parameters are insensitive to a change in galectin-3 concentration. Indeed, the advantage of such MCMC data visualisation is that is is a powerful tool for identifying a sensible protein concentration range over which to conduct experiments, and validates that R_{ct} values from measurements at different analyte concentrations have statistically significant differences.

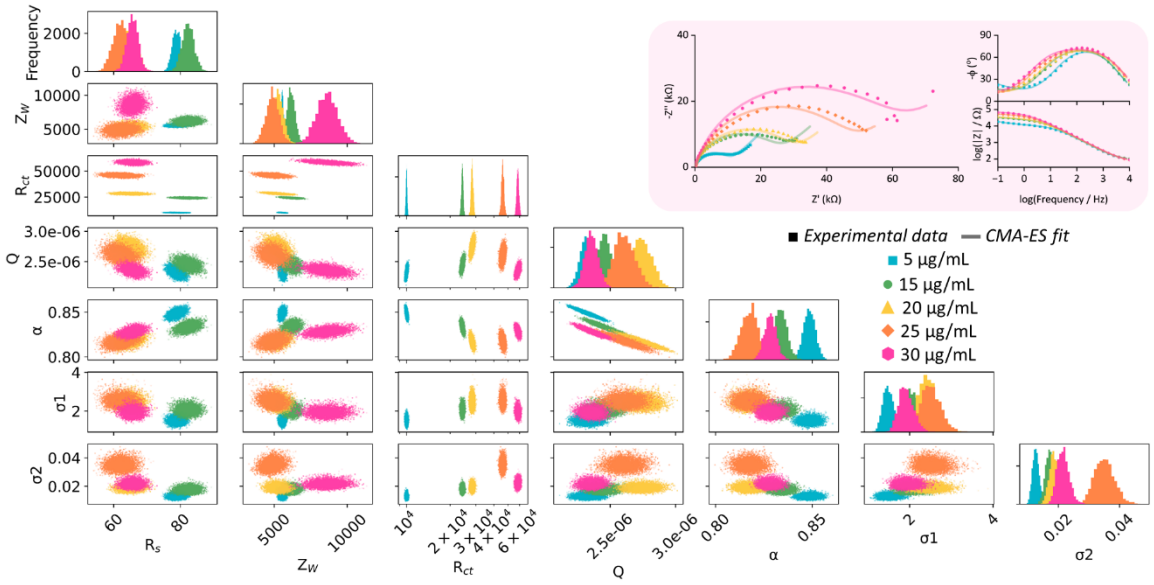

Figure 2.29. *2D scatter plots showing correlations for circuit parameters used to infer parameter distributions from a representative galectin-3 incubation experiment. The diagonal represents the 1D histograms for each parameter showing the distribution of the fitted values. The MCMC used to generate these chains was run for 10,000 samples, with the first 3,000 discarded as burn-in. Inset: Resultant Nyquist plots (dots) and the computational fitting (line) and Bode plots for the galectin-3 incubation experiments. EIS measurements were performed in the presence of 10 mM $K_3[Fe(CN)_6]$ in pH 7 aqueous buffer (100 mM sodium phosphate, 233 mM sodium chloride) with the following parameters: $t_{(equilibration)}$ = 180 s, E_{DC} = 0.230 V, E_{AC} = 10 mV, f = 0.05 Hz – 10 kHz. R_s = solution resistance, R_{ct} = resistance to charge transfer, Z_W = Warburg element, Q and α are the parameters used to model a constant phase element, and σ1 and σ2 are noise parameters.*

Given the substantive variation shown between P-GFF modified Au-SPEs, we repeated the galectin-3 titration experiments on a total of 15 different P-GFF modified SPEs (**Figure 2.30**), this allowed the determination of the viable galectin-3 sensing range and the quantification of electrode-to-electrode variation. Both the raw Nyquist data and the extracted R_{ct} values (plotted on a logarithmic scale) from equivalent circuit fitting are shown (**Figure 2.30 and Figure 2.31**). A general trend of increasing R_{ct} with increasing galectin-3 across a protein concentration range of 15 – 30 µg mL^{-1} was observed, below this region the response is variable although generally above 5 µg mL^{-1} a consistent increase is observed. In **Figure**

2.31(a), data collected over too low a galectin-3 concentration range to permit further analysis, repeats 1 – 7, and datasets with an anomalous initial protein-free measurement (outside the 5^{th} – 95^{th} percentile range from **Figure 2.20(d)**), are shown in grey. **Figure 2.31(b)** shows the distribution in R_{ct} values obtained from MCMC analysis of the experiments depicted in black in **Figure 2.31(a).** It can be seen that there is a large variation in binding signal observed even for repeats covering the same concentration range, e.g. Repeat 1 and Repeat 3, and, Repeat 14 and Repeat 15. This variation is likely related to the differences in gold-thiol immobilisation due to inconsistencies in the gold environments present on different SPEs as discussed. As each electrode has a different extent of gold-thiol bonds present they will each be presenting different levels of glycofluoroform into solution to interact with the galectin-3. Therefore, the ease at which galectin-3 binds to the electrode surface and the resultant observed EIS response is different for each electrode. Attempts to normalise these differences by identifying complementary parameters through MCMC analysis was unsuccessful showing there is not a simple mathematical route to collapse this variation.

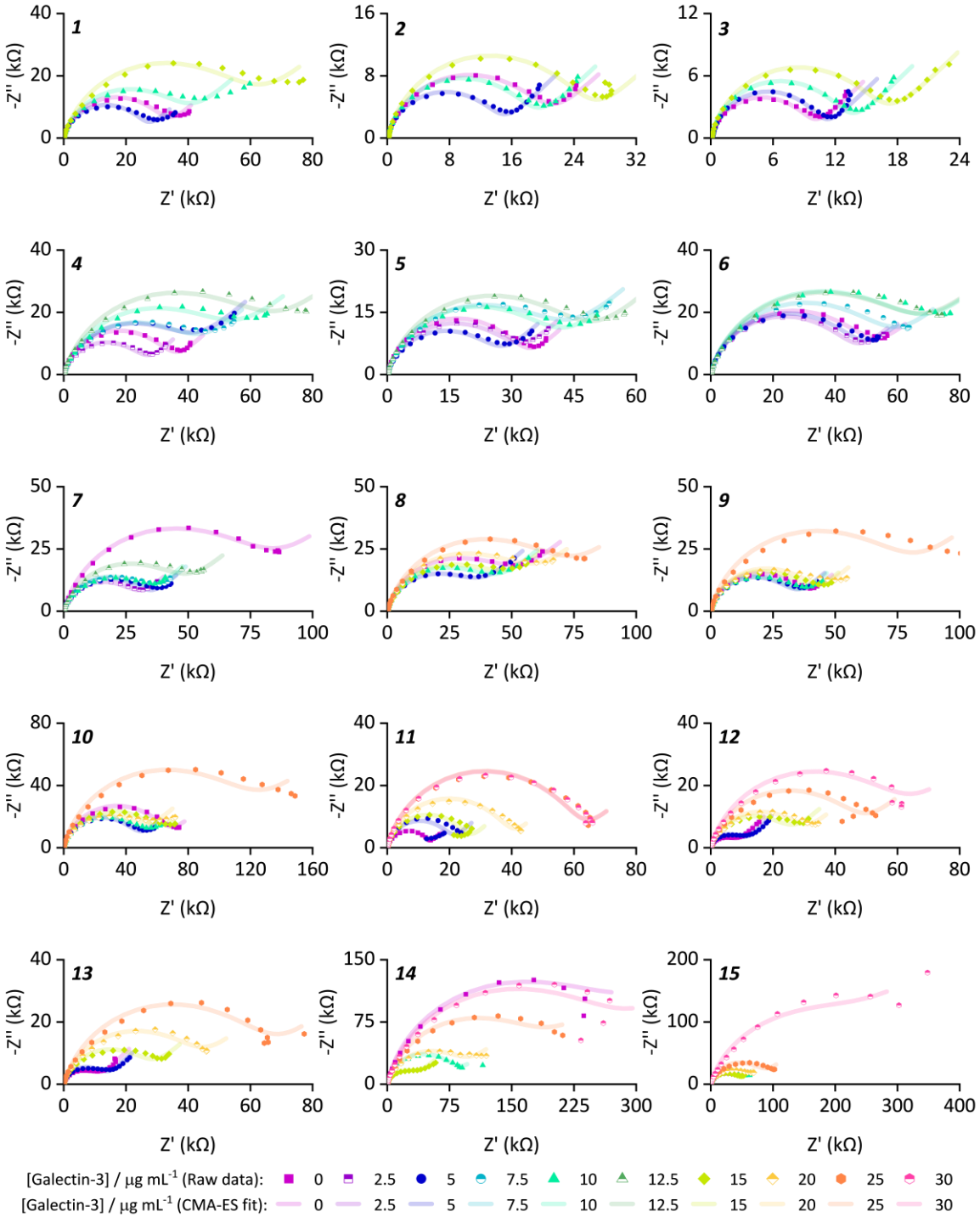

Figure 2.30. *Nyquist plots, where the dots are the experimentally measured datapoints and the lines are the equivalent circuit fits, for galectin-3 titration experiments performed on different P-GFF modified Au-SPEs, the number is the top-left corner corresponds to the repeat number referenced in* ***Figure 2.31****. EIS measurements were performed in the presence of 10 mM* $K_3[Fe(CN)_6]$ *in pH 7 aqueous buffer (100 mM sodium phosphate, 233 mM sodium chloride) with the following parameters:* $t_{(equilibration)}$ *= 180 s,* E_{DC} *= 0.230 V,* E_{AC} *= 10 mV, f = 0.05 Hz – 10 kHz.*

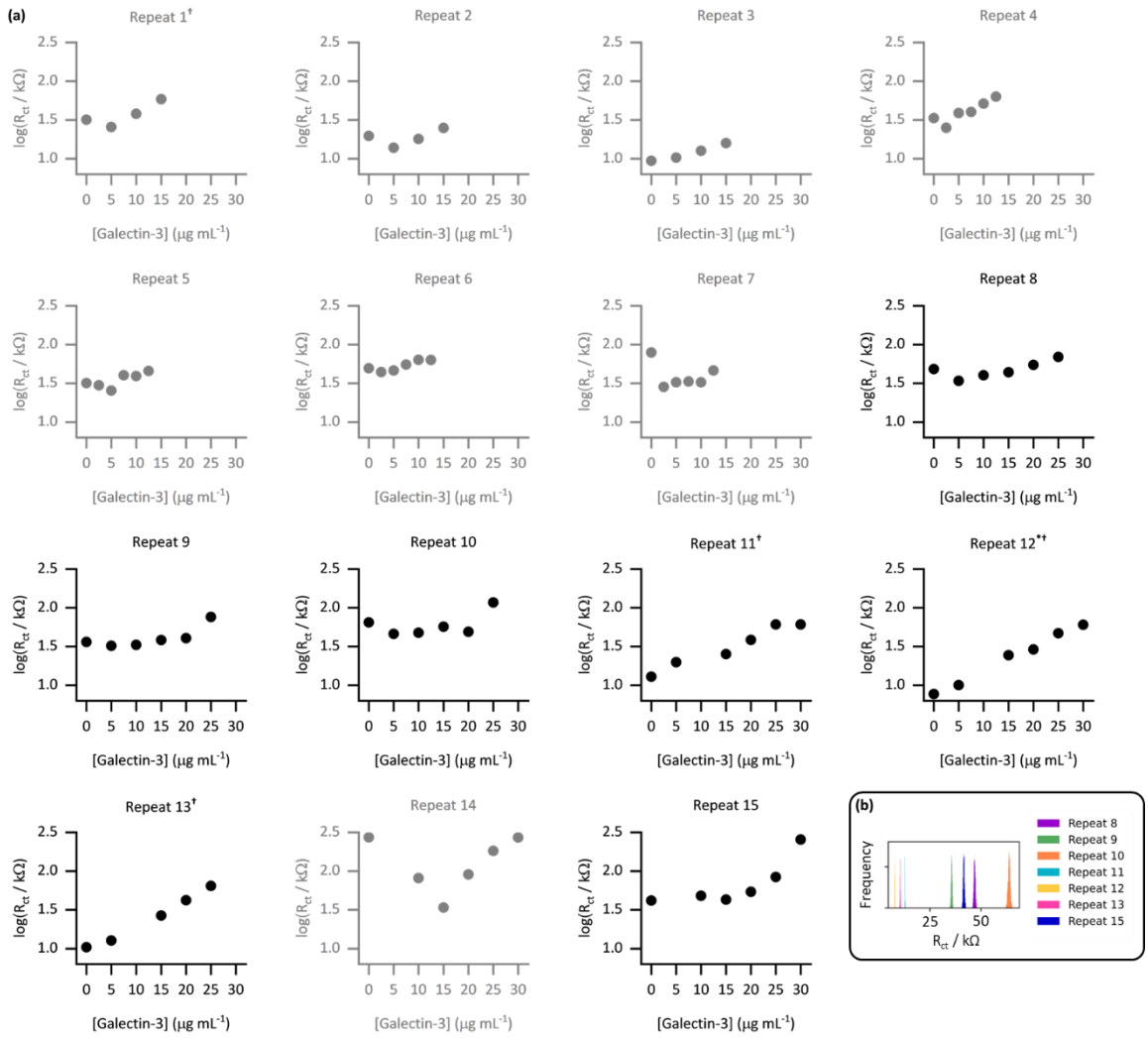

Figure 2.31. *Extracted R_{ct} parameters for the experiments shown in* ***Figure 2.30****. (a) Best-fit point values obtained from CMA-ES analysis. * denotes the dataset shown in* ***Figure 2.29*** *and repeats marked with a † are the datasets combined in* ***Figure 2.32****. (b) Distributions obtained from MCMC analysis for the initial measurement (i.e. 0 μg mL^{-1} galectin-3 concentration). EIS measurements were performed in the presence of 10 mM $K_3[Fe(CN)_6]$ in pH 7 aqueous buffer (100 mM sodium phosphate, 233 mM sodium chloride) with the following parameters: $t_{(equilibration)}$ = 180 s, E_{DC} = 0.230 V, E_{AC} = 10 mV, f = 0.05 Hz – 10 kHz.*

Ideally, it would be possible to combine all the datasets from all the repeats for a comprehensive binding analysis. However, it can be seen that the binding response varies. This is likely due to the variability in modification conferring different binding capabilities onto different modified electrodes. Instead, MCMC analysis was used to identify three electrodes which had sufficiently similar R_{ct} values in the initial protein-free EIS experiments (12.9, 7.7, and 10.4 kΩ) to justify amalgamation (**Figure 2.31(b)**). Attempts in the next chapter will be made to develop a more consistent immobilisation method to reduce this variability and allow all datasets to be considered. However, a filtering step was used akin

to a quality control stage where uniform modified electrodes were identified by a similar starting EIS response. This allows the binding response for a sub-set of the modified electrodes to accurately be determined. While other electrodes are likely to operate under a slightly different binding regime, this approach allows more certainty in quantifying a sub-set of electrodes in order to draw comparisons with the previously established nanoparticle-based optical assay. The R_{ct} vs galectin-3 concentration plot for this combined dataset is shown in **Figure 2.32**, and this confirms that a reproducible galectin-3 binding response is achieved across repeat electrodes where they have a similar initial R_{ct}.

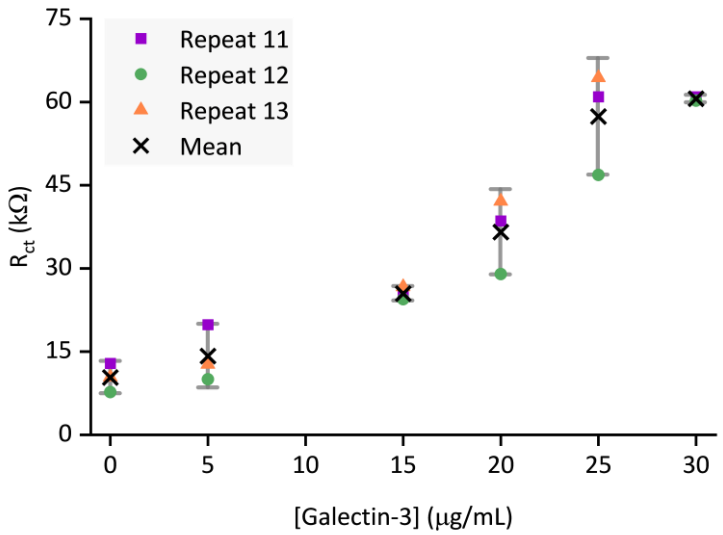

Figure 2.32. *Extracted R_{ct} parameter plotted against galectin-3 concentration for three SPEs with similar values of protein free initial measurements, the mean value and 95% confidence limits are shown with a black cross and grey vertical error bars, respectively.*

2.3.4.2. Quantification of binding using Langmuir and Hill equations

Applying the analysis described by Bandyopadhyay *et al.*,[162] assuming a Langmuir isotherm, enables the dataset to be linearised as shown in **Figure 2.33(a)** with the gradient of the plot corresponding to $1/K_d$ as shown in Equation 2.10, where C is the galectin-3 concentration and $R_{ct,0}$ and $R_{ct,i}$ are the resistance to charge transfer at a protein-free stage and after protein incubation, respectively. This assumes that R_{ct} is a direct measure of binding (Equation 2.8) and uses the relationship between θ and K_a (Equation 2.9). Using this analysis and setting a y-intercept of zero yields a K_d of 6.3 µg mL^{-1} which equates to 240 nM assuming a molecular weight of 26 kDa for galectin-3. The K_d value for the GFF EIS biosensor is notably higher than the K_d of 6.0 nM achieved using the same P-GFF binding system on Au nanoparticles,[84] we attribute this to the differences in the grafting density and the

increased steric repulsion in the interaction between solution-phase galectin-3 and a planar Au-SPE surface compared to a solution suspension of Au nanoparticles.

$$\theta = 1 - \frac{R_{ct,0}}{R_{ct,i}} \qquad \textit{Equation 2.8}$$

$$\theta = \frac{K_a C}{(1 + K_a C)} \qquad \textit{Equation 2.9}$$

$$\frac{R_{ct,i} - R_{ct,0}}{R_{ct,0}} = \frac{C}{K_d} \qquad \textit{Equation 2.10}$$

where: θ: fraction of occupied binding sites; C: galectin-3 concentration (mol dm^{-3}); $R_{ct,i}$: charge transfer resistance after incubation (Ω); K_a: association constant (mol^{-1} dm^3); $R_{ct,0}$: charge transfer resistance before incubation (Ω); K_d: dissociation constant (mol dm^{-3})

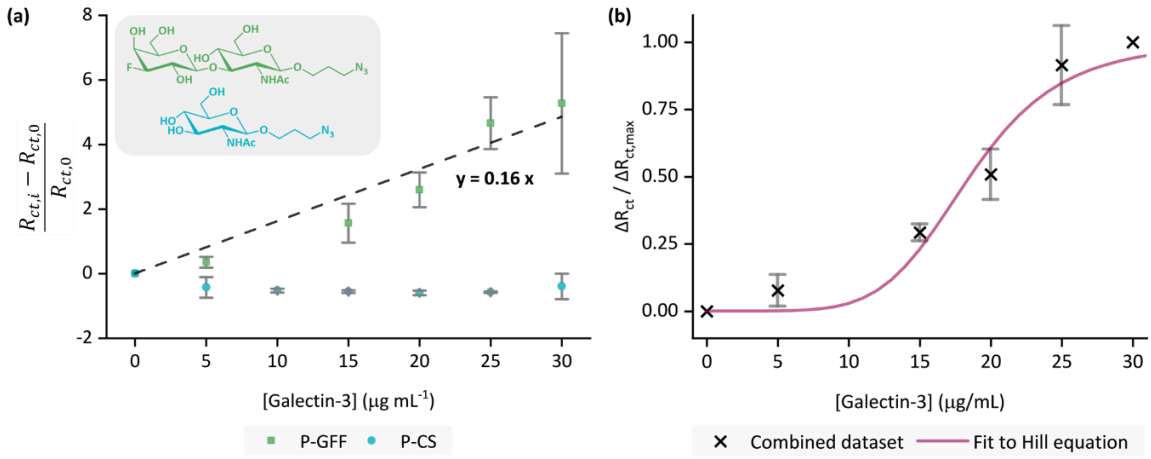

Figure 2.33. *(a) Combined datasets from three different P-GFF (green squares) and P-CS (blue dots) modified Au-SPEs titrated against galectin-3. The P-GFF dataset is fit to a straight line (black dashed line, equation shown on plot) to enable determination of K_d, as described in the text. Inset: chemical structures of GFF (green) and CS (blue). The datapoints represent the average values from the combined datasets, while vertical error bars represent the standard deviation. (b) Analysis of the combined response-versus-protein concentration dataset (**Figure 2.32**), where datapoints (black crosses) are the average value from the dataset and vertical error bars denote the standard deviation. A best fit to the Hill equation is shown by the pink line, as described in the text. Here, n =5.7 and K_A (sometimes referred to as the "EC_{50}" value) = 18.5 μg mL-1 (equivalent to 713 nM).*

An alternative method of assessing ligand-protein binding affinity is to use the Hill equation (Equation 2.11), as has been previously reported in the EIS biosensor literature and provides an insight into binding cooperativity.[163–165] An n value greater than 1 indicatives positive binding cooperativity which means the binding of one ligand facilitates the binding of another. An n value less than 1 indicates negative cooperativity where the binding of one ligand disfavours further ligand binding. An n value equal to one means there is no positive

or negative effect on initial ligand binding.[166] As shown in **Figure 2.33(b)**, such an analysis can also be used to generate a good fit to the data. The best-fit Hill coefficient value, n = 5.7, is consistent with the notion that the proposed multimeric-multivalent binding mode of galectin-3 supports cooperative binding between the protein and the P-GFF surface.[167] The best-fit value for K_A, the ligand concentration producing half occupation, was 18.5 μg mL^{-1} (equivalent to 713 nM).

$$\frac{\Delta R_{ct}}{\Delta R_{ct,max}} = \frac{[Gal-3]^n}{{K_A}^n + [Gal-3]^n} \qquad \textit{Equation 2.11}$$

where: ΔR_{ct}: change in charge transfer resistance (i.e. $R_{ct,i} - R_{ct,0}$) (Ω)
$\Delta R_{ct,max}$: maximum change in charge transfer resistance (i.e. $R_{ct,max} - R_{ct,0}$) (Ω)
K_A: ligand concentration producing half occupation (mol dm^{-3})
n: Hill coefficient

2.3.4.3. Control experiments to determine selectivity and specificity

To confirm that the observed galectin-3 concentration dependent response is a result of the specific affinity of the protein for the 3F-lacto-*N*-biose glycofluoroform, further protein titration experiments were carried out using a non-galactoside control monosaccharide with negligible affinity for galectin-3 (GlcNAc-N_3, **Figure 2.33(a)**). Once again, the DBCO polymer was subjected to SPAAC with the azide containing monosaccharide, before the polymer-control sugar (P-CS) modified electrodes were incubated with galectin-3. A non-concentration dependent R_{ct} response to galectin-3 was seen across three P-CS modified Au-SPEs (**Figure 2.34**) indicating that binding of galectin-3 to modified electrodes is glycofluoroform specific. To best summarise this, the EIS response for P-CS modified electrodes was compared to P-GFF electrodes using the K_d analysis described above, as shown in **Figure 2.33(a)**).

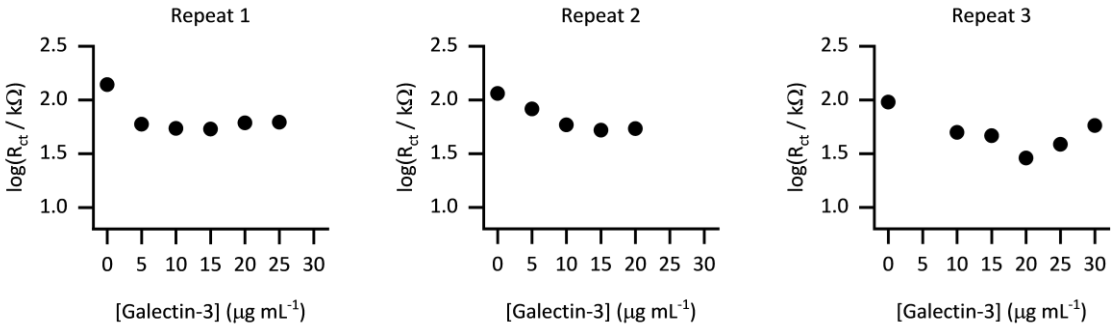

Figure 2.34. *Extracted R_{ct} parameters for the P-CS modified Au-SPEs.*

Finally, an ideal diagnostic biosensor would show minimal off-target binding to other biomolecules present in biological samples; this can be very challenging to achieve because

serum contains albumins and immunoglobins, and plasma additionally contains fibrinogen[168] which are all proteins which are capable of non-specific surface-binding interactions. We therefore explored whether the incorporation of the P-GFF within the biosensor would act to advantageously reduce any non-specific binding, using albumin (BSA) as a model analyte. Importantly, although EIS experiments using increasing concentrations of BSA (**Figure 2.35**) show a significant change in R_{ct} on bare electrodes, this non-specific binding to the gold electrode is reduced when using electrodes modified with the P-GFF.

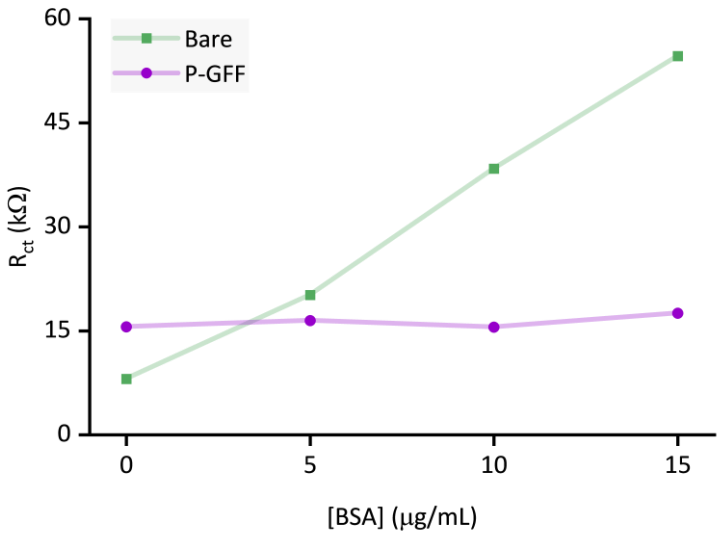

Figure 2.35. *Extracted R_{ct} parameters for BSA incubation of both bare and P-GFF modified Au-SPEs.*

2.4. Summary and conclusions

This work establishes how the enhanced protein-binding specificity of a glycofluoroform can be harnessed for electrochemical biosensing. The potential of this platform is showcased in the detection of galectin-3 using glycofluoroform modified Au-SPEs, establishing charge transfer resistance as a proxy measurement for protein binding. By detecting a biomedically relevant protein, we aim to demonstrate the potential for long-term diagnostic device development.

Before titration experiments were performed electrode types, chemoenzymatic synthesis optimisation, and redox probes were explored. It was determined the concentration of the enzyme used does affect the synthetic yield, SPEs are a suitable platform for immobilisation, and potassium ferricyanide provides the greater sensitivity for electrochemical measurements.

The electrode surface modification ensures sensitivity and selectivity for the target analyte, the glycofluoroform-polymer also exhibits robust stability over a prolonged period, an advantage over other less chemically stable/storable biosensing biomolecules,[151,169] and the P-GFF also pacifies the gold surface to non-specific albumin binding. Although it was demonstrated that Au-SPEs exhibit electrode-to-electrode variation that must be accounted for during analysis, they are also compatible with low-volume measurements and this enticing combination of electrochemical cell miniaturization with sensitive and specific binding is highly desirable in point-of-care diagnostic applications.[170,171] This chapter shows GFF can be used as a new class of bioreceptors, adding a new and powerful tool to the biosensing toolkit.

Chapter Three: Utilising emerging triazabutadiene molecules to employ a carbon surface for biosensing

As shown in chapter two, an electrochemical impedance spectroscopy biosensor platform utilising glycofluoroforms shows promise in galectin-3 detection. However, one of the main issues with this initial biosensor design is the stability of the gold-thiol bond tethering the polymer-glycofluoroform conjugate to the gold electrode surface. Electrode modification is a rich topic in the literature, and a different immobilisation strategy could yield a more stable sensor surface for our measurements and enable a switch to a carbon-based sensor. The usage of carbon-based sensors is commonplace due to the relative low cost, high surface area, ease of functionalisation, high thermal stability, and favourable electrochemical properties, namely high conductivity, low background currents and wide potential stability.[96,127,172] An overview of some relevant electrode modification strategies for biosensing are outlined in the next section. The history and development of the triazabutadiene molecules that form the basis of the immobilisation strategy this result chapter focuses on are discussed in more detail. This chapter then describes the usage of these triazabutadiene molecules as masked diazonium ions to enable a carbon surface to be employed for sensing. A novel conjugation and purification method to conjugate the thiol-polymer to the triazabutadiene molecule is described. Comprehensive studies of the modified surface are performed using both the polymer and polymer-glycofluoroform substrates as well as a ferrocene derivative to enable voltammetric enquiry of the modification. Finally, galectin-3 binding to this new sensor platform is monitored using electrochemical impedance spectroscopy and the results are assessed with Hill-Langmuir binding analysis.

3.1. Introduction

3.1.1. Electrode modification and substrate immobilisation

This thesis aims to develop new methods for building an electrochemical biosensor that detects galectin-3. Bare surfaces of C, Au, Hg and Pt have found extensive use in biosensing applications.[173] However, these electrode surfaces also suffer from fouling, slow reaction rates and non-specific redox behaviour, therefore electrode modification strategies are often employed in the electrochemical biosensing literature. The modification of working electrodes has been a topic of interest in the electrochemical community since the late 1970s,[174] originally motivated by electrochemists seeking more complex surfaces to

investigate. Developing new modification techniques as well as materials to exploit continues to be integral to electroanalysis.[96] Electrode modification can be via electrostatic, non-specific adsorption, non-covalent or covalent interactions and tunes both the electronic, i.e. conductivity and resistivity, chemical, i.e. specificity and selectivity, and sensing properties. Tailored electrode surfaces have subsequently found use beyond purely electrochemical study in applications such as corrosion studies, molecular electronics,[175] energy conversion and enzymatic fuel cells,[176] industrial electro- or bio-catalysis reaction,[177] as well as immunoassays and sensors.[178,179]

Figure 3.1. *Requirements of a selected modification method to be suited for biosensors.*[180]

Electrode modifications for electrochemical biosensing can provide both benefits and drawbacks to a biosensor and must meet the requirements shown in **Figure 3.1**. The benefits of surface modification should be: increased specificity, selectivity, sensitivity and the improvement of performance due to the prevention of surface fouling.[181–183] The drawbacks of surface modifications are that they can require expensive and timely procedures, can introduce irreproducibility if the modifiers are unstable, and may make the application of the sensor too niche, reducing profit capability. Therefore, the performance of the electrode modification chemistry must be optimised for the sensing application. This chapter focuses on using triazabutadiene functionality to "smuggle" diazonium groups onto the glycofluoroform-polymer conjugate used in the previous chapter. To provide some context, diazonium electrode modifications will be briefly reviewed.

3.1.2. Diazonium electrografting in biosensing

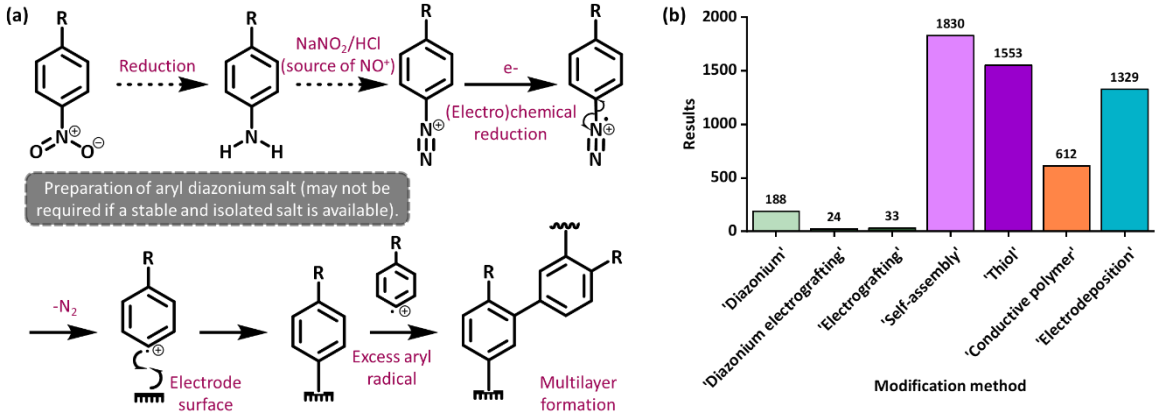

Figure 3.2. *(a) Reaction scheme for aryl diazonium electrografting onto an electrode surface and (b) Web of Science results for searches performed with keywords 'biosensor' and 'column titles' in the topic field to compare modification method popularity.*

Diazonium electrografting is a modification method that can be carried out under chemical or electrochemical control. It is suited for many electrode materials, having first been reported for carbon electrodes, the scope of this modification strategy has since been expanded to electrodes comprised of gold, indium tin oxide (ITO), silicon, and iron.[184] Beyond this versatility, other advantages to the diazonium-electrode modification strategy include the fact that the resulting carbon-electrode covalent bond is generally thermally, temporally, and electrochemically stable. Diazonium electrografting is a well-studied procedure that occurs via the mechanism shown in **Figure 3.2(a)** and involves the loss of nitrogen due to a reductive step which forms an aryl radical, followed by radical attack forming a covalent bond with the electrode surface. When this process is induced and observed by cyclic voltammetry (CV) a broad irreversible peak signifies successful electrografting.

While there are examples of diazonium electrografting being used in the literature to prepare biosensors, it is significantly less popular than other surface modification techniques involving self-assembled monolayers, electrodeposition, or conductive polymers.[185,186] This is evidenced in **Figure 3.2(b)** which shows the results of Web of Science searches. The relatively small number of examples of diazonium-modified electrodes used for electrochemical sensors include examples of environmental and biological sensing for the detection of a wide range of analytes including metal ions, small molecules, proteins, DNA, and whole cells, as summarised in the schematic **Figure 3.3** and **Table 3.1**.[185] For the copper(II) sensor, the cyclam ring chelates the copper ions and the binding is detected

through linear sweep stripping voltammetry.[181] For glucose sensing, glucose oxidase (GOx), an enzyme that catalyses the oxidation of glucose to H_2O_2 and gluconolactone, is immobilised onto an electrode. The presence of glucose is detected through amperometric studies due to its effect on the flavin adenine dinucleotide (FAD) activity.[187] For the α-fetoprotein (AFP) an immunosensor is formed where a capture-AFP antibody is immobilised onto the electrode, the anti-AFP antibody is conjugated to horseradish peroxidase. Detection of AFP binding is coupled to the electrocatalysis of horseradish peroxidase.[188] For DNA, a mixed layer is formed. One component has a carboxylic acid unit which can be activated and coupled to amine-terminated DNA complementary to the target. The other has a quinone unit which undergoes electron transfer and intercalates DNA. In the absence of the target the appended DNA is intercalated which slows the electron transfer of the quinone unit but this hinderance is removed in the presence of the target DNA as both strands will hybridise. This increase in electron transfer of the quinone unit is observed as increasing current in square wave voltammetry.[186]

Table 3.1. *Summary of the key information for four diazonium-based sensors.* [181,186–188]

Target Analyte	Cu(II)	Glucose	α-fetoprotein	DNA
Sensitivity	10^{-10} – 10^{-9} M	10 μM – 4.5 mM	0.03 – 2 ng mL^{-1}	10 pM detection limit
Selectivity	Interference by Pb^{2+}	Recovery between 96.1 – 104.0 % in plasma	No binding from BSA or CEA (carcino-embryonic antigen)	No interaction with random DNA strand
Diazonium source	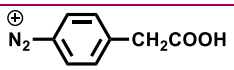	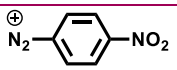	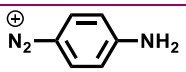	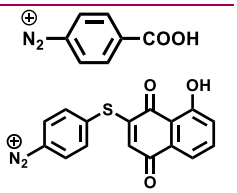
Commercial availability?	✗	✓	✗	✗
Grafting conditions	-0.2 V vs SCE in 0.5 M HCl for 5 min under N_2	CV scans between 0.4 and -0.3 V vs Ag/AgCl (3 M KCl) at 0.1 V s^{-1} in MeCN	CV scans between 0.2– 0.6 V vs Ag/AgCl at a scan rate of	CV scans between 0.8 and -1 V vs SCE at 0.1 V s^{-1}, in 0.1 M $HClO_4$, 0.1 M Et_4BF_4

			0.5 V s^{-1} in 0.5 M HCl	
Further modification?	1. DCM, Ar, 0 °C 2. DAST, RT, 5 h stirring *(activation of carboxyl groups)* 3. Cyclam, base, Ar, RT, 24 h stirring *(cyclam coupling)*	1. Electro-chemical reduction in 0.1 M KCl solution in H_2O:EtOH (9:1) *(reduction of NO_2)* 2. GOx in pH 7.0 phosphate buffer for 25 cycles between -1.0 and 1.2 V *(peptide bond formation)*	1. 2h incubation in glutaraldehyde *(introduces tethering site for antibodies)* 2. Anti-AFP capture antibody, 2h, 4 °C, aqueous *(crosslinks antibody)* 3. 1.5% BSA, 30 min *(to block non-specific sites)*	1. EDC, NHS, 2 h *(carboxylic activation)* 2. DNA-NH_2, 37°C, PBS, overnight *(peptide bond formation)*
Reference	181	187	188	186

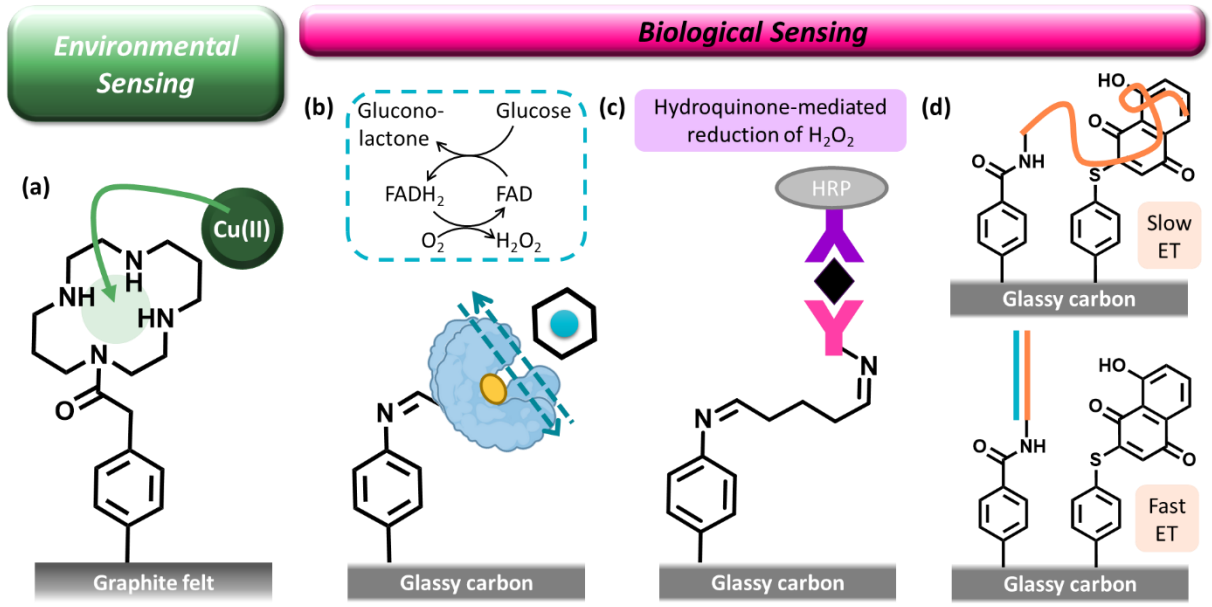

Figure 3.3. *Schematic figure of various sensors that use diazonium electrografting in their construction and sense (a) copper ions, (b) glucose, (c) α-fetoprotein, and (d) DNA. In (b) the blue globular protein is GOx, the yellow oval is the FAD (flavin adenine dinucleotide) active site, and the hexagon with the blue circle is glucose. In (c) the pink antibody is the capture antibody, the black diamond is AFP (α-fetoprotein), and the purple antibody is anti-AFP. In (d) the orange line is the complementary appended DNA and the blue line is the target DNA.*

The highlighted sensors generated via diazonium-modification generally perform well when considering selectivity and sensitivity and are clearly suited to a wide range of target analytes. However, diazonium salts are generally not stable due to the high reactivity of the diazonium ion. Therefore, the "commercial availability" row of **Table 3.1** indicates whether the diazonium salt must be generated *in situ*. The *in situ* generation of a diazonium normally requires an aryl amine reacting with NO^+, usually from $NaNO_2$ and HCl (see **Figure 3.2(a)**). The necessity for acidic conditions make this method incompatible with some biomolecules that would be ideal biorecognition elements in a biosensor. As an alternative *in situ* method for diazonium generation, triazenes are compounds that can generate diazonium ions under milder conditions (**Scheme 3.1**). The top route (shown with purple arrows) can use an electrochemically generated acid as a source of protons therefore allowing careful experimental control.[189] The bottom route (shown with green arrows) uses a methylating agent with no other additives other than buffer salts.[190] Another approach of particular biological relevance is a specific sub-class of triazenes, triazabutadienes, which have been utilised in this chapter.

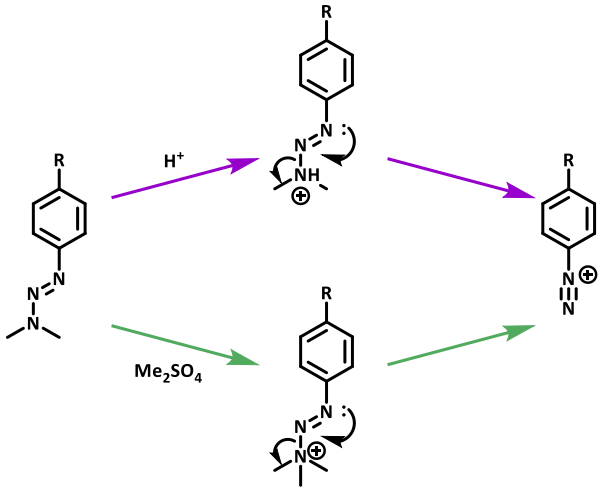

Scheme 3.1. *Proposed mechanism for diazonium ion formation from triazenes with an electrochemically generated acid (purple arrows) or with a methylating agent (green arrows).*

Following diazonium electrografting the presentation of the biorecognition element generally requires several lengthy steps with additional, and in some cases hazardous, chemicals. This adds complexity to sensor construction. An additional issue observed with diazonium electrografting is multi-layer formation, the final stages of **Figure 3.2(a)**, caused by the homogenous reaction of unsaturated aryl rings or the heterogeneous reaction with an aromatic residue on the electrode surface.[191] For ease of sensor production, the most

attractive strategy to alleviate multilayer formation would be by using a bulky diazonium molecule, where steric hinderance prevents multilayer formation, as it doesn't require additional reagents or steps post-modification.[192] Triazabutadienes are an interesting avenue to explore as they can provide a solution to both issues – post-graft functionalisation and multilayer formation.

3.1.3. Triazabutadienes

3.1.3.1. History of Triazabutadienes

Triazenes are organic compounds containing three sequential nitrogen atoms with a double bond between N^1 and N^2.[193] There are three structural classes of triazenes:[193] linear (the first triazene reported in 1866 was a linear triazene),[194] π-conjugated (first reported in 1965),[195] and cyclic (**Figure 3.4**).[196] The π-conjugated triazenes (**Figure 3.4(d)**) have unique reactivity and are also known as "triazabutadienes", this nomenclature will be used throughout the rest of this thesis.

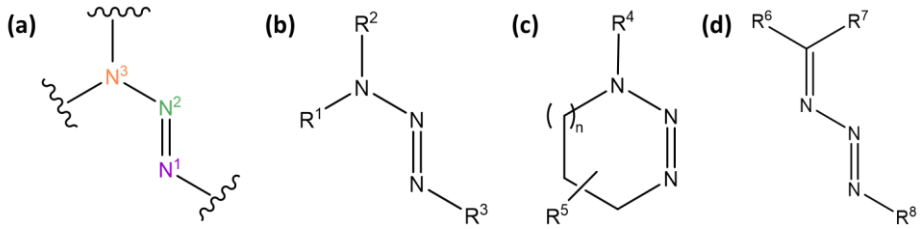

Figure 3.4. *(a) Triazene moiety and the general structures of the three sub-classes: (b) linear, (c) cyclic, and (d) π-conjugated triazenes.*

Triazabutadienes have been studied as anticancer agents in medicinal chemistry, as anionic ligands in organometallic chemistry, as protecting groups in synthetic organic chemistry, and, of particular relevance to this research, as a source of diazonium ions in biological chemistry.[197] A range of triazabutadiene molecules are highlighted in **Figure 3.5** as these molecules exemplify key advancements to, and, relevant properties of this class of molecules. Various synthetic routes to triazabutadienes have been developed since the first reported synthesis in 1965. The simplest method, reported by Bielawski and co-workers,[198] combines imidazolium salts (deprotonated *in situ* to produce a reactive carbenes) and azides (**Figure 3.5(a)**). A range of azides (alkyl, aryl, acyl, and sulfonyl) were tolerated.[198] Khramov and co-workers made a series of molecules to assess the electronic properties of triazabutadienes (**Figure 3.5(b)**). X-ray crystallography shows bond alteration patterns consistent with donor-acceptor molecules, and UV-Vis spectroscopy indicated electron

delocalisation.[199] This proves the triazabutadiene link allows for electronic communication across the molecule. The thermal properties of triazabutadienes have also been explored. In the solid state they can be air and moisture stable for months, while in solution phase the stability depends on the electronic effects. Generally, electron rich triazabutadienes decompose rapidly when heated and when left in solution at ambient temperatures, whereas electron deficient analogues tolerate high temperatures for prolonged periods without decomposition.[200] One thermal decomposition pathway is the loss of nitrogen to form a guanidine by-product, the results from the studied compounds are presented in **Figure 3.5(c)**. In terms of steric effects, increasing the size of the N-substituent (i.e. R'') increases stability.[199] Some triazabutadienes have been synthesised that exhibit reversible redox properties, non-linear optoelectronic properties, and pH-sensitive diazonium release.[193,201] The latter effect, tuned diazonium release, is particularly attractive for biological labelling applications. Jewett and co-workers have developed water-soluble triazabutadienes (**Figure 3.5 (d)**) that release diazonium ions under physiologically relevant conditions (pH 5 – 7 in phosphate or phosphate citrate buffers), as detailed in the next sub-section.[201]

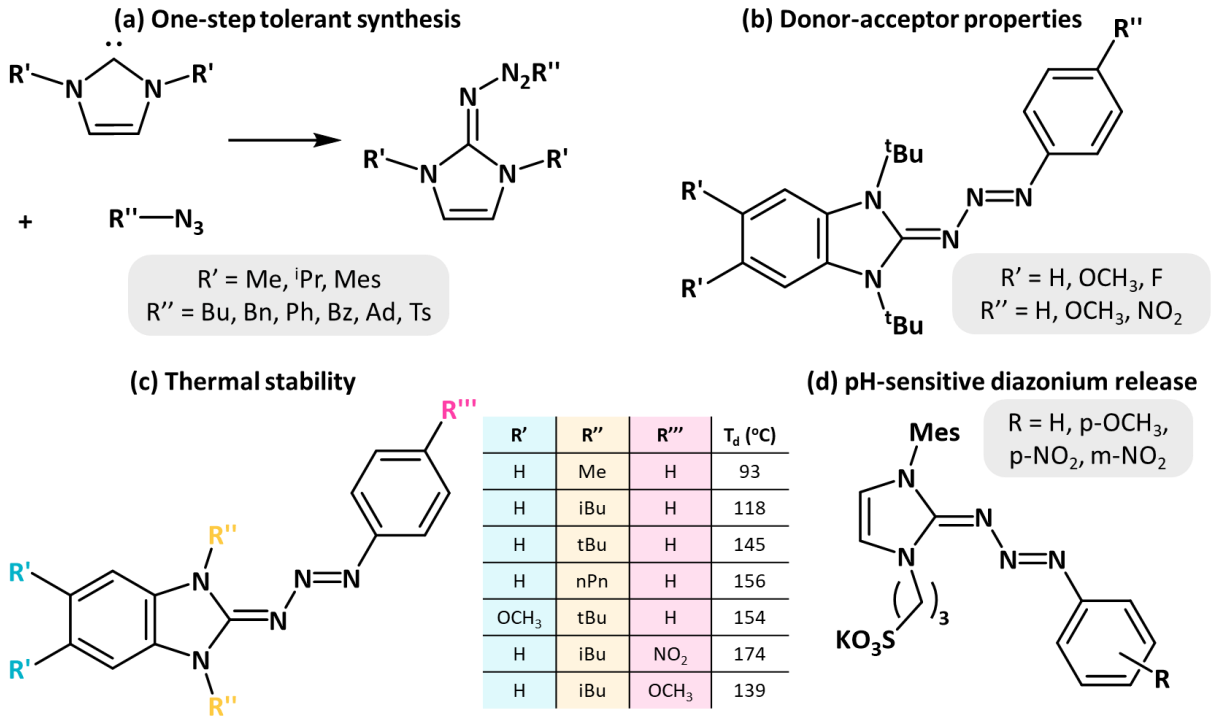

R'	R''	R'''	T_d (°C)
H	Me	H	93
H	iBu	H	118
H	tBu	H	145
H	nPn	H	156
OCH_3	tBu	H	154
H	iBu	NO_2	174
H	iBu	OCH_3	139

Figure 3.5. *Key triazabutadiene molecules from: (a) the study reporting a one-step substituent tolerant synthetic pathway and studies exploring the (b) donor-acceptor, (c) thermal, and (d) pH-dependent properties. Me = methyl, ^{i}Pr = iso-propyl, Mes = mesitylene, Bu = butyl, Bn = benzyl, Ph = phenyl, Bz= benzoyl, Ad = adamantyl, Ts = tosyl, nPn = neopentyl, T_d = decomposition temperature.* [198,199,201]

3.1.3.2. Biological Applications of Triazabutadienes

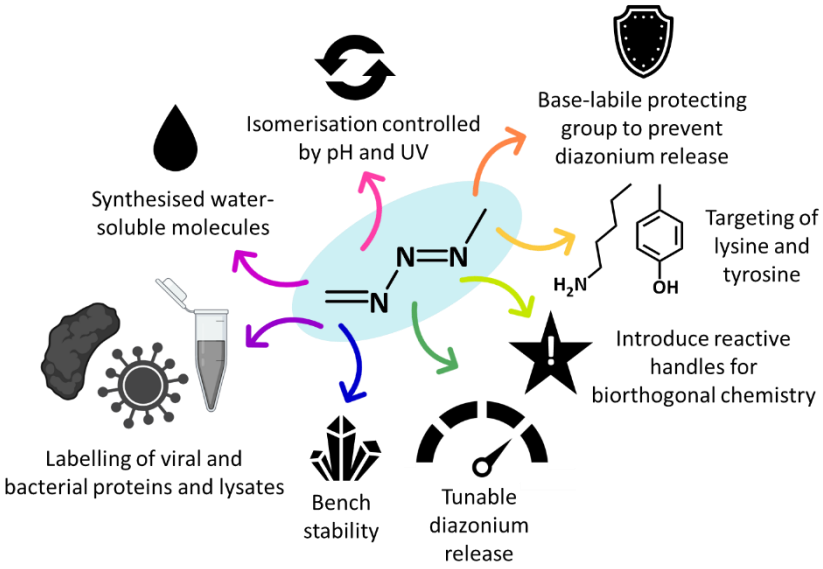

Figure 3.6. *Key findings from studies on triazabutadienes reported by the Jewett group.*[201–209] *Labelling icons from BioRender.*

In pioneering the application of triazabutadienes in biochemical and chemical biology applications, the Jewett group have developed several different ways to tune triazabutadiene chemistry, as highlighted in **Figure 3.6**. The first breakthrough was the development of a stable and water-soluble triazabutadiene molecule.[201] These molecules were shown to release diazonium ions by the mechanism provided in **Scheme 3.2**. In 2016 three Jewett group papers were published almost simultaneously which gave the first examples of protein labelling using diazonium groups released by photoactivation of triazabutadienes. The first paper reported the introduction of an alkyne handle to the triazabutadiene molecule to allow for Cu-click reactions to further functionalise the molecule. The alkyne-containing triazabutadiene was clicked to a fluorophore and then acid-mediated diazonium release labelled the protein bovine serum albumin (BSA) through reaction between the *in situ* generated diazonium and a tyrosine from the protein. This was the first example of aryl diazonium chemistry being used in a one-step attachment of a protein and fluorophore.[206] The second paper introduced a lysine-targeting triazabutadiene. This probe was reacted with both BSA and a dengue virus protein and showed UV-controlled fluorescent labelling to be controlled by photo-isomerism that exposes the previously buried N^3 (labelled in **Scheme 3.2**).[204] The third paper introduces a protecting group strategy where N^1 undergoes a reaction with ethyl chloroformate. The resultant

molecule does not undergo diazonium release. This group can be removed under basic conditions and subsequent acidification leads to diazonium release.[205]

Further developments in bio-labelling using triazabutadienes include: the development of molecules that undergo diazonium release under basic conditions,[203] triazabutadiene scaffolds that fluorescently label BSA, egg yolk protein, and an *E. coli.* lysate protein,[207] a strategy for triazabutadiene-mediated installation of biorthogonal handles onto proteins across a wide pH range (pH 4 – 7),[208] and labelling in gut proteins of *Ae. aegypti* mosquito larvae using protected triazabutadienes which were deprotected due to the basic gut conditions of the larvae.[209] The Jewett group has shown that triazabutadienes can act as a 'masked' source of diazonium ions and compared to other 'masked' forms (e.g. triazenes, aryl diazotates, and azo sulfides),[197,210,211] they have bench stability and release diazonium cations under mild conditions. Additionally, the conditions in which these molecules release diazonium ions are tuneable based on the scaffold of the molecule.

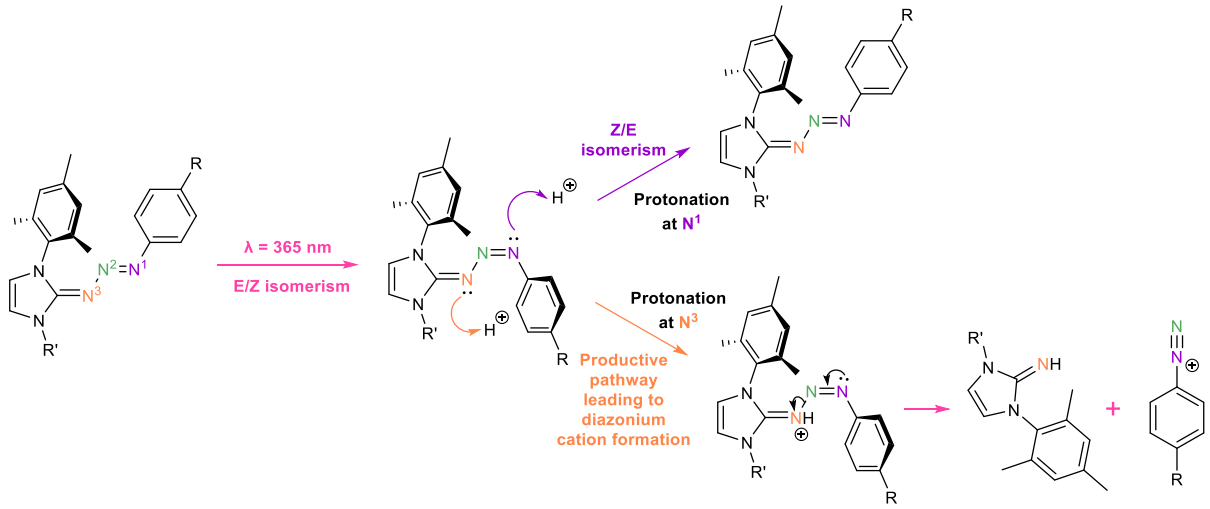

Scheme 3.2. *Proposed mechanism showing diazonium release from triazabutadienes showing the productive pathway due to N^3 protonation and the unproductive pathway due to N^1 protonation.*

3.1.3.3. Emerging Electrochemical Significance

Within the Parkin group at York, Dr Nick D. J. Yates has been working to combine the well-established electrografting of diazonium-containing species onto an electrode with the more recent work of the Jewett group using triazabutadienes as 'masked diazoniums' in biological contexts. The aim is to develop a robust and versatile electrode-modification method suited to different electrode surfaces and biomolecules. The stability of the triazabutadiene probe is crucial – there must be a balance between solution stability to allow

for bioconjugations, and the ability of the molecule to break down and release diazonium cations. Stability depends on the basicity of the nitrogen atoms.[212]

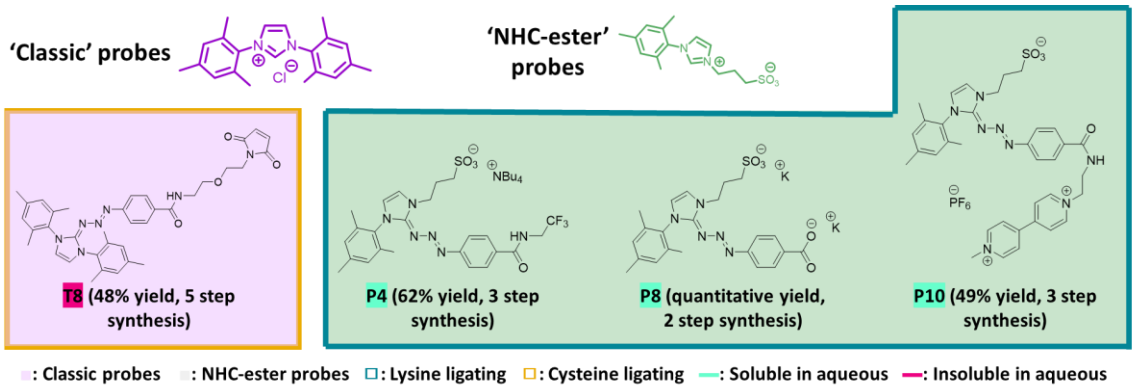

Figure 3.7. *Summary of the structural, ligation, and solubility properties of the triazabutadiene probes discussed in section 3.1.3.3.*[213,214]

In published Parkin group work,[214] a maleimide triazabutadiene probe **(T8)** has been site selectively installed onto a protein by reaction with an amino acid cysteine residue at neutral pH with a reaction duration of 30 minutes. The subsequent diazonium ion release from the triazabutadiene installed onto the protein was tracked by UV-Vis by the appearance and then UV-dependent decay of a peak at 390 nm. This was further confirmed by ESI-LC/MS analysis and through SDS-PAGE and lectin blot analyses following reaction with a resorcinol functionalised α-mannose. Although not used for electrografting, this study provides comprehensive evidence of the conjugation of this probe to a thiol group and UV-mediated diazonium activity. As the polymer used in the previous chapter contains a thiol group it is likely that it can be conjugated to **T8**, importantly the hydrophilicity of the P-GFF conjugation should improve aqueous solubility. Following (i) UV exposure to convert the triazabutadiene into a diazonium and (ii) diazonium-electrografting, the polymer(-sugar conjugates) will be immobilised onto an electrode surface via covalent bond formation.

Table 3.2. *Surface coverage determination following immobilisation of the viologen-containing triazabutadiene molecule under a range of treatment conditions.*

Treatment	Surface coverage / pmol cm^{-2}	
	Glassy carbon	Gold
UV exposure, electrograft	215	313
No UV exposure, electrograft	29	6
UV exposure, no electrograft	23	36
No UV exposure, no electrograft	15	1

In more recent Parkin group work, a new variant of triazabutadiene was synthesised (**P4**, **P8** and **P10** in **Figure 3.7**) with a hydrophilic sulfonate group.[215] This replaced one of the mesityl groups on the scaffold which reduces the hydrophobicity of the molecules. A CF_3 group was incorporated into **P4** to enable XPS analysis of modified surfaces. A carboxylate functionality was introduced to **P8** to allow for further functionalisation including the coupling to an amine-functionalised viologen which yields **P10**. Electrografting on carbon SPEs, glassy carbon disc electrodes, and gold-coated silicon wafers was studied. Importantly, electrografting behaviour was observed in CVs for all surfaces showing this immobilisation method is suited to a wide range of substrates. The introduction of a carboxylate (**P8**) and subsequent viologen conjugation (**P10**) provides a redox signal to use as a successful marker of electrografting. After grafting and washing, a surface-confined redox peak was observed on GC, gold, and ITO. Comprehensive control experiments followed by surface coverage determination (**Table 3.2**) proves the immobilisation of the viologen relies on both UV exposure and an electrografting potential application. This in-house Parkin group triazabutadiene development work has set the basis for this chapter; the intention is to explore the feasibility of combining the thiol-conjugating triazabutadiene molecule with the glycofluoroform-polymer to enable electrografting of the biorecognition element to further advance the galectin-3 electrochemical biosensing approach described in chapter two.

3.2. Aims

Triazabutadiene-mediated electrografting is an emerging strategy which combines covalent stability and biological compatibility to provide a straightforward immobilisation method compatible with multiple surface materials. This chapter aims to use a maleimide-functionalised triazabutadiene to attach our surface modifiers to a SPE and characterise the resultant surfaces and galectin-3 binding response. To achieve this several objectives will be explored:

1. Synthesis, purification, and characterisation of triazabutadiene conjugates to be used in electrografting studies including the development of a novel, straight-forward, chromatography-free purification strategy.
2. Optimisation of the triazabutadiene electrografting strategy including the consideration of electrode material and grafting methodology.

3. Analysis of polymer and polymer-glycofluoroform modified electrodes to probe reproducibility and determine the stability of the triazabutadiene molecule with regards to storage.
4. Development of a surface-click ferrocene derivatisation strategy to allow for surface coverage analysis to confirm the usage of a ferrocene label as a proxy for presentation of glycofluoroform and to make comparison between EIS data and the extent of surface modification.
5. Examination of galectin-3 binding to the glycofluoroform including comparison of oppositely charged redox probes, determination of selectivity using a non-fluorinated control sugar, and quantification of binding via Langmuir-Hill analysis.

3.3. Results and Discussion

3.3.1. Synthesis and purification of maleimide triazabutadiene for polymer conjugation

To enable covalent immobilisation of the polymer – glycofluoroform (P-GFF) conjugate via electrografting methods, a suitable triazabutadiene (TABD), molecule **(8)** was synthesised according to **Scheme 3.3**. This is the literature "maleimide-triazabutadiene" molecule which showed conjugation to a cysteine residue in a protein.[214] As the P-GFF contains a terminal thiol, the aim is to conjugate the same triazabutadiene to the P-GFF conjugate instead of a protein, and then use UV to mediate diazonium electrografting onto a carbon surface. This synthetic pathway was completed by L. Gregg, an MChem student working under the co-direction of the author and Dr N. D. J. Yates and primarily mirrors the literature synthesis of this molecule. Any non-literature processes are highlighted in bold text, and the yields are presented for both literature, in italicised pink text, and the batch synthesised for this study, in black text in **Scheme 3.3**. Two minor divergences from the literature were: (i) the purification of **(4)** via FCC (flash column chromatography) as published wasn't successful, so the crude was dissolved and reconcentrated *in vacuo*, first in toluene then in chloroform twice, and (ii) for the work-up of **(6)** the crude was dissolved in DCM instead of ethyl acetate due to poor solubility in ethyl acetate. A more substantial non-literature change was the difference in equivalents used for the conversion of **(7)** to **(8)**. This was due to a discrepancy between the amounts given in the scheme of the main paper opposed to the written method in the SI. The written method in the SI used a ratio of 1:1.5:3 for **(4)**:**(7)**:Et_3N, but the scheme and this synthesis used a ratio of 1.5:1:3 for **(4)**:**(7)**:Et_3N. This means there was

effectively one less equivalent of triethylamine relative to **(4)**. In the final step of **Scheme 3.3**, **(4)** needs to be formally deprotonated for the reaction to occur, so reducing the amount of triethylamine could be responsible for the low yield. Additionally, the reaction was carried out at room temperature in a non-temperature-controlled lab in the winter, so this could also play a role in the low yield observed.

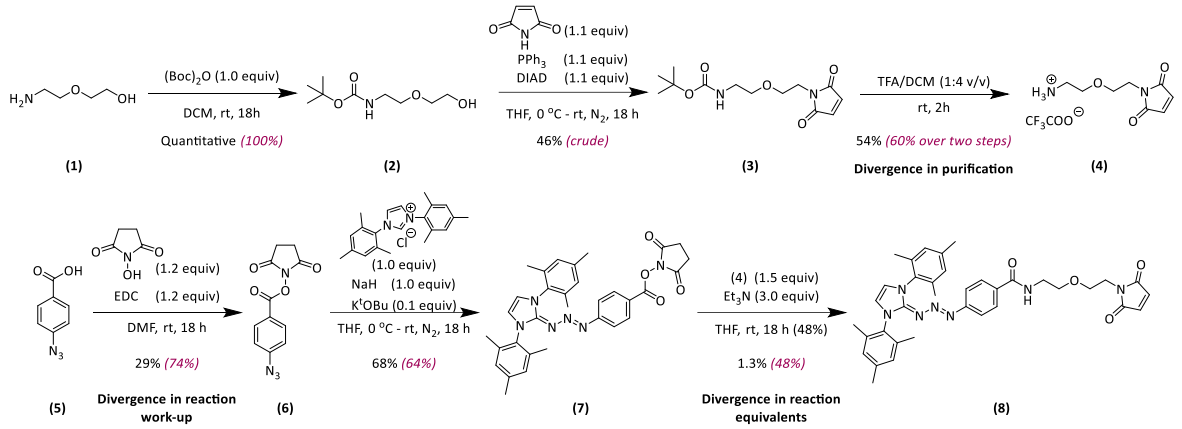

Scheme 3.3. *The synthetic route followed to access the triazabutadiene molecule (8) to be used for electrografting. The yields for this batch are given, black test, and compared to the literature yields,*[214] *italicised pink text, points of divergence from the literature method are noted in bold.*

3.3.2. Development of a covalent electrografting strategy for polymer immobilisation

3.3.2.1. Triazabutadiene-polymer conjugation and purification

Once the triazabutadiene molecule was synthesised, the first stage of the work used only the polymer to carry out proof of concept studies. This decision was made because the synthesis of GFF is both time consuming and low yielding. Additionally, since the GFF functionality is added to the opposite end of the polymer to the thiol, and given that this adds a relatively small mass to the polymer, it was rationalised that GFF-free controls would still give an accurate insight into how the chemistry would proceed in the presence of GFF. The polymer-triazabutadiene conjugate (TABD-P) was made via a straightforward 30-minute reaction shown in **Scheme 3.4**.

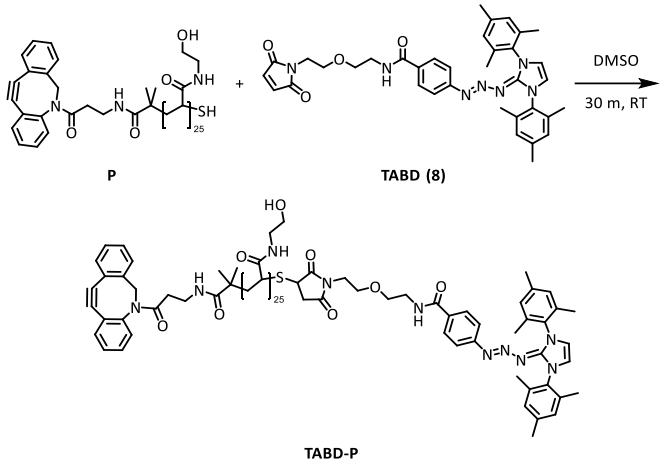

Scheme 3.4. *One-step reaction scheme showing the pathway for the formation of the TABD-P conjugate to be employed in electrografting.*

The large difference in mass between the TABD molecule, 633.75 g mol^{-1}, and the TABD-P conjugate, 3254.72 g mol^{-1}, and the difference in solubility were exploited to purify the TABD-P conjugate from excess TABD. The TABD molecule has very poor water solubility but due to the polarity and large number of hydrogen bonding functionalities within the polymer, the TABD-P product is water soluble. Therefore, the crude lyophilised TABD-P was resuspended in ethyl acetate, an organic solvent, which solubilised the unreacted TABD but not the TABD-P. Centrifugation formed a pellet of TABD-P and the TABD solution was pipetted off, this process could be repeated successively, as shown in **Figure 3.8**, until the organic solvent supernatant was clear, showing there is no remaining unreacted TABD. The identity of the compound in the supernatant was identified as **(8)** by HR-MS (high resolution mass spectrometry).

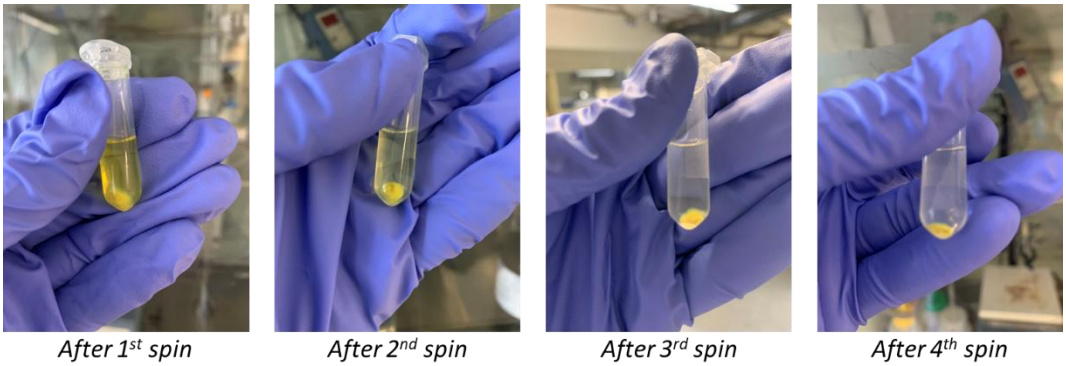

Figure 3.8. *The results of the purification of the TABD-P, sequential dissolutions in ethyl acetate followed by centrifugation shows the removal of unreacted TABD as the supernatant becomes more clear.*

Traditional characterisation of TABD-P, i.e. via one-dimensional ^{1}H NMR (nuclear magnetic resonance spectroscopy) and HR-MS, is challenging due to the polymer's large size giving

rise to a whole series of molecular ions in different charge states making interpretation challenging. Additionally, the hydrophilicity of the polymer can cause issues with the sample being retained on the column. Overlap in the ^{1}H NMR spectra of the polymer's dibenzocycloocytne and the TABD's 1,3-bis(mesityl)imidazolium region would make any attempt to resolve the purity very challenging. Instead the absorbance capabilities of triazabutadienes are exploited to prove conjugation; the UV responses, shown in **Figure 3.9(a)**, of the P (orange line) and the P-TABD (yellow line) show a stark difference, proving the successful conjugation of the two molecules. Subsequent electrode-modification via diazonium electrografting will rely on the revelation of a diazonium ion upon exposure to UV light. This was also probed using spectroscopy and the optimum exposure time was determined as 10 minutes since, as seen in **Figure 3.9**, there is a significant (over 3-fold) decrease of the λ_{max} absorbance upon irradiation (yellow to blue line). This is accompanied by a colour change from yellow to colourless as the triazabutadiene portion of the polymer-conjugate breaks down (**Figure 3.9(b)**). A normalised absorbance is used where for each sample all absorbance values are divided by the maxima absorbance for the sample to account for difference in concentration and the absorbance by the polymer in the non-triazabutadiene region.

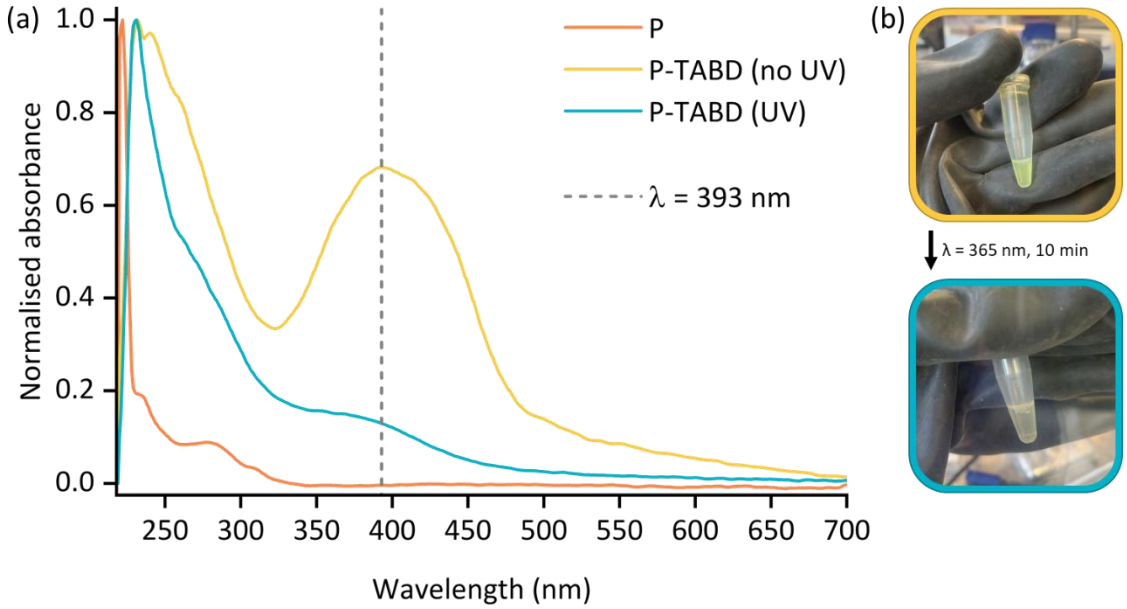

Figure 3.9. *(a) Overlay of the UV-Vis absorbance spectra of P (orange) and the P-TABD before (yellow) and after (blue) UV exposure. The grey dashed line shows the position of λ_{max}. (b)The yellow colour of the TABD-P solution disappears after 10 minutes of UV exposure at 365 nm.*

3.3.2.2. Determination of the most suitable electrode surfaces for electrografting studies

The intention was that usage of a triazabutadiene-modified polymer would enable compatibility with more working electrode surfaces than the gold-thiol modification. Surface stability is crucial for sensing technologies, therefore an assessment of the bare, i.e. unmodified, working electrode surfaces available to us was carried out via EIS (electrochemical impedance spectroscopy) measurements to identity suitable surfaces to modify via our triazabutadiene electrografting strategy. There were four screen-printed electrodes to be tested, three from a commercial supplier, BVT, with working electrodes consisting of Au, C, or ITO, and one from an industrial collaborator, Eluceda, comprising of a C working electrode.

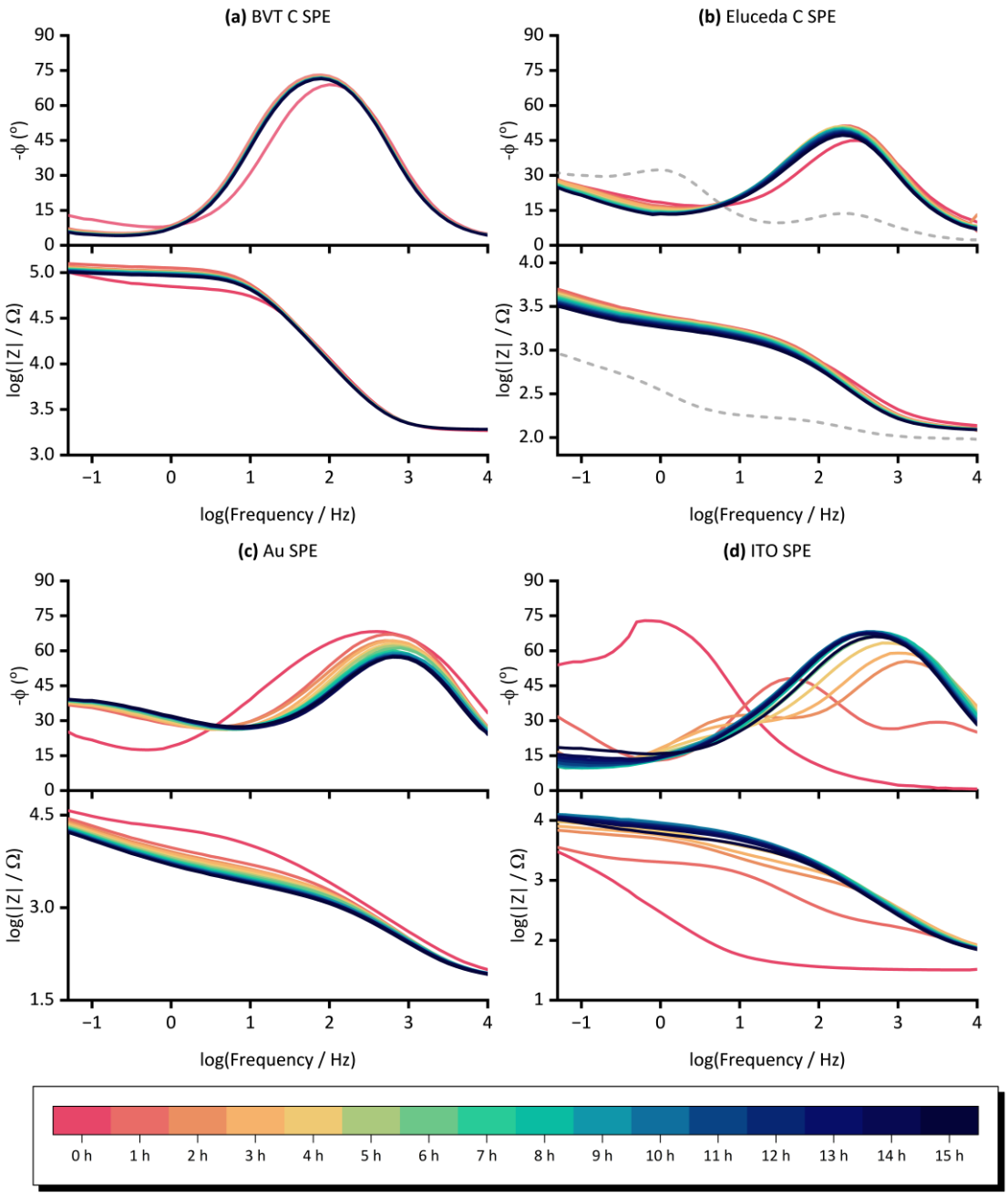

Figure 3.10. *Bode plots showing 16 sequential measurements of unmodified SPEs with varying working electrode materials in buffer. The materials studied were: (a) carbon supplied by BVT, (b) carbon supplied by Eluceda), (c) gold supplied by BVT, and (d) ITO supplied by BVT. The grey dashed line in (b) is an equivalent single measurement taken on a different Eluceda carbon SPE. EIS measurements were performed in the presence of 10 mM* $K_3[Fe(CN)_6]$ *in pH 7 aqueous buffer (100 mM sodium phosphate, 233 mM sodium chloride) with the following parameters:* $t_{(equilibration)}$ *= 180 s,* E_{DC} *= 0.230 V vs. Ref,* E_{AC} *= 10 mV, f = 0.05 Hz – 10 kHz (10 datapoints per decade).*

To assess the stability, unmodified (i.e. 'bare') electrodes were submerged in buffer and impedance measurements under standard conditions were carried out immediately, and then every hour for 15 hours. The Bode plots for each electrode type: BVT carbon, Eluceda carbon, BVT gold, and BVT ITO are presented in **Figure 3.10(a) – (d)** respectively. It can be seen from these results that the BVT carbon electrodes are the most stable due to displaying

the most consistency over the 16 repeat measurements. The high phase angle, approximately 75°, shows a highly capacitive bare electrode surface which indicates high surface roughness which would provide more surface area for modification and thus greater presentation of the GFF biorecognition element. In addition, the flat response for impedance at lower frequencies is a good indication of stability.

Unlike the BVT carbon electrodes, the ITO electrodes are clearly unsuitable, showing large variation in both EIS plots as a function of measurement time. This variation is likely caused by the ITO stripping off the electrode, exposing the carbon support surface; this is based on the visual observation of solid formation within the electrolyte droplet throughout the experiment. This explains the transition in the EIS of (i) one peak at a low frequency, attributed to the ITO surface, to (ii) two peaks in the middle time period measurements, as the ITO is delaminating from the surface, and then (iii) eventual equilibration to just one higher frequency peak, presumably from the exposed carbon surface. These ITO surfaces were a manufacturing trial where the ITO was plated onto a carbon working electrode, hence why they display such poor electrochemical stability.

The Au and Eluceda C electrodes show surface homogeneity, unlike ITO, but less stability than the BVT C electrode. The phase maxima for these electrodes are also lower, ca. 50° for Eluceda C-SPEs and ca. 59° for Au-SPEs, which could mean a lower surface area for modification. However, in other experiments on further electrodes, the Eluceda electrodes did show surface inhomogeneity. This data, the grey dashed line in **Figure 3.10(b)**, shows two peaks corresponding to multiple environments. Based on this initial electrode screen, the surfaces explored further were the BVT Au and C.

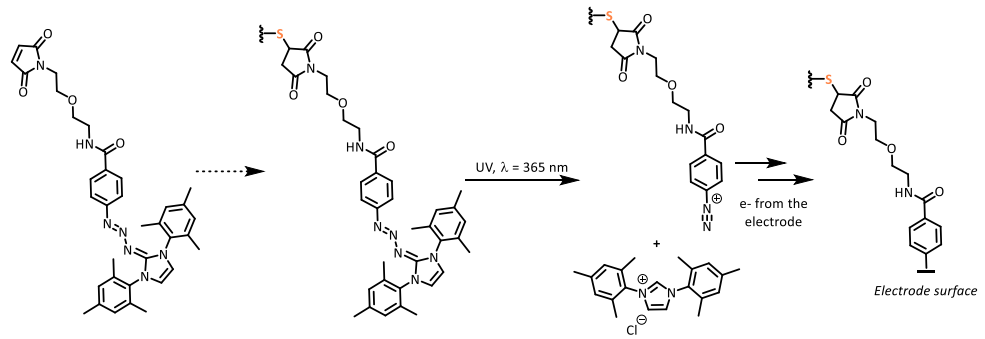

Scheme 3.5. *Electrografting of the triazabutadiene to the electrode surface, which involves UV exposure to reveal the diazonium ion followed by the abstraction of an electron to form a covalent bond to the electrode surface. The dashed arrow symbolises the prior conjugation to the thiol unit of the P or P-GFF.*

To prime the sample for electrografting, the TABD-P was dissolved in pH 5 buffer and exposed to UV for 10 minutes. The electrograft was carried out using CV where the voltage was swept from a high to a low potential and then back over several scans in order to electrochemically reduce the diazonium to yield a covalently grafted species, this process is shown in **Scheme 3.5** and follows the mechanism in **Figure 3.2(a)**. The 'classic' diazonium electrografting response is a large irreversible reductive peak due to the electrochemical reduction of the diazonium cation, and if large peaks remain in subsequent scans it is indicative of multilayer formation. **Figure 3.11(b)** shows classic behaviour in the first scan of experiments conducted on BVT C-SPE electrodes, this indicates that the electrograft of the triazabutadiene-polymer has been successful. Since this peak does not persist it is assumed that the bulky size of the maleimide-polymer motif prevents multilayer formation. The current spikes in the CV response for SPE 5 are often observed and this is attributed to poor connectivity to the screen-printed electrodes. This can make the signals challenging to interpret on carbon.

When testing Au-SPEs, a reduction process at around -0.5 V in the first scan, attributable to gold chemistry, 'swamps' the signal, **Figure 3.12(b)**, which makes confirmation of triazabutadiene grafting solely by cyclic voltammetry response impossible. Although the triazabutadiene functionality is no longer present, the modified electrodes are denoted as TABD-P modified SPEs to signify the diazonium electrografting process that has occurred and to differentiate from the previous modification involving gold-thiol bond formation.

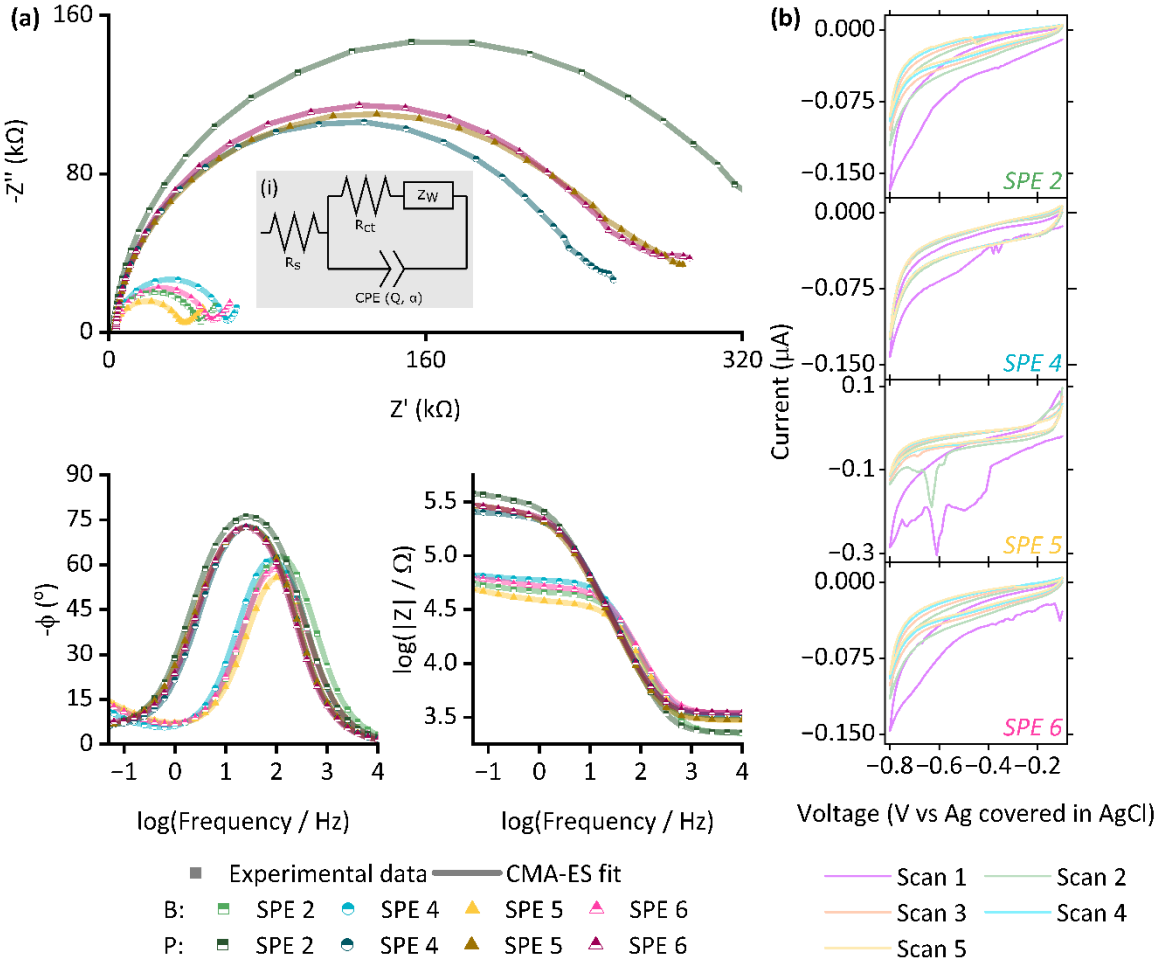

Figure 3.11. *(a) Resultant Nyquist and Bode plots of bare, B, (lighter colours) and polymer-modified, TABD-P, (darker colours) showing experimental data (points) and the computational fitting (lines) to the circuit given in (i) following electrografting on C-SPEs. EIS measurements were performed in the presence of 10 mM $K_3[Fe(CN)_6]$ in pH 7 aqueous buffer (100 mM sodium phosphate, 233 mM sodium chloride) with the following parameters: $t_{(equilibration)}$ = 180 s, E_{DC} = 0.230 V vs. Ref, E_{AC} = 10 mV, f = 0.05 Hz – 10 kHz (10 datapoints per decade). (b) Corresponding electrograft for each electrode. CVs were collected by scanning between -0.1 to -0.8 V vs Ag covered in AgCl at 20 mVs^{-1} for 5 scans. R_s = solution resistance, R_{ct} = resistance to charge transfer, Z_W = Warburg element, and Q and α are the parameters used to model a constant phase element (CPE).*

EIS measurements were also made to determine if electrografting was successful. Inspection of the impedance responses reveals differences between the graft on the carbon, **Figure 3.11**, and gold, **Figure 3.12**, surfaces. For the carbon electrodes there is one well-defined semi-circle in the Nyquist plots and symmetrical phase-angle Bode plots. All the data is well-modelled by the standard Randles circuit, **Figure 3.11(a)(i)**, showing that the carbon surface is modified evenly and likely with a singular species. The diffusional contributions are significantly decreased in the impedance response following electrografting compared to the bare electrode. This is likely due to the formed layer increasing the effective surface area which provides more sites for charge transfer meaning these processes persist over a wider

frequency range before these species are depleted at the electrode interface resulting in the transition to the electron transfer being governed by diffusion to the electrode. However, modelling this data without a Warburg element (appendix 7.7) provides a worse fit, so the modified electrode data has been modelled with a Warburg element despite the reduction in diffusion-controlled electron transfer. As the phase angle maxima shifts to a lower frequency after electrografting it shows that the current begins to flow through the capacitor at a slower oscillation rate. This is caused either by an increase in resistance to charge transfer or an increase in capacitance (total impedance is inversely related to capacitance). Surface modification with the TABD-P would cause both of these changes, so this indicates successful diazonium electrografting electrode modification using the TABD-P conjugate.

Conversely, on gold electrodes the EIS data is consistent with the surface starting off as homogeneous, but after the graft the 'stretched' Nyquist plot data and two peaks in the phase angle Bode plot are consistent with a heterogenous surface as similar electron transfer processes are occurring with two different time constants. This is confirmed by computational fitting, as the modified electrode datasets show a better fit to the circuit given in **Figure 3.12(a)(ii)**. This equivalent circuit contains multiple elements in order to account for multi-environment surfaces which undergo multiple electron transfer processes under different kinetic regimes.[216] Circuits with a similar arrangement of elements can be found in the literature to model adsorbed species or failed coatings. [217–219] As increasing the number of circuit elements increases the likelihood of a 'good fit' it is challenging to use these more complex circuits to conclude exactly how the gold surface has been modified but it's suggestive of a more heterogenous, porous layer compared to C SPEs. The observed shouldering in the phase angle Bode plot (as opposed to two entirely distinct peaks) shows that the multiple processes aren't happening with completely distinct time constants, i.e. this is consistent with two similar environments.

The differences between the gold and carbon electrode post-modification EIS results are seen when the same aliquot of TABD-P is used, so this result is attributed to the electrode chemistry. In the literature, diazonium electrografting on gold has been observed to show two peaks in the first reductive sweep, and these have been attributed to bond formation with different gold crystal structures, namely Au(111) and Au(100).[220] The gold surfaces in

SPEs are likely to be impure and contain other metals so multiple surface-modified environments, and therefore kinetic regimes, is probable. Additionally, in various studies which compared diazonium grafting onto gold and glassy carbon electrodes it was found that the modification had greater stability on the carbon electrodes.[221,222] This proves the carbon surface is most appropriate for the exploration of this immobilisation method in terms of chemistry. This is also justified from an economic viability point of view since carbon is a cheaper and more available element than gold.[96,223]

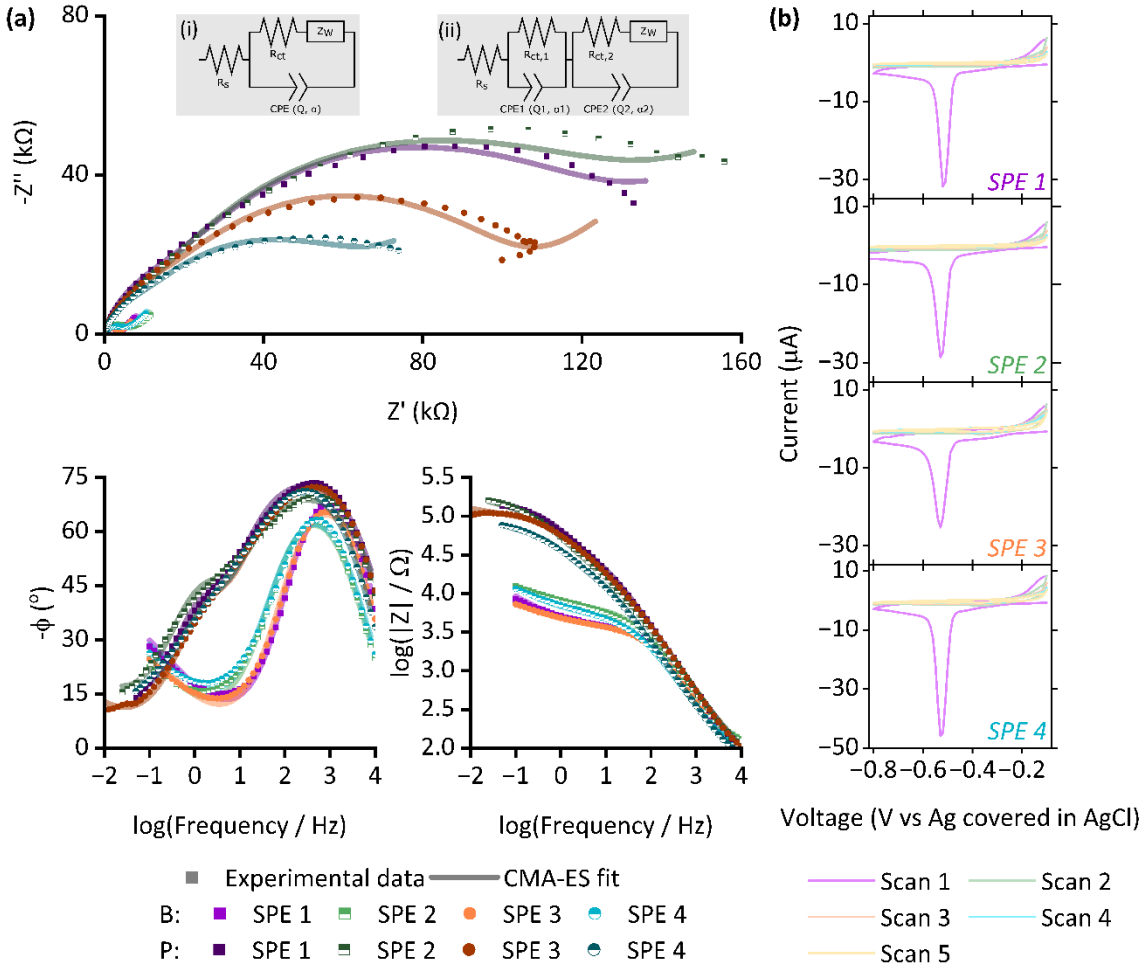

Figure 3.12. *(a) Resultant Nyquist and Bode plots of bare, B, (lighter colours, fitted to circuit(i)) and polymer-modified, P, (darker colours, fitted to circuit (ii)) showing experimental data (points) and the computational fitting (line) following electrografting on Au-SPEs. EIS measurements were performed in the presence of 10 mM $K_3[Fe(CN)_6]$ in pH 7 aqueous buffer (100 mM sodium phosphate, 233 mM sodium chloride) with the following parameters: $t_{(equilibration)}$ = 180 s, E_{DC} = 0.230 V vs. Ref, E_{AC} = 10 mV, f = 0.05 Hz – 10 kHz (10 datapoints per decade). (b) Corresponding electrograft for each electrode. CVs were collected by scanning between -0.1 to -0.8 V vs Ag covered in AgCl at 20 mVs^{-1} for 5 scans. R_s = solution resistance, R_{ct} = resistance to charge transfer, Z_W = Warburg element, and Q and α are the parameters used to model a constant phase element (CPE).*

3.3.2.3. Statistical assessment of carbon surface studies

The EIS results from modification of the different C-SPEs were analysed with CMA-ES and MCMC fitting, similar to the analysis of Au-SPEs performed in chapter two. Again, there is no parameter correlation other than that expected for Q and α (as these both model the CPE). When looking at the frequency distributions for each parameter (the top plot of each column), there is no clear ordering of the SPE numbering that is consistent between the parameters. This means that each parameter changes in a different way so there is no obvious parameter that could be used for normalisation to collapse the variation we see in the impedance response after modification.

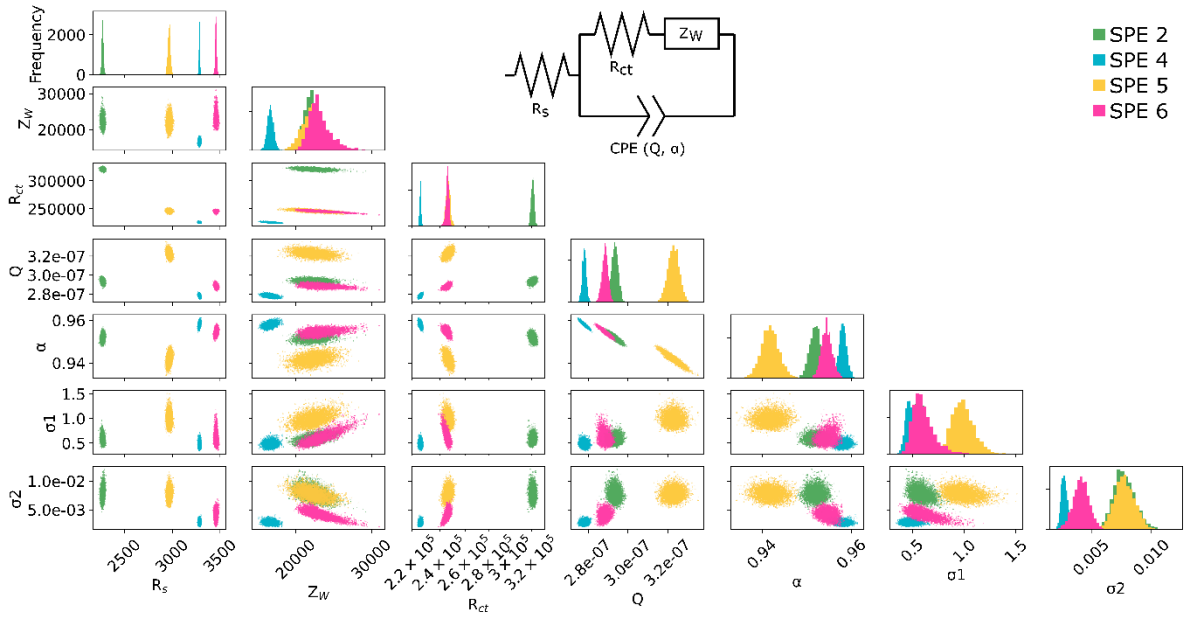

Figure 3.13. *2D scatter plots showing correlations for circuit parameters used to infer parameter distributions from 4 carbon electrografting studies. The diagonal represents the 1D histograms for each parameter showing the distribution of the fitted values. The MCMC used to generate these chains was run for 10 000 samples, with the first 3000 discarded as burn-in. R_s = solution resistance, R_{ct} = resistance to charge transfer, Z_W = Warburg element, Q and α are the parameters used to model a constant phase element, and σ1 and σ2 are noise parameters.*

To further probe the chemistry of the TABD-P conjugate, and to complement the control experiments presented in a recent publication by Yates *et al.*,[215] EIS comparisons were made between different stages of modification. The value of $\bar{R}_{ct}$ was used as a measure of surface modification to compare bare C-SPEs, surfaces modified with the TABD-P conjugates that had not been exposed to UV (no UV), and TABD-P modified surfaces with the standard UV exposure (**Figure 3.14(a)**). According to the chemistry presented in the introduction of this chapter, the TABD-P aliquots that have had no UV exposure should not have any diazonium functionality and thus should not be modified. However, the no UV control studies show an

intermediate value between a bare SPE and the TABD-P modified SPE. This is interpreted as meaning that the mesityl groups in the TABD promote non-specific adsorption to the carbon surface via π- π stacking interactions. The higher R_{ct} value and 10 – 20° lower phase shows that converting the TABD into diazonium generates a more uniform, well-packed surface, presumably because of covalent bond formation. Additionally, a comparison between cyclic voltammetry (CV) and chronoamperometry (CA) electrografting methods was carried out as part of this analysis (**Figure 3.14(b)**). The results suggest that the CV method gives more efficient and less variable modification, so this was continued in all further experiments (CA: n = 5, $\bar{R}_{ct}$ = 186.1 kΩ, S.D. = 87.7 kΩ; CV: n = 4, $\bar{R}_{ct}$ = 258.4 kΩ, S.D. = 34.6 kΩ).

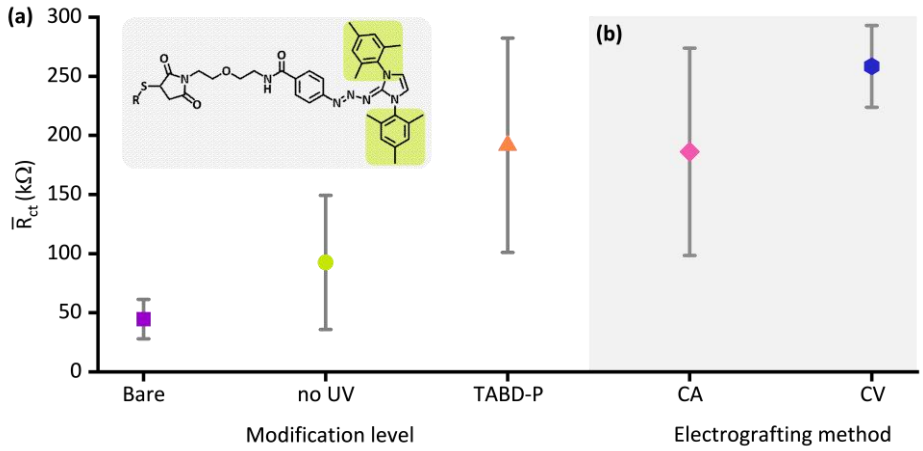

Figure 3.14. *A comparison of $\bar{R}_{ct}$ for (a) UV control experiments where bare (purple square, n=16), no UV (lime circle, n=7), and TABD-P (orange triangle, n=11) were compared and (b) electrografting comparison where chronoamperometric (pink diamond, n=5) and voltammetric (dark blue hexagon, n=4) were compared. The dark grey bars show the population standard deviation for each set of experiments. Inset: triazabutadiene structure with the mesityl groups capable of π-π stacking highlighted in lime.*

As a further control experiment, a C-SPE was immersed in just the polymer solution. The same conditions were used as that for the gold-thiol polymer self-assembly to show that even with a large time exposure, a minimal change is observed in both the Nyquist and the Bode plots (**Figure 3.15**). This proves that unreacted/non-TABD-labelled polymer will not immobilise on the electrode, so it won't interfere with the experiments.

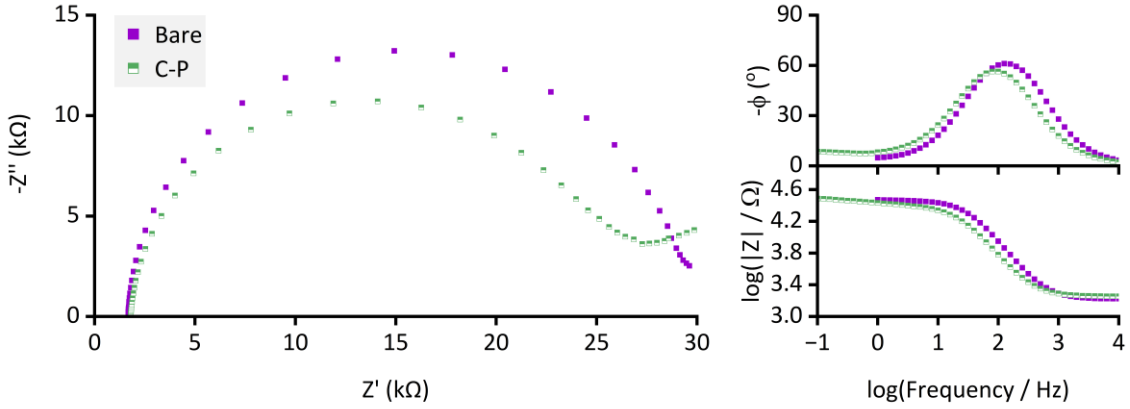

Figure 3.15. *Nyquist (left) and Bode (right) plots for both a bare (purple) and polymer-incubated (green) C-SPE. EIS measurements were performed in the presence of 10 mM $K_3[Fe(CN)_6]$ in pH 7 aqueous buffer (100 mM sodium phosphate, 233 mM sodium chloride) with the following parameters: $t_{(equilibration)}$ = 180 s, E_{DC} = 0.200 V vs. Ref, E_{AC} = 10 mV, f = 0.1 (for C-P) and 1 (for bare) Hz – 10 kHz (10 datapoints per decade).*

3.3.3. Surface-click ferrocene immobilisation to determine surface coverage following electrografting

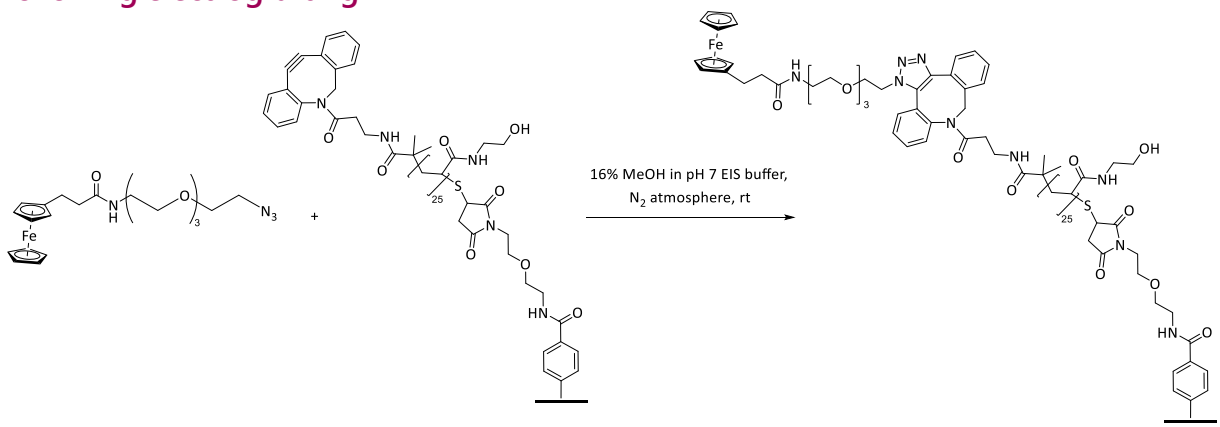

Scheme 3.6. *The surface strained-promoted azide-alkyne click reaction which immobilises a ferrocene functionality onto the electrode surface.*

The ferrocene derivative, FD-01, was previously synthesised, as described in **Scheme 6.7**; again, the azide functionality was used to conjugate FD-01 to the alkyne within the polymer via strain-promoted click chemistry. Because ferrocene can react with aryldiazoniums,[224] the TABD-P was electrografted as described in the previous section and then the ferrocene-derivative was clicked to the polymer. Square wave voltammetry (SWV) involves oscillating the voltage in a step-wise fashion (inset of **Figure 3.16**) and enhances the faradaic redox signals compared to the non-faradaic background current, therefore, SWV measurements were performed at different points during the click reaction to monitor the immobilisation of ferrocene on the electrode.[52] As shown in **Figure 3.16**, there is a large peak in the

oxidative scan at around 0.04 V which interferes with the ferrocene signal, therefore only the reductive square wave scan has been visualised in the remaining plots.

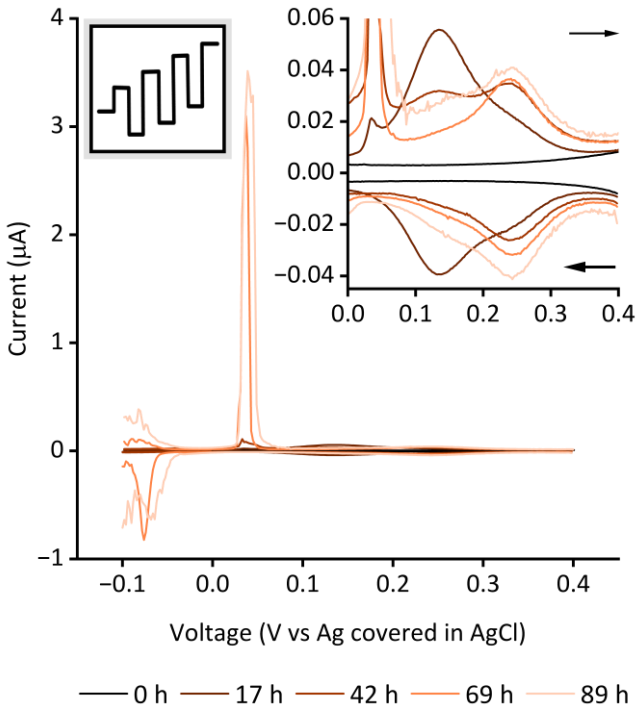

Figure 3.16. *Voltammograms showing the interference from an oxidative peak at around 50 mV. Inset: Cropped time course voltammograms showing the change in peaks as the surface click reaction progresses. SWV measurements were taken between -0.1 (E_{start} for oxidative sweep) and 0.4 (E_{start} for reductive sweep) V vs Ref, with an amplitude of 10 mV and a frequency of 2 Hz.*

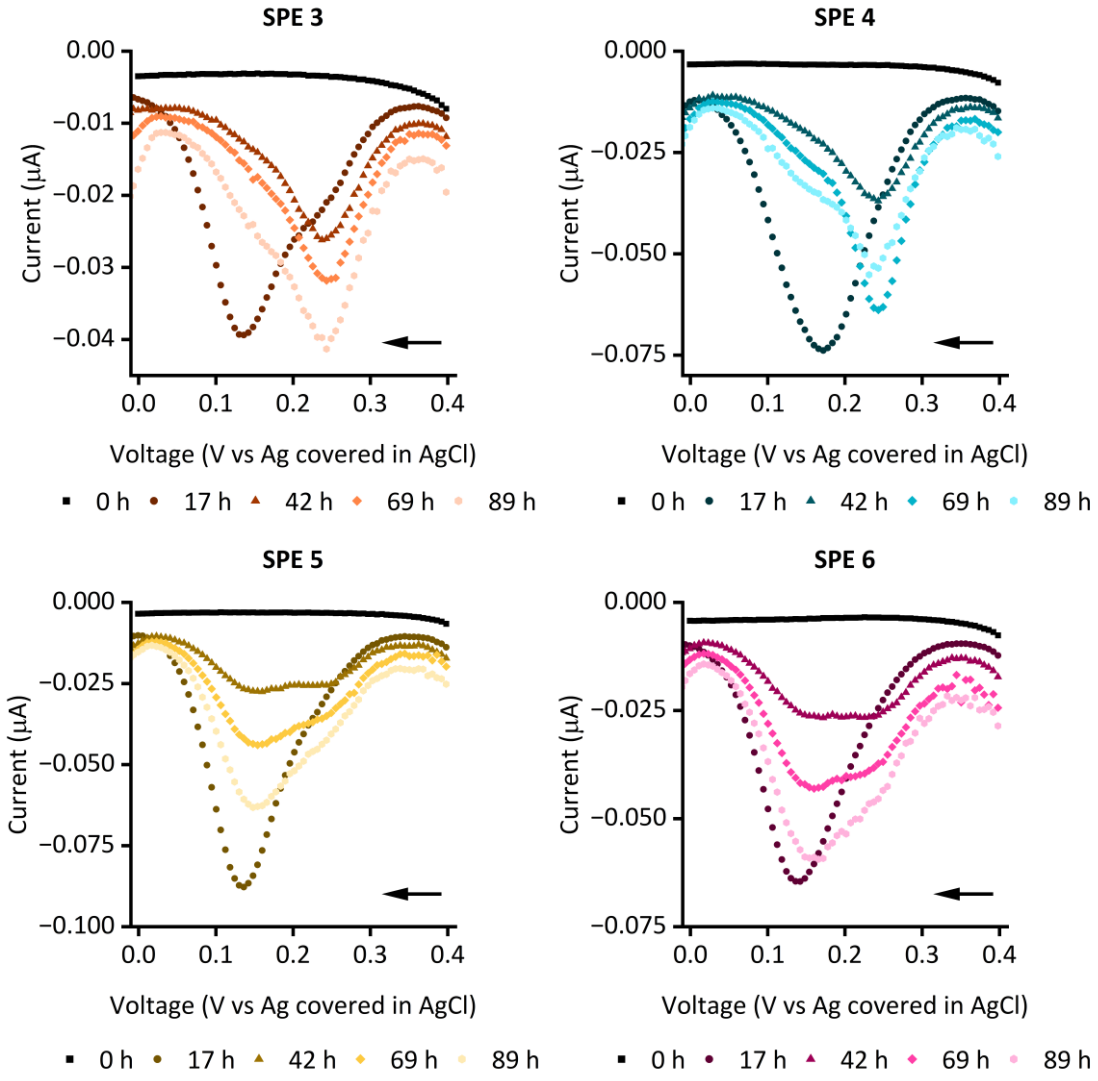

Figure 3.17. *Time course voltammograms showing the change in reductive peaks as the surface click reaction progresses. SWV measurements were taken between 0.4 and -0.1 V vs Ref, with an amplitude of 10 mV and a frequency of 2 Hz. Every 3rd point is shown on each scatter plot.*

$$i_p = 0.4463nFAC\sqrt{\frac{nF\nu D}{RT}} \qquad \textit{Equation 3.1}$$

where: i_p: peak current (A); n: number of electrons; F: Faraday constant (C mol^{-1}); A: electrode surface area (cm^2); C: concentration (mol cm^{-3}); ν: scan rate (V s^{-1}); D: diffusion coefficient (cm s^{-1}); R: gas constant (J K^{-1} mol^{-1}); T: temperature (K)

$$i_p = \frac{n^2F^2}{4RT}\nu A\Gamma^* \qquad \textit{Equation 3.2}$$

where: i_p: peak current (A); n: number of electrons; F: Faraday constant (C mol^{-1}); R: gas constant (J K^{-1} mol^{-1}); T: temperature (K); ν: scan rate (V s^{-1}); A: electrode surface area (cm^2); Γ^*: surface coverage of adsorbed species (mol cm^{-2})

The click reaction to label a P-TABD electrografted surface with ferrocene was carried out on four C-SPE electrodes simultaneously, and the reductive waves shown in **Figure 3.17** show there are two ferrocene species present. Attempts to deconvolute these species were

carried out via probing the effect of scan rate (ν) in cyclic voltammetry experiments. The Randles-Sevcik equation (Equation 3.1)[102,141] shows that for diffusion-controlled species $i_p \propto \nu^{1/2}$ and Equation 3.2 shows that for surface-confined species $i_p \propto \nu$. [102,141] As shown in **Figure 3.18**, two species are observed at lower scan rates, akin to the observations in SWV. However, at higher scan rates only the higher potential peak is observed, attributed to the faster potential sweep rate outpacing the slower electron transfer event that gives rise to the lower potential peak. This suggests the low potential peak arises from a solution-phase or semi-confined ferrocene species (i.e. FD-01 molecules trapped within the polymer network). Conversely, for the faster electron-transfer species the linear relationship between peak current and scan rate (R^2=0.9983) correlates with this species being surface-confined and therefore attributable to clicked FD-01. This indicates that the surface click chemistry has been successful and further validates covalent immobilisation of the polymer on the electrode via the diazonium electrografting facilitated by the TABD group.

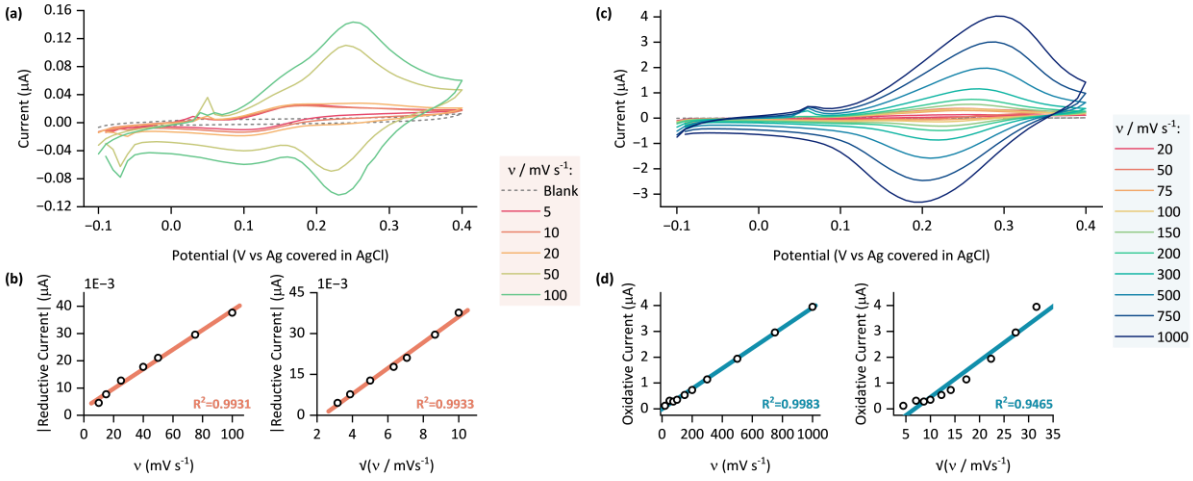

Figure 3.18. *Scan rate analysis of surface-confined FD-01. Cyclic voltammograms of FD-01 modified SPEs cycling between -0.1 and 0.4 V vs Ref at (a) low and (c) high scan rates and extracted peak current plotted against both raw and square root of scan rate for (b) low and (d) high potential peak. Data in (c) and (d) collected by Lucy Gregg. Two different modified electrodes were used for the two groups of scan rates studied.*

Having concluded that fast scan rate CVs reveal only the surface immobilised ferrocene, an analysis was then done to correlate the R_{ct} value of the P-modified electrode with the corresponding clicked ferrocene surface coverage. As previously, the surface coverage estimation of ferrocene is performed through baseline fitting and subtraction and integration of the resulting peak (**Figure 3.19(b)**). There are two findings. First, even at the lowest value, the amount of ferrocene immobilised on a C-SPE is over ten times higher than

the surface coverage determined for Au-SPEs (0.350 pmol). This is explained as C-SPEs are likely to have a greater degree of surface roughness. This increased coverage means there should be a greater display of the GFF on the C-based sensor, which may improve the sensitivity.[225] Second, there is a general positive correlation between R_{ct} and ferrocene, showing a larger value of R_{ct} after modification does indicate a greater degree of surface modification. Further study to fully define this correlation could provide a route to normalisation to remove the effect of electrode-to-electrode variability.

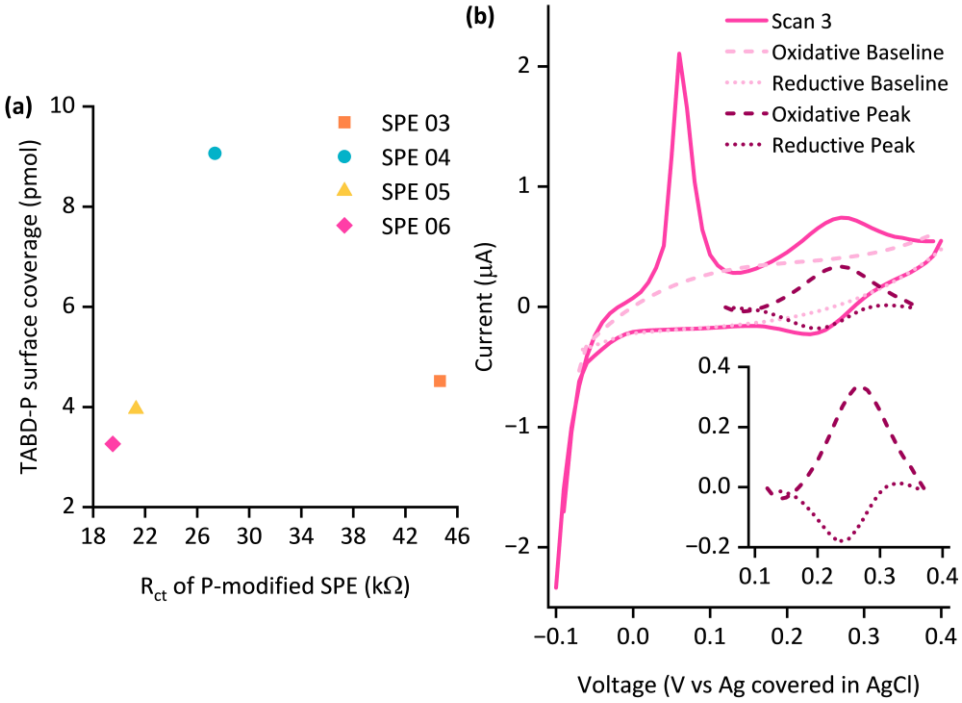

Figure 3.19. *(a) Visualisation of the relationship between R_{ct} value and surface coverage of TABD-P modified SPEs, average surface coverage equals 5.201 pmol. (b) Example of the determined surface coverage of the FD-01.*

3.3.4. Evaluation of immobilised polymer-glycofluoroform reveals reduced surface variation despite time instability of triazabutadiene conjugates

3.3.4.1. Conjugation and grafting of triazabutadiene-polymer-glycofluoroform

Although the previous section detailing the work on ferrocene immobilisation shows that surface-click reactions are viable post-electrograft, the GFF is attached prior to electrografting, as shown in **Scheme 3.7**. This is both quicker, because it removes the steric restrictions of surface click, and also requires significantly less GFF. The conjugation and purification processes are identical to the process described for the polymer in section 3.3.2.1.

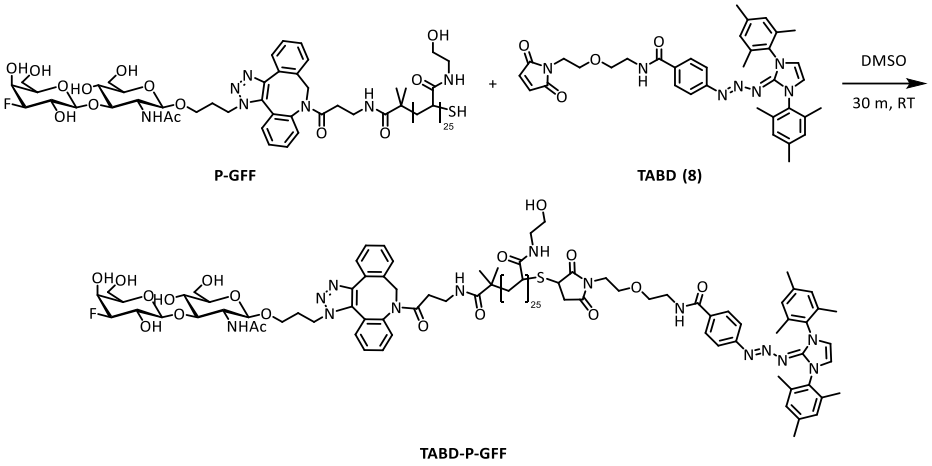

Scheme 3.7. *One-step reaction scheme showing the pathway for the formation of the TABD-P-GFF conjugate to be employed in electrografting. The P-GFF is accessed as described in chapter 2.*

An aliquot of TABD-P-GFF was dissolved in pH 5 buffer (1 M NaOAc) to a concentration of 3 mg mL^{-1} and exposed to UV (λ = 365 nm) for 10 minutes. The CV electrografting process was carried out on five different C-SPEs with sub-aliquots of the same batch of TABD-P-GFF; the characteristic large electrograft reductive current can be seen in the first scan (**Figure 3.20(b)**). Evidence for a successful electrograft can also be seen in the EIS plots (**Figure 3.20(a)**) where there is a large increase in Nyquist signal after electrografting, with the TABD-P-GFF modified SPEs having diameters between 400 and 800 kΩ. A similar increase is seen in both the phase and magnitude Bode plots. The flattening at the lower frequencies of the magnitude Bode plot indicates the successful formation of a modified layer. This impedance data shows a good fit (lines in **Figure 3.20(a)**) to the standard Randles circuit (**Figure 3.20(a)(i)**) showing a well-organised single environment is present after the modification. This data does not show diffusional behaviour over the frequency range studied so the Warburg element has been removed for the modelling of this data. Additionally, these five electrodes appear to fall into two classes of bare electrodes, one with a lower initial response, SPE 1, 4 and 5, with diameters ca. 5-10 kΩ and a -ϕ value ca. 30° and one with a higher initial response, SPE 6 and 10, with diameters ca. 100 kΩ and a -ϕ value ca. 80°. However, this doesn't seem to affect the modification process with all five electrodes being modified to similar extents; indeed, the modification seems to reduce some of the variability seen between electrodes which contrasts to the Au-SPE results in the previous chapter.

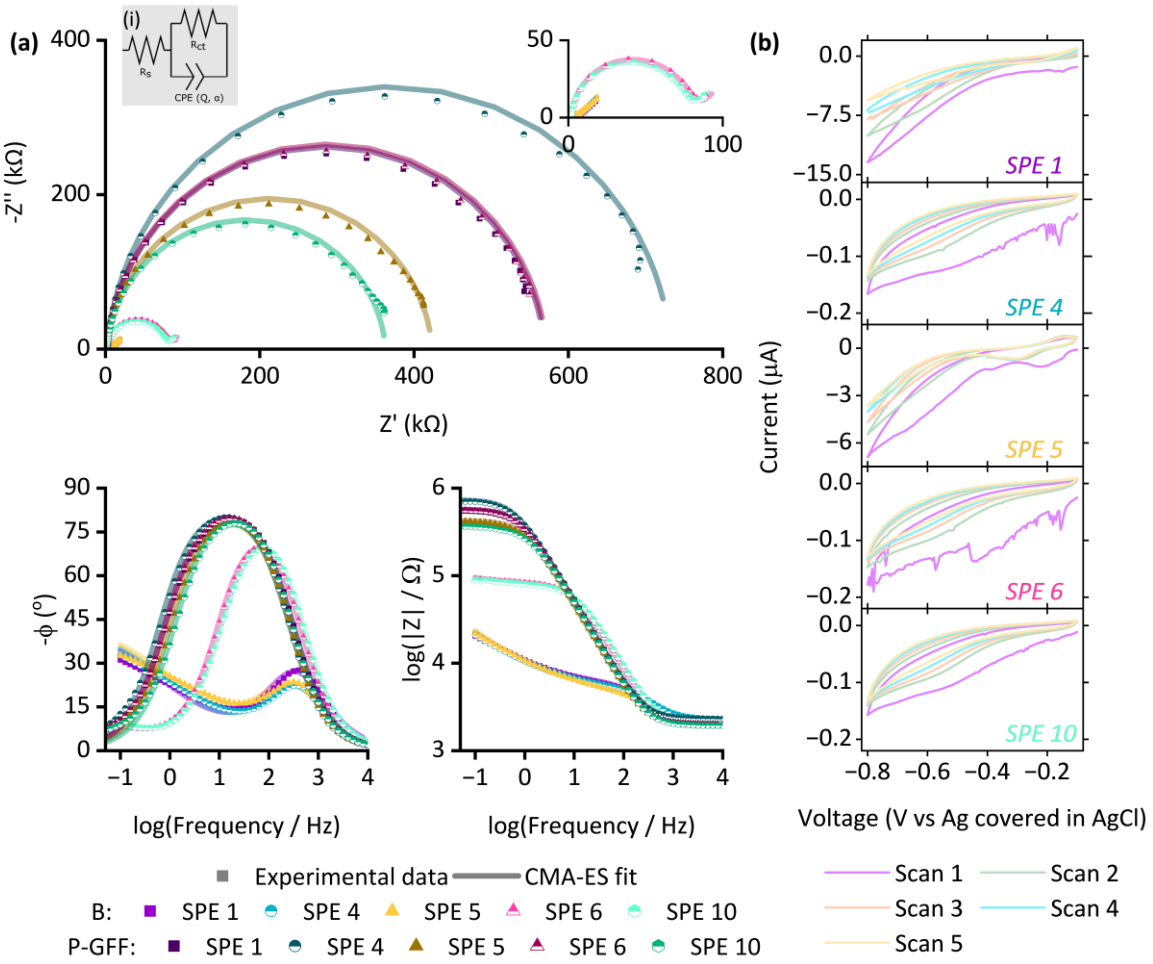

Figure 3.20. *(a) Resultant Nyquist and Bode plots of bare, B, (lighter colours) and polymer-glycofluoroform modified, P-GFF, (darker colours) showing experimental data (points) and the computational fitting (line, fitted to (a)(i)) following electrografting on C-SPEs. EIS measurements were performed in the presence of 10 mM $K_3[Fe(CN)_6]$ in pH 7 aqueous buffer (100 mM sodium phosphate, 233 mM sodium chloride) with the following parameters: $t_{(equilibration)}$ = 180 s, E_{DC} = 0.230 V vs. Ref, E_{AC} = 10 mV, f = 0.05 Hz – 10 kHz (10 datapoints per decade). (b) Corresponding electrograft for each electrode. CVs were collected by scanning between -0.1 to -0.8 V vs Ag covered in AgCl at 20 mVs^{-1} for 5 scans. R_s = solution resistance, R_{ct} = resistance to charge transfer, and Q and α are the parameters used to model a constant phase element (CPE).*

The MCMC plot, **Figure 3.21**, is again used to monitor electrode-to-electrode variability and shows that they are distinctly different in terms of their R_{ct} response, even when the distribution in viable fitting parameter values is taken into consideration via Bayesian statistical analysis.

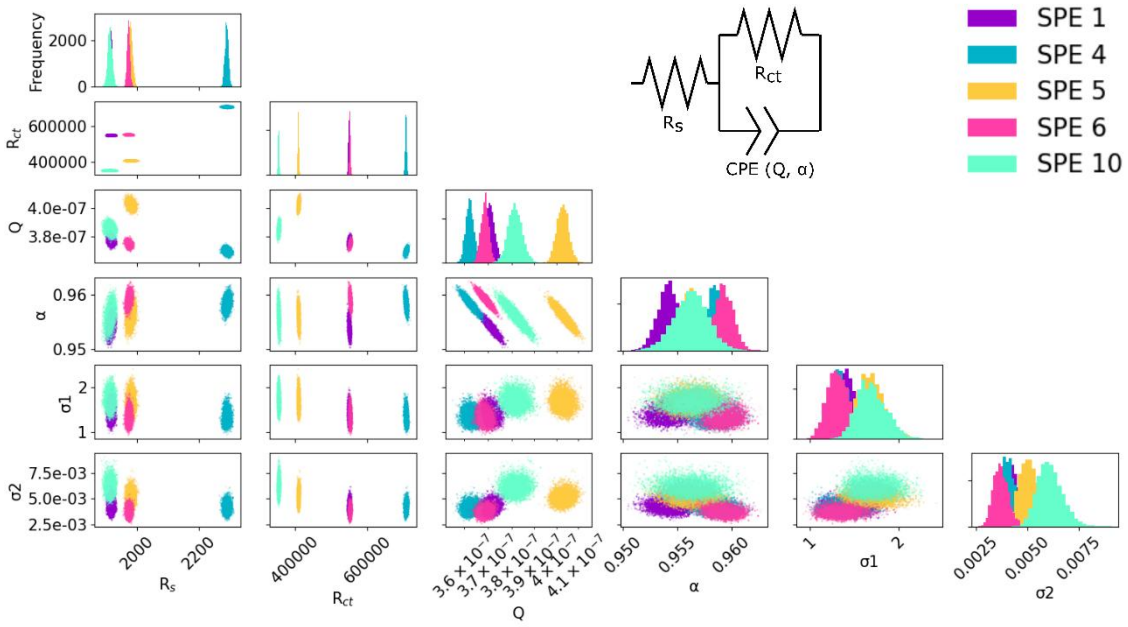

Figure 3.21. *2D scatter plots showing correlations for circuit parameters used to infer parameter distributions from 5 carbon electrografting studies. The diagonal represents the 1D histograms for each parameter showing the distribution of the fitted values. The MCMC used to generate these chains was run for 10 000 samples, with the first 3000 discarded as burn-in. R_s = solution resistance, R_{ct} = resistance to charge transfer, Q and α are the parameters used to model a constant phase element, and σ1 and σ2 are noise parameters.*

3.3.4.2. Modification comparison

Results in chapter two show that no significant stability issues are observed with the P-GFF conjugate over a 300-day timescale. In contrast, the average R_{ct} of C-SPEs modified with TABD-P-GFF conjugates show a significant decrease as function of time, **Figure 3.22**. This is attributed to the degradation of the TABD component, despite precautions being taken to protect the conjugates from exposure to ambient light. Any degradation in the triazabutadiene will reduce the concentration of diazonium species available for electrografting and, as electrografting is highly dependent on the concentration of diazonium species, will reduce the extent of electrode modification. Therefore, when considering reproducibility, it has been important to consider which datapoints should be included, to ensure that TABD degradation does not dominate although it is impossible to completely remove the variability induced by this degradation. Thus, when comparing modification, for the TABD-P modified SPEs the data up until day 13 was pooled and for TABD-P-GFF modified SPEs the data up until day 20 was pooled.

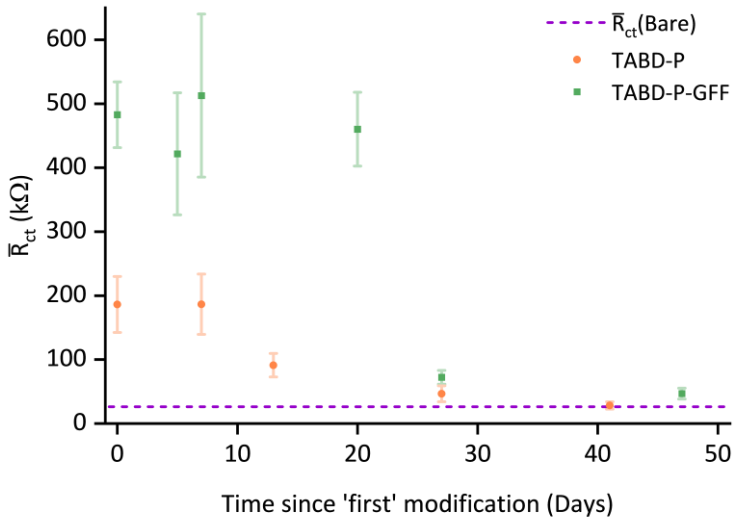

Figure 3.22. *Extracted R_{ct} parameters for modified TABD-P (orange circles) and TABD-P-GFF (green squares) plotted against the time since the first usage of the TABD. The error bars are calculated standard errors where n ranges from 2 to 7. The mean R_{ct} value ($\bar{R}_{ct}$) for bare (purple dashed line) C-SPEs is shown for comparison.*

However, a separate sample of TABD-P was capable of producing TABD-P modified SPEs with an $\bar{R}_{ct}$ value of 125.5 kΩ after 374 days (**Figure 3.23**). This sample was lyophilised on 29th April 2024 and grafted on the 7th of May 2025. The $\bar{R}_{ct}$ value achieved after 374 days for this sample is an intermediate value between 186.5 kΩ after 7 days and 91.2 kΩ after 13 days observed in with different aliquots presented in **Figure 3.22**. This is a marked difference in stability to the data represented in **Figure 3.22** despite the samples having similar storage conditions. The two aliquots were synthesised on separate occasions so the difference in stability may be due to light exposure during the synthetic phase opposed to the storage phase. While the exact reason is not known it does show that under some conditions the TABD conjugates have similar stability to the P-GFF aliquots used in chapter two (**Figure 2.21(a)**). This is crucial when considering implementing the triazabutadiene molecules in marketable devices.

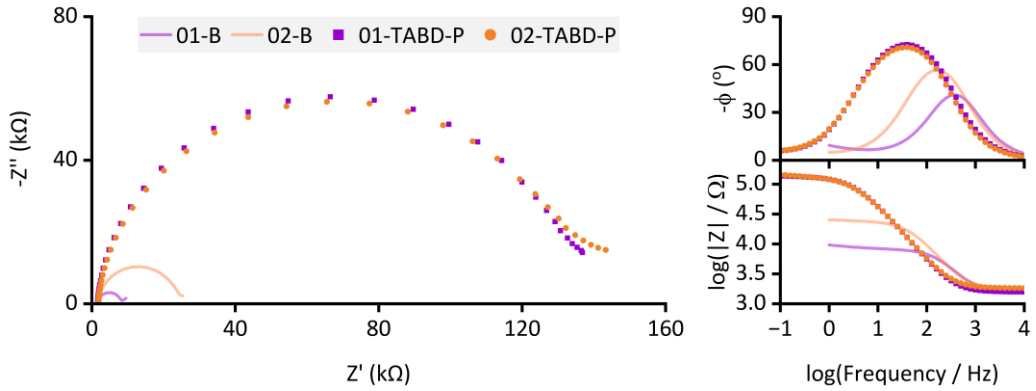

Figure 3.23. *Nyquist and Bodes plots for bare (lines) and TABD-P modified (datapoints) SPEs using a TABD-P aliquot that had been stored for 374 days. EIS measurements were performed in the presence of 10 mM $K_3[Fe(CN)_6]$ in pH 7 aqueous buffer (100 mM sodium phosphate, 233 mM sodium chloride) with the following parameters: $t_{(equilibration)}$ = 180 s, E_{DC} = 0.200 V vs. Ref, E_{AC} = 10 mV, f = 0.1 (for TABD-P) and 1 (for bare) Hz – 10 kHz (10 datapoints per decade).*

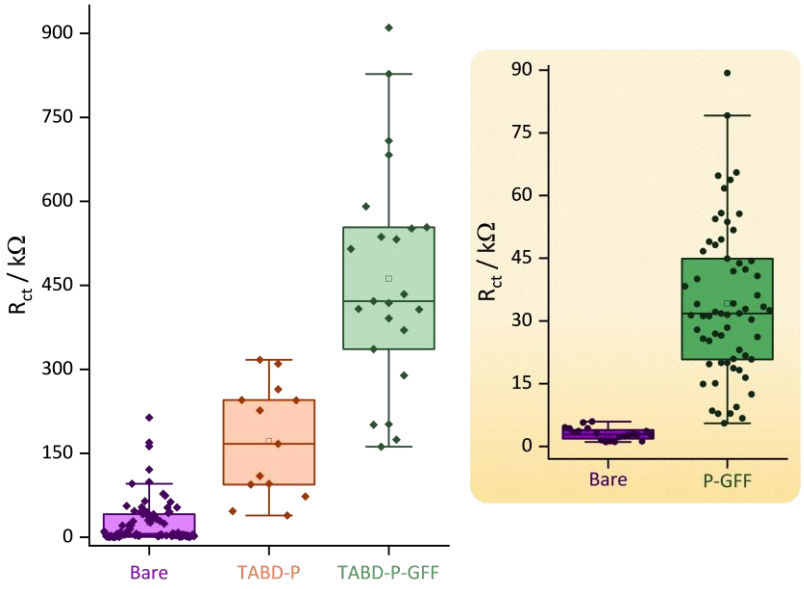

Figure 3.24. *A box and whisker plot showing the variation in the extracted R_{ct} parameters for experiments on different bare (purple diamonds, n = 89), TABD-P modified (orange diamonds, n=13), and TABD-P-GFF (green diamonds, n=23) C-SPEs. Inset: The same plot for bare (purple circles, n=20) and P-GFF (green circles, n=63) Au-SPEs. The limits of the solid box represent the 25th and 75th percentile, the central horizontal line in the box shows the position of the median and the upper and lower horizontal "whisker" lines represent the 5th and 95th percentiles. The values of these parameters are given in* ***Table 3.3****.*

.

$$Measure\ of\ distribution\ = \left({}^{|IQR\ -\ median|}/_{median}\right) \times 100\% \qquad Equation\ 3.3$$

Table 3.3. *Summary of distribution parameters for all electrode stages for both carbon and gold SPEs. A measure of distribution is given by calculating the size of the interquartile range (IQR) relative to the median value via Equation 3.3.*

R_{ct} Distribution Parameter / kΩ	Electrode stage				
	Carbon			Gold	
	Bare	TABD-P	TABD-P-GFF	Bare	P-GFF
Mean	26.2	171.7	461.3	3.0	34.2
5th Percentile	0.6	38.9	161.6	1.0	2.2
25th Percentile	2.8	66.7	336.2	1.9	20.8
Median	6.4	109.5	421.8	3.0	31.7
75th Percentile	41.1	244.7	553.8	4.0	44.9
95th Percentile	95.6	317.0	827.4	6.1	79.1
IQR	38.3	178.0	217.6	2.1	24.1
Measure of distribution / %	501.4	62.5	48.4	30.0	24.0

Comparison of the box and whisker plot for the modified Au and C-SPEs (**Figure 3.24**) the degree of variation appears quite similar between the triazabutadiene mediated immobilisation on carbon and the thiol mediated immobilisation on gold. However, it is important to consider the different magnitudes of the R_{ct} values and the difference in variability of the bare carbon and gold SPEs. In this regard a measure of distribution was calculated to see how the interquartile range compares to the median value to account for the magnitude differences. From this we can see the relative distributions are similar on the gold SPEs but for the carbon the distribution gets smaller relative to the median value from bare to TABD-P modified to TABD-P-GFF modified (501.4 versus 62.5 versus 48.4). The bare carbon SPEs are significantly more variable than the bare gold surfaces but it seems that the triazabutadiene modification helps to reduce this variability.

3.3.5. Improved surface coverage results in increased binding affinity of the carbon-based sensor towards galectin-3

3.3.5.1. Galectin-3 titration experiments

Following immobilisation of the TABD-P-GFF onto the electrode, EIS galectin-3 incubation titration experiments were carried out, similar to those detailed in the previous chapter. The impedance results following a set of these experiments are shown in **Figure 3.25**.

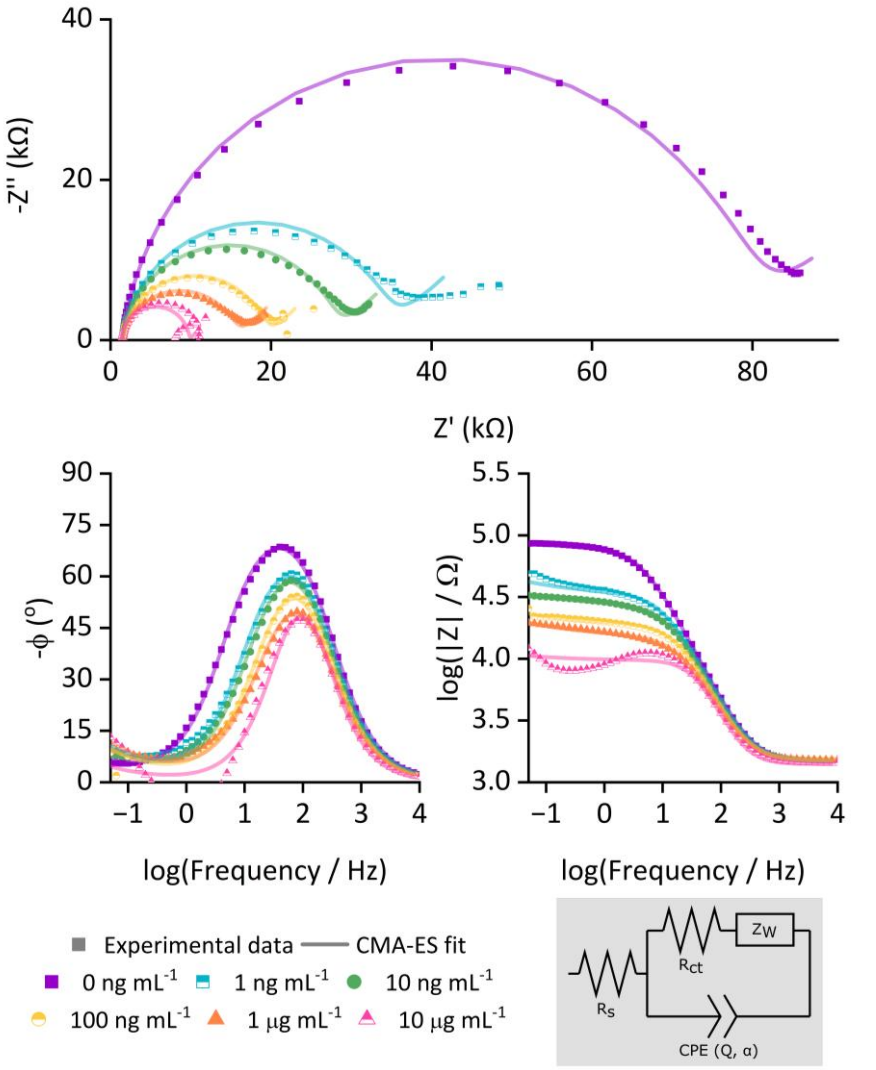

Figure 3.25. *Resultant Nyquist and Bode plots for a galectin-3 titration experiment showing experimental data (points) and the computational fitting (lines, fitted to equivalent circuit in grey box). EIS measurements were performed in the presence of 10 mM $K_3[Fe(CN)_6]$ in pH 7 aqueous buffer (100 mM sodium phosphate, 233 mM sodium chloride) with the following parameters: $t_{(equilibration)}$ = 180 s, E_{DC} = 0.150 V vs. Ref, E_{AC} = 10 mV, f = 0.05 Hz – 10 kHz (10 datapoints per decade). R_s = solution resistance, R_{ct} = resistance to charge transfer, Z_W = Warburg element, and Q and α are the parameters used to model a constant phase element (CPE).*

It is immediately clear that with the TABD-P-GFF modified C-SPEs the biosensor platform has a much higher sensitivity to galectin-3 since significantly lower analyte concentrations, 1 ng mL^{-1} to 10 µg mL^{-1}, can be distinguished compared to the titration experiments carried out on gold (galectin-3 concentration range of 10 µg mL^{-1} to 30 µg mL^{-1}). This is attributed to the higher surface coverage of the GFF on C compared to Au, as determined through the ferrocene immobilisation experiments detailed in section 3.3.3. Another contrast between the biosensor platforms is that the R_{ct} decreases with increasing galectin-3 concentration on carbon whereas it increased with protein concentration on gold. This is attributed to theelectrostatic repulsion between the electronegative surface groups on the C-SPE

electrode surface and the negatively charged solution ferricyanide ions.[226,227]. This repulsion will be passivated in the presence of a greater concentration of surface-bound galectin-3, as this can shield the carbon surface charge from the solution ferricyanide redox probe. Comparative studies with a positively charged redox probe, hexaammineruthenium(III) chloride, were carried out to confirm this hypothesis and are presented in section 3.3.5.3.

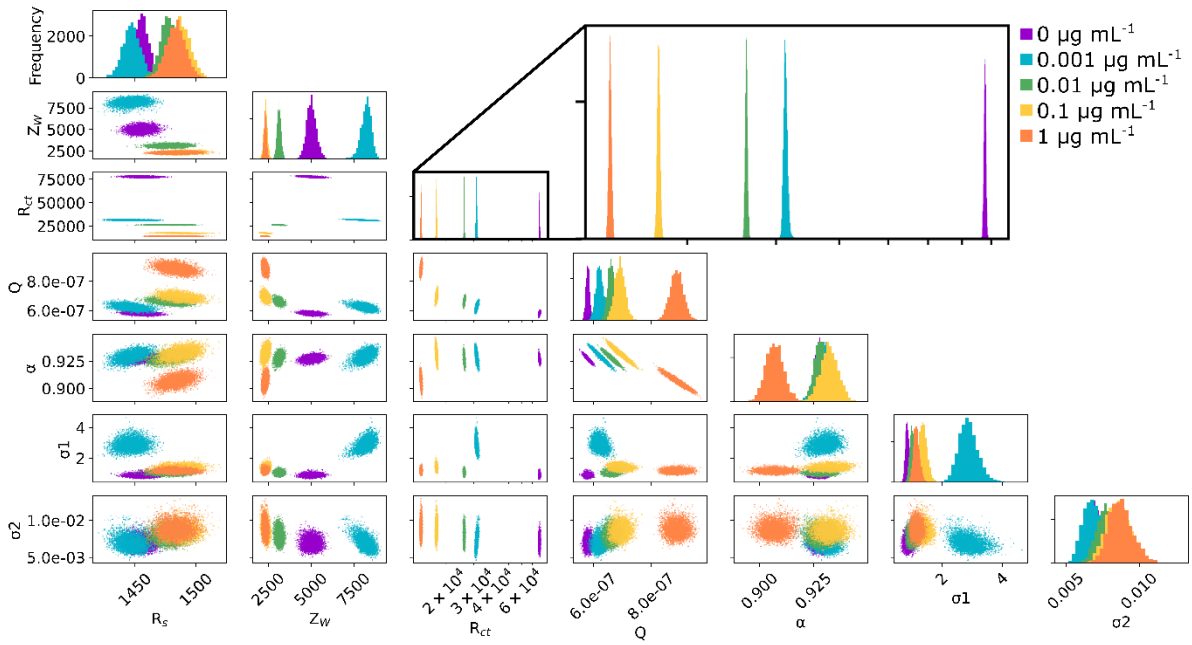

Figure 3.26. *2D scatter plots showing correlations for circuit parameters used to infer parameter distributions from galectin-3 titration experiments on a single electrode. The diagonal represents the 1D histograms for each parameter showing the distribution of the fitted values. The MCMC used to generate these chains was run for 10 000 samples, with the first 3000 discarded as burn-in. The zoomed inset shows the distribution of Rct fits with changing concentration of galectin-3. R_s = solution resistance, R_{ct} = resistance to charge transfer, Z_W = Warburg element, Q and α are the parameters used to model a constant phase element, and σ1 and σ2 are noise parameters.*

Again, MCMC analysis of the galectin-3 EIS experiments, shown in **Figure 3.26**, validates the choice of R_{ct} as the parameter that best reflects protein binding since the histograms show distinct and narrow distributions that correlate with galectin-3 concentration. In addition, Q and Z_W also display some correlation between the peak value and galectin-3 concentration, but the overlap in the distributions suggests insufficient certainty in these correlations to use these parameters to determine galectin-3 concentration. The presence of diffusional behaviour (shown by diagonal lines at lower frequencies) justifies including a Warburg element in the modelling of this data. Simplistic attempts at normalisation of R_{ct} values with these parameters did not collapse electrode-to-electrode variability (data not shown) and more complex data processing approaches, such as principal component analysis, fell outside of the scope of this project. The 2D scatter plots show no parameter-

to-parameter correlation besides the expected relationship observed between Q and α which is explained by the fact that these two parameters model a single circuit component, the constant phase element.

The data for the 10 μg mL^{-1} galectin-3 experiment is omitted as the code used for MCMC was unable to determine suitable starting values for the fit to this data, likely due to the negative values of phase. This shows that there in some inductor behaviour within the circuit, there are many possible origins for such behaviour.[109] In this system, it is most likely due to some adsorbed species or some type of film formation/dissolution due to successive incubations and measurements, since this behaviour was only ever seen at this final stage in the galectin-3 titration experiments.

In total, 36 galectin-3 titration experiments were carried out on the GFF-modified carbon SPEs. The extracted R_{ct} values from CMA-ES analysis are shown in **Figure 3.27** and are sub-classified into three different groups, those conducted over an inappropriately high range of galectin-3 concentrations or with an aliquot of TABD-P-GFF that displayed a significantly different level of degradation to the measurements shaded in green (shaded in orange), those included in binding analysis later in this section (shaded in green), and those that show a degree of correlation between galectin-3 concentration and R_{ct} value but were not included in the binding analysis (shaded in yellow). The unshaded plots were performed over an appropriate galectin-3 concentration range but do not show a concentration-dependent galectin-3 response. Some of the data shaded in orange does show a level of concentration-dependent signal decrease (plots 1, 4 and 5 in the third row) but as the magnitude of these datapoints is significantly higher than other data it shows these surfaces are behaving differently to the data used for binding analysis. This is likely due to the degradation of triazabutadienes discussed above and means these electrodes could be operating under different binding affinities or kinetics, so the choice was made to quantify the binding of the larger group of electrodes that displayed a consistent response.

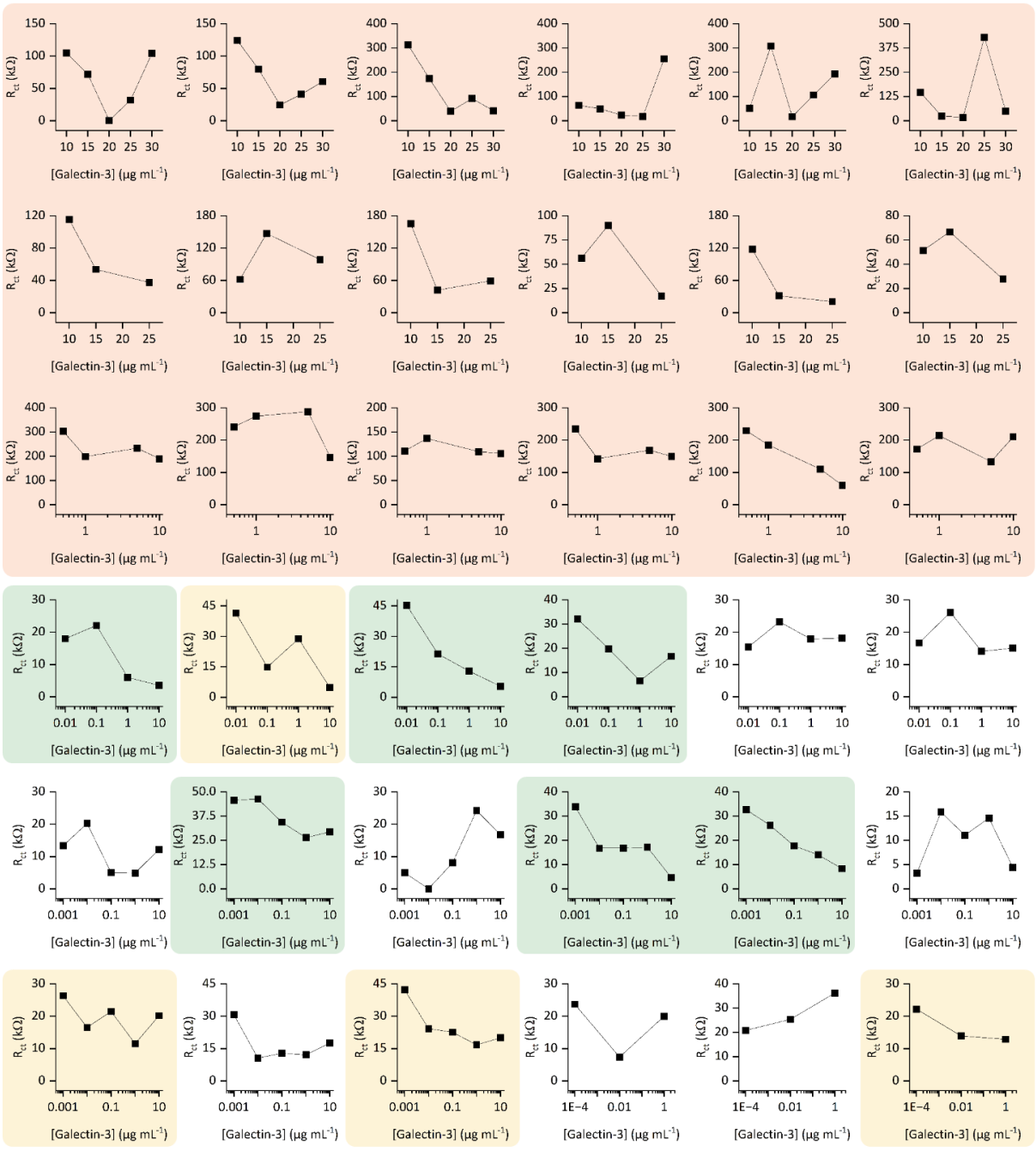

Figure 3.27. *Extracted R_{ct} 'best-fit' point-values from CMA-ES analysis for the 36 galectin-3 titration experiments carried out on GFF-modified C-SPEs. Datasets highlighted in orange were early experiments conducted over an insufficient galectin-3 range, in green are the six datasets pooled for binding analysis, and in yellow were not included in the binding analysis but do show correlation between R_{ct} and [galectin-3].*

Similar to the dataset gathered on gold electrodes in chapter two, the raw data values display significant electrode-to-electrode variation due to inconsistencies within modification efficiency. Additionally, any differences in the surface oxides between SPEs will change the interactions with the solution ferricyanide ions and thus influence the electrochemical behaviour observed. This variation will be heightened for the carbon-based

biosensor platform due to the greater distribution of the bare surfaces of C-SPEs compared to Au-SPEs, and the decrease in the initial R_{ct} value observed due to the decay of the triazabutadiene over time (demonstrated in **Figure 3.22**). The zero-point measurements, i.e. the characterisation of the surface prior to any galectin-3 exposure immediately following modification via electrografting of TABD-P-GFF, are excluded from the plots in **Figure 3.27** for two reasons: (i) the necessity of a logarithmic x-axis for experiments conducted over a wide concentration range, and (ii) the presence of a large signal drop between the first and second measurement (i.e. between the 'zero-point' and the first galectin-3 measurement) which skews the y-axis hindering the determination of the relationship between R_{ct} and galectin-3 concentration. This large initial signal drop persists in a variety of experiment types and will be demonstrated and discussed later in this chapter.

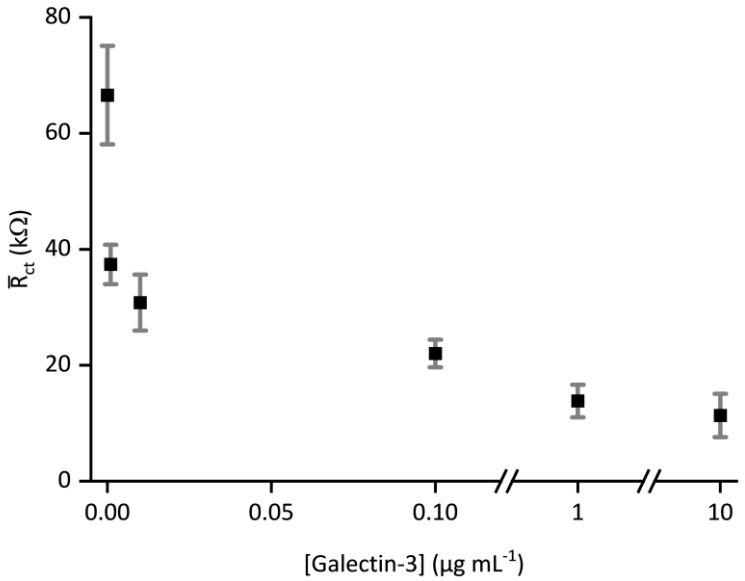

Figure 3.28. *Mean R_{ct} values for the six datasets highlighted in green in* ***Figure 3.27****. The error bars represent standard errors where n=6 for all concentrations except 0.001 µg mL^{-1} where n=3.*

A clear decay curve, shown in **Figure 3.28**, can be constructed by simply averaging the raw values for the extracted R_{ct} values for the six datasets selected for binding analysis (plots highlighted in green in **Figure 3.27**) and plotting this against galectin-3 concentration. Evidently a logarithmic x-axis would be better for visualisation of a dataset spanning five orders of concentration magnitude, however the removal of the zero-point makes the decay curve incomplete. Thus, in order to quantify the binding of galectin-3 a similar Hill analysis to that conducted in chapter two can be performed, but a logarithmic linear form of the equation will be considered.

$$\theta = \frac{C^n}{K_d^n + C^n} \qquad \textit{Equation 3.4}$$

$$\theta = \frac{1}{K_d^n/_{C^n} + 1} \qquad \textit{Equation 3.5}$$

$$\frac{1}{\theta} = \frac{K_d^n}{C^n} + 1 \qquad \textit{Equation 3.6}$$

$$\frac{1}{\theta} - 1 = \frac{K_d^n}{C^n} \qquad \textit{Equation 3.7}$$

$$\frac{1-\theta}{\theta} = \frac{K_d^n}{C^n} \qquad \textit{Equation 3.8}$$

$$\frac{\theta}{1-\theta} = \frac{C^n}{K_d^n} \qquad \textit{Equation 3.9}$$

$$log\left(\frac{\theta}{1-\theta}\right) = log\left(\frac{C^n}{K_d^n}\right) \qquad \textit{Equation 3.10}$$

$$log\left(\frac{\theta}{1-\theta}\right) = nlog(C) - nlog\ (K_d) \qquad \textit{Equation 3.11}$$

$$log\left(\frac{\theta}{1-\theta}\right) = nlog(C) - log\ (K_d)$$

$$\textit{where:} \quad \theta = \frac{\left|R_{ct,i} - R_{ct,0}\right|}{R_{ct,max}} \qquad \textit{Equation 3.12}$$

where: n: binding coefficient; C: galectin-3 concentration (mol dm^{-3}); K_d^n: dissociation constant (mol dm^{-3}); $R_{ct,0}$: protein-free charge transfer resistance (kΩ); $R_{ct,i}$: charge transfer resistance of a single concentration (kΩ); $R_{ct,max}$: maximum value of charge transfer resistance (kΩ); K_d: apparent dissociation constant (mol dm^{-3}); θ: proportion of occupied binding sites

The rearrangement of the Hill equation to the linearised form, the so-called Hill-Langmuir equation, is provided in Equation 3.4 to Equation 3.11. A 'simplified' version, given in Equation 3.12, is often used for binding analysis. The difference is in the intercept terms where in Equation 3.12 K_d is considered an apparent K_d and accounts for the binding cooperativity within the value. These calculations give an apparent K_d value of 0.33 μg mL^{-1} which assuming a molecular weight of 26 kDa for galectin-3 is equivalent to a K_d value of 13 nM, this is approximately 20-fold lower than the apparent K_d determined for the biosensor platform on gold and much closer to the apparent K_d observed with the original nanoparticle detection system. This shows the higher presentation of GFF on the carbon surface facilitates multivalent binding and helps to overcome the different steric interactions of a planar electrode binding surface compared to solution-based modified nanoparticles. Importantly, the assay is sensitive over a larger concentration range on carbon and, therefore, more suitable for biologically relevant samples which typically contain

concentrations of galectin-3 in the ng mL^{-1} range (i.e. 0.001 μg mL^{-1} which is the lowest concentration tested here). The raw θ for this lowest concentration is 0.37, this suggests the potential for making measurements at lower concentrations so the biologically relevant range falls in the middle of the titrated region. The cooperativity determined from the gradient is less than one which suggests negative cooperativity. This is unexpected considering the multivalency of galectin-3. However, it may be that the high packing of the GFF onto the carbon surface is creating steric hinderance on binding, or that a monomeric form of galectin-3 is the preferred binding conformation again due to this high packing.

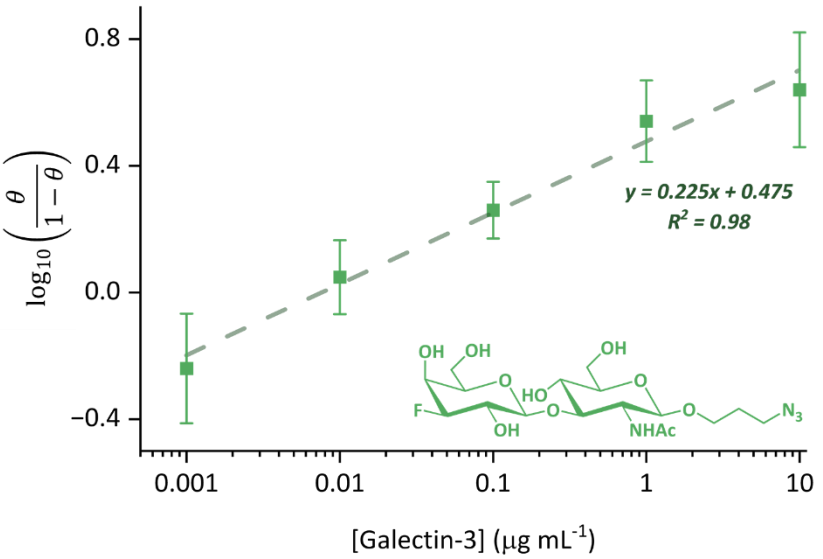

Figure 3.29. *Combined datasets from six different TABD-P-GFF modified C-SPEs titrated against galectin-3. The y-axis is a logarithmic value representing the proportion of bound species and the dataset is fit to a straight line (green dashed line, equation shown on plot) to enable determination of K_d, as described in the text. Inset: chemical structures of GFF (green). The datapoints represent the average values from the combined datasets, while vertical error bars represent the standard error (where n=6 for all concentrations except 0.001 μg mL^{-1} where n=3).*

3.3.5.2. Control experiments to confirm selectivity and specificity

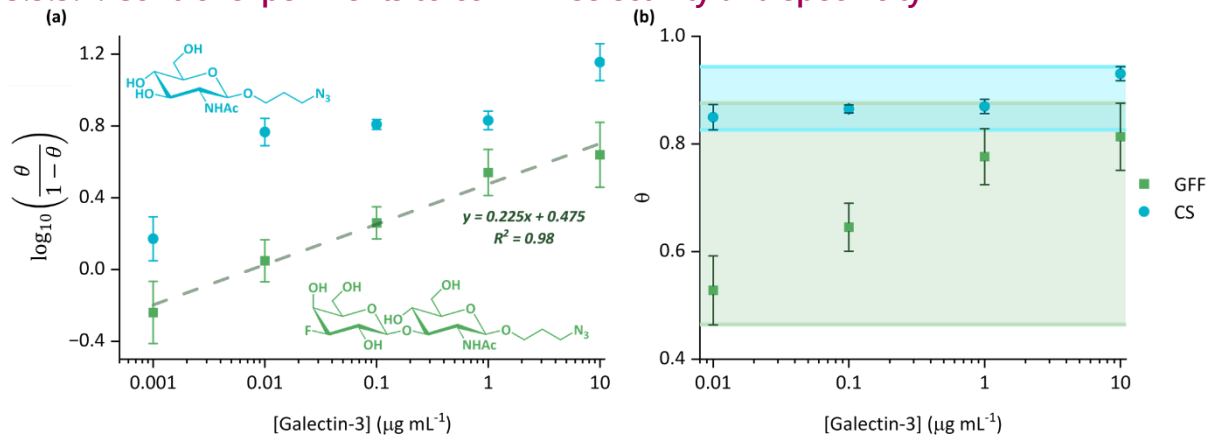

Figure 3.30. *(a) Hill Langmuir analysis for the glycofluoroform (green squares) and the control sugar (blue circles) with corresponding structures shown. (b) The upper and lower bounds shaded for the glycofluoroform's (green) and control sugars's (blue) response (θ) over the galectin-3 concentration range of 0.01 to 10 μg mL^{-1}.*

When comparing the control sugar to the GFF it is clear that there is not a linear relationship between binding response and galectin-3 concentration in the absence of GFF (**Figure 3.30**). The initial decrease seen does skew the data slightly for the first data point, however (**Figure 3.30(b)**) shows when that first data point is excluded it is clear from the highlighted areas that the GFF exhibit a drastic change in response with changing galectin-3 concentration whereas the CS response is comparably static. Any fluctuations observed in the response of the TABD-P-CS modified surface are likely due to surface rearrangements in solution because the TABD-P is a dynamic linker. The high surface-sensitivity of EIS will detect these subtle changes. This shows that the galectin-3 binding observed is selective to the glycofluoroform.

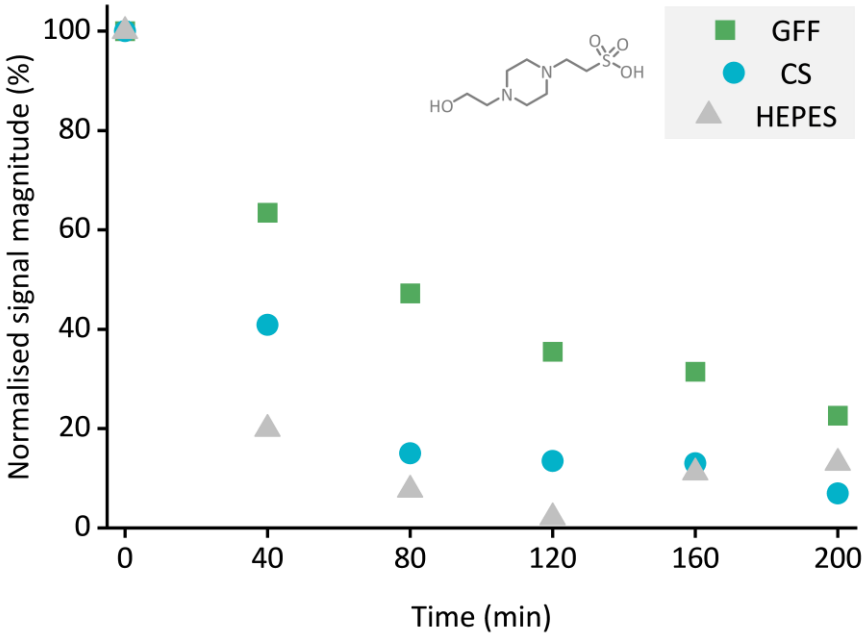

Figure 3.31. *Fluctuations in signal strength of a modified electrode incubated in HEPES buffer (structure shown on the graph) over 200 minutes (grey triangles) compared to the change on galectin-3 incubation of TABD-P-GFF (green square) and TABD-P-CS (blue circles). The GFF and CS data is equivalent to that in* ***Figure 3.30(a)*** *expressed as normalise signal magnitude.*

A buffer-only control experiment (**Figure 3.31**, grey triangles) show that a portion of the observed decrease in R_{ct} with galectin-3 incubation may be independent of analyte binding. This experiment is designed to match up the time points with those of the titration experiments: 30 minutes for the incubation, an 8-minute EIS measurement, and 2 minutes to allow for changing and rinsing the SPEs between the potentiostat and the Eppendorfs. This is compared to the galectin-3 binding response of both TABD-P-GFF and TABD-P-CS modified electrodes (**Figure 3.31**, green squares and blue circles). In the buffer-only experiment the initial decrease is larger than that observed in the galectin-3 titration experiments. However, in all subsequent experiments there is fluctuation in the signal size opposed to a continued signal decrease and these changes are of a smaller magnitude to those observed in the titration experiments for TABD-P-GFF modified electrodes. The TABD-P-CS modified electrodes show a similar response to the buffer-only control experiment showing that there is no galectin-3 binding by the control sugar, and the big initial decrease in signal is likely due to the effect of the buffer. This additional effect clearly is only observed in the early time points and does not persist throughout the experiment.

This suggests that the signal decrease observed in titration experiments on TABD-P-GFF modified electrodes may have multiple contributions: galectin-3 binding and buffer

interference. However, it is distinct from the buffer-only control experiments, so the galectin-3 binding does influence the observed signal, therefore, conclusions regarding galectin-3 binding affinity remain valid. The significant signal decrease in the presence of buffer is likely to have a cause beyond surface rearrangement. The signal change could be due to coordination of buffer salts of buffer-induced surface degradation. HEPES is often considered a non-coordinating buffer but it does show a small degree of chelation and reduction.[228] Additionally, HEPES can undergo photooxidation to produce H_2O_2 or can form radicals under certain conditions, both of which could have a destructive effect.[229,230] This effect is not observed with the TABD-P-GFF modified electrodes suggesting galectin-3 binding prevents this degradation. This is akin to what was observed in the mediation of degradation of gold electrodes by potassium ferricyanide in the presence of galectin-3 discussed in chapter two.

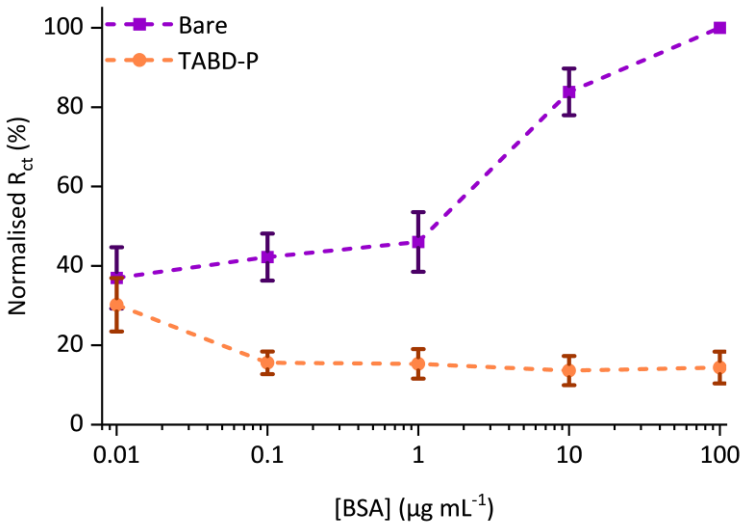

Figure 3.32. *Extracted R_{ct} parameters for BSA incubation of both bare (purple squares) and TABD-P (orange circles) modified C-SPEs. The datapoints represent the average values from the combined datasets, while vertical error bars represent the standard error (where n=4 for bare and n=6 for TABD-P).*

$$Normalised\ R_{ct} = \frac{R_{ct,i}}{R_{ct,max}} \times 100\% \qquad Equation\ 3.13$$

The BSA controls (**Figure 3.32**) show that the modification of the electrode does passivate against non-specific binding and that the triazabutadiene moiety does not interfere with the passivating effect observed in chapter two. Due to the difference in magnitude of the responses for bare and TABD-P a normalised R_{ct} value is plotted to allow for easier comparison. This value is calculated using Equation 3.13, for each experiment each recorded

R_{ct} value is divided by the maximum and expressed as a percentage. For the TABD-P data the maximal value was the 'zero-point' and therefore is absent on this logarithmic plot. The TABD-P is used instead of TABD-P-GFF to conserve the GFF for galectin-3 titration experiments however the passivation of the electrode is likely to be due to the polymer, so the TABD-P is a valid choice for this control experiment.[136]

3.3.5.3. Usage of hexaammine ruthenium (III) chloride in impedance studies

When investigating galectin-3 binding with potassium ferricyanide a different response is observed on gold and carbon SPEs. To probe this difference, some galectin-3 titration experiments were carried out with hexaammineruthenium(III) chloride. These experiments contain positively charged hexaammineruthenium(III) ions and thus would be expected to observe the opposite effect. In the absence of galectin-3, the electrostatic attraction between the oppositely charged carbon electrode surface and hexaammineruthenium(III) ions favours electron transfer. This facilitation will decrease in the presence of galectin-3, meaning the resistance to charge transfer will increase. The expected response was observed (**Figure 3.33**) which validates the conclusions made regarding EIS response in the presence of galectin-3 measured by potassium ferricyanide.

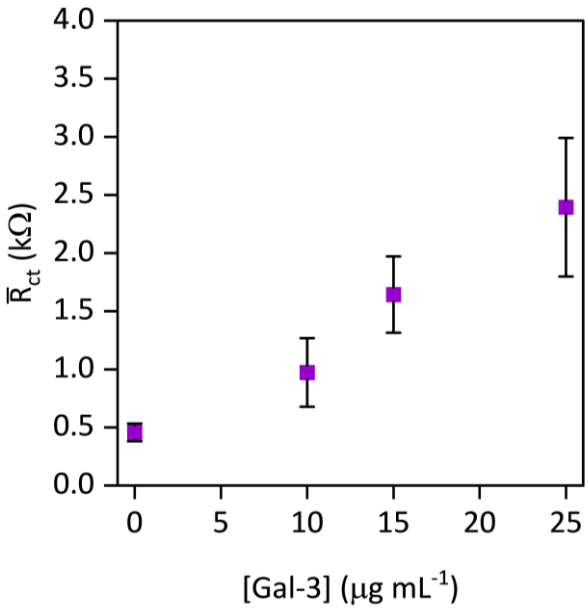

Figure 3.33. *Average extracted R_{ct} values and standard errors for galectin-3 titrations on three SPEs using a Ru-based redox probe. EIS measurements were performed in the presence of 10 mM $[Ru(NH_3)_6]Cl_3$ in pH 7 aqueous buffer (100 mM sodium phosphate, 233 mM sodium chloride) with the following parameters: $t_{(equilibration)}$ = 180 s, E_{DC} = -0.250 V vs. Ref, E_{AC} = 10 mV, f = 10 Hz – 500 kHz (10 datapoints per decade).*

However, although signal enhancement opposed to signal quenching with increasing target analyte is preferable for a biosensor system,[231] for impedance measurements, using the ferricyanide redox probe is preferred. Electron transfer rates depend on multiple factors including electrode surface and electrolyte but typically species that undergo electron transfer via outer sphere mechanisms are rapid.[232] As hexaammineruthenium(III) chloride transfers electrons via an outer sphere mechanism and potassium(III) ferricyanide chloride transfers electrons via an inner sphere mechanism, in the same system, hexaammineruthenium (III) chloride will undergo faster electron transfer than potassium ferricyanide. In EIS, measuring high frequencies is limited by instrumentation whereas measuring low frequencies is limited by time, our instrumentation is unable to reach high enough frequencies to get reliable EIS measurements in a reasonable time frame using hexaammineruthenium(III) chloride, especially on unmodified electrodes where electron transfer is even less hindered. Additionally, in the next chapter voltammetry approaches will be used to assess changes in observed current when galectin-3 binds to immobilised glycofluoroforms. This means using potassium ferricyanide will give an increase in current with increasing galectin-3 concentration due to the inverse relationship between resistance and current.

3.4. Summary and conclusions

This chapter presents the second example of the usage of a triazabutadiene-mediated electrografting strategy for electrode modification. This strategy is employed in aqueous media suited for biosensing applications. The novel attachment of triazabutadiene molecules to thiol-containing polymers (and subsequently glycofluoroforms) is demonstrated. A simple purification strategy exploiting solubility and centrifugation isolates these conjugates for electrografting. This strategy enabled the development of a new sensor platform on carbon SPEs. Carbon was identified as the most suitable surface from a comparison of carbon, gold, and ITO-based SPEs and control experiments align with previously published data showing that UV exposure is crucial to the immobilisation.

The alkyne functionality on a TABD-P modified SPE was attached to a ferrocene-containing molecule via a surface-click reaction. A voltammetric study, using both direct current and square-wave methods, confirmed ferrocene immobilisation and determined this to be a surface-confined species. The reaction duration for the ferrocene immobilisation was several

days and the modified surface remained stable in solution over this time frame indicated by an increase in the signal associated with surface-confined ferrocene over time. Surface coverage determination revealed a ten times higher surface coverage on the carbon surface compared to the coverage achieved via gold-thiol immobilisation. This proves triazabutadiene-based immobilisation to be a stable modification method which yields surfaces highly decorated in galectin-3 binding glycofluoroform functionalities.

This improved surface coverage compared to that achieved on gold electrodes conferred higher sensitivity when studying the galectin-3 binding onto the new biosensor scaffold where the P-GFF conjugate is immobilised onto the surface via the TABD molecules. A K_d value of 13 nM was calculated, showing this sensor's potential utility in patient testing. Complementary controls are presented where the selectivity and specificity of the sensor platform is studied; while there may be multiple factors, galectin-3 binding and buffer contributions, contributing to the signal decrease, they do confirm the GFF-modified carbon electrodes show both selectivity of the galectin-3 binding to the GFF and specificity of only binding the desired protein.

Chapter Four: Exploring the potential of applying alternating current voltammetric techniques in biosensing

The previous two chapters have relied upon EIS measurements for the detection of galectin-3 binding to GFF-modified electrodes. However, as shown in chapter three, triazabutadiene-mediated diazonium electrografting can be used to immobilise the glycofluoroform-polymer conjugate onto a carbon surface via a covalent bond. Immobilisation using a covalent bond provides high stability to the modified electrodes allowing alternative electrochemical techniques to be used which destabilised the original modified gold sensor platform. This chapter will explore the use of Fourier transformed alternating current voltammetry (FTV) and purely sinusoidal voltammetry (PSV) for sensing. The introduction explains the background and applications of these techniques as well as the benefits these techniques can provide to sensing applications. The results show that the covalent immobilisation strategy confers the required stability for these alternating current voltammetry techniques to be applied to our sensing platform to enable highly sensitive measurements on the benchtop.

4.1. Introduction

Voltammetry is a common electrochemical technique in which the voltage is swept across a potential range and the resultant current response is recorded. This voltage-time sweep can be applied in a number of ways which gives rise to sub-classifications of the technique. Moving to a covalent immobilisation strategy for attaching the P-GFF to the electrode allows the employment of voltammetric techniques for sensing. Therefore, while EIS has been used to study galectin-3 binding to the biosensor in previous chapters alternating current voltammetry (ACV) will be used in this chapter. EIS, DCV, and the ACV methods explored in this chapter: FTV and PSV are summarised in **Figure 4.1**.

4.1.1. Direct current voltammetry

Direct current voltammetry (DCV) involves applying a potential to the working electrode that changes linearly with time. The voltage is commonly scanned in both an oxidative and reductive direction – known as cyclic voltammetry.[141] The total current output consists of the sum of capacitive non-faradaic current and faradaic current arising from the formal electron transfer.[233] Oxidative processes are observed when moving to a more positive potential and reductive processes are observed in when moving to a more negative

potential. The current response is measured and plotted against the potential; this data representation is known as a voltammogram.[141]

DCV is a useful technique because experiments are straightforward, the kinetics can be probed by varying scan rate and, in some cases, the faradaic signal and its peak potentials are easily identified. Thus, it has found utility in 'fingerprinting' redox signals, electron transfer rate quantification, and determination of electron transfer mechanism.[141,234–236] Often, the capacitive current is a large contributor to the total signal, so DCV can lack sensitivity. The faradaic current must be isolated from the background current resulting in complex and potentially misleading analysis.[237] Simple background subtraction (akin to the subtraction of a 'blank' measurement in spectroscopy) can be an oversimplification as both faradaic and non-faradaic current can change in the 'redox region'.[234]

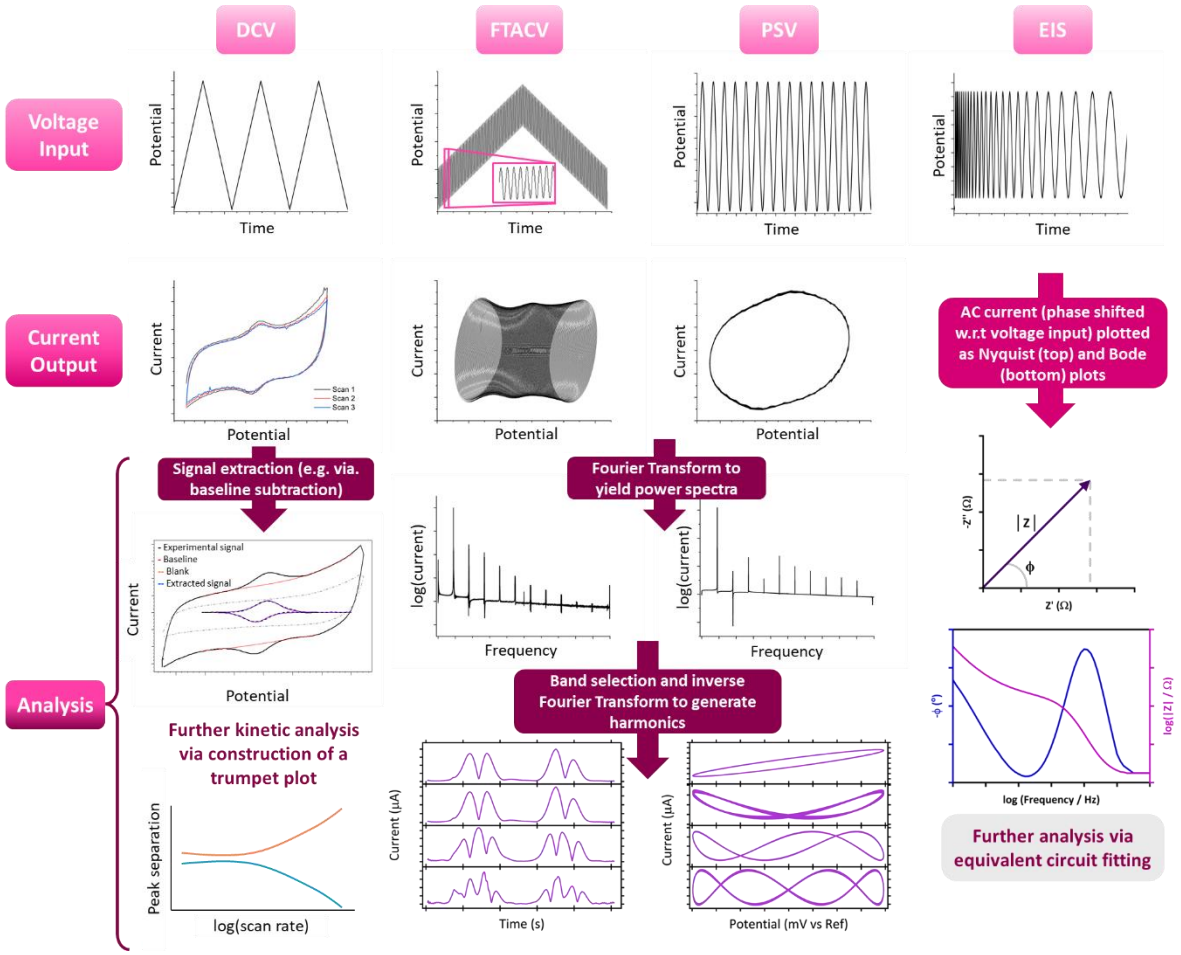

Figure 4.1. *Comparison of the voltammetric techniques relevant to this thesis (from left to right: DCV, FTV, PSV and EIS) showing the inputs and outputs of each type of voltammetric experiment and some common visualisation and analytic paths.*

4.1.2. Alternating current voltammetry

Alternating current electrochemical methods include EIS, SWV, FTV, PSV, and pulse voltammetry.[237] As explained previously, in EIS the oscillatory voltage-time input typically employs a small amplitude to avoid significant non-linearity in the resultant current.[238] However, as will be discussed later the usage of a large amplitude to induce non-linearity is crucial in other wave forms (i.e. SWV and differential pulse voltammetry).[237] However, fundamentally, there is no reason to constrain specific techniques to a particular amplitude magnitude.

4.1.2.1. Fourier transformed alternating current voltammetry

In FTV, the voltage applied is the combination of a cyclic ramp and an oscillating sine wave (**Figure 4.2**). This potential is described in Equation 4.1 to Equation 4.3 and has a characteristic starting and reverse potential, linear scan rate, and sinusoidal frequency and amplitude.[239] A particular advantage of FTV is the post-measurement processing. As detailed in **Figure 4.1**, the Fourier transform function converts the current output from the time (and therefore potential) domain to the frequency domain. This generates a power spectrum with peaks at integer frequencies of the input frequency. These peaks can be 'selected' (i.e. a region of a set width, usually 0.1 – 0.5 x ω, around nω is selected and the rest of the spectrum is zeroed) and inverse Fourier transformed to yield distinct current-time plots which are known as harmonics.[240] These harmonics can be represented as total current or envelope plots. Envelope plots simplify the output by removing the oscillation, essentially 'tracing' the maxima across the timepoints, so are the chosen visualisation throughout this thesis because they make overlay plots easier to interpret. The additional parameters describing the sine wave, amplitude and frequency, provide an experimentalist with a greater degree of control as to what their experiment will probe. A large amplitude provides access to a greater number of harmonics but also means a greater proportion of the system is being activated in each oscillation. Activating a larger proportion of the system can result in peak broadening which can distort the harmonics shape. Therefore, in some cases, a balance must be reached between maintaining resolution in harmonic shape while ensuring a suitable harmonic limit is reached. The frequency controls what kinetic processes are being probed throughout the measurement.[234]

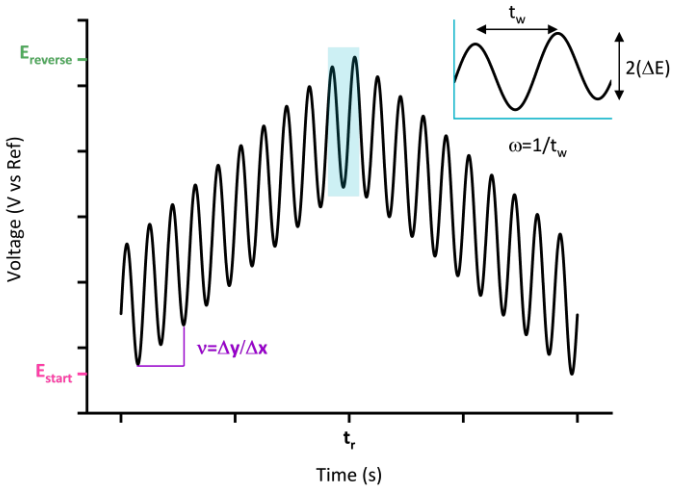

Figure 4.2. *Potential waveform applied in an FTV experiment, highlighting start and reverse potential (E_{start} and $E_{reverse}$), linear scan rate (ν), and the amplitude (ΔE) and frequency (ω) of the sine wave, t_w = time taken for a full oscillation (s). Inset: zoomed in of the portion of the wave highlighted in blue.*

$$E_{dc}(t) = \begin{matrix} E_{start} + \nu t & if\ t \leq t_r \\ E_{reverse} - \nu(t-t_r) & if\ t > t_r \end{matrix} \qquad Equation\ 4.1$$

where: $E_{dc}(t)$: applied potential (V); E_{start}: initial potential (V); $E_{reverse}$: switching potential (V); ν: scan rate (V s^{-1}); t: measurement time (s); t_r: switching time (s)

$$E_{ac}(t) = \Delta E \sin(\omega t + \phi) \qquad Equation\ 4.2$$

where: ΔE: sinusoidal amplitude (V); ω: sinusoidal frequency (Hz); t: measurement time (s); ϕ: phase shift (radians)

$$E_{app}(t) = E_{dc}(t) + E_{ac}(t) \qquad Equation\ 4.3$$

In order for this processing to be possible the sampling time of the experiment must be constant to enable Fourier transformation of the current output.[234] Additionally, the amplitude must be large enough (typically >50 mV)[234] to induce the non-linearity required for higher harmonics to be recoverable. An electrochemical cell is a non-ideal system and thus when probed with a large amplitude voltage wave will have a non-linear response. This current response will contain a dc component and harmonic contributions at the fundamental (i.e. input) frequency and at integer multiples of this frequency. Capacitance (non-faradaic current contributions) is linear. But, in a real experiment there will be some non-linear current attributable to capacitance which will only contribute to early harmonics (generally up to third harmonic).[237] Conversely, faradaic current contributions will be seen at higher harmonics as long as the electron transfer rate is fast enough. Therefore, sufficiently high harmonics can report solely on faradaic processes. Not only does the Fourier transform process extract the faradaic current it also filters noise, as the noise present in the experiment is spread across the entire power spectrum so only a fraction is

present in the inverse Fourier transformed portions. Therefore, the FTV method is more sensitive than DCV. FTV has mainly found applications in mechanistic studies because the shape and position of the harmonics inform on the redox processes occurring. For one-electron redox processes, the midpoint of the harmonics – the central peak for odd harmonics and the central trough for even harmonics – is the oxidative or reductive potential. Additionally, the symmetry in the magnitude of the oxidative and reductive harmonics and the lobes of the harmonics give an insight into the reversibility of the reaction.[234] In this thesis, the aim is to explore the value of FTV in electrochemical biosensing.

4.1.2.2. Purely sinusoidal voltammetry

In PSV, an oscillating sinusoidal voltage wave is employed. Essentially it is like an EIS experiment at a single frequency, but far higher amplitudes are employed than in typical EIS (**Figure 4.3**). This potential-time oscillation is described in equations Equation 4.4 and Equation 4.5, and is defined by the starting and reverse potential which govern the amplitude of the wave which also has a defined frequency. Historically, this technique was known as oscillographic polarography which involved applying fast potential sweeps at a mercury electrode.[239] Compared to other voltammetric methods it is less prevalent but has been used for signal amplification compared to background noise,[241] theoretical study of surface-confined redox species,[242] and some detection of small molecules (neurotransmitters, nucleotides, amino acids and peptides).[243–245]

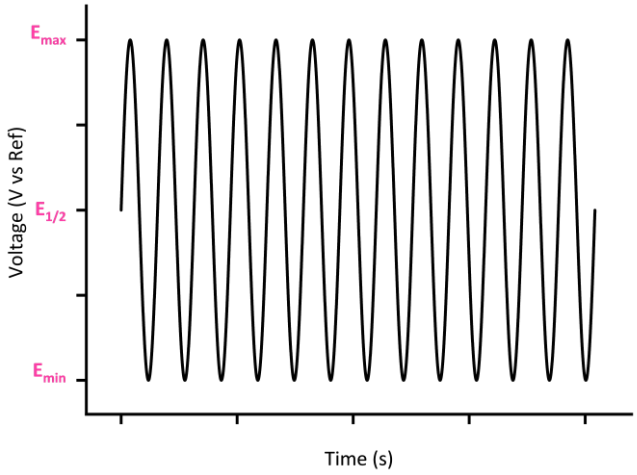

Figure 4.3. *Potential waveform applied in a PSV experiment, highlighting minimum, maximum, and midpoint potential ($E_{minimum}$, $E_{maximum}$, and $E_{1/2}$).*

$$E_{app}(t) = E_{1/2} + \Delta E \sin(\omega t + \eta) \qquad \textit{Equation 4.4}$$

$$\text{where: } E_{1/2} = \frac{E_{max} + E_{min}}{2} \qquad \textit{Equation 4.5}$$

Alongside collaborators, the author has been a contributor in using PSV measurements to enable improved parameter inference in both chemical and biological systems.[239,240] This work used DCV, FTV, and PSV experimental data to inform Bayesian parameter fitting of surface-confined reversible electron-transfer systems. The advantage of PSV in this context is that the computational requirements for simulating and modelling data are significantly lower for PSV compared to FTV.[239] In sensing, PSV may provide a higher level of sensitivity due to the large amplitude applied in the voltage waveform resulting in larger current outputs. The aim of this chapter is to test if there are advantages to using PSV when interrogating binding events.

4.1.3. Applying these techniques in sensing

Until recently the large amplitude ACV techniques have relied upon bespoke homebuilt instruments limiting their applications. However, a recent paper presented a practical guide to FTV that describes the use of commercial instruments to apply these waveforms.[234] This advancement in instrumentation is crucial when considering using these methods commercially. Within the sensing literature, FTV has been used for DNA sensing, examining the electrostatic repulsion of $[\alpha\text{-}SiW_{12}O_{40}]^{4-}$ following DNA hybridization and for detecting the binding of SH3 (SRC Homology 3 domains) to viologen-labelled SHIRT (*Streptococcus* High Identity Repeat Tandem) proteins.[246,247] These sensors and the PSV sensing performed in the late 1990s and early 2000s examine how harmonic response changes with analyte concentration.

4.2. Aims

This chapter aims to incorporate FTV and PSV into the galectin-3 biosensor toolkit and explore the advantages these methods can provide. To achieve this, several objectives will be explored:

1. Confirming the hypothesis that the diazonium-mediated electrografting approach renders the sensing stable to wide voltage sweeps.
2. Using ACV techniques to measure the galectin-3 binding to the glycofluoroform and compare these results to previously obtained EIS data.
3. Performing comparative label and label-free FTV and PSV experiments to establish if these techniques could be applied in label-free measurements for the first time.

4.3. Results and Discussion

4.3.1. Sensors based on an electrografted TABD-P-GFF scaffold are compatible with FTV detection of galectin-3 binding

The TABD-P-GFF scaffold was investigated with FTV detection methods. Evidence of a successful graft is observed in both the CVs obtained during the electrografting process (**Figure 4.4(a)**) and the comparison of current response of the solution-based potassium ferricyanide in FTV experiments carried out before and after the grafting process (**Figure 4.4(b)**). The FTV current response shows a large increase in capacitive current following grafting which correlates with the EIS changes after electrografting demonstrated in chapter three. The electrografting process will increase the effective electrode size increasing the charge storage capacity and therefore it is observed as an increase in capacitance.

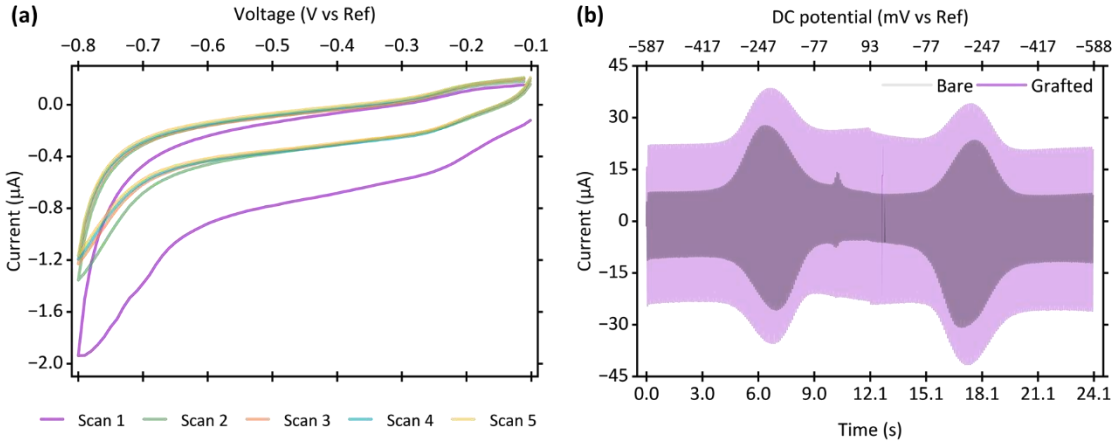

Figure 4.4. *(a) Electrograft of TABD-P-GFF shows characteristic diazonium electrografting shape and (b) comparison of current response for bare (grey) and grafted (purple) SPEs. CVs were collected by scanning between -0.1 to -0.8 V vs Ag covered in AgCl at 20 mVs^{-1} for 5 scans. FTV experiments were collected by scanning between -0.6 and 0.1 V vs Ag covered in AgCl with a linear scan rate of 60 mV s^{-1}. The sinusoid has an amplitude of 80 mV and a frequency of 9 Hz. For (b) the solution in 10 mM $K_3[Fe(CN)_6]$ in pH 7 buffer (100 mM sodium phosphate, 233 mM sodium chloride).*

As discussed in chapter two, scaffolds based on gold-thiol bonds are unstable when large voltage windows are employed in CV measurements. This 'stripping' effect is observed via a decreasing ΔE for a solution $[Fe(CN)_6]^{4-/3-}$ couple as scan number increases (**Figure 4.5(b)**). However, when similar scans are performed on a C-SPE where the P-GFF is immobilised via triazabutadiene-mediated electrografting, there is no change in ΔE with scan number (**Figure 4.5(a)**). This shows the covalent linkage is more stable and should withstand the voltage waveforms applied during ACV measurements.

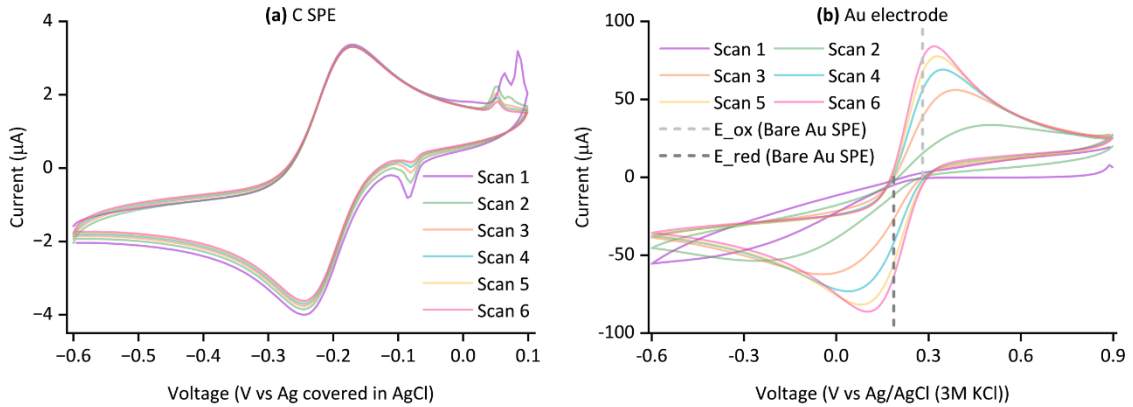

Figure 4.5. *Successive CVs on a modified (a) C-SPE and (b) Au disc electrode both in solutions of 10 mM $K_3[Fe(CN)_6]$ in pH 7 buffer (100 mM sodium phosphate, 233 mM sodium chloride). For (a) the voltage was cycled between -0.6 to 0.1 V vs Ag covered in AgCl at 52.15 mV s^{-1}. For (b) the voltage was cycled between 0.9 to -0.6 V vs Ag/AgCl (3M KCl) at 100 mV s^{-1}.*

A set of galectin-3 titration experiments were performed on TABD-P-GFF modified SPEs studied with both potassium ferricyanide and hexaammineruthenium(III) chloride solution redox probes. The second harmonic for each concentration is shown for the galectin-3 binding response observed through probing potassium ferricyanide redox chemistry (**Figure 4.6(a)**) and through probing hexaammineruthenium(III) chloride redox chemistry (**Figure 4.6(b)**). To compare the binding response, an oxidative faradaic current was extracted for harmonic 2 by averaging the maximum values of the two peaks observed in the oxidative sweep. As expected, based on the EIS results reported in chapter three, the relationship between maximum current and galectin-3 concentration displays positive correlation for potassium ferricyanide and negative correlation for hexaammineruthenium(III) (**Figure 4.6(c)**). This is because there is an inverse relationship between resistance to charge transfer and observed current. As previously stated, observing a signal increase on binding is preferable to observing a signal decrease so galectin-3 binding will be studied with potassium ferricyanide in the remaining experiments.

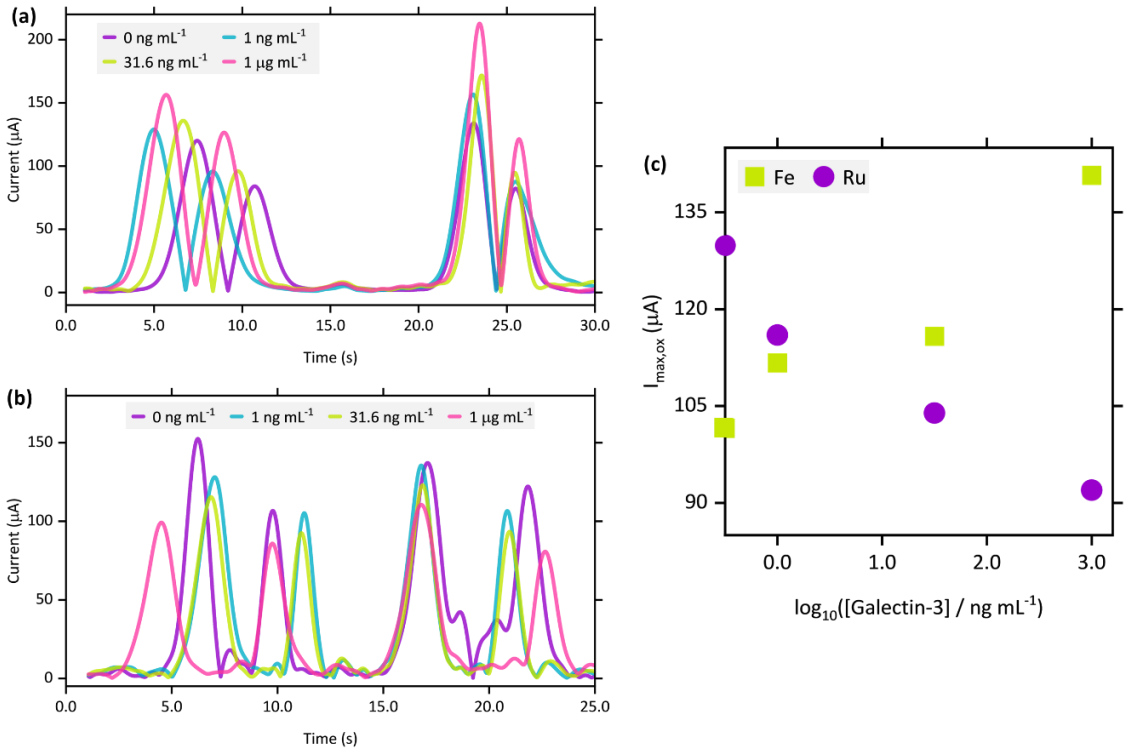

Figure 4.6. *2nd harmonic for galectin-3 binding studied with (a) potassium ferricyanide and (b) hexaammineruthenium(III) chloride and (c) extracted oxidative current from these harmonics. The points plotted on the y-axis represented the response after electrografting (i.e. the response at 0 ng mL^{-1}).*

As discussed in the introduction, changing the parameters of the FTV experiment helps to 'tune in' to specific electron-transfer kinetic regimes. In this case, the dynamics of the galectin-3 binding event and the resultant increase in potassium ferricyanide electron transfer current. The same titration experiments as above were run with sinusoids with all permutations of a frequency of 4, 9, or 12 Hz and an amplitude of 50, 100 or 150 mV in potassium ferricyanide. A signal enhancement factor was calculated by comparing the maximum current after incubation in 1 ng mL^{-1} and 31.6 ng mL^{-1} galectin-3 solutions (**Table 4.1**). The currents were extracted from harmonic 1 to simplify data processing and the two lower concentrations were used as it is preferable to optimise at lower concentrations for sensing applications. There is not a significant difference in signal enhancement in the parameter space explored, and so the combination of a frequency of 9 Hz and an amplitude of 100 mV was selected. Measurements at 50 mV and 9 or 12 Hz outperformed the selected conditions slightly, but this lower amplitude reduces the maximum accessible harmonic which may contain important information.

Table 4.1. *Signal enhancement factors calculated for a range of FTV sinusoid parameters. The signal enhancement factor is calculated by:* $\frac{maximum\ current\ after\ 31.6\ ng\ mL^{-1} incubation}{maximum\ current\ after\ 1\ ng\ mL^{-1} incubation}$*. The table is shaded with light hues corresponding to minima and dark hues corresponding to maxima.*

Amplitude / mV	Frequency / Hz		
	4	9	12
50	1.006	1.119	1.151
100	1.088	1.109	1.080
150	1.024	1.069	1.067

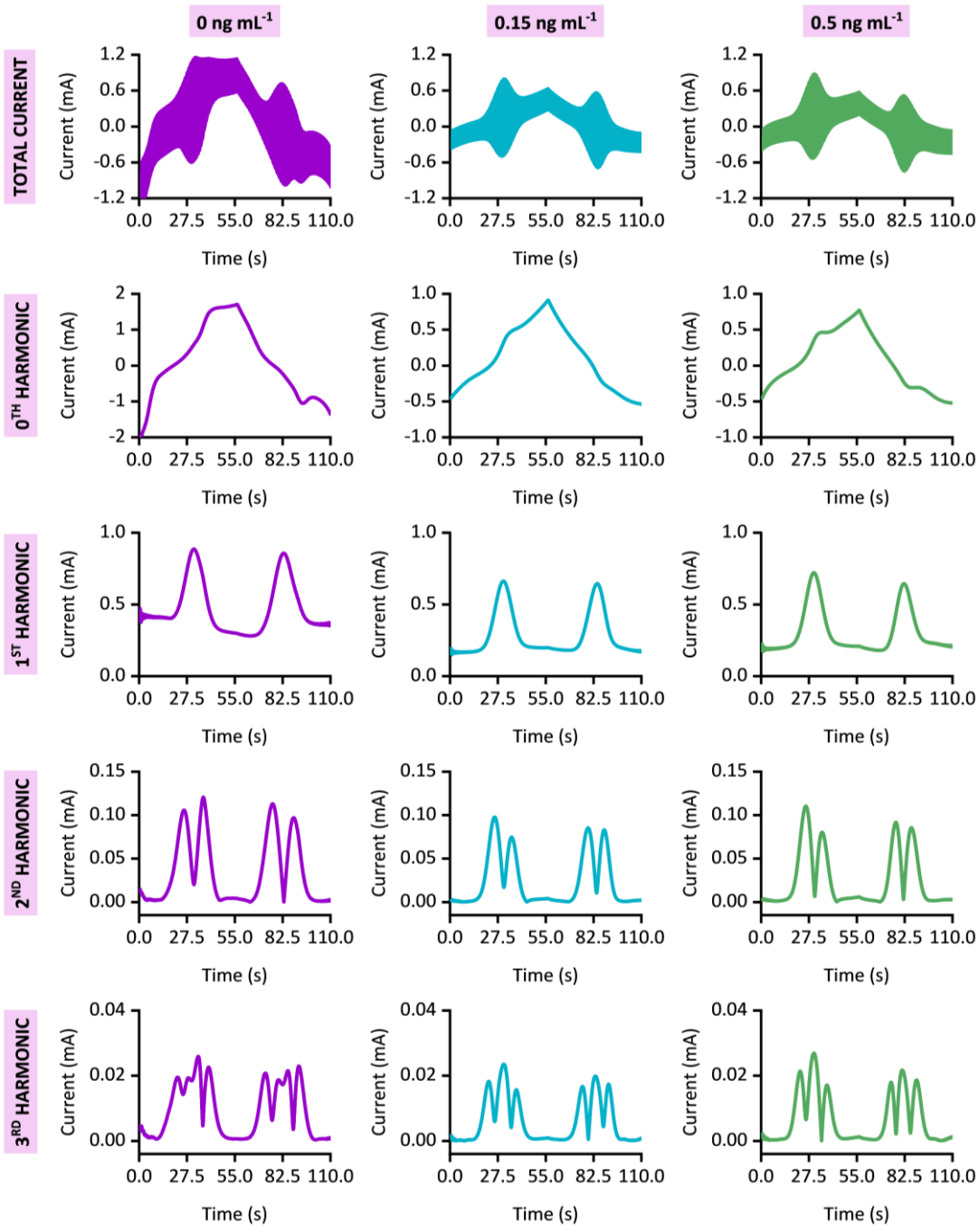

Figure 4.7. *Resultant (top to bottom) FTV time-current and 0th – 3rd harmonic plots for a galectin-3 titration experiment (increasing concentration from left to right). FTV measurements were performed in*

the presence of 10 mM $K_3[Fe(CN)_6]$ in pH 7 aqueous buffer (100 mM sodium phosphate, 233 mM sodium chloride) scanning between -300 and 500 mV at 14 mV s^{-1} with a sinusoid of amplitude 100 mV and frequency 9 Hz.

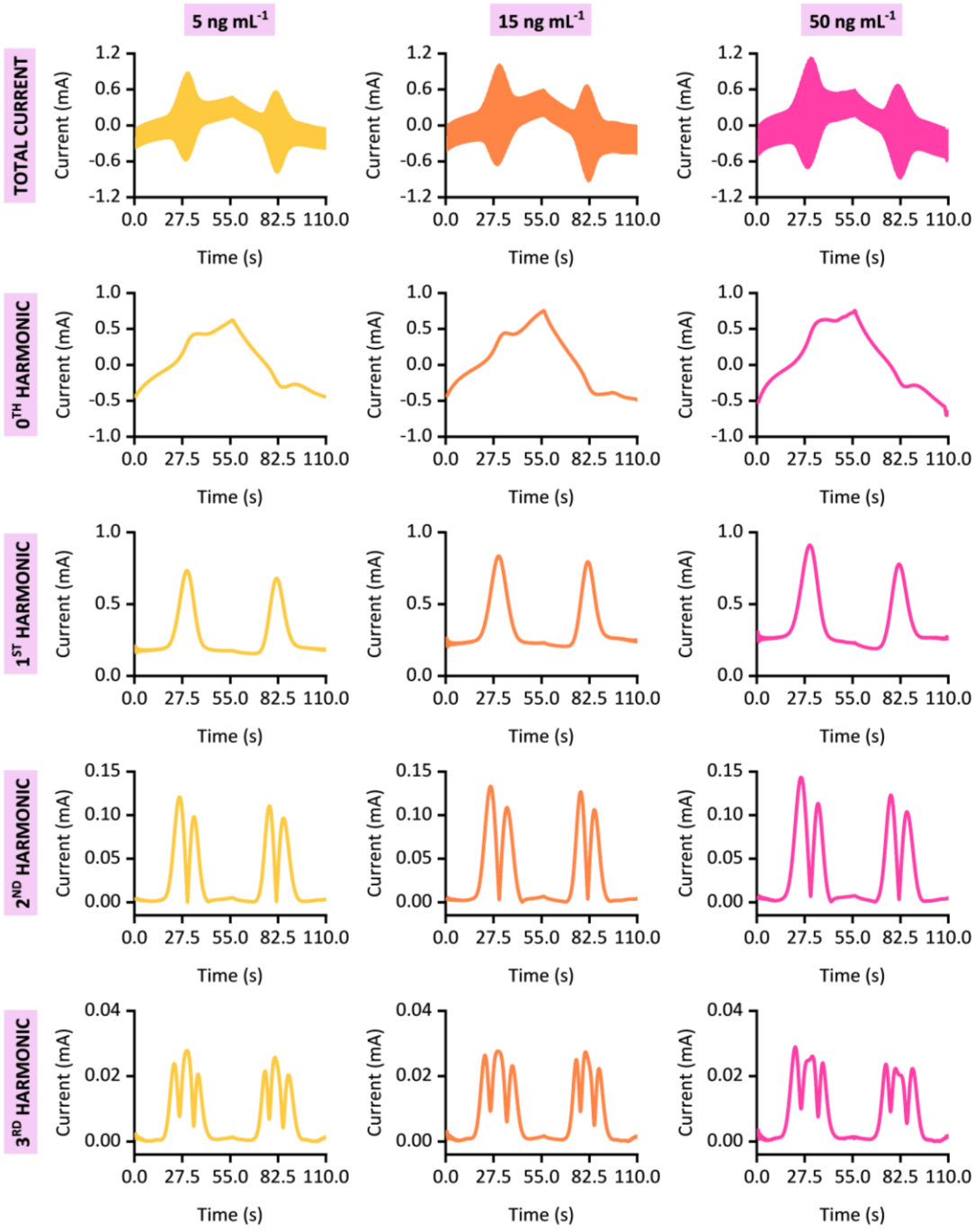

***Figure 4.7**. ctd.*

Having screened the FTV experimental parameters, galectin-3 titration experiments were conducted in a similar manner to those performed in previous chapters (**Figure 4.7**). There is an increase in the observed current as the concentration of galectin-3 is increased, this is observed not only in the harmonics but also in the total current plots. Harmonic 1 also contains non-faradaic contributions, as shown by a non-zero value of current outside the

faradaic region. The increased sensitivity of an FTV experiment compared to a DCV experiment is shown in **Figure 4.8**. The overlay of the oxidative time-current response (**Figure 4.8(a)**) shows distinct responses at different concentrations of galectin-3, and these differences are primarily seen in the faradaic region. However, when considering the 0^{th} harmonic (**Figure 4.8(b)**) the current-time responses display significant overlap and there isn't an obviously clear relationship between signal magnitude and galectin-3 concentration. The 0^{th} harmonic is essentially the current response to the voltage sweep with a 0 Hz sinusoid and therefore it can act as a pseudo-DCV experiment. From the comparison of the two experiments the enhanced sensitivity of FTV is shown. As mentioned above, the concentration-dependent current increase is observed in both the total current and the higher harmonics. Choosing to analyse the effect of concentration on the total current removes the need for the Fourier transform processing and thus reduces the computational demand that would be required for a device to use these methods in a clinical setting. Therefore, for the remainder of this section the galectin-3 response will be assessed using information extracted from the total-current response.

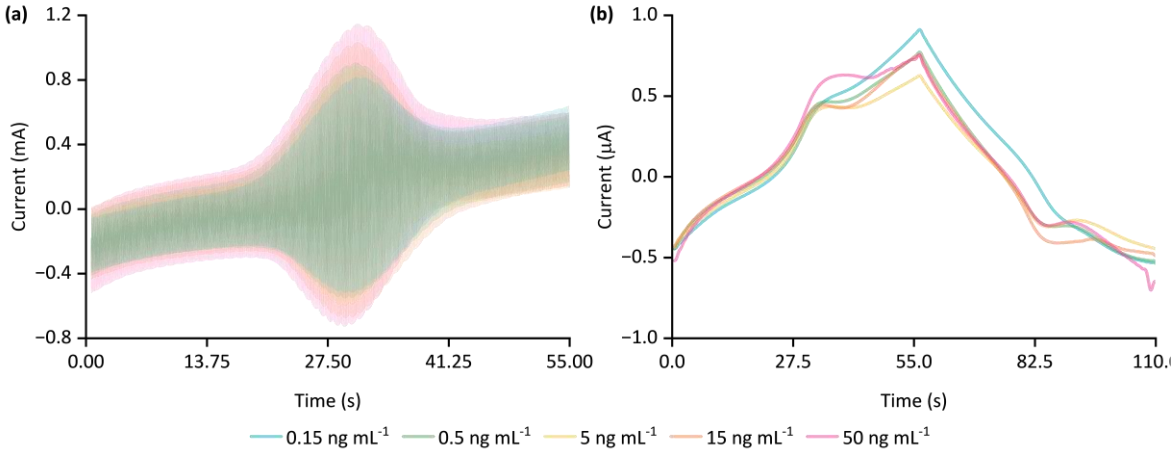

Figure 4.8. *Comparison of (a) total current-time response from an FTV experiment and (b) the 0^{th} harmonic. Only the oxidative sweep is shown in (a) for increased clarity due to the large number of datapoints resulting in highly dense overlays making it challenging to compare datasets even when transparency is increased.*

To analyse the binding response, the faradaic current was extracted from the current-time response of each experiment. This was estimated by taking the difference in the maximum and minimum value of the current in the oxidative peak to get the total current. The average of the current in the 'flat' region before and after the oxidation event was subtracted from

the total current to get the faradaic current. This processed is explained in **Figure 4.9** and Equation 4.6.

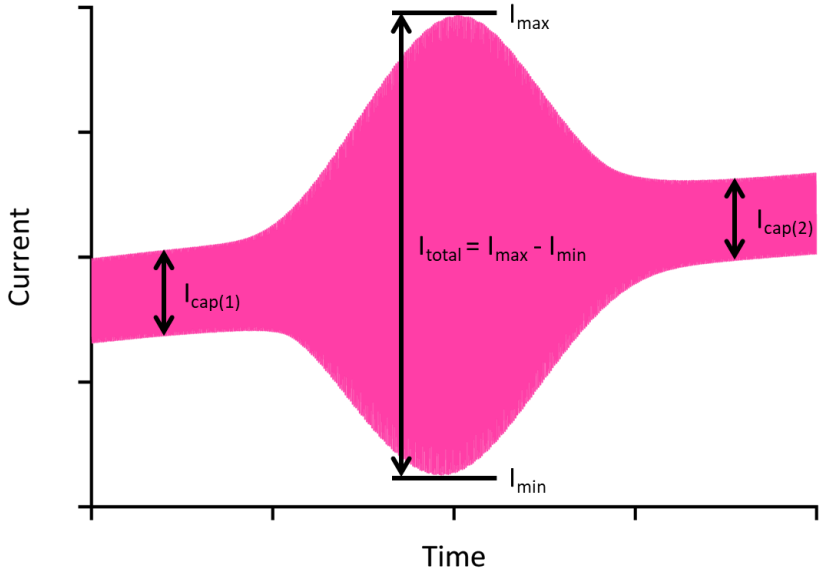

Figure 4.9. *Schematic figure showing the current extraction process (along with Equation 4.6) following FTV galectin-3 binding experiments.*

$$I_{faradaic} = I_{total} - \left(\frac{I_{cap(1)} + I_{cap(2)}}{2}\right) \qquad \textit{Equation 4.6}$$

A series of galectin-3 titration experiments were performed on a range of TABD-P-GFF modified SPEs and the extracted faradaic current is plotted against the galectin-3 concentration (**Figure 4.10**). A clear positive binding relationship is observed throughout these repeats. Detection was observed at 5 pg mL^{-1}, plots 10 and 11 on **Figure 4.10**, the zero-points are not shown due to the logarithmic scale of the graph but for the two experiments that considered this concentration the extracted faradaic currents at 0 pg mL^{-1} were 0.218 and 0.151 mA and at 5 pg mL^{-1} were 0.865 and 0.912 mA respectively). The detection of these lower concentrations suggest FTV would be a suitable method for screening patient samples as galectin-3 levels in patient samples are typically in the low nanogram to sub-nanogram per millilitre range. Further repeats would be required to fully elucidate the detection limits and quantify the binding response, but the data presented in **Figure 4.10** shows the promise of applying FTV in sensing.

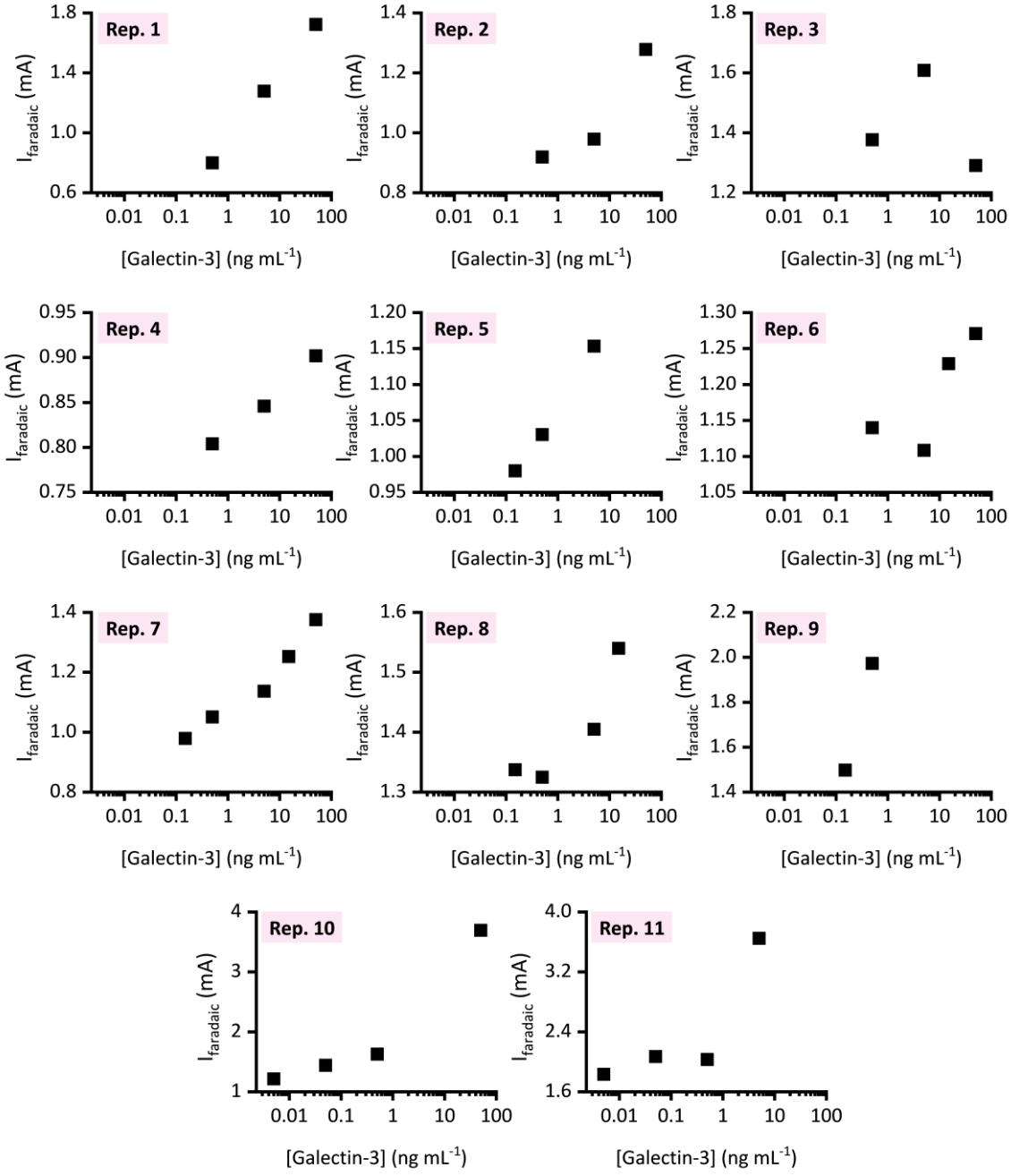

Figure 4.10. *Extracted oxidative faradaic current from the time-current response following a series of galectin-3 titration experiments for 11 repeats. The concentration range studied spans from 5 pg mL^{-1} to 50 ng mL^{-1}. FTV experiments were cycled between -0.3 and 0.5 V with an amplitude of 100 mV and a frequency of 9 Hz. Repeat numbers as referenced in-text are provided in the top-left corner of each plot.*

The results in **Figure 4.10** are not yet at the stage to fully quantify the binding relationship through measurements made with FTV. However, **Figure 4.11** suggests an approach that is likely to yield an accurate analysis. An overlay of all the datasets is provided in **Figure 4.11(a)**, this shows the expected variation due to electrode-to-electrode differences in extent of modification. Qualitatively, this data does seem less variable than data collected

on both Au-SPEs and C-SPEs by EIS, however, this observation has not been statistically confirmed. A similar filtering approach to those carried out in previous chapters where electrodes with the most similar responses were pooled was executed, this selected the six datasets in **Figure 4.11(b)** – repeat 2, 4, 5, 6, 7, and 8. As well as filtering the datasets at this stage, a normalisation step was taken. All of these datasets contain a measurement corresponding to incubation in a solution of 0.5 ng mL^{-1} galectin-3; for each electrode the current response following every incubation was divided by the value at the 0.5 ng mL^{-1} stage. This yields the normalised current plotted in **Figure 4.11(b)** and does reduce the variation between repeats to a degree. Following this, a pseudo binding proportion was calculated, "θ", this was achieved by defining the response at 0.5 ng mL^{-1} as 0 and the response at 50 ng mL^{-1} as 1. This was possible for four repeats – repeats 2, 4, 6, and 7 (**Figure 4.11(c)**). This pseudo-binding response show these titration experiments are in the appropriate range. However, no K_d analysis is performed as we have selected the minimum and maximum values. Further experiments at the two extremes of the titration range are needed to find the detection limit and saturation point to fully quantify FTV detection of galectin-3 binding.

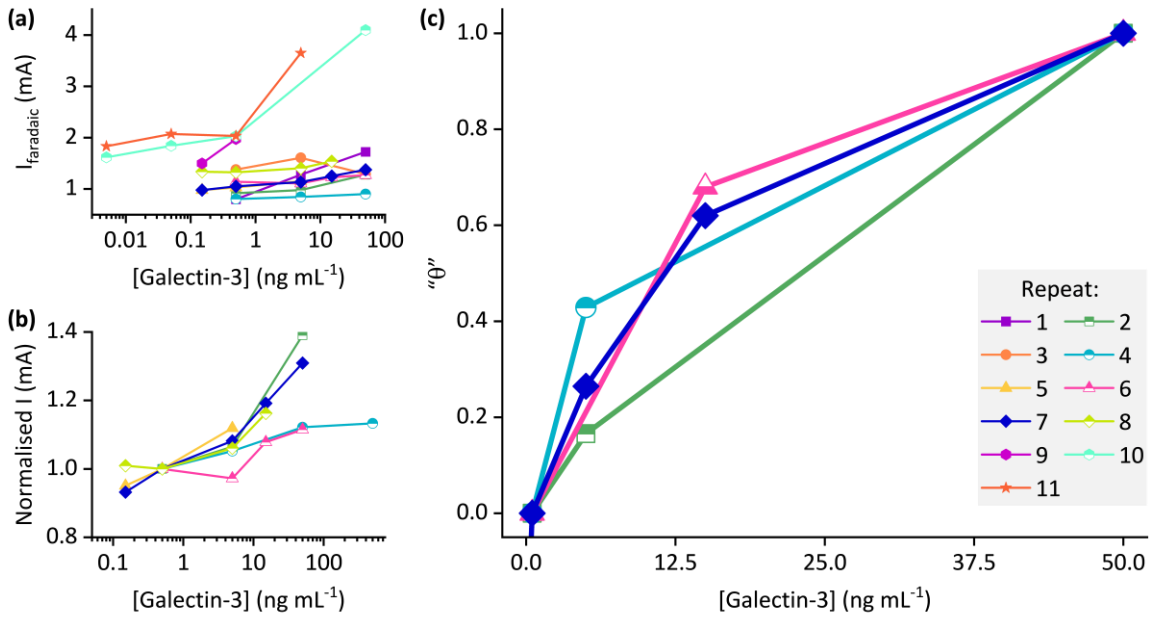

Figure 4.11. *Preliminary modelling of the binding response. (a) Overlay of the data presented in* ***Figure 4.10****, (b) normalised current response following the filtering process, and (c) approximation of the proportion of binding ("θ") for four modified SPEs.*

4.3.2. BSA titration experiments show the potential of label-free detection

BSA binding experiments were performed as a proof of concept to prove the ability of the ACV techniques to detect binding events and to explore the possibility of label-free detection. Label-free detection is advantageous due to having a lower cost as there are no additives, fewer user steps, and it can simplify storage requirements and quicken analysis.[248,249] For these studies, two SPEs were incubated in four BSA concentrations (1, 10, and 100 ng mL^{-1} and 1 μg mL^{-1}). FTV and PSV measurements were performed at after each incubation. For one electrode the electrolyte was spiked with a redox probe and for one electrode the electrolyte was free of redox probe. A current maximum was extracted for each harmonic and plotted against BSA concentration (**Figure 4.12**). Generally, there is an increase in the current observed as BSA concentration increases. These experiments were performed with hexaammineruthenium(III) chloride which contains a positively charged ruthenium complex. As more BSA non-specifically binds to the electrode there is an accumulation of negative charge at the electrode surface. This is because BSA is negatively charged above its isoelectric point – the isoelectric point for BSA is 4.7 and these experiments were performed at pH 7.[250] There will be electrostatic attraction between the negatively charged surface and positively charged solution ruthenium complex ions. This will decrease resistance to electron transfer resulting in an increase in observed current. Generally, this expected increase is observed for harmonics in both FTV and PSV, and, label and label-free experiments. The first and second harmonics are the most consistent across the experiments. In the higher harmonics of the labelled experiments the trends are slightly inconsistent. Particular issues are observed with the highest concentration of the labelled FTV experiments (**Figure 4.12(a)**) and the lowest concentration of the labelled PSV experiments (**Figure 4.12(b)**) being too low or too high to fit the trend, respectively. Whereas, for the label-free experiments (**Figure 4.12(c)** and **(d)**) all harmonics show the expected trend aside from harmonic 4 of the label-free FTV experiment. It should be noted that although the experiments are over the same concentration range, the label-free experiments appear to be reaching saturation. These are single repeats so this conclusion cannot be made with absolute confidence, but it appears that it is likely that label-free measurements will reach an upper detection limit before labelled measurements. This is suggestive that once the sensor has reached a high level of non-specific adsorption the

capacitance changes will become less detectable as the adsorbed layer grows. However, generally the lower detection limit is more important to sensing applications.

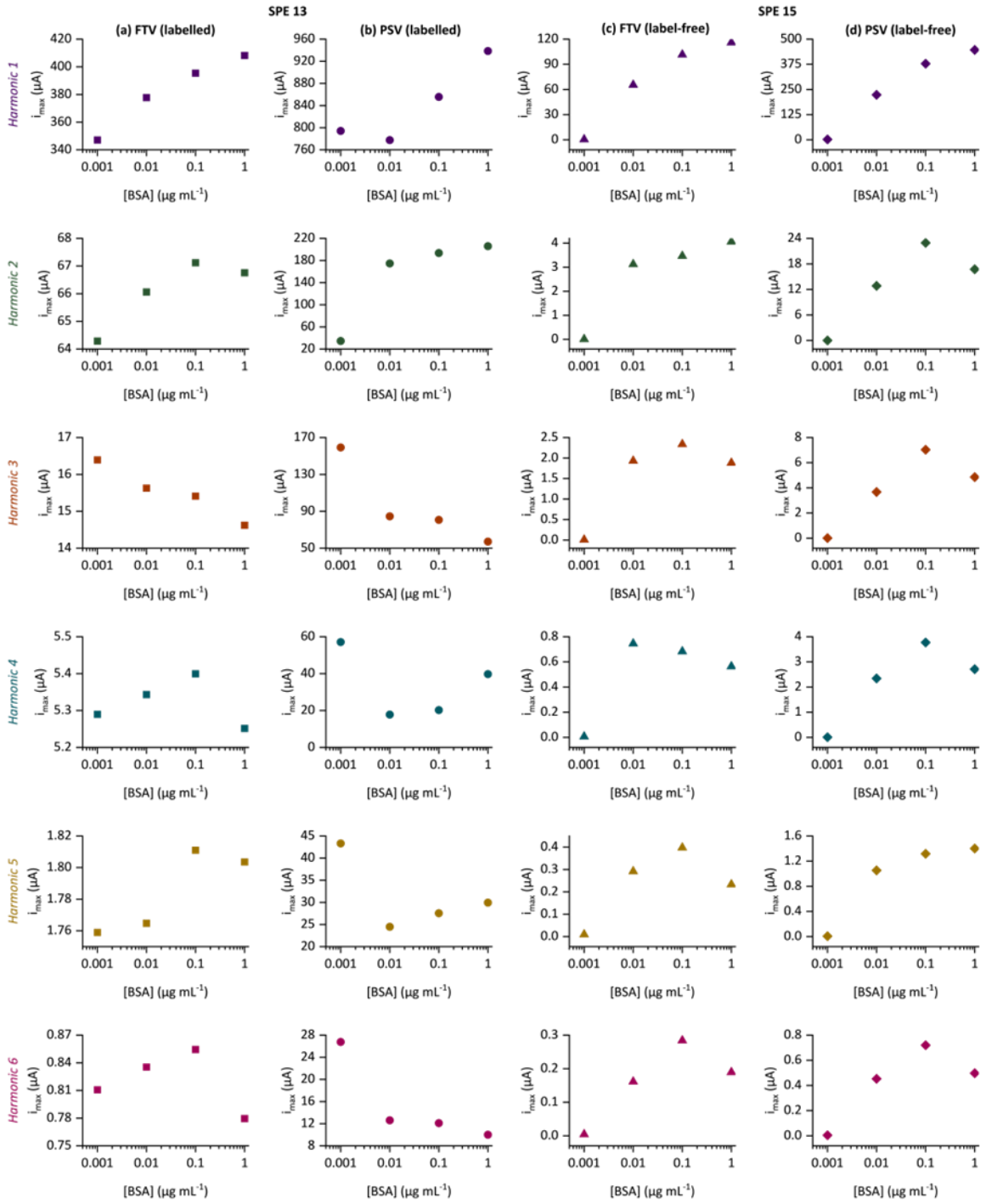

Figure 4.12. *Extracted i_{max} values for harmonics 1 – 6 (purple, green, orange, blue, yellow and pink symbols respectively) of FTV (a,b) and PSV (b,d) experiments for: (a,b) a BSA titration carried out in the presence of a redox probe (FTV data: squares, PSV data: circles) and (c,d) a BSA titration carried out in the absence of a redox probe (FTV data: triangles, PSV data: diamonds).*

These proof-of-concept experiments show the possibility of label-free detection with these ACV measurements. In particular, PSV shows promise due to its consistent increase in

current response observed throughout the harmonics. PSV experiments result in a higher observed current due to a larger applied amplitude compared to the amplitude applied in FTV. This is helpful for label-free experiments as the overall current is lower in label-free experiments compared to labelled experiments (comparison of equivalent harmonics of (a) and (c) and (b) and (d) in **Figure 4.12**) as capacitive contributions are lower than faradaic contributions. This means that PSV may increase sensitivity over FTV in label-free methods. The amplitude that can be employed in FTV experiments is limited as the DCV ramp needs to span the entire voltage window of the redox couple, so adding the FTV amplitude to this range could enter the region of solvent breakdown. However, the use of PSV will limit the usage of higher harmonics for the label-free experiments as non-faradaic contributions are constrained to lower harmonics. Therefore, both techniques have advantages and disadvantages so the choice of technique will depend on the exact sensing requirements.

4.4. Summary, conclusions and future work

This work presents a clear advancement in the biosensing of galectin-3 with electrochemical methods. Firstly, the triazabutadiene-mediated electrografting method confers the required stability of the GFF immobilisation to enable the study of this system with FTV. Successful detection of galectin-3 binding via FTV measurements has been proven. The lowest detected concentration was 5 pg mL^{-1}, showing the using FTV measurements to detect concentrations below the typical level found in patient samples. This highlights that FTV is a highly sensitive method which shows promise in biosensing.

PSV shows particular promise for label-free detection. The proof-of-concept experiments analysing BSA binding showed the observed harmonic current consistently increased with BSA concentration, proving capacitance is sensitive to non-specific adsorption, and therefore likely to be able to be applied to monitor specific binding events. Both ACV methods, but particularly PSV, are quicker to run than EIS measurements with the methods running in seconds opposed to minutes.

However, this work does require further development to comprehensively explore the application of ACV in biosensing. The binding response needs to be fully assessed which requires further repeats across a wide concentration range. This is likely to require conducting each experiment on different modified SPEs and constructing a calibration curve for the whole population opposed to assessing each individual SPE's binding response.

However, the amount of GFF accessible at one time limits the feasibility of these experiments. This individual comparison has been briefly explored in other sensing systems which is detailed in chapter five.

The process of collecting and analysing data could be further optimised. For example, employing a linear oxidative oscillating sweep would further reduce measurement time. These quicker measurements, as well as being more industrially attractive, reducing both time and data storage requirements, could allow for some inference of binding kinetics to give a greater understanding of the interactions at the sensor surface. In terms of the analysis, a more in-depth study needs to be performed to identify further trends between galectin-3 concentration and extractable experimental parameters. There appears to also be a potential dependence as seen in the shifting peak positions in **Figure 4.6**. However, the time constraints of this work led to the focus on changes in current, especially due to the relationship of observed current with the parameter extracted from EIS analysis (R_{ct}). Fully characterising these complexes relationships could help to normalise electrode-to-electrode variation.

One way to approach further quantification of this system would be to use the modelling approaches akin to those performed when interrogating confined ferrocene and cytochrome species.[239,240] Within the Parkin group, this analysis has only been used for surface-confined species not solution-based species, therefore the code was not available to allow the author to conduct simulations for this solution-based work. However, this fully parameterised analysis described by the equations governing electron transfer is physically meaningful and non-ambiguous – in contrast with equivalent circuit fitting which is semi-empirical. This would provide greater insight, especially regarding the voltage dependence observed in **Figure 4.6**, and should distinguish between specific and non-specific binding. This would be invaluable when exploring the binding response in real patient samples.

Chapter Five: Future perspectives and conclusions

5.1. Further development

As established in chapter four, further experiments need to be performed over a wider concentration range to fully characterise the galectin-3 binding response. Following this, the aim is to publish the demonstration of covalent immobilisation of the polymer-glycofluoroform via triazabutadiene-mediated elecrografting, and compare the measured binding response from electrochemical impedance spectroscopy with that from Fourier transformed alternating current voltammetry. Beyond this, there is potential to further develop the analysis of Fourier transformed alternating current voltammetry experimental data using modelling to extract multiple parameters that fully describe the electron transfer parameters of the solution-phase redox probe.

Importantly, the increased surface coverage of the glycofluoroform achieved by immobilisation onto a carbon electrode means the sensitivity is now high enough to explore the response to patient samples. Some passivation towards non-specific binding has been explored through BSA experiments performed in chapter three, but complex patient samples may pose further challenges. As established in chapter one, the priority would be to test samples from patients with prostate cancer, thyroid cancer, or heart failure.

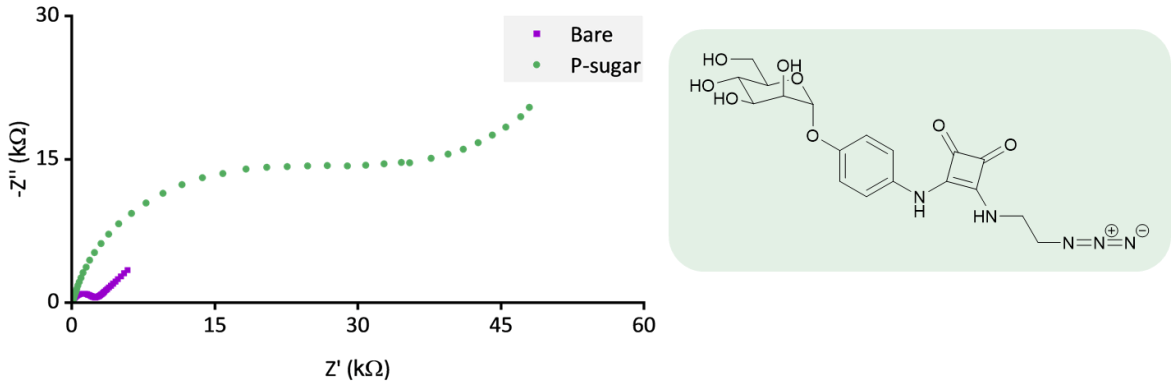

Figure 5.1. *Nyquist plots showing the difference between the response of a bare (purple) and a polymer-sugar (green) modified SPE. Inset: Structure of the squarate mannoside probe with high affinity for FimH.*

Also, further glycofluoroforms could be explored, when this research began the enhanced sensitivity of the glycofluoroform we have studied had recently been published and was one of the first examples of glycofluoroforms in the literature.[84] However, this field has developed significantly and during this PhD, a study has been published where 150 glycofluoroforms were synthesised, 24 on a preparative scale.[77] These ligands are potential

biomarkers of pancreatic, lung, and colorectal cancer.[251] Therefore, there is great potential in exploring these sugars as additional glycofluoroforms candidates for electrochemical sensing. Aside from glycofluoroforms, other unnatural sugars could also be explored. The goal of this approach is that it should be straightforward to use different sugars to target new analytes as long as they have a motif that can be used to immobilise the sugar onto an electrode. Hatton *et al.* have explored squarate mannoside probes (**Figure 5.1**) with high affinity for FimH, a glycoprotein present on the surface of uropathogenic *E. coli*.[252] A sample of one of these probes, p-[((1-amino-2-azidoethane)-2,3-dioxocyclobut-1-enyl)amino]phenyl α-D-mannopyranoside was kindly provided for testing to the author by Dr N. Hatton (University of York). This molecule contains an azido group allowing the polymer conjugation and subsequent immobilisation onto gold electrodes to be performed. The Nyquist plots (**Figure 5.1**) show successful immobilisation of this sugar. Further work was not performed; however, this squarate mannoside sugar would enable the exploration of non-protein target analytes. This could be of particular interest for examining through label-free detection, as the binding of a large molecule should induce a large surface change.

Covalent immobilisation using triazabutadiene molecules results in a highly stable surface. This surface was stable in solution for several days as shown through the surface-clicked ferrocene studies. Therefore, the enzymatic synthesis of the glycofluoroform, or other sugars, could be performed on the electrode. As shown in **Figure 5.2,** we propose that the action of BiGalHexNAcP could attach the fluorinated and phosphorylated galactose to the acceptor sugar that has already being immobilised onto the surface via a polymer-triazabutadiene linkage. This would likely reduce the reaction time because only a small volume of enzyme would be required, which makes it viable for the enzyme concentration to be significantly higher than what is currently possible. Additionally, the complete separation of glycofluoroform and acceptor sugar in size exclusion chromatography is very challenging, as described in chapter two, but on-electrode synthesis removes the need for this separation. Instead, the electrode can simply be washed. This conserves both sugars and removes a time-consuming process from the sensor construction workflow. If this was successful, it could enable electrochemical screening of libraries of sugars, where previously

the requirement for individual purifications would make this very challenging to achieve on a reasonable timescale.

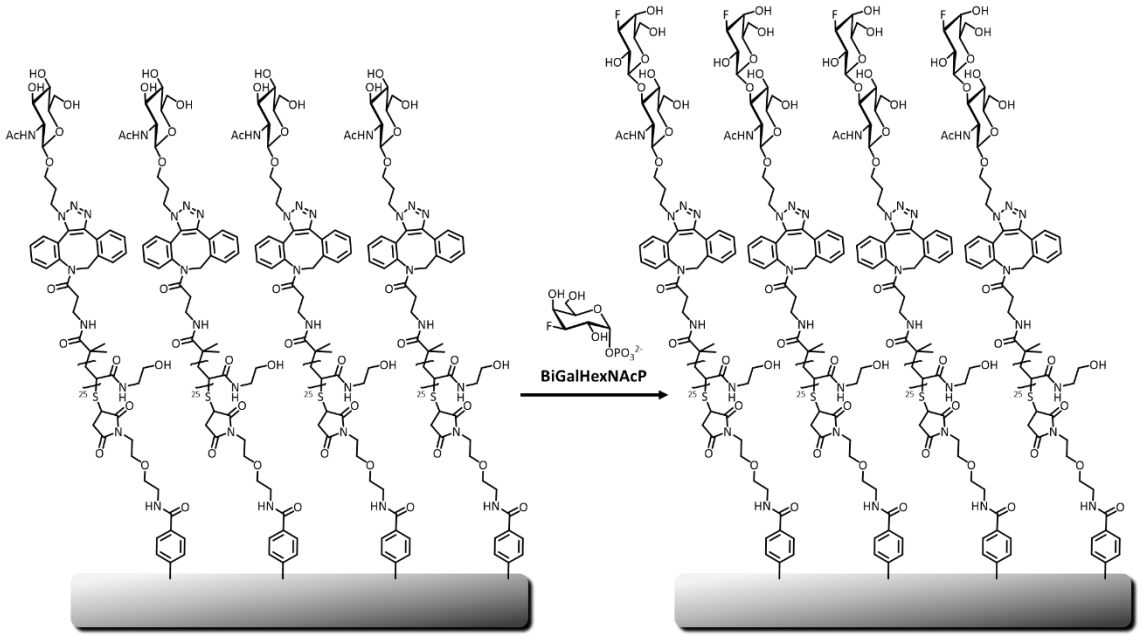

Figure 5.2. *Schematic demonstrating the proposed on-electrode glycofluoroform synthesis.*

In addition to the focus of exploring glycofluoroform-galectin-3 sensing throughout the duration of the PhD, secondary studies have been performed with the focus of applying FTV in commercial sensing settings through collaboration with two electrochemical sensing companies. Full details regarding the studied systems are omitted due to confidentiality, but the ways in which FTV was employed to analyse these systems is described.

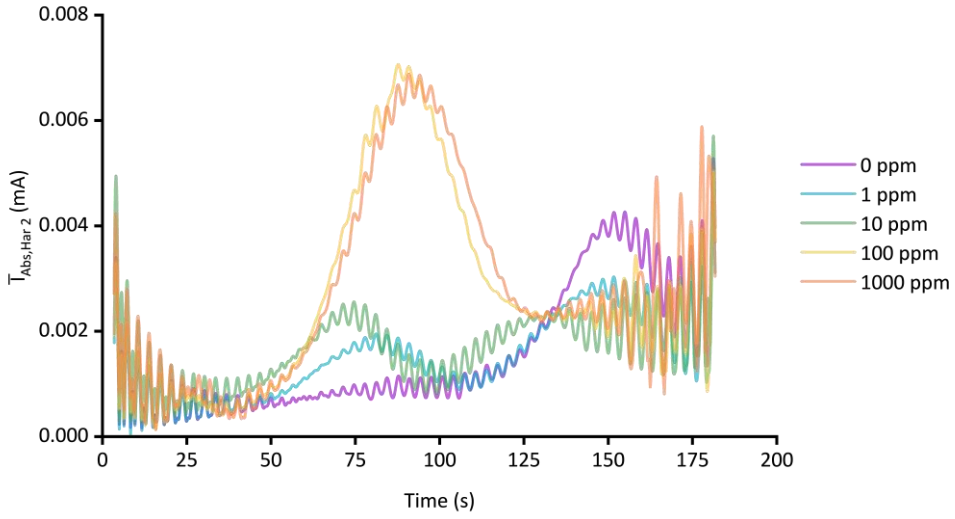

Figure 5.3. *Average (n=3) absolute current extracted from harmonic 2 for a range of concentrations of fuel marker. FTV measurements were performed scanning from 400 to 1150 mV at 4 mV s^{-1} with a sinusoid of amplitude 50 mV and frequency 3 Hz. Data collected by Niamh Burhouse, a summer intern supervised by the author.*

With the first company, the ability of FTV to detect a fuel marker in a complex electrolyte mixture which included petrol was studied. The electron transfer of the fuel marker is slow, so a low frequency, slow scan rate method was employed, and the second harmonic was analysed. As the concentration of fuel marker increases, the observed harmonic current also increases, reaching saturation at 100 ppm (**Figure 5.3**). This method detects extremely low levels of fuel marker, (1 ppm) particularly when compared to that observed in parallel linear sweep voltammetry, (4 ppm, data not shown). Decreasing the required quantity of fuel marker would mean a significant reduction in cost to the company. Also, with a simple averaging of three repeats, there was high reproducibility observed throughout all the experiments, conducted across different electrodes, showing distinct responses at each concentration.

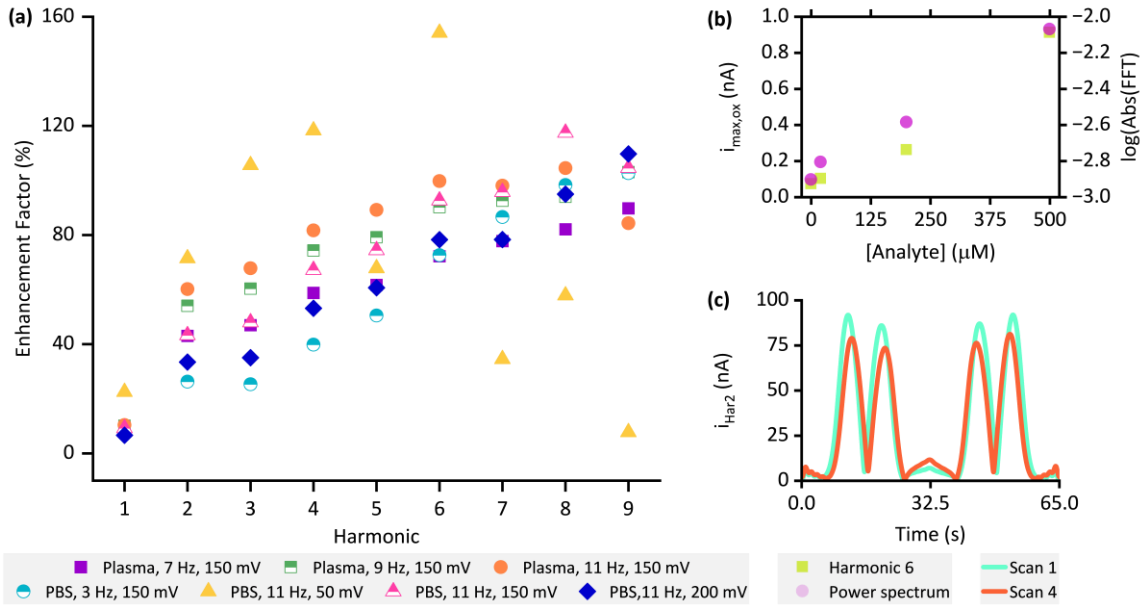

Figure 5.4. *(a) Signal enhancement factors for a range of FTV sinusoid parameters comparing measurements at 200 µM and 20 µM, (b) relationship between analyte concentration and maximum oxidative current from harmonic 6 (lime squares) or magnitude of power spectrum at 66 Hz (magenta circles), and (c) comparison of harmonic 2 response after one (blue line) and four (orange line) scans.*

$$Enhancement\ Factor = \left(\frac{I_{200\ \mu M} - I_{20\ \mu M}}{I_{20\ \mu M}}\right) \times\ 100\% \qquad Equation\ 5.1$$

With the second company, FTV was used to explore the binding of an analyte by a redox-labelled aptamer. This system uses a thiol-terminated methylene blue-modified aptamer, immobilised onto gold screen-printed electrodes to detect a small molecule via square wave voltammetry. A range of parameters were screened to investigate the signal enhancement between measurements at 20 and 200 µM of analyte, which are considered to be the lower

and upper biological limits, respectively. The enhancement factor was calculated as described in Equation 4.6, and **Figure 5.4(a)** shows that the optimal parameters are when using a sinusoid with a 50 mV amplitude and a frequency of 11 Hz. For a set of experiments where the concentration of analyte was varied, the oxidative current maximum of harmonic 6 was compared with the magnitude of the power spectrum at the equivalent frequency (66 Hz, **Figure 5.4(b)**). A similar response is observed for both parameters, but the power spectrum requires a much smaller file size than the harmonic – 250 vs 90000 KB, respectively. Although not yet extensively examined, the fact that the power spectrum may contain the required information in considerably less data could be important for commercial applications. Finally, in this preliminary work, the sensor stability was assessed (**Figure 5.4(c)**). This sensor, unlike the sensor system studied in chapter two, shows stability over multiple wide voltage sweeps (-600 to 0 mV) likely due to the presence of two gold-thiol bonds per immobilised aptamer increasing stability. FTV measurements can therefore be employed when investigating this aptamer-based sensor.

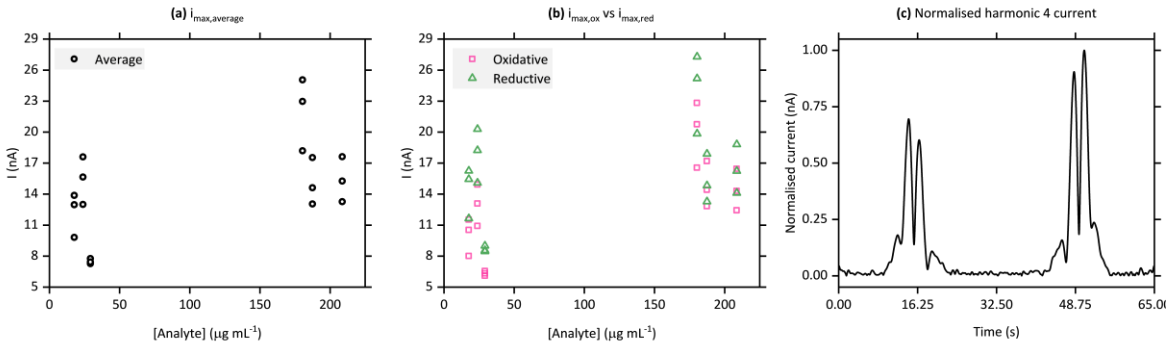

Figure 5.5. *(a) Averaged maximum harmonic current for the analyte titration experiments, (b) oxidative and reductive peak current for the same set of experiments, and (c) normalised harmonic 4 current showing the peak asymmetry.*

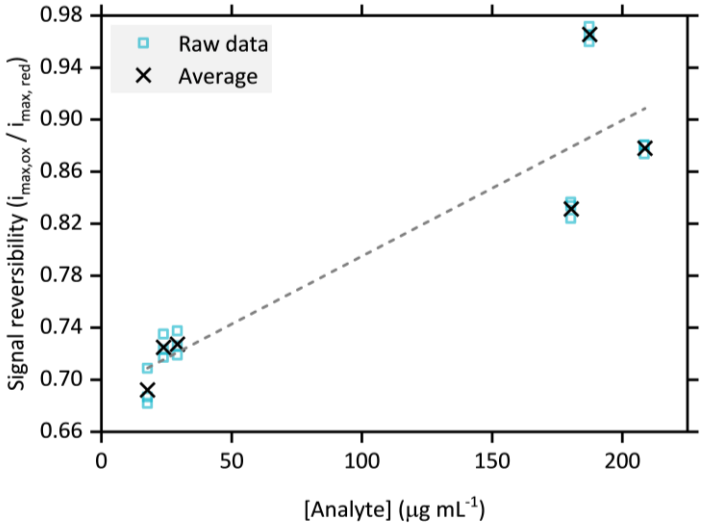

Figure 5.6. *The effect of analyte concentration on the signal reversibility of harmonic 4.*

The reproducibility between patient serum samples was also compared. Six different patient serum samples with a determined analyte concentration were compared, and three repeats for each concentration were made. All these 18 measurements were made on a different aptamer-modified electrode. The patient samples are a complex media as each will contain different levels of each component in serum. Additionally, there will be variability in the amount of aptamer immobilised onto each electrode. The challenge was therefore to see how consistent FTV methods would be, using the optimal parameters previously determined. When examining the average maximum current response for each electrode (**Figure 5.5(a)**), a weak positive correlation was observed, but there was high variability within repeats. Further inspection of the harmonic signal revealed irreversibility in the redox reaction (**Figure 5.5(b) and (c)**). The reductive process, observed in the reverse sweep, has a larger current, meaning the difference is a property of the aptamer-analyte binding and not induced by the measurement. This signal reversibility was quantified by dividing the oxidative current by the reductive current. The relationship between signal reversibility and analyte concentration shows a more pronounced positive correlation and significantly decreased intra-sample variation (**Figure 5.6**). The increased reversibility with analyte concentration is likely attributed to the analyte holding the aptamer in a conformation that facilitates the reversible electron transfer. The apparent anomalous result for a concentration of 187.45 μM of analyte was also observed in standard square wave measurements performed by the industrial collaborators, so it is assumed to be an issue with the 'typing' of that sample. Not only are the FTV methods faster than the standard

square-wave methods currently used, 1 minute compared to 6 minutes, they revealed a previously unobserved relationship between signal reversibility and analyte concentration. This analysis provides a simple way to achieve remarkable reproducibility in complex patient samples.

These two collaborations highlight the potential of using these techniques in biosensing, therefore further work would seek to continue to explore these alternating current voltammetry methods, particularly regarding aptamer-based sensing. There are two obvious primary objectives for this study. First, performing a side-by-side comparison of the sensitivity of Fourier transformed alternating current voltammetry with square wave voltammetry. Second, exploring commercially available aptamer-analyte systems to see if signal (ir)reversibility is a common occurrence that can be exploited in other systems, or if it is unique to the system studied here.

5.2. Final remarks

This thesis is the first example of the use of glycofluoroforms for electrochemical detection of galectin-3. The association of galectin-3 with disease is a growing area of interest; currently there are numerous studies discussing links between galectin-3 and prostate cancer, thyroid cancer, and heart failure. Despite the high impact of these diseases, there are limitations in diagnosis surrounding early detection, the absence of routine screening, and the requirement of painful biopsies for diagnosis. Glycofluoroforms are an unexplored biorecognition element for galectin-3 but possess favourable binding thermodynamics and kinetics compared to native ligands, as well as enhanced selectivity. Electrochemical methods are attractive for point of care applications due to their speed, simplicity, affordability, and ability to be miniaturised into portable devices. This thesis has highlighted the advantages of coupling glycofluoroforms and electrochemical methods.

Initially, well-established gold-thiol self-assembly chemistry was used to tether the thiol terminating polymer-glycofluoroform conjugates onto a gold electrode. Electrochemical impedance spectroscopy was used to characterise the surfaces and quantify the binding response. Surface characterisation revealed a high level of electrode-to-electrode variability, attributed to irreproducibility in self-assembled monolayer formation. Importantly, instability within the polymer-glycofluoroform conjugate was determined to not be the cause as the conjugate displayed remarkable stability throughout multiple freeze-thaw

cycles. Quantification of binding revealed a K_d of 240 nM, showing poor surface packing and a planar binding interface is hindering galectin-3 binding.

With aims to improve both modification stability and packing, an emerging electrografting strategy was employed using a triazabutadiene molecule. This molecule acts as a 'masked diazonium' to immobilise the polymer-glycofluoroform onto a carbon electrode. Electrode-to-electrode variability is not removed, but it is mediated to an extent. This immobilisation methodology does yield greater polymer-glycofluoroform presentation which lowered the observed K_d to 13 nM. Throughout, control experiments using a non-fluorinated sugar proved galectin-3 binding was specific and selective.

Finally, the improved stability from the covalent immobilisation enabled the exploration of alternating current voltammetry techniques for sensing. Compared to other electrochemical techniques, there has been comparatively little literature focus in sensing applications. However, these methods are highly sensitive and recently have been shown to be compatible with commercial instruments. While further development is needed, Fourier transformed alternating current voltammetry detected the lowest galectin-3 concentration in this thesis and purely sinusoidal voltammetry shows early promise in label-free detection.

With computers more powerful than those that took us to space in our pockets, personalised healthcare monitoring is surely the next frontier. This work explored highly sensitive, rapid, and information-dense electrochemical measurements using novel biorecognition elements, enabling specific capture of critical biomarkers. Additionally, the simplicity and affordability, combined with the stability of the glycofluoroform recognition element, should enable affordable and accessible devices. The combination of all these factors could be transformative in healthcare and play a role in allowing all individuals to know what is happening inside their body and when to seek help.

Chapter Six: Materials and methods

All chemicals were sourced from commercial sources and used without further purification. These commercial sources include Abcam, Apollo Scientific, Biosynth, Duchefa Biochemie, Fischer Scientific, Fluorochem, Melford, Merck, Prozomix, Sigma Aldrich, Thermo Scientific, and Tokyo Chemical Industries (TCI). Milli-Q H_2O was obtained from a Purite HP 320 water purification system.

6.1. General thesis methods

6.1.1. Preparation of electrode modifiers

The telechelic polymer, DBCO-$(PHEA)_{25}$-SH, was kindly provided by Dr S-J. Richards (University of Manchester) and was synthesised via reversible addition–fragmentation chain transfer polymerisation as described previously.[84] The control sugar, GlcNAc-N_3, formally 3-azidopropyl 2-acetamido-2-deoxy-β-D-glucopyranoside, was synthesised as described previously,[84] and was kindly provided to the author by Dr N. Hatton and J. Fair (both University of York).

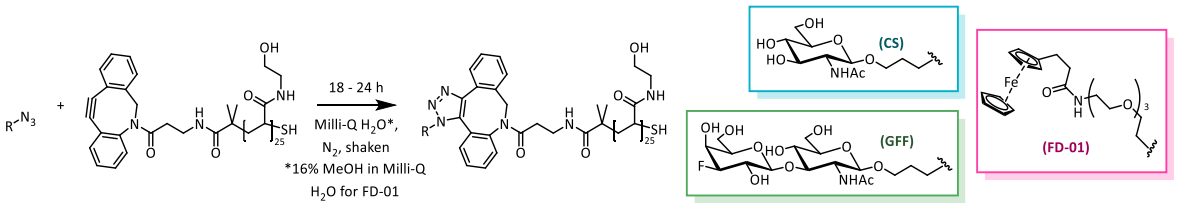

Scheme 6.1. *SPAAC reaction scheme for the production of P conjugates, where R is either the control sugar (CS), glycofluroform (GFF), or ferrocene derivative (FD-01).*

Polymer-sugar conjugates were made by reacting the thiol polymer and either the glycofluoroform, Gal3F-β(1,3)-GlcNAc-N_3, or the control sugar, GlcNAc-N_3, via a strain-promoted azide-alkyne cycloaddition (SPAAC) reaction. Appropriate volumes of polymer (0.320 µmol, 1 equiv.) and sugar (0.352 µmol, 1.1 equiv.) solutions (both in Milli-Q H_2O) were added to a 2 mL Eppendorf tube and made up to 450 µL with Milli-Q H_2O and shaken at room temperature in an anaerobic glovebox environment for 18 - 24 hours. Following the SPAAC reaction these aliquots were either used for electrode modification or stored at -20 °C. For the ferrocene-polymer conjugates the same procedure and quantities were used except the reaction solvent was 16% MeOH in Milli-Q H_2O to aid dissolution of ferrocene.

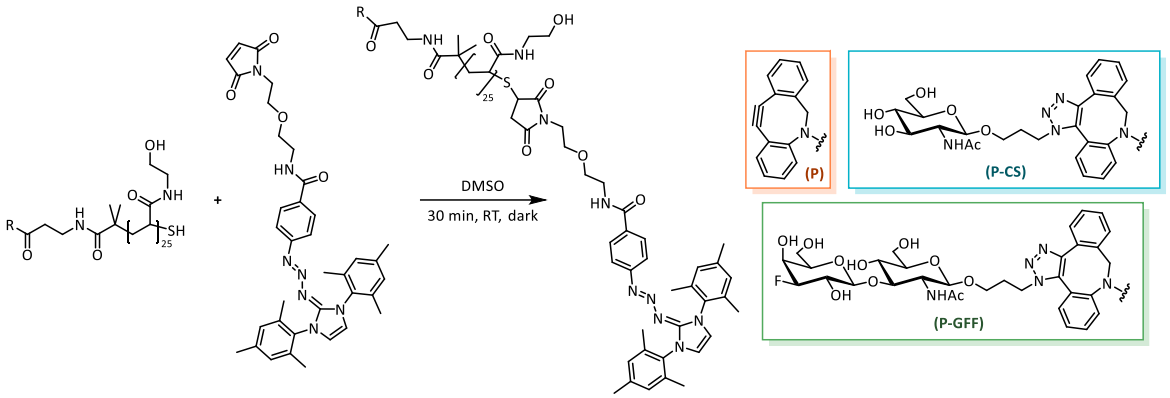

Scheme 6.2. *Conjugation of triazabutadiene to polymer for electrografting studies. R is either the polymer (P), control sugar (CS), or glycofluroform (GFF).*

Polymer and both polymer-sugar conjugates were functionalised with the triazabutadiene molecule **(8)** via the following procedure. In a glovebox, solutions of the polymer-containing component (either P, P-CS, or P-GFF) and triazabutadiene (both in DMSO) were mixed in a 1:5 molar ratio. If needed DMSO was added so the final solution concentration of triazabutadiene was 0.5 mg mL^{-1}. The solution was incubated at room temperature, in the dark, for 30 minutes. It was subsequently removed from the glovebox, diluted with dioxane (ca. 10 mL per mL of DMSO) and lyophilised. Ethyl acetate (1 mL per number of desired aliquots) was added, the solution was sonicated and split into aliquots at this stage. Aliquoting must be performed before centrifugation as the pellet produced following spinning is hard to divide. The aliquots were spun in a centrifuge (8000 x*g*, 4 °C, 5 minutes). The yellow supernatant was decanted and kept; this procedure was repeated until the supernatant was clear. The resultant yellow solid, the conjugate of triazabutadiene and polymer/polymer-sugar was dried on a high-vacuum line.

Note: The supernatant can be concentrated in vacuo to recover any unreacted triazabutadiene. The triazabutadiene recovered following separation of the supernatant post-centrifugation remains suitable for derivatisation of other polymer samples. The identity of the unreacted triazabutadiene was detected via HRMS:

(ESI)HRMS: Found [M]+ 634.3150, $C_{36}H_{40}N_7O_4$ requires 634.3136.

6.1.2. Electrode modification and titration experiments

Gold (Au-SPE), carbon (C-SPE), and ITO screen printed electrodes produced by BVT were purchased. These comprise a central 2 mm diameter disk working electrode made of gold, carbon, or ITO, a surrounding reference electrode made up of silver covered in silver

chloride, and surrounding counter electrode made of the same material as the working electrode. These electrodes are printed onto a 7.26 mm x 25.40 mm corundum ceramic chip. C-SPE were also provided to the author by Eluceda (Burnley, UK), a sensing company who collaborate with the Parkin group.

All experiments have been conducted in home-built, Perspex gloveboxes with a nitrogen gas supply and Belle purifying recirculation unit (O_2 ≤50 ppm) at ambient temperature unless otherwise stated.

6.1.2.1. Self-assembled monolayers

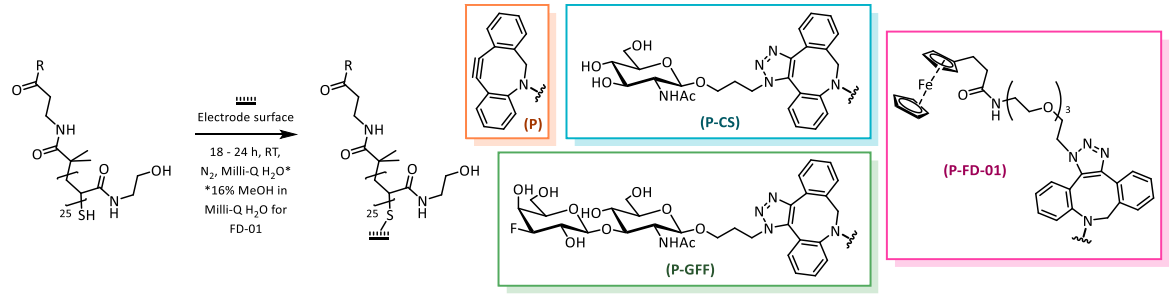

Scheme 6.3. *Self-assembled monolayer formation due to gold-thiol bond formation. R is either the polymer (P), or polymer conjugated to the control sugar (CS), glycofluroform (GFF), or ferrocene derivative (FD-01).*

Unless otherwise stated, following the SPAAC reaction 450 µL aliquots of the reaction mixture in 2 mL Eppendorf tubes were used to modify two Au-SPEs simultaneously by immersing the SPEs to a depth where the working, counter and reference electrodes were covered. The SPE modification was left to proceed at room temperature in an anaerobic glovebox environment for 18 – 24 hours. Following Au-SPE modification, the SPAAC reaction aliquots are stored at -20 °C and then thawed for subsequent Au-SPE modifications.

6.1.2.2. Electrografting

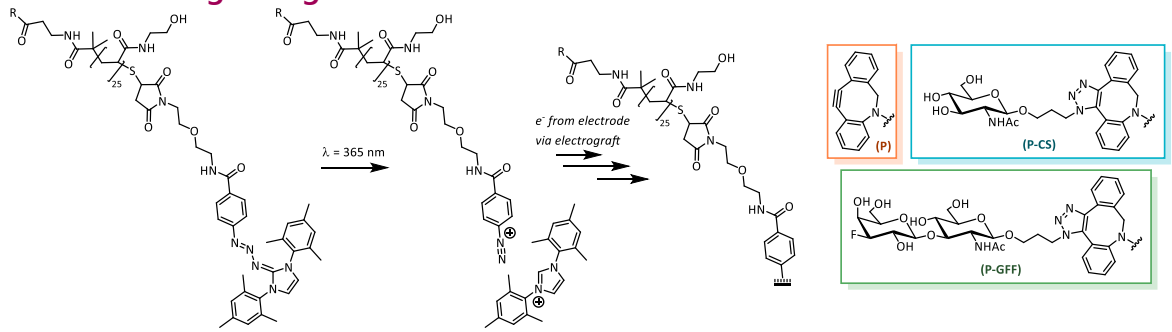

Scheme 6.4. *Triazabutadiene mediated electrografting. R is either the polymer (P), control sugar (CS), or glycofluroform (GFF).*

Solutions of 3 mg mL^{-1} of TABD-P, TABD-P-CS, or TABD-P-GFF in electrografting buffer (pH 5.0, 1 M sodium acetate) were prepared. These solutions were exposed to UV light (365 nm, 12 W UV LED Helios Nail Lamp (Item Code: HGPK25)) for 10 minutes (for non-UV control experiments this step was skipped). For the electrografting experiments, 50 µL (unless otherwise stated) of the required solution was applied to the electrode and a cyclic voltammetry (CV) scan was carried out (conditions provided in relevant figure captions). Following electrografting the solution was removed and SPEs were rinsed with EIS buffer (pH 7, 100 mM sodium phosphate, 233 mM sodium chloride).

6.1.2.3. Protein affinity measurements

Both galectin-3 (recombinant human protein purchased from Abcam, ≥98% purity) or bovine serum albumin (purchased from Sigma Aldrich) were supplied as freeze-dried powders. The galectin-3 was resuspended in Milli-Q H_2O to 1 mg mL^{-1} for long term storage (frozen at -20 °C). For protein binding assays using galectin-3, the stock solution was defrosted and appropriate aliquots were diluted in pH 7 aqueous buffer (10 mM HEPES, 150 mM NaCl) to yield the protein concentrations reported in this paper. The bovine serum albumin (BSA) was resuspended in pH 7 aqueous buffer (10 mM HEPES, 150 mM NaCl) to yield the protein concentrations reported in this paper.

To assess the protein binding affinity of a single electrode, if necessary, the electrode was first modified with sugar-polymer. Next, a protein-free initial electrochemical impedance spectroscopy (EIS) measurement was carried out, as described below. The electrode was then rinsed thoroughly to remove all potassium ferricyanide solution before being incubated in the appropriate protein solution, starting at the lowest concentration to be tested within the dataset. The electrode was immersed in approximately 400 µL of protein (sufficient to cover all working electrode surface area) for 30 min (timed using a stopwatch) at room temperature, before being rinsed with Milli-Q H_2O and measured in a solution of buffered potassium ferricyanide using EIS (i.e. electrochemical measurements conducted without protein in solution). Following EIS, the electrode was then rinsed thoroughly with Milli-Q H_2O before being incubated in the next concentration of protein, followed by another EIS measurement. This two-step, protein incubation followed by EIS measurement, process is repeated for each protein sample to be tested within the dataset, with an incremental increase in concentration each time.

6.1.3. Electrochemical measurements and analysis

Various set-ups are used throughout the work and will be detailed below but all are based on the premise of a standard three-electrode electrochemical cell. The three electrodes are connected and submerged in electrolyte. The voltage is applied to the working electrode relative to the reference electrode and current flows at the counter electrode to complete the circuit and balance the process at the working electrode.

Any disc electrode experiments were carried out in a three-electrode electrochemical cell (custom-built by the University of York's Chemistry Department's Glass Workshop) which allows for a fixed distance between the working and reference electrode, shown in **Figure 6.1**. The cell consisted of a gold disc (Ø 3 mm) working electrode (eDAQ, BASi), a Ag/AgCl (3 M KCl) reference electrode housed within a Luggin capillary (BASi), and a platinum wire (Ø 0.2 mm) counter electrode (Electronics Workshop, Department of Chemistry, University of York).

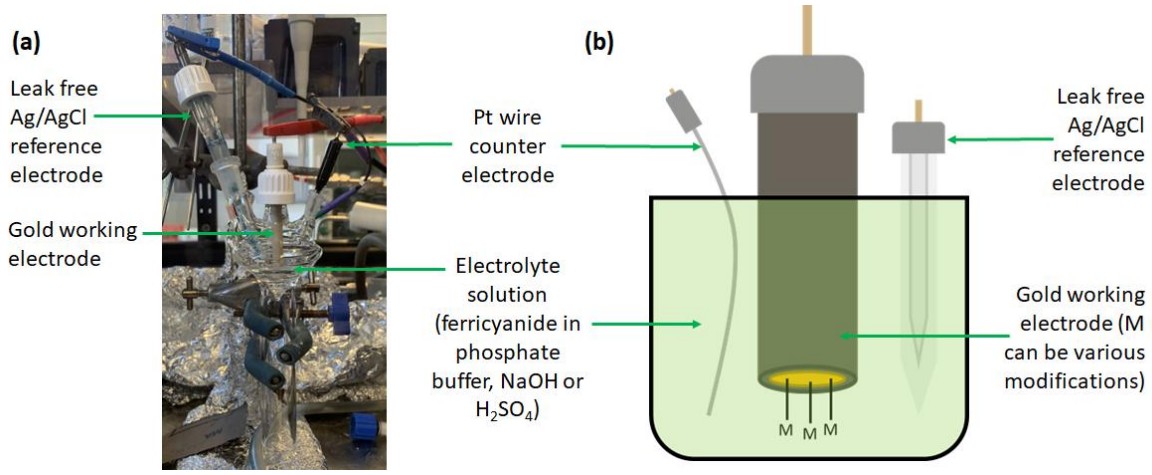

Figure 6.1. *Electrochemical cell set-up for gold disc electrodes. (a) Annotated photograph of cell inside the glovebox, and (b) Schematic of the three-electrode cell.*

For SPE electrochemical experiments various connectors were used to interface the SPEs and the potentiostat. A PalmSens MUX8-R2 multiplexer interfaced with the PalmSens4 potentiostat, a PalmSens SPE connector (2 mm banana) interfaces with PalmSens4 and Ivium's pocketSTAT2.LC. Bespoke connectors, shown in **Figure 6.2**, made in-house by the University of York's Chemistry Department's Electronics Workshop were used to interface with the bespoke potentiostat used for early ACV experiments or to perform high volume experiments to reduce evaporation.

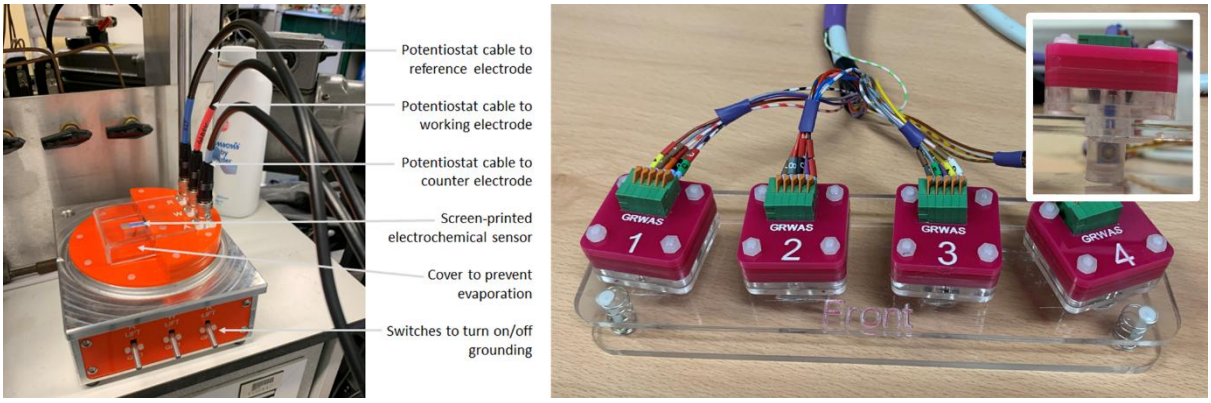

Figure 6.2. *Bespoke connectors made in the University of York's Chemistry Department's Electronics Workshop for interfacing with SPEs.*

All electrochemical techniques used broadly within this thesis are presented in the following sections with technical details followed by, if relevant, the common analytical methods employed.

6.1.3.1. Electrochemical impedance spectroscopy

Note: The electrochemical impedance experiments were all carried out in potassium ferricyanide (not equimolar ferro/ferricyanide). This is a deviation to the common literature procedure which may mean the experiments are operating outside the standard EIS conditions. However, the long equilibration time (180 s) and the plateauing current observed in the pretreatment suggests that although the bulk solution is not at chemical equilibrium the electrode-electrolyte interface is likely to be at an equilibrium point.

Prior to the impedance measurement, on a separate electrode a DCV measurement is recorded by scanning between two potentials cyclically at 100 mV s^{-1} for 3 – 10 scans to determine the midpoint potential of the redox probe. Measurements were conducted on either a PalmSens4 potentiostat using PSTrace (version 5.9.4515) software or an Ivium pocketSTAT2.LC potentiostat using IviumSoft (version 4.1216) with an applied sinusoidal voltage centred at the determined midpoint potential with a 10 mV amplitude and collected from 10^{x} Hz to 10^{x-n} Hz with 10n+1 readings taken at regular logarithmic intervals in this frequency range. Electrochemical impedance spectroscopy measurements were performed either in bulk solution or were made by applying a 50 - 100 µL droplet (a sufficient volume to cover all electrodes, dependent on surface tension) of 10 mM potassium ferricyanide in pH 7 aqueous buffer (100 mM sodium phosphate, 233 mM sodium chloride) to the SPE. Conditions for each experiment are provided in the relevant figure captions.

Each EIS experiment was analysed by fitting the Bode data to a modified Randles circuit with two noise parameters using a covariance matrix adaptation evolution strategy (CMA-ES) algorithm to find the 'best fit' parameter values.[253] These were obtained by maximising a Gaussian log-likelihood function (found in the SI), and assuming independent and identically distributed noise. The model parameters are as follows: solution resistance, R_s; charge transfer resistance, R_{ct}; Warburg element, Z_w; double-layer capacitance, modelled by a constant phase element (CPE) made up of Q and α; and noise parameters for the impedance phase and magnitude, $\sigma 1$ and $\sigma 2$, respectively. Parameter values were proposed from within hard-coded boundaries for each parameter, as detailed in appendix 7.5 alongside additional method details. The data was fitted to the polar form of the data (Bode plot) because when fitting to the complex form (Nyquist plot) of impedance data, very large complex values (as found at lower frequencies) were over-prioritised relative to the high-frequency values.

To generate posterior distributions for the parameter values, Markov chain Monte Carlo (MCMC) analysis was utilised, using the adaptive covariance MCMC algorithm as implemented in the PINTS repository,[254] using the same log-likelihood function as maximised by CMA-ES, and an uninformative log-prior using the boundaries for CMA-ES. Three chains were run independently for 10,000 iterations, initialised from the maximum likelihood point determined by CMA-ES. The pooled samples from these chains are plotted as histograms, with the first 3,000 samples discarded as "burn-in".

6.1.3.2. Voltammetric studies

DCV and SWV experiments were performed on either a PalmSens4 potentiostat using PSTrace (version 5.9.4515) or an Ivium pocketSTAT2.LC potentiostat using IviumSoft (version 4.1216). Method parameters are provided in the relevant figure captions. Following measurements data was analysed in-software for extracting parameters including peak potential and currents or via OriginPro 2025 for data visualisation and surface coverage calculations.

6.2. Characterisation methods

6.2.1. SDS-PAGE

SDS-PAGE gels were poured in house using a resolving gel and a stacker gel, the composition of these is shown in **Table 6.1**.

Table 6.1. *Composition of resolving and stacker gels.*

Component	Resolving Gel (12% acrylamide)	Stacking Gel
Water / mL	3.2	3.2
30% acrylamide stock / mL	4.2	0.5
20 % ammonium persulfate solution / µL	50	12.5
Tetramethylethylenediamine / µL	10	8
Resolving buffer (pH 8.8, 1.5 M Tris-HCl, 0.4% SDS) / mL	2.5	-
Stacking buffer (pH 6.8, 0.5 M Tris-HCl, 0.4% SDS) / mL	-	1.3

Gel samples were prepared by taking an aliquot of the solution (diluting with Milli-Q H_2O if required) and then adding the appropriate amount of 5× concentrated reducing buffer (pH 6.8, 200 mM Tris-HCl, 10 mM 2-mercaptoethanol, 20% glycerol, 10% SDS, 0.05% bromophenol blue). The samples were boiled at 95 °C for 10 minutes. The samples were added to the gel alongside a low molecular weight marker (Bio-Rad) and ran at 0.2 V in running buffer (25 mM Tris, 192 mM Gly, not pH adjusted) until completed (approx. 30 – 50 minutes). Once ran, the gels were immersed in fixing solution (50 % methanol, 40 % water, 10% ethanol) and rocked for around 15 minutes. The gels were then immersed in a solution of 0.1% Coomassie Brilliant Blue R-250 stain (in 50 % methanol, 40 % water, 10% ethanol), microwaved, and rocked for 30 minutes. The gels were finally submerged in destaining solution (50 % water, 40 % methanol, 10% ethanol) which was regularly replaced until the bands were clear. Gels were imaged either using a lightbox or GeneSys system.

6.2.2. TLC analysis

Thin Layer Chromatography (TLC) analysis was carried out by spotting ca. 1 µL of solutions directly onto pre-coated 0.25 mm Merck KgaA 60 F254 silica gel plates. For the chemoenzymatic synthesis TLCs were run in a 2:1:1 n-butanol:acetic acid:H_2O solvent system. For the synthesis of the ferrocene derivative (FD-01) TLCs were run in DCM (spiked with MeOH and Et_3N when necessary). Plates were stained with p-anisaldehyde sugar, 10 % (v/v) H_2SO_4 in EtOH and exposed to heat to visualise spots.

6.2.3. LC-MS analysis

For reaction monitoring and fraction screening, High Performance Liquid Chromatography-Electrospray Ionisation Mass Spectrometry (HPLC-ESI-MS) was carried out on a Dionex

UltiMate® 3000 LC system (Thermo Scientific) in line with a Bruker HCTultra ETD II system (Bruker Daltonics) at the University of York Centre of Excellence in Mass Spectrometry (CoEMS). All mass spectrometry was conducted in positive ion mode. For all analyses solvent A was water with 0.1% v/v formic acid and solvent B was acetonitrile with 0.1% v/v formic acid. Data was processed using DataAnalysis Version 4.4 software (Bruker Daltonics).

The fifteen-minute column method, for tracking chemoenzymatic reaction progress, was carried out using a SeQuant ZIC®-HILIC (3.5 µM, 200 Å) 100 X 2.1 mm HPLC column with a flow rate of 0.3 mL min^{-1} and a 5% A:95% B solvent system used for the mobile phase. A multi-step gradient of 9 min was programmed as follows: 95 % B for 0.5 min, followed by a linear gradient to 5 % B over 4.5 min, followed by 5 % B for an additional 0.5 min. A linear gradient to 95 % B was used to re-equilibrate the column.

A similar method with a shorter four-minute run was carried out without a column for screening fractions following gel filtration.

A ten-minute method using a Symmetry C18 5 µm 3.0 x 150 mm reverse-phase column was used to analyse imidazolium tagged samples.

6.2.4. HRMS analysis

For structure confirmation, High Resolution Electrospray Ionisation Mass Spectrometry (HRMS) data was obtained at room temperature on a Bruker Daltonics microTOF mass spectrometer coupled to an Agilent 1200 series LC system at The University of York Centre of Excellence in Mass Spectrometry (CoEMS). Nominal and exact m/z values are reported in Daltons.

6.2.5. NMR analysis

^{1}H-NMR (400 MHz), ^{19}F-NMR{^{1}H} (400 MHz), and ^{13}C-NMR{^{1}H} (100 MHz) experiments were conducted using a JEOL 400 instrument at The University York Centre for Magnetic Resonance. Where NMR is reported, multiplicities are given as singlet (s), doublet (d), triplet (t), quartet (q), or multiplet (m). All NMR chemical shifts (δ) were recorded in ppm and coupling constants (*J*) are reported in Hz. Data processed using MestReNova software.

6.3. Methods specific to chapter two

6.3.1. Expression and purification of BiGalK and BiGalHexNAcP

6.3.1.1. Transformation of BiGalK and BiGalHexNAcP

The expression and purification of BiGalK was based off the work reported by Lei Li *et al.*,[255] similarly the expression and purification of BiGalHexNAcP was based off the work previously reported by Tessa Keenan *et al.*[138]

BL21-Gold competent *E. coli* cells were thawed on ice. Once defrosted and mixed, 50 μL of cells were pipetted into a 14 mL falcon tube on ice. 1 μL of the relevant plasmid was added (approximately 50 ng of DNA) to the cells which were then incubated for 30 minutes on ice. The cell mixture was heat shocked at 42 °C for 20 seconds and then placed on ice for 2 minutes. 900 μL of preheated (42 °C) LB (Luria Broth) was added to the transformation reactions. The reactions were incubated at 37 °C with 250 rpm shaking for 1 hour. The cells were concentrated by centrifugation (200 x*g*, 4 minutes) and spread onto an agar plate which was incubated at 37 °C overnight.

6.3.1.2. Expression of BiGalK and BiGalHexNAcP

A starter culture was prepared by inoculating 5 mL of LB with ampicillin (1 μL mL^{-1}) with an individual colony from the overnight plate from the previous stage. The culture was grown at 37 °C with 180 rpm stirring for 8 hours. The cells in solution were transferred to 100 mL of LB with ampicillin (1 μL mL^{-1}) and incubated overnight at 37 °C with 180 rpm shaking.

10 mL of overnight culture was added to 1L of LB with ampicillin (1 μL mL^{-1}) and grown at 37 °C with 180 rpm shaking until OD_{600} reached ca. 0.6 for BiGalK and 0.8 for BiGalHexNAcP. IPTG was added to a final concentration of 0.2 mM for BiGalK and 0.1 mM for BiGalHexNAcP and the cultures were grown for 20 h with 180 rpm shaking at 16°C for BiGalK and 25 °C for BiGalHexNAcP.

The cells were harvested by centrifugation at 6000 x*g* and 6 °C for 10 minutes. The cells were resuspended in 50 mL of cold lysis buffer (pH 8.0, 30 mM Tris, 300 mM NaCl, 1 mg mL^{-1} lysozyme) and placed on ice. A protease inhibitor tablet (Thermo Scientific) and 20 μL of benzonase were added and the cells were lysed by sonication on ice and the lysate was clarified by centrifugation (18 000 rpm, 4°C, 50 min). The supernatant was removed and imidazole was added to give a 20 mM concentration.

6.3.1.3. Expression tests

If an expression test was to be carried out the following procedure was performed after the initial 100 mL overnight culture. A small sample (1-2 mL) of the induced and non-induced (media without additions of IPTG) cell solutions were centrifuged to obtain cell pellets, which were resuspended in 50 µL of BugBuster® Protein Extraction Reagent and incubated at room temperature for 30 minutes. Centrifugation yielded supernatant, which was taken as the soluble fraction, and a pellet, which was taken as the insoluble fraction and resuspended in 50 µL of H_2O. Alongside the marker, 10 µL of the insoluble fraction, and 2, 5, and 10 µL of the soluble fractions (to ensure one lane is of appropriate concentration for analysis) for both the induced and non-induced samples were loaded into a gel which was processed as described above in section 6.2.1.

6.3.1.4. Purification of BiGalK and BiGalHexNAcP

A nickel HisTrap HP column (5 mL column, GE Healthcare) was used to purify the protein via nickel-affinity chromatography. The column was connected to an AKTA Start (GE Healthcare). The sample, A, and B pumps and lines were washed with deionised water. The sample and A line were then washed with Buffer A (pH 8.0, 30 mM Tris, 300 mM NaCl, 20 mM imidazole) and B was washed with Buffer B (pH 8.0, 30 mM Tris, 300 mM NaCl, 250 mM imidazole), that were both filtered prior to use. The lysate was loaded onto the column, rinsed with 20 column volumes of buffer A, and the bound protein was then eluted at a flow rate of 5 mL min^{-1} over a gradient of 15 column volumes with the concentration of imidazole increasing from 20-250 mM (the concentration of Buffer B increasing 0-100%) over this range. The fractions were analysed on a 12% SDS-PAGE using the method described in in section 6.2.1.

Selected fractions were placed inside dialysis tubing in buffer (pH 8.0, 30 mM Tris, 200 mM NaCl) and left to dialyse at 4 °C overnight. The dialysed fractions were concentrated using a 10 or 30K centricon centrifugal filter. An additional purification step can be carried out by using gel filtration chromatography (HiLoad 16/600 Superdex 200 pg) in 30 mM Tris pH 8.0 buffer. Once purified and concentrated the protein was aliquoted and stored at -20 °C. The concentration was determined from the resultant standard curve of a BCA assay (Pierce™ BCA Protein Assay Kits, Thermo Scientific™).

6.3.2. Accessing the glycofluoroform via chemoenzymatic synthesis

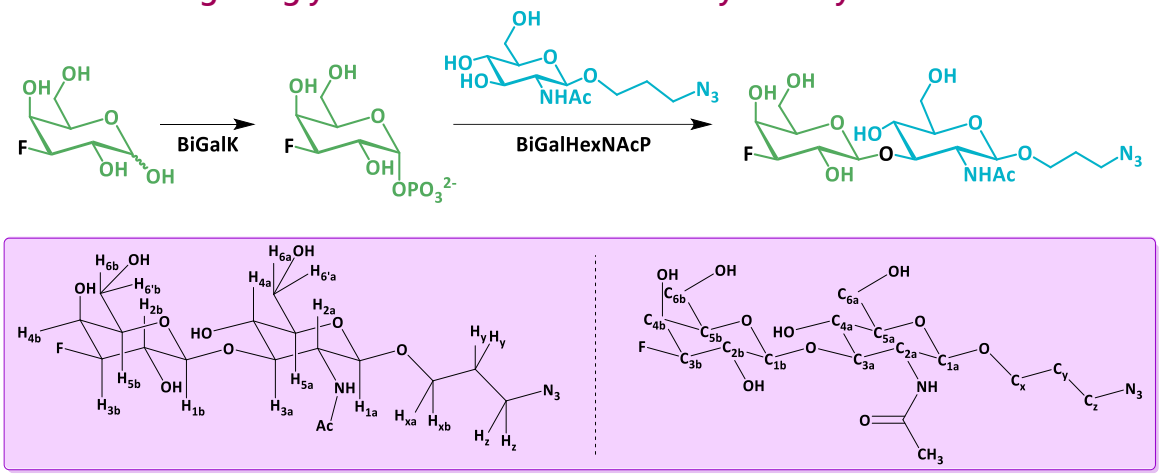

Scheme 6.5. *Reaction scheme for the BiGalK-catalysed phosphorylation of 3F-galactose followed by the BiGalHexNAcP-catalysed transfer of phosphorylated galactose to a N-acetylglucosamine acceptor by reverse phosphorylysis yielding the fluorinated disaccharide, 3FGal-β(1,3)-GlcNAc-N_3 (GFF). Inset: Annotated structures relating to NMR assignment.*

The author was kindly provided with crude phosphorylated 3F-galactose by Dr T. Keenan (University of York). The following synthetic step and purification was performed by the author.

6.3.2.1. Synthesis

3FGal-β(1,3)-GlcNAc-N_3 was synthesised as previously reported,[84] but in a modified two-step approach as this was found to be higher yielding. A reaction containing 3FGal (8 mM, 91 mg), ATP (10 mM, 344 mg), $MgCl_2$ (5 mM, 3125 µL of a 100 mM stock), Tris HCl buffer pH 8.0 (100 mM) and BiGalK (0.12 mg mL^{-1}, 7.496 mg) was assembled in a sterile pot to a final reaction volume of 62.5 mL, and adjusted to pH 8.0. Following mixing, the reaction was separated into 2 mL aliquots and incubated at 37 °C for 24 h. Completion of the reaction was validated by TLC (R_f = 0.34, N-butanol, acetic acid, H_2O 2:1:1). Aliquots were subsequently pooled and BiGalK was removed using a centrifugal spin concentrator (10 kDa MWCO) and lyophilised. For the second step the reaction was assembled on a 2000 µL scale in a sterile pot containing 100 mM Tris. HCl buffer (pH 6.5), crude 3FGal1P (25 mM, 13 mg), acceptor monosaccharide, GlcNAc-N_3, (10 mM, 6.1 mg), $MgCl_2$ (15 mM, 2.9 mg) and BiGalHexNAcP (42.3 mg). Following mixing, the reaction was separated into 500 µL aliquots in 2 mL Eppendorfs and incubated at 37 °C. Reaction progress was monitored via TLC (R_f = 0.66 N-butanol, acetic acid, H_2O 2:1:1) and LC-MS and additional BiGalHexNAcP (2.12 mg) was added to each aliquot every 24 hours until completion. Reaction mixtures were pooled

and BiGalHexNAcP was removed using a centrifugal spin concentrator (10 kDa MWCO) and the sample was lyophilised to yield the crude disaccharide.

6.3.2.2. Purification

The crude disaccharide was resuspended in Milli0Q H_2O, lyophilised onto silica and dry loaded onto a silica column in EtOAc and eluted along a EtOAc-MeOH gradient using a CombiFlash® NextGen system (Teledyne). LC-MS was used to identify glycofluoroform-containing fractions which were pooled and lyophilised. This was then applied to a gel filtration column (BioGel P2 gel) in dH_2O. Resulting fractions were analysed by TLC and LC-MS and all glycofluoroform containing fractions were lyophilised and characterised by ^{1}H, ^{13}C, and ^{19}F NMR and MS.

^{1}H NMR (400 MHz, D_2O) δ 4.60 (ddd, *J* = 10.0, 3.7, 1.3 Hz, 1H, H-3b), 4.53 (d, *J* = 7.7 Hz, 1H, H-1b), 4.46 (d, *J* = 7.8 Hz, 1H, H-1a), 4.21 – 4.16 (m, 1H, H-4b), 3.97 (ddd, *J* = 10.6, 5.7, 1.7 Hz, 1H, H-xa), 3.91 (dt, *J* = 12.6, 2.2 Hz, 1H, H-6a), 3.87 – 3.60 (m, 8H, H-2a, H-2b, H-4a, H-5b, H-6a', H-6b, H-6b', H-xb), 3.57 – 3.50 (m, 1H, H-3a), 3.50 – 3.40 (m, 1H, H-5a), 3.35 (td, *J* = 6.5, 3.2 Hz, 2H, H-z), 2.04 – 2.00 (m, 3H, NHAc), 1.89 – 1.78 (m, 2H, H-y).

^{13}C {^{1}H) NMR (100 MHz, D_2O) δ 174.61 (C=O), 102.86 (C-1a), 100.93 (C-1b), 93.65 (C-3b), 82.48, 73.95, 69.46, 69.27, 60.72 & 54.61 (C-2a, C-2b, C-4a, C-5b, C-6a, C-6b), 75.39 (C-5a), 68.68 (C-3a), 67.19 (C-x), 66.69 (C-4b), 47.81 (C-x), 28.12 (C-y), 22.21 ($NHCOCH_3$).

^{19}F {^{1}H} NMR (400 MHz, D_2O) δ -198.95.

HRMS (ESI): $C_{17}H_{29}FN_4NaO_{10}$ [M+Na]+ Calculated: 491.1760; Found: 491.1755 (mean error 0.6 ppm).

$C_{17}H_{28}FN_4O_{10}$ [M-H]- Calculated: 467.1795; Found: 467.1816 (mean error 0.9 ppm).

6.3.2.3. Fraction screening with an imidazolium reagent

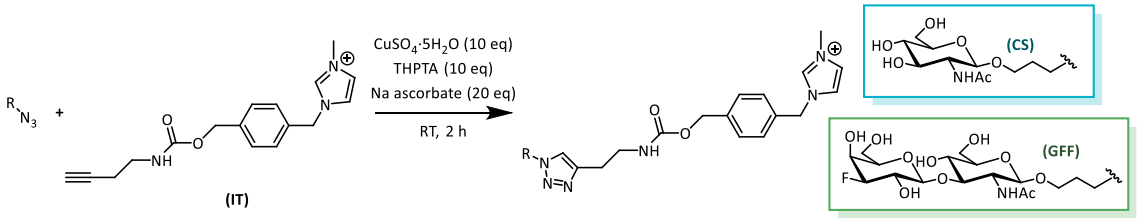

Scheme 6.6. *Reaction between iTag reagent and both the acceptor monosaccharide and glycofluoroform for quantification of fraction impurity.*

Imidazolium functionalisation was performed to gain a more quantitative ratio of acceptor monosaccharide, GlcNAc-Pr-N_3 **(CS)**, to glycofluoroform, 3FGal-β(1,3)-GlcNAc-Pr-N_3 **(GFF)**. To a small sample of an impure fraction (10 mM, 24 µL, Milli-Q H_2O) was added iTag reagent (250 mM in DMSO, 1 µL, **(IT)**) and the solution was vortexed. 10 µL of 'iTag solution' (500 mM $CuSO_4.5H_2O$, 500 mM THPTA, Milli-Q H_2O) was added and the solution was vortexed before the addition of sodium ascorbate (1 M, 5 µL). The mixture was incubated at 20 °C for 2 hours with 300 rpm shaking and subsequently was diluted with 1 mL of Milli-Q H_2O, flash frozen and lyophilised. The lyophilised sample was analysed via LC-MS.

6.3.3. Gold disc electrode polishing

The gold disc electrodes (eDAQ, BASi) were first polished with alumina slurries (MetPrep) on a felt polishing pad (Buehler). Three grades of slurry are used (1, 0.3, and 0.05 µm) and the electrode is polished in a figure of eight motion for 2 minutes per slurry, with a direction change after one minute, starting with the 1 µm slurry. The electrode is rinsed with Milli-Q H_2O in between any change of direction or particle size. Following the mechanical polish, the electrode is sonicated in water and then ethanol for 3 minutes. An electrochemical polish in 0.5 M NaOH polish is then carried out by cycling the voltage from -1.095 V to 0.905 V (vs SHE) at 100 mV s^{-1} for 50 scans which is followed by a polish in 0.5 M H_2SO_4 cycling the voltage from -0.045 V to 1.755 V (vs SHE) at 100 mV s^{-1} for 50 scans. After polishing the electrode is dried under N_2 flow and used immediately.

6.3.4. Synthesis of ferrocene derivative, FD-01

A sample of 3-ferrocenyl propanoic acid N-hydroxyphthalimide ester was kindly provided by Dr N. D. J. Yates (University of York) and was synthesised as previously reported.[256]

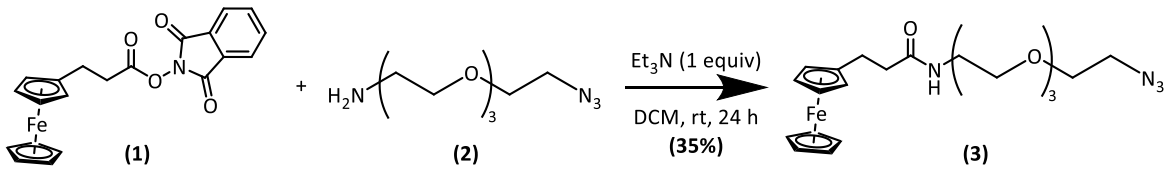

Scheme 6.7. *Synthesis of FD-01 (3).*

3-ferrocenyl propanoic acid N-hydroxyphthalimide ester **(1)** (5 mg, 12.4 µmol, 1.0 equiv), 11-azido-3,6,9-trioxaundecan-1-amine **(2)** (13.6 6 µmol, 1.1 equiv), and triethylamine (1.73 µL, 1.0 equiv) were dissolved in DCM (100 µL) and stirred at room temperature for 24 hours. The solvent was removed in vacuo. The resultant solid was semi-purified via flash column chromatography (starting with DCM + 1% Et_3N and moving to DCM + 1% Et_3N + 2% MeOH

once the first band had eluted) to yield an orange solid of the title compound FD-01 **(3)**; 3.7 mg, 8.06 µmol, 65%.

HRMS (ESI): $C_{21}H_{31}FeN_4O_4$ [M+H]+ Calculated: 459.1689; Found: 459.1695 (mean error 2.2 ppm).

$C_{21}H_{30}FeN_4NaO_4$ [M+Na]+ Calculated: 481.1509; Found: 481.1520 (mean error 1.3 ppm).

6.3.5. Optimisation of redox probe and buffer screening

For the buffer screening with potassium ferricyanide the bespoke connector developed with the Electronic Workshop (**Figure 6.2**) was used in tandem with the MUX8-R2 multiplexer and the in-software scripting ability to run regular EIS measurements over an 85.5 hour timescale. All buffers were made in Milli-Q H_2O to the same ionic strength with 100 mM of the buffering salt so the composition of the buffers were as follows:

- 100 mM sodium phosphate, 233 mM sodium chloride
- 100 mM 2-(N-morpholino)ethanesulfonic acid (Mes), 375 mM sodium chloride
- 100 mM (4-(2-hydroxyethyl)-1-piperazineethanesulfonic acid) (HEPES), 441 mM sodium chloride
- 100 mM tris(hydroxymethyl)aminomethane (Tris), 381 mM sodium chloride

Two tethered ferrocene molecules were studied. For the study of 6-(ferrocenyl)hexanethiol a solution of 6-(ferrocenyl)hexanethiol and polymer was made up in 50:50 ethanol:Milli-Q with a 1:10 molar ratio. A polished gold disc electrode was submerged overnight to enable SAM formation, and the modified electrode was studied via DCV. The FD-01 was synthesised and immobilised onto the electrode as described in section 6.1. The electrode was analysed via CV and EIS measurements with E_{DC} = 0.13 V.

6.4. Methods specific to chapter three

6.4.1. Triazabutadiene synthesis and purification

The synthesis (**Scheme 3.3**) for the triazabutadiene molecule was performed by L. Gregg, an MChem student under the supervision of the thesis author. This molecule was then used by the author for the preparation of conjugates for electrografting. The synthesis is based

on a literature procedure with any deviations detailed in section 3.3.1. The final product was isolated as a yellow residue (4.91 mg, 7.75 µmol, 1.3% yield) and detected by HRMS.

(ESI)HRMS: Found [M]+ 634.3138, $C_{36}H_{40}N_7O_4$ requires 634.3136.

6.4.2. Electrode surface assessment

To assess the surface of the four electrode types the bespoke connector developed with the Electronic Workshop was used in tandem with the MUX8-R2 multiplexer and the in-software scripting. A BVT C-SPE, an Eluceda C-SPE, a BVT Au-SPE, and a BVT ITO-SPE were connected and submerged in potassium ferricyanide containing EIS buffer. Measurements were run every 30 minutes.

6.4.3. Surface click ferrocene studies

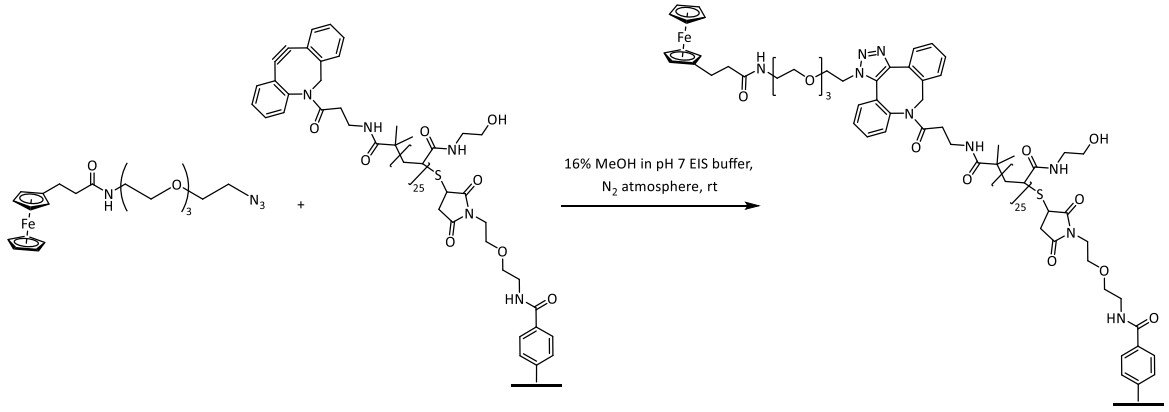

Scheme 6.8. *Surface-click between the polymer immobilised on a electrode and azide containing ferrocene to allow electrochemical interrogation of a modified surface.*

In a glovebox, FD-01 (1 mg, 1.93 µmol) was dissolved in 2 mL of 16% methanol in EIS buffer then 500 µL of this was taken and put in a 2 mL Eppendorf. The previously prepared (via triazabutadiene electrografting of TABD-P described in section 6.1.2.2) polymer-modified electrodes were immersed in this solution, the lids of the Eppendorfs were closed, the Eppendorfs were then left for the amounts of time specified in the figure captions. After this time and prior to any DCV or SWV experiments, the electrode was removed and left in 500 µL of a 50:50 mixture of EIS buffer and methanol, with rocking, for 5 minutes to remove any unreacted FD-01. Buffer was then pipetted on and off the electrode surface once the rinse was complete, to remove any methanol that may have still been present.

Note: The remaining FD-01 solution can be lyophilised and stored in a -20 ºC freezer to allow for reuse.

6.4.4. Buffer control experiments

For control experiments to assess the time dependence of the signal magnitude a modified electrode was submerged in buffer (pH 7, 10 mM HEPES, 150 mM NaCl) for 30 minutes to mirror the incubation in galectin-3 solutions. Electrodes were rinsed, EIS experiments run and then rinsed and placed back into solution until the appropriate number of experiments were completed.

6.5. Methods specific to chapter four

6.5.1. Fourier transformed alternating current voltammetry experiments

Experiments were performed on either a bespoke commercial potentiostat using custom software "pot_ver237" or on an Ivium pocketSTAT2.LC using IviumSoft (version 4.1216). For FTV potential waveforms are defined in terms of starting potential, switching potential, linear scan rate, sinusoidal amplitude, and frequency. These parameters are defined within figure captions. An equilibration time of 10 seconds was used for all experiments. An interval time is defined for measurements made on the Ivium pocketSTAT2.LC potentiostat so recorded datapoints are ≤500,000 as this is the limit of the software.

Time, current, potential data is extracted as an SQLite file and processed via python code written by Dr H. O. Lloyd-Laney but used and manipulated by the author. This performs the Fourier transform function and harmonic generation. For FTV harmonics, a bandpass filter of 0.1ω was used, the absolute values of harmonics were plotted against time, there was no hanning filter employed, and the data was decimated by a degree of 32.

6.5.2. Purely sinusoidal voltammetry experiments

Experiments were performed on either a bespoke commercial potentiostat using custom software "pot_ver237" or on an Ivium pocketSTAT2.LC using IviumSoft (version 4.1216). For PSV potential waveforms are defined in terms of starting potential and switching potential which govern the wave amplitude, sinusoidal frequency, and a number of oscillations to be completed. These parameters are defined within figure captions. The phase is defined at 270° for the sinusoid. An equilibration time of 10 seconds was used for all experiments. An interval time is defined for measurements made on the Ivium pocketSTAT2.LC potentiostat so recorded datapoints are ≤500,000 as this is the limit of the software.

Time, current, potential data is extracted as an SQLite file and processed via python code written by Dr H. O. Lloyd-Laney but used and manipulated by the author. This performs the

Fourier transform function and harmonic generation. For PSV harmonics, a bandpass filter of 0.1ω was used, the real values of harmonics were plotted against potential, there was no hanning filter employed, and the data was decimated by a degree of 32.

Appendices

7.1. BiGalK and BiGalHexNAcP: AKTA traces and gels

AKTA traces and SDS page gels are provided for the purification of BiGalK and BiGalHexNAcP showing successful expression and purification.

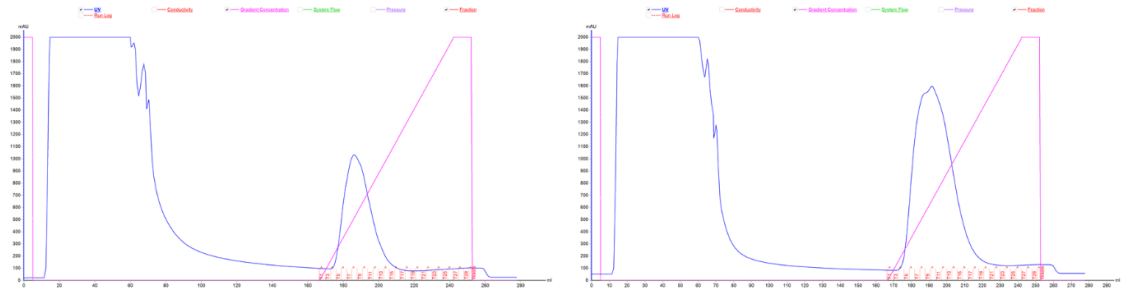

Figure 7.1. *AKTA trace (from affinity chromatography) showing absorbance change (blue) and buffer B concentration (pink) throughout elution for the purification of BiGalK (left) and BiGalHexNAcP (right).*

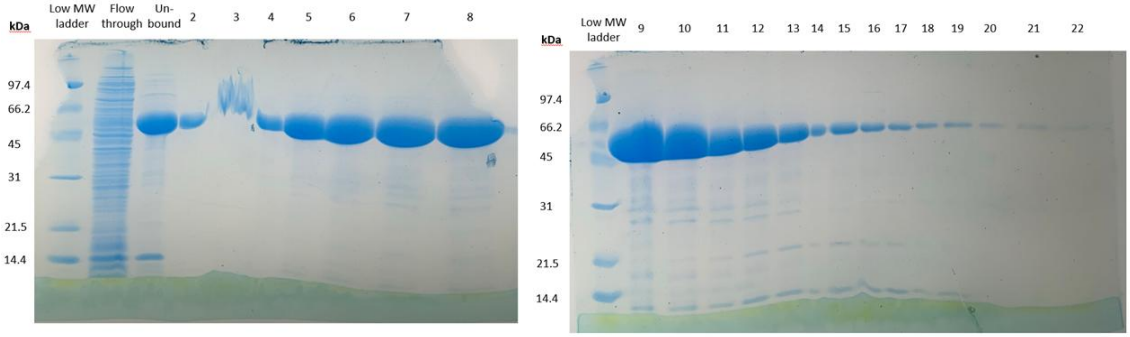

Figure 7.2. *12% SDS page gels post Ni-affinity chromatography illustrating the presence of BiGalK.*

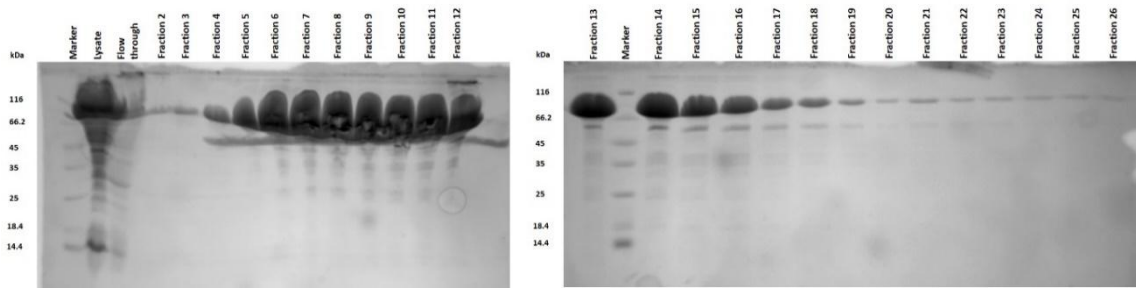

Figure 7.3. *12% SDS page gels post Ni-affinity chromatography illustrating the presence of BiGalHexNAcP.*

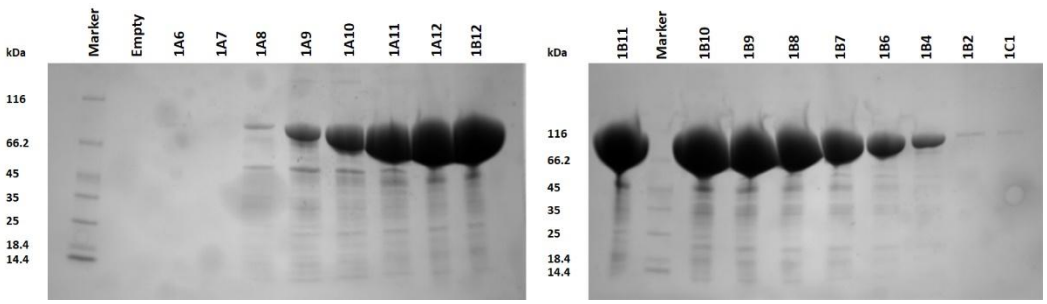

Figure 7.4. *12% SDS page gels post gel filtration illustrating the presence of BiGalHexNAcP.*

7.2. Full Nyquist datasets for bare, P and P-GFF repeats

Many different bare and P-GFF modified Au-SPE (and several P-modified electrodes) were interrogated using EIS and the resulting data was analysed by fitting to a modified Randles circuit (as described in section 2.3.2) as shown in figures **Figure 7.5Figure 7.7**. The extracted R_{ct} values from the data fitting were used to generate the box and whisker plot in **Figure 2.20**.

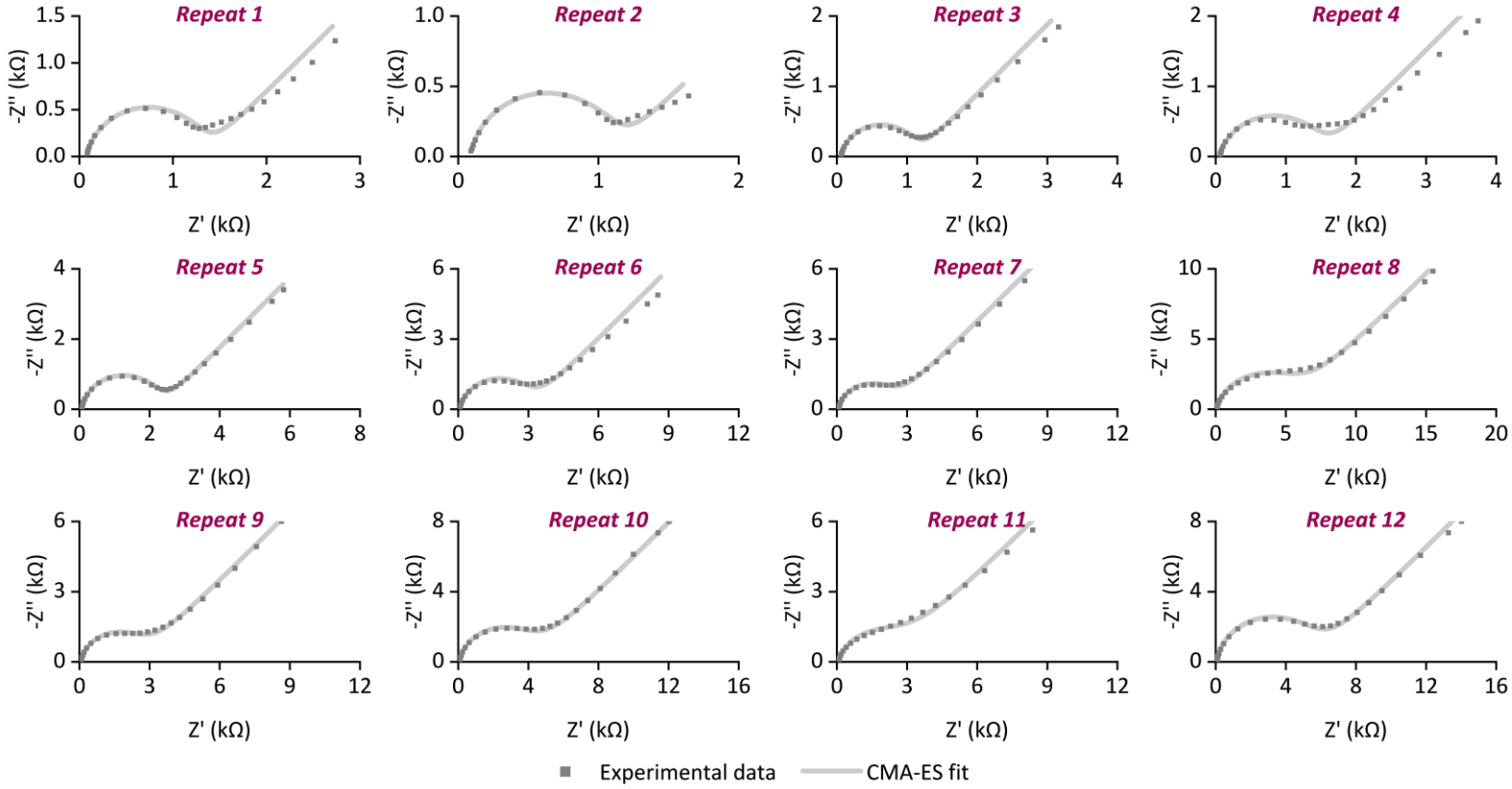

Figure 7.5. *Nyquist plots (experimental datapoints in dark grey and fits in light grey) for all the bare Au-SPE datasets included in* ***Figure 2.20****.*

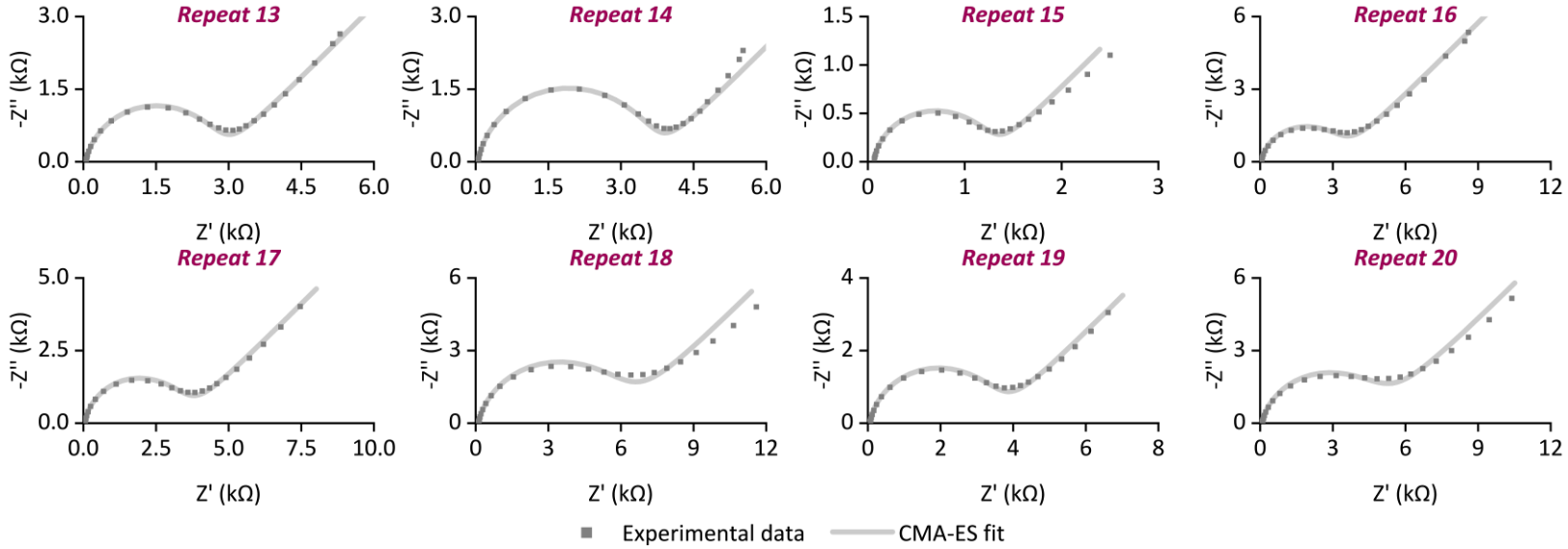

***Figure 7.5**. ctd.*

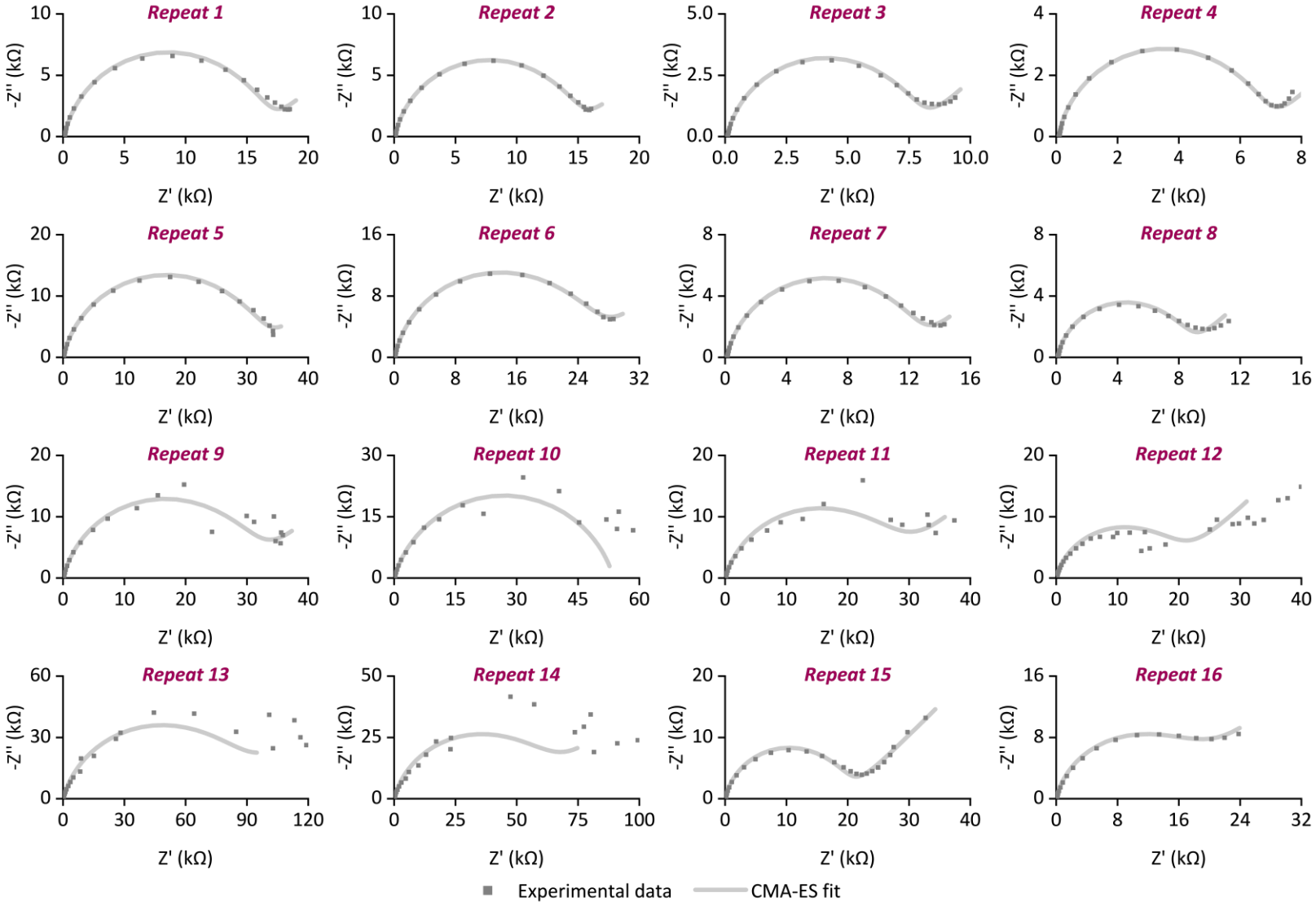

Figure 7.6. *Nyquist plots (experimental datapoints in dark grey and fits in light grey) for all the P-GFF Au-SPE datasets included in* ***Figure 2.20****.*

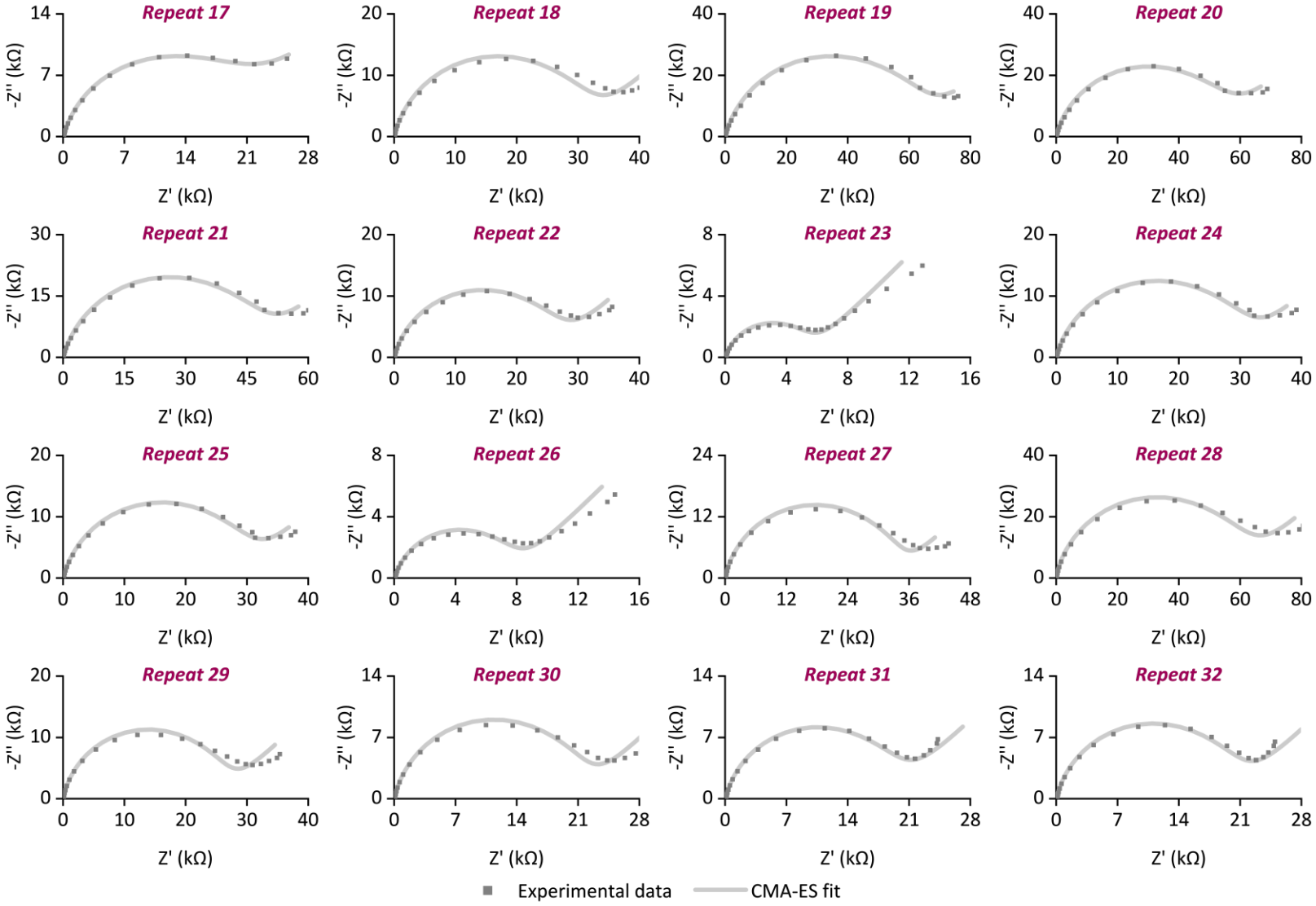

Figure 7.6. *ctd.*

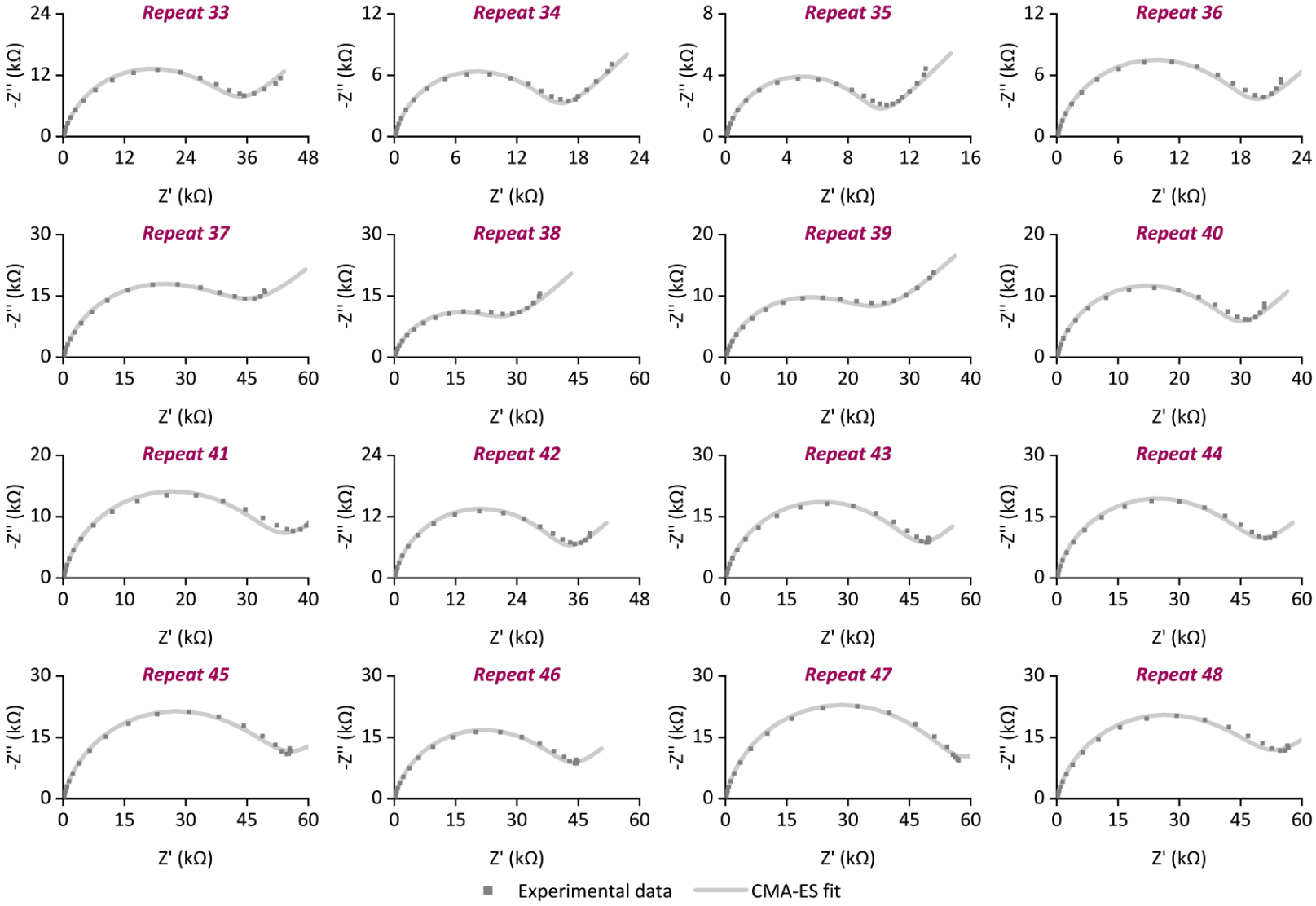

Figure 7.6. *ctd.*

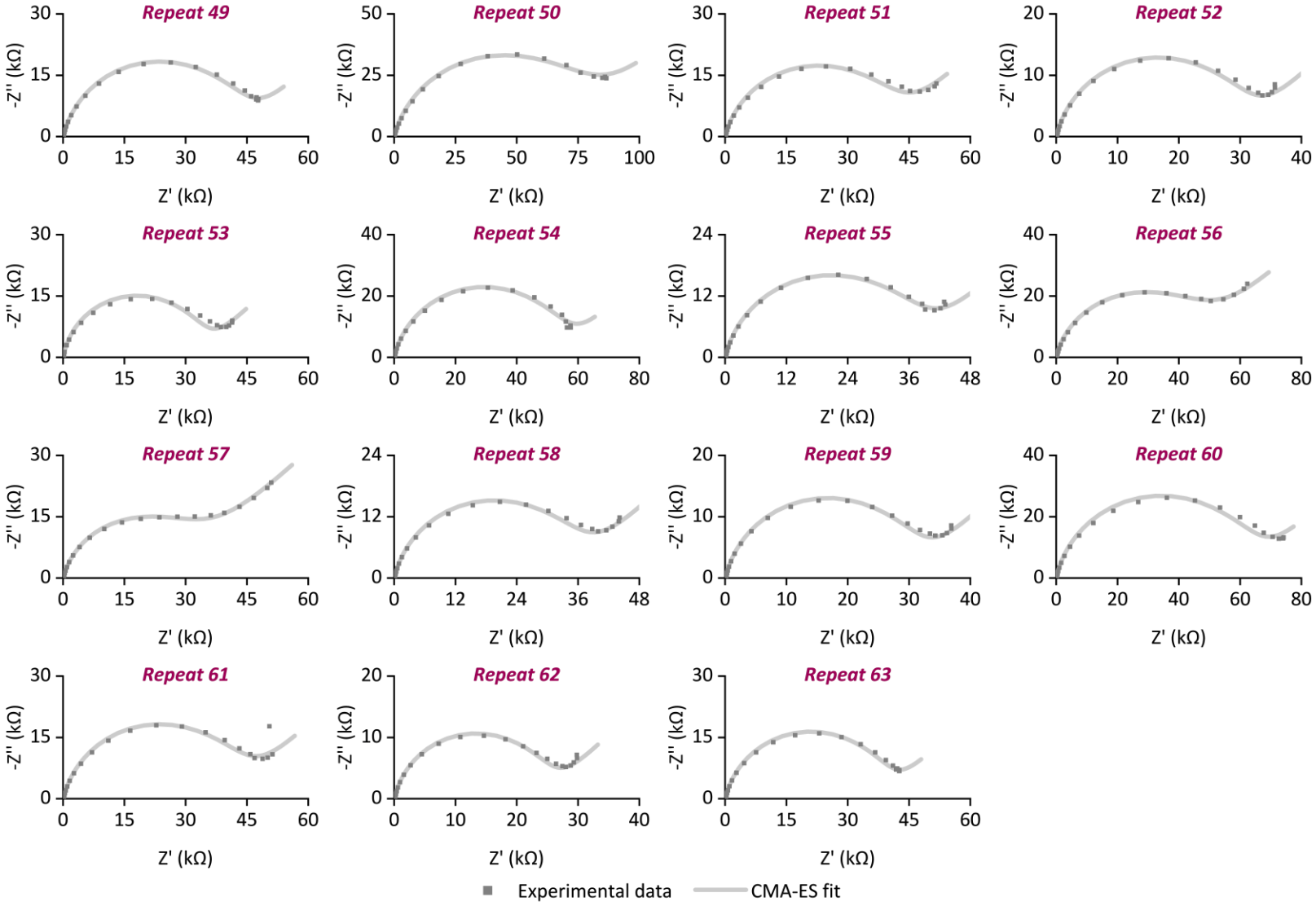

Figure 7.6. *ctd.*

For the polymer-only modified electrodes less repeats were collected so it is not appropriate to present this data alongside the bare and P-GFF modified data on the box and whisker plot. However, for the data collected the mean R_{ct} value for the collected P-modified SPEs was 89.4 kΩ which is significantly different from that determined for P-GFF modified SPEs which was 34.2 kΩ. This is likely to be due to difference in polarity of the presenting head groups in the two cases, the polar hydroxy-containing sugar units versus the relatively apolar dibenzocyclooctyne units, interacting differently with the ferricyanide containing aqueous solution.

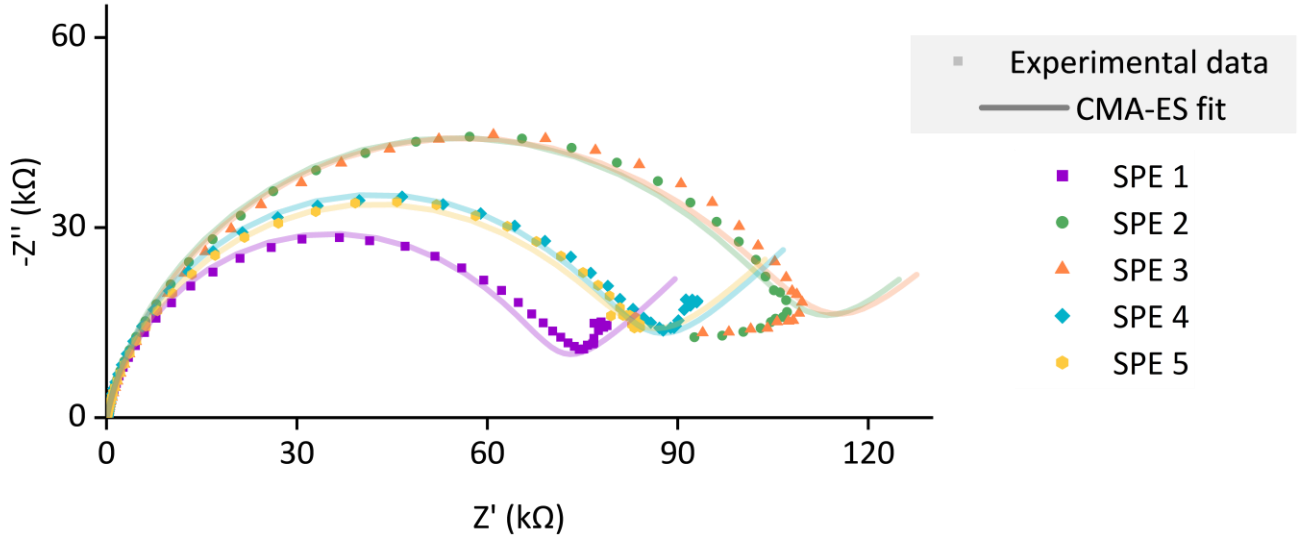

Figure 7.7. *The electrochemical response of different Au-SPEs modified with just thiol-terminated dibenzocyclooctyne-functionalised poly(hydroxyethyl acrylamide) (DBCO-$(PHEA)_{25}$-SH); i.e. "polymer-only", GFF-free controls, where the dots are the experimental data and the lines are the computational fits to a modified Randles circuit, the extracted R_{ct} values for the five repeats are as follows: 68.8, 107, 109, 81.8, and 81.0 kΩ.*

7.3. Determination of CMA-ES fitting method

The plots in this appendix were generated by Dr Henry Lloyd-Laney. This analysis of 1 CPE vs 2 CPE and comparing the fits to the Bode vs Nyquist data was carried out on P-GFF modified electrodes before and after galectin-3 incubation.

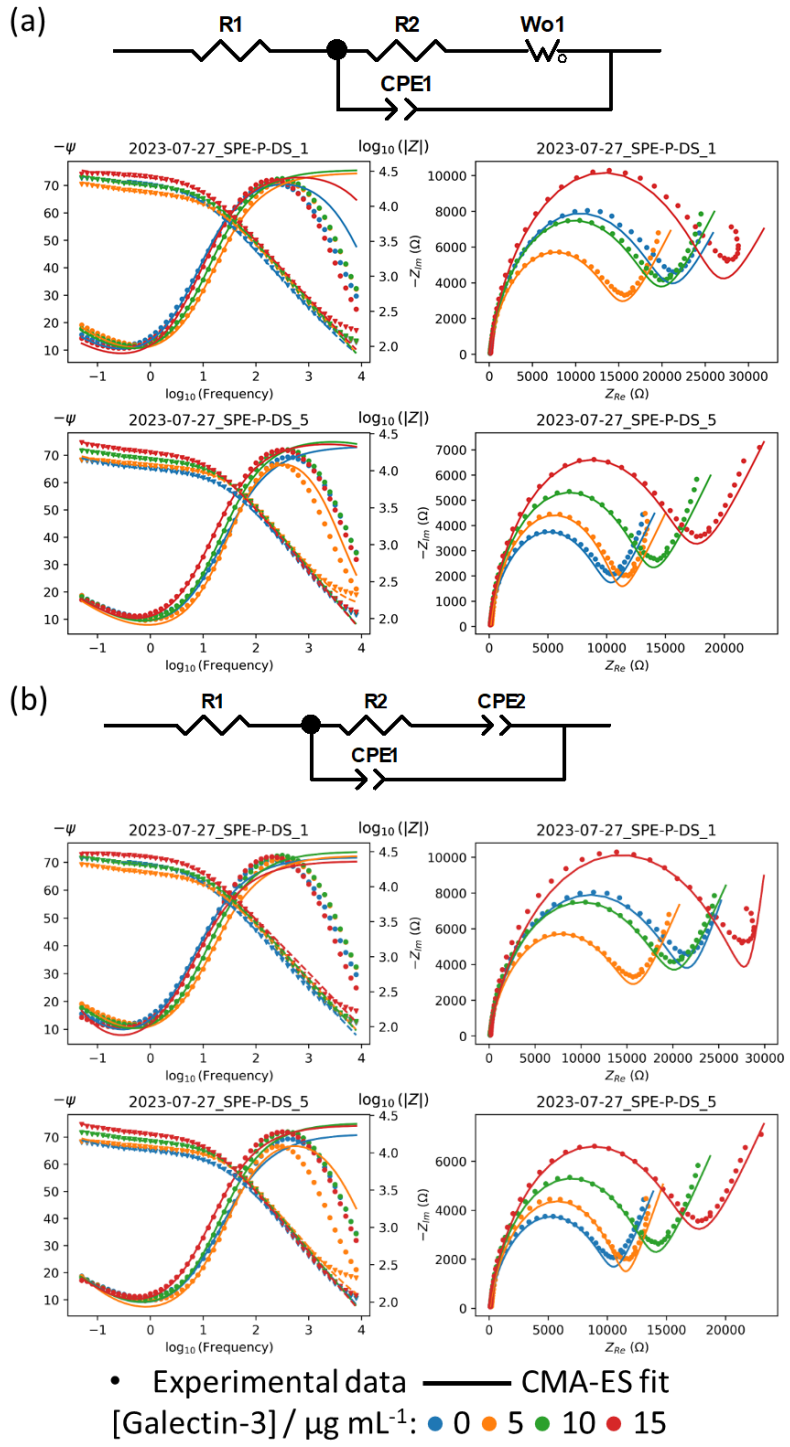

Figure 7.8. *Comparison of (a) one CPE and (b) two CPE circuit fits to two sets of P-GFF modified galectin-3 incubations. R1: solution resistance, R2: resistance to charge transfer, Wo1: Warburg element, and CPE: constant phase element.*

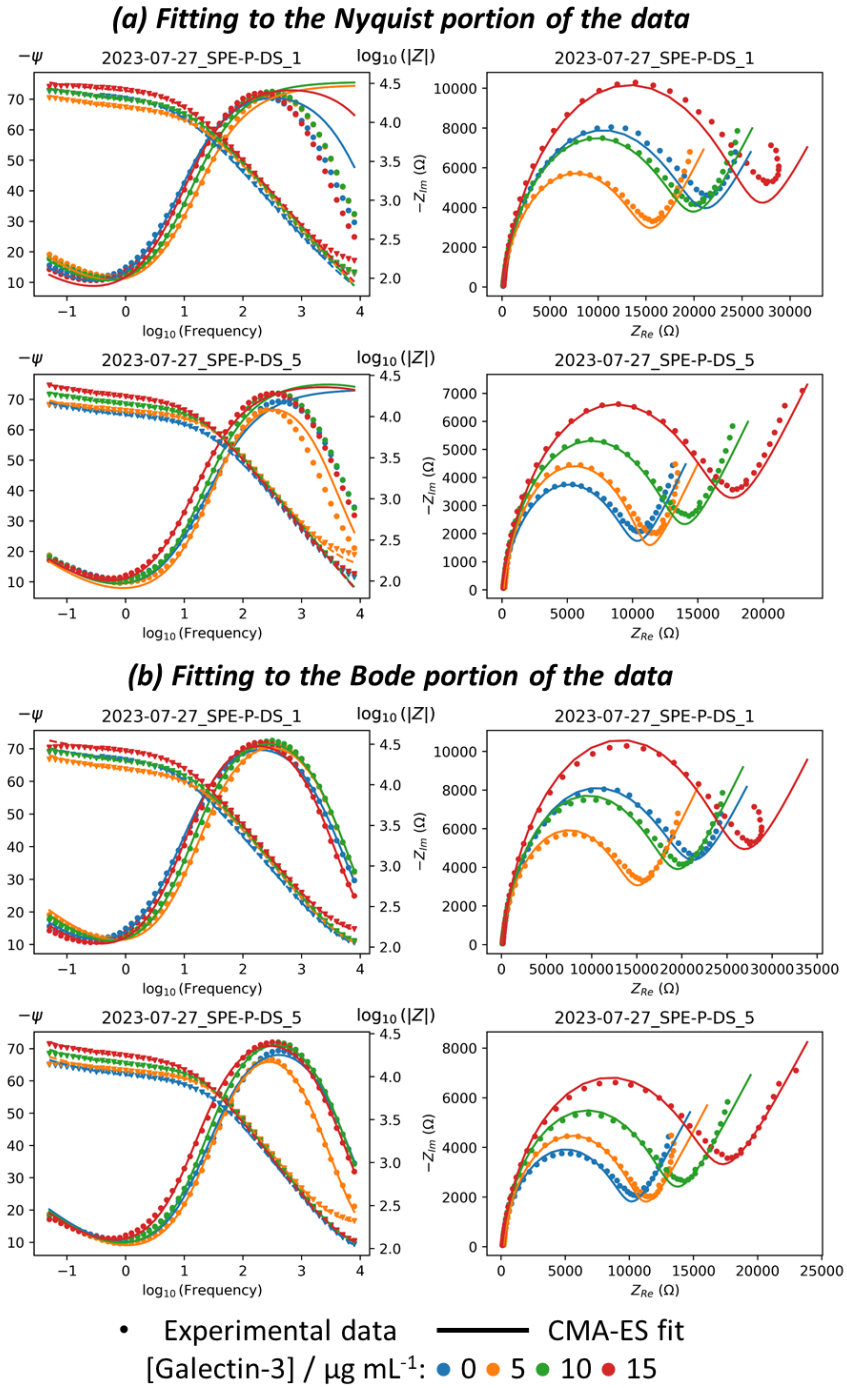

Figure 7.9. *Comparison of fitting to the (a) Nyquist or the (b) Bode portion of the electrochemical impedance analysis of two sets of P-GFF modified electrodes incubated in galectin-3.*

Figure 7.8 compares a one CPE and two CPE circuit whereas **Figure 7.9** compares fitting to the Nyquist versus the Bode portion of the data. A Warburg element is used to model diffusion when circuit fitting to electrochemical impedance data which contain processes under diffusion control. Processes under diffusion control exhibit a phase shift of 45° so when fitting using a Warburg element the phase shift is confined to this value. However, a constant phase element (CPE) is mathematical the same except it has the ability to vary the

phase shift which may give a better fit. **Figure 7.8(a)** and **(b)** compare the fits using one CPE versus two CPEs and while there isn't a significant difference the one CPE circuit seems to provide a better fit especially when examining the low and high frequency regions of the Bode plot. Additionally, using a one CPE circuit makes more scientific sense so all fits have been performed with this circuit.

When considering the differences between fitting to the Nyquist or the Bode data it can be observed that fitting to the Nyquist plot (**Figure 7.9(a)**) provides a better fit to low frequency data compared to fitting to the Bode plot (**Figure 7.9(b)**) which fits better to high frequency data. Overall, fitting to the Bode data gives better fits to the two forms of the data so the CMA-ES algorithm has been employed to fit to Bode data throughout our experiments.

7.4. Statistical t-test analysis

The statistics hypothesis testing tool in Origin was used to prove that we can be confident that the bare electrode dataset is significantly different from the data for P-GFF modified Au-SPEs. Conversely, the sub-dataset of measurements on P-GFF electrodes modified with the same solution over a long period of time is not significantly different from the mean of R_{ct} measurements taken from all P-GFF experiments.

- **Two Sample t Test Comparing Bare (N = 16) to P-GFF (N = 63)**

Descriptive Statistics

		N	Mean	SD	SEM	Median
"R\-(ct)"		63	34.1882	17.93713	2.25987	31.78281
		16	2.80768	1.51653	0.37913	2.72767
	Difference		31.38052		4.50985	
	Overall	79	27.83266	20.42722	2.29824	26.93427

Standard Error of Mean (SEM) of difference is computed under the condition that equal variance is assumec

t-Test Statistics

	t Statistic	DF	Prob>|t|
Equal Variance Assumed	6.95822	77	9.9725E-10
Equal Variance NOT Assumed (Welch Correction)	13.69462	65.32533	7.17624E-21

Null Hypothesis: mean1-mean2 = 0
Alternative Hypothesis: mean1-mean2 <> 0
At 0.05 level, when equal variance is assumed, Mean1 - Mean2 is significantly different from 0
At 0.05 level, when equal variance is NOT assumed, Mean1 - Mean2 is significantly different from 0

Confidence Intervals for Mean

	Conf. Levels in %	Lower Limits	Upper Limits
	90	23.87215	38.8889
	95	22.40027	40.36078
	99	19.46912	43.29192

Plots

Histogram	Box Plot
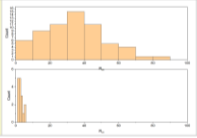	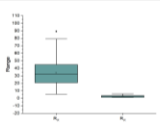

- **One Sample t Test Comparing Inter-Day Variability (N = 20) to the P-GFF Population Mean**

One Sample t Test (27/08/2024 16:44:07

Descriptive Statistics

	N	Mean	SD	SEM
"R\-(ct)"	20	32.15328	13.92686	3.11414

Test Statistics

	t Statistic	DF	Prob>|t|
"R\-(ct)"	-0.65345	19	0.5213

Null Hypothesis: Mean = 34.1882
Alternative Hypothesis: Mean <> 34.1882
"R_{ct}": At the 0.05 level, the population mean is NOT significantly different from the test mean (34.1882).

Confidence Intervals for Mean

	Conf. Levels in %	Lower Limits	Upper Limits
"R\-(ct)"	90	26.76852	37.53804
	95	25.63531	38.67125
	99	23.24393	41.06263

Plots

Histogram	Box Plot
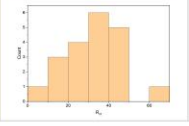	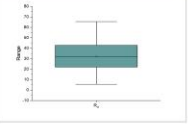

7.5. CMA-ES and MCMC parameter bounds

The Gaussian log-likelihood function is defined as follows for a set of equivalent circuit parameters *p* that are combined to predict an impedance response *f(p)* at *n* frequencies *ω*, and compared to impedance data ***x*** (both the model and data are in their polar forms, and so take the form of a 2xn matrix). We assume an independent joint likelihood for the phase and magnitude, and assume the noise in both variables is identically and independently distributed. This results in the following log-likelihood

$$\mathrm{L}(p, \sigma \mid x) = -n\, log 2\pi - \sum_{i=1}^{2} n log(\sigma_i) - \sum_{i=1}^{2} \left[\frac{1}{2{\sigma_i}^2} \sum_{j=1}^{n} (x_{i_j} - f_{i_j}(p))^2 \right]$$

Table 7.1. *Parameter bounds used for both the CMA-ES and MCMC algorithms (in the form of a log prior for the latter).*

Parameter	Lower Bound	Upper Bound
R_s / Ω	0	1 x 10^4
W / Ω $s^{-½}$	0	1 x 10^6
R_{ct} / Ω	1 x 10^{-6}	1 x 10^6
Q	0	2
α	0	1

7.6. NMR spectra for 3FGal-β(1,3)-GlcNAc-N_3

^{1}H NMR spectrum for 3FGal-β(1,3)-GlcNAc-N_3

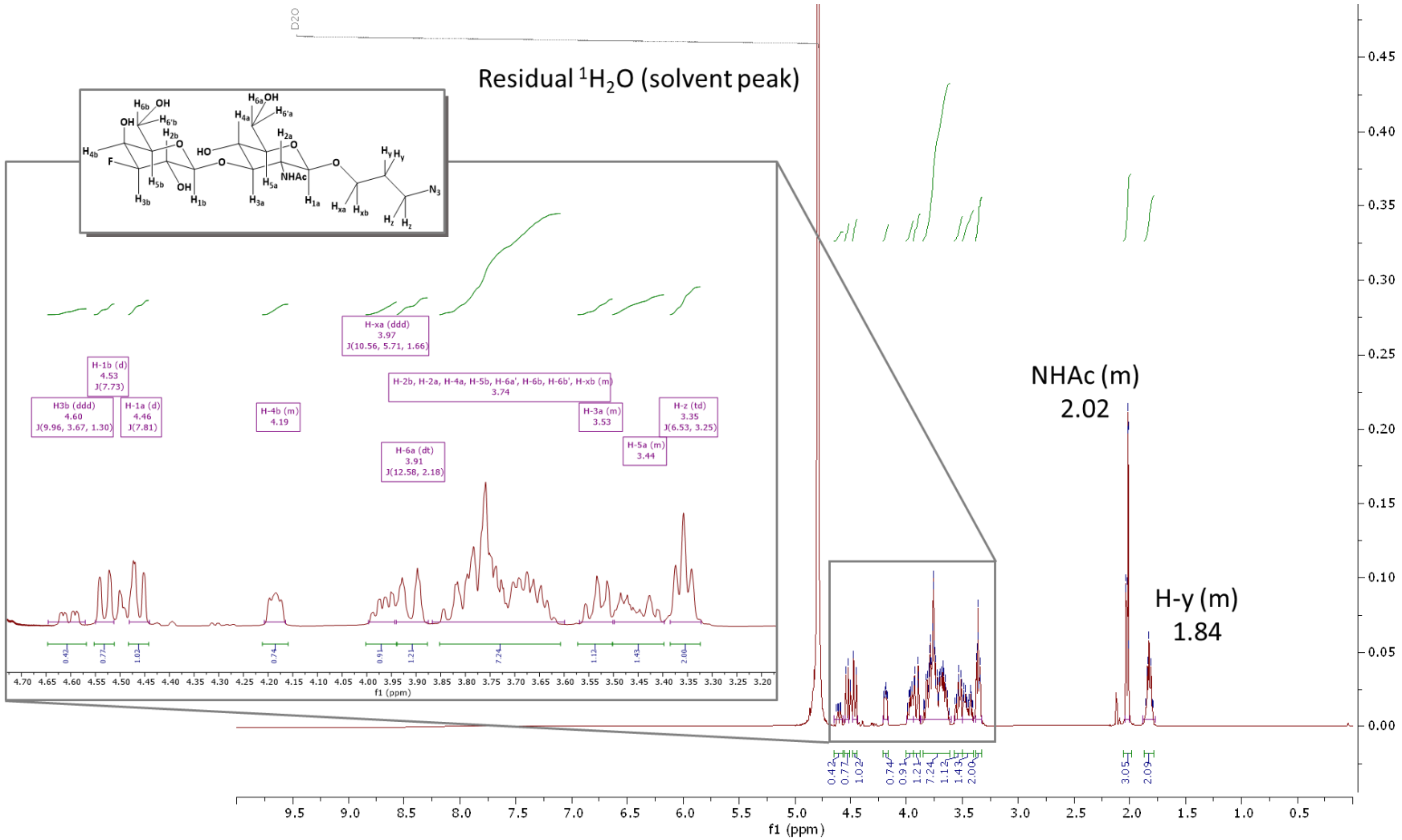

Figure 7.10. *^{1}H NMR (400 MHz) of 3FGal-β(1,3)-GlcNAc-Pr-N_3.*

^{13}C NMR spectrum for 3FGal-β(1,3)-GlcNAc-N_3

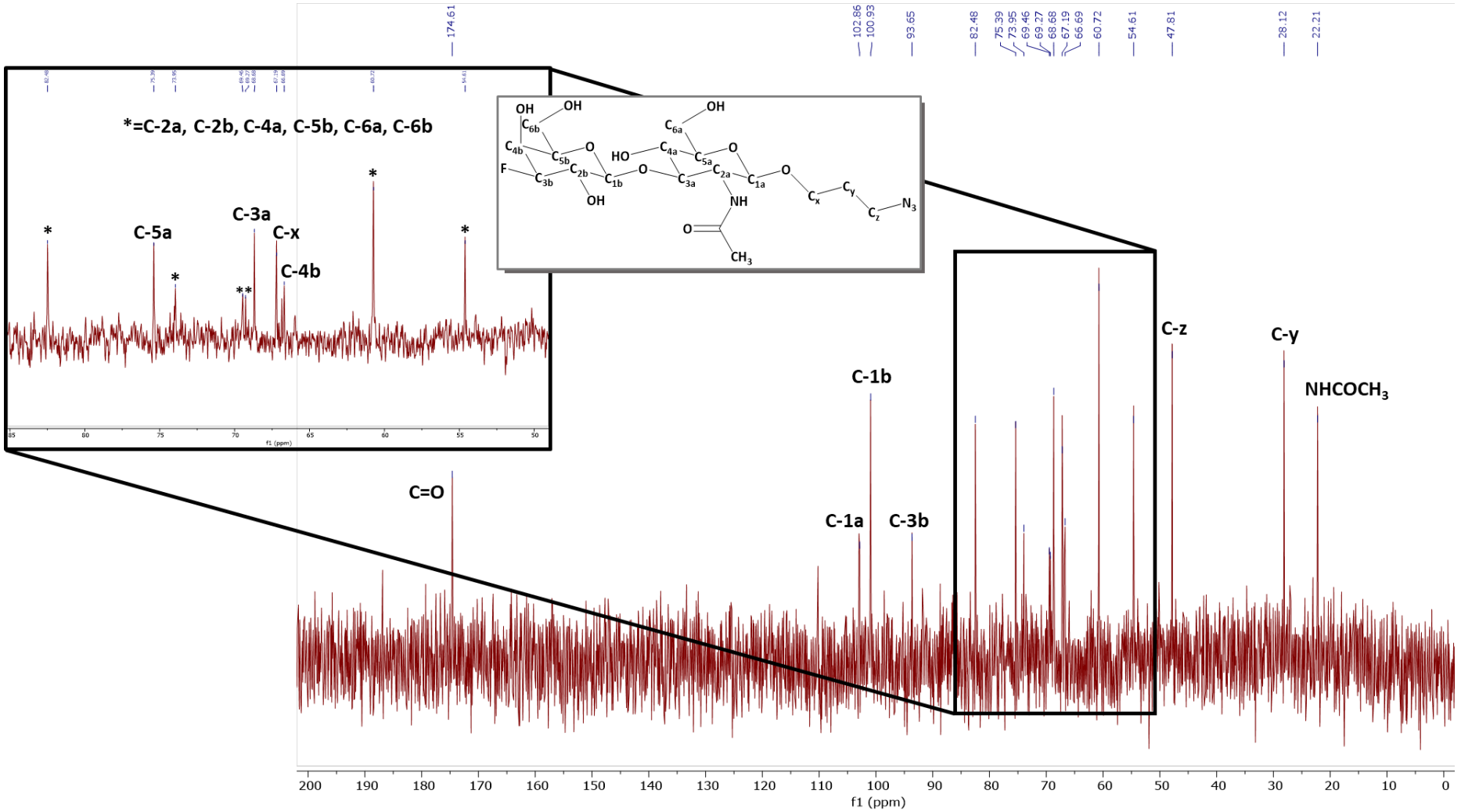

Figure 7.11. *^{13}C NMR (100 MHz) of 3FGal-β(1,3)-GlcNAc-Pr-N_3.*

^{19}F NMR spectrum for 3FGal-β(1,3)-GlcNAc-N_3

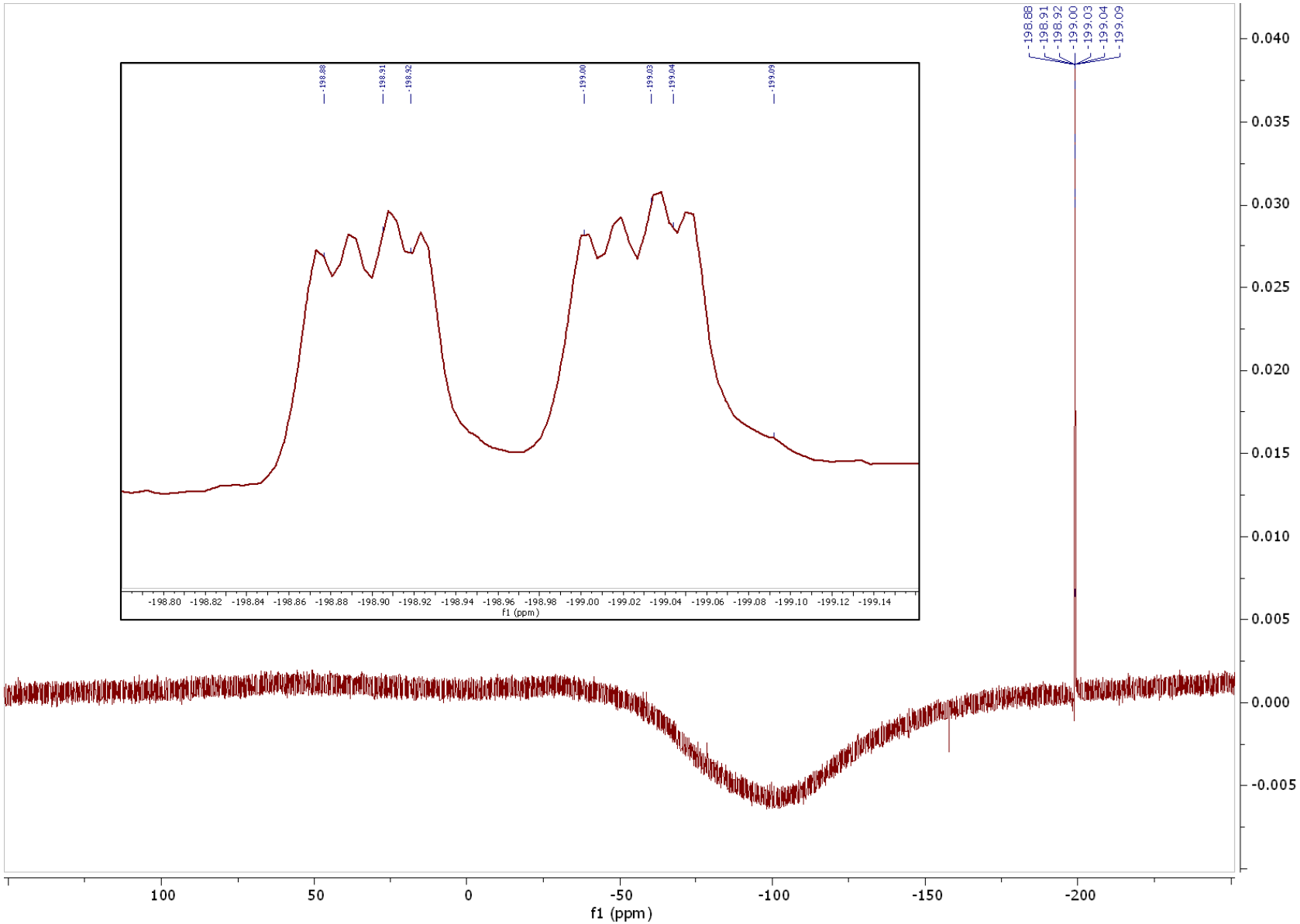

Figure 7.12. *^{19}F NMR (400 MHz) of 3FGal-β(1,3)-GlcNAc-Pr-N_3.*

7.7. Circuit fitting without Warburg element post-electrografting

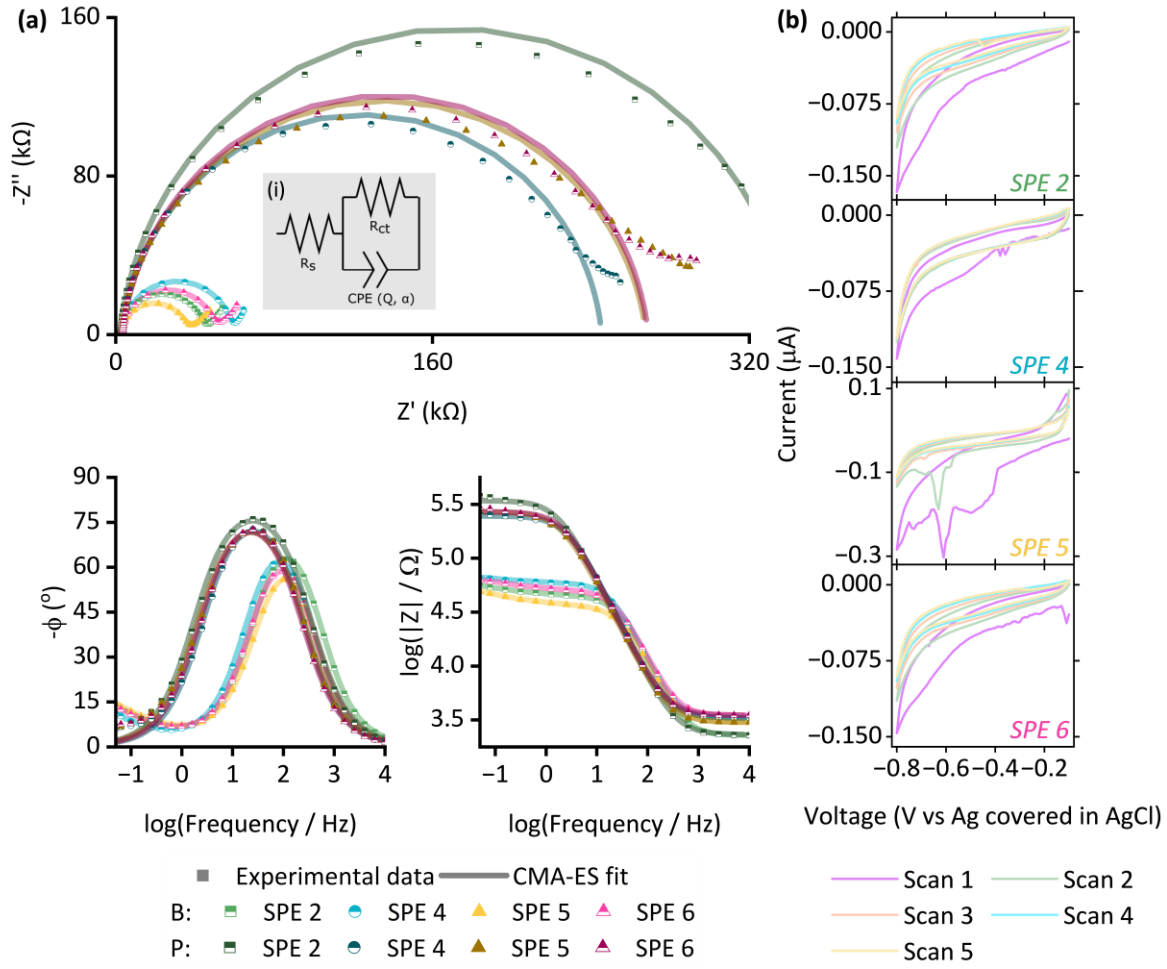

Figure 7.13. *(a) Resultant Nyquist and Bode plots of bare, B, (lighter colours) and polymer-modified, TABD-P, (darker colours) showing experimental data (points) and the computational fitting (lines) to the circuit given in (i) following electrografting on C-SPEs. EIS measurements were performed in the presence of 10 mM $K_3[Fe(CN)_6]$ in pH 7 aqueous buffer (100 mM sodium phosphate, 233 mM sodium chloride) with the following parameters: $t_{(equilibration)}$ = 180 s, E_{DC} = 0.230 V vs. Ref, E_{AC} = 10 mV, f = 0.05 Hz – 10 kHz (10 datapoints per decade). (b) Corresponding electrograft for each electrode. CVs were collected by scanning between -0.1 to -0.8 V vs Ag covered in AgCl at 20 mVs^{-1} for 5 scans. R_s = solution resistance, R_{ct} = resistance to charge transfer, and Q and α are the parameters used to model a constant phase element (CPE).*

References

1 V. Naresh and N. Lee, *Sensors (Basel)*, 2021, **21**, 1–35.

2 D. R. Thevenot, K. Tóth, R. A. Durst and G. S. Wilson, *Pure Appl. Chem.*, 1999, **71**, 2333–2348.

3 N. Sandhyarani, in *Electrochemical Biosensors*, Elsevier, 2019, pp. 45–75.

4 A. C. Carpenter, I. T. Paulsen and T. C. Williams, *Genes (Basel).*, DOI:10.3390/GENES9080375,.

5 Point Of Care Diagnostics Market | Industry Report, 2030, https://www.grandviewresearch.com/industry-analysis/point-of-care-poc-diagnostics-industry, (accessed 6 September 2025).

6 O. B. Daramola, · Richard Kolade Omole, · Bolanle and A. Akinsanola, *Discover Sensors 2025 1:1*, 2025, **1**, 1–26.

7 A. Zamora-Gálvez, E. Morales-Narváez, C. C. Mayorga-Martinez and A. Merkoçi, *Appl. Mater. Today*, 2017, **9**, 387–401.

8 A. A. Lahcen and A. Amine, *Wearable Physical, Chemical and Biological Sensors: Fundamentals, Materials and Applications*, 2022, 41–70.

9 Z. Fu, Y.-C. Lu and J. J. Lai, *Chonnam Med. J.*, 2019, **55**, 86–98.

10 J. P. Chambers, B. P. Arulanandam, L. L. Matta, A. Weis and J. J. Valdes, *Current Issues in Molecular Biology 2008, Vol. 10, Pages 1-12*, 2008, **10**, 1–12.

11 B. Sequeira-Antunes and H. A. Ferreira, *Biomedicines*, 2023, **11**, 3201.

12 M. Gheorghiu, *J. Biomed. Res.*, 2020, **35**, 255.

13 E. P. Randviir and C. E. Banks, *Anal. Methods*, 2022, **14**, 4602–4624.

14 G.-P. Nikoleli, C. G. Siontorou, M.-T. Nikolelis, S. Bratakou and D. K. Bendos, *Appl. Sci.*, 2019, **9**, 1745.

15 G.-P. Nikoleli, D. P. Nikolelis, G. Evtugyn and T. Hianik, *TrAC, Trends Anal. Chem.*, 2016, **79**, 210–221.

16 A. Blsakova, F. Kveton and J. Tkac, *Curr. Opin. Electrochem.*, 2019, **14**, 60–65.

17 A. N. Baker, S. J. Richards, S. Pandey, C. S. Guy, A. Ahmad, M. Hasan, C. I. Biggs, P. G. Georgiou, A. J. Zwetsloot, A. Straube, S. Dedola, R. A. Field, N. R. Anderson, M. Walker, D. Grammatopoulos and M. I. Gibson, *ACS Sens.*, 2021, **6**, 3696–3705.

18 A. Varki, *Glycobiology*, 2017, **27**, 3–49.

19 H. J. Gabius, *Biosystems*, 2018, **164**, 102–111.

20 L. Han and C. E. Costello, *Biochemistry (Moscow)*, 2013, **78**, 710–720.

21 J. Lloyd, *Biochem. (Lond).*, 2021, **43**, 52–57.

22 S. Dedola, M. D. Rugen, R. J. Young and R. A. Field, *ChemBioChem*, 2020, **21**, 423–427.

23 E. F. J. Cosgrave, J. J. Kattla, M. P. Campbell, W. B. Struwe, M. R. Wormald and P. M. Rudd, *Comprehensive Biotechnology*, 2009, 413–434.

24 A. N. Baker, S. J. Richards, S. Pandey, C. S. Guy, A. Ahmad, M. Hasan, C. I. Biggs, P. G. Georgiou, A. J. Zwetsloot, A. Straube, S. Dedola, R. A. Field, N. R. Anderson, M. Walker, D. Grammatopoulos and M. I. Gibson, *ACS Sens.*, 2021, **6**, 3696–3705.

25 S. Hargol Zadeh, S. Kashanian and M. Nazari, *Biosensors (Basel).*, 2023, **13**, 619.

26 Y. H. Tang, H. C. Lin, C. L. Lai, P. Y. Chen and C. H. Lai, *Biosens. Bioelectron.*, 2018, **116**, 100–107.

27 Y. Chevolot, S. Vidal, E. Laurenceau, F. Morvan, J.-J. Vasseur and E. Souteyrand, in *Recognition Receptors in Biosensors*, Springer New York, New York, NY, 2010, pp. 275–341.

28 H. Lis and N. Sharon, *Chem. Rev. (Washington, DC, U. S.)*, 1998, **98**, 637–674.

29 G. D. Brown, J. A. Willment and L. Whitehead, *Nat. Rev. Immunol.*, 2018, **18**, 374–389.
30 J. F. Kennedy, P. M. G. Palva, M. T. S. Corella, M. S. M. Cavalcanti and L. C. B. B. Coelho, *Carbohydr. Polym.*, 1995, **26**, 219–230.
31 K. K. Kumar, K. L. P. Chandra, J. Sumanthi, G. S. Reddy, P. C. Shekar and B. Reddy, *J. Orofacial Sci.*, 2012, **4**, 20.
32 A. Varki, R. D. Cummings, J. D. Esko, P. Stanley, G. W. Hart, M. Aebi, D. Mohnen, T. Kinoshita, N. H. Packer, J. H. Prestegard, R. L. Schnaar and P. H. Seeberger, *Essentials of Glycobiology*, Cold Spring Harbor Laboratory Press, 4th edn., 2022.
33 F. A. Quiocho, *Annu. Rev. Biochem.*, 2003, **55**, 287–315.
34 L. Otten and M. I. Gibson, *RSC Adv.*, 2015, **5**, 53911–53914.
35 A. Hushegyi, T. Bertok, P. Damborsky, J. Katrlik and J. Tkac, *Chem. Commun. (Cambridge, U. K.)*, 2015, **51**, 7474–7477.
36 F. Cui, Y. Xu, R. Wang, H. Liu, L. Chen, Q. Zhang and X. Mu, *Biosens. Bioelectron.*, 2018, **103**, 94–98.
37 X. Guo, A. Kulkarni, A. Doepke, H. B. Halsall, S. Iyer and W. R. Heineman, *Anal. Chem.*, 2012, **84**, 241–246.
38 F. Kveton, A. Blšáková, A. Hushegyi, P. Damborsky, O. Blixt, B. Jansson and J. Tkac, *Langmuir*, 2017, **33**, 2709–2716.
39 A. Hushegyi, D. Pihíková, T. Bertok, V. Adam, R. Kizek and J. Tkac, *Biosens. Bioelectron.*, 2016, **79**, 644–649.
40 S. Hargol Zadeh, S. Kashanian and M. Nazari, *Biosensors (Basel).*, 2023, **13**, 619.
41 Y. H. Tang, H. C. Lin, C. L. Lai, P. Y. Chen and C. H. Lai, *Biosens. Bioelectron.*, 2018, **116**, 100–107.
42 A. Shitrit, S. Mardhekar, I. Alshanski, P. Jain, R. Raigawali, C. D. Shanthamurthy, R. Kikkeri, S. Yitzchaik and M. Hurevich, *Chem. - Eur. J.*, 2022, **28**, e202202193.
43 A. N. Baker, S.-J. Richards, C. S. Guy, T. R. Congdon, M. Hasan, A. J. Zwetsloot, A. Gallo, J. R. Lewandowski, P. J. Stansfeld, A. Straube, M. Walker, S. Chessa, G. Pergolizzi, S. Dedola, R. A. Field and M. I. Gibson, *ACS Cent. Sci.*, 2020, **6**, 2046–2052.
44 D. Capasso, L. Pirone, S. Di Gaetano, R. Russo, M. Saviano, V. Frisulli, A. Antonacci, E. Pedone and V. Scognamiglio, *TrAC Trends in Analytical Chemistry*, 2023, **159**, 116952.
45 L. Johannes, R. Jacob and H. Leffler, *J. Cell Sci.*, 2018, **131**, jcs208884.
46 R. J. Pieters, *ChemBioChem*, 2006, **7**, 721–728.
47 S. H. Barondes, V. Castronovo, D. N. W. Cooper, R. D. Cummings, K. Drickamer, T. Felzi, M. A. Gitt, J. Hirabayashi, C. Hughes, K. ichi Kasai, H. Leffler, F. T. Liu, R. Lotan, A. M. Mercurio, M. Monsigny, S. Pillai, F. Poirer, A. Raz, P. W. J. Rigby, J. M. Rini and J. L. Wang, *Cell*, 1994, **76**, 597–598.
48 N. Martínez-Bosch, A. Rodriguez-Vida, N. Juanpere, J. Lloreta, A. Rovira, J. Albanell, J. Bellmunt and P. Navarro, *Nat. Rev. Urol.*, 2019, **16**, 433–445.
49 T. J. Hsieh, H. Y. Lin and C. H. Lin, 2016, preprint, DOI: 10.2210/pdb5h9q/pdb.
50 H. Yoshida and S. Kamitori, 2010, preprint, DOI: 10.2210/pdb3nv1/pdb.
51 K. Saraboji, M. Hakansson, C. Diehl, U. J. Nilsson, H. Leffler, M. Akke and D. T. Logan, 2011, preprint, DOI: 10.2210/pdb3zsj/pdb.
52 J. D. Kaminker and A. V. Timoshenko, *Biomolecules 2021, Vol. 11, Page 1909*, 2021, **11**, 1909.
53 N. W. van der Hoeven, M. R. Hollander, C. Yildirim, M. F. Jansen, P. F. Teunissen, A. J. Horrevoets, T. C. T. M. van der Pouw Kraan and N. van Royen, *Vascul. Pharmacol.*, 2016, **81**, 31–41.

54 N. Zhang, Q. Liu, D. Wang, X. Wang, Z. Pan, B. Han and G. He, *Biomark. Res.*, 2025, **13**, 49.
55 P. Demetter, N. Nagy, B. Martin, A. Mathieu, P. Dumont, C. Decaestecker and I. Salmon, *J. Pathol.*, 2008, **215**, 1–12.
56 H. Barrow, X. Guo, H. H. Wandall, J. W. Pedersen, B. Fu, Q. Zhao, C. Chen, J. M. Rhodes and L. G. Yu, *Clinical Cancer Research*, 2011, **17**, 7035–7046.
57 E. Ramos-Martínez, I. Ramos-Martínez, I. Sánchez-Betancourt, J. C. Ramos-Martínez, S. I. Peña-Corona, J. Valencia, R. Saucedo, E. K. P. Almeida-Aguirre and M. Cerbón, *Biomolecules*, DOI:10.3390/BIOM12081062,.
58 M. F. Troncoso, R. Chammas, V. F. Carvalho, F. L. Oliveira and D. M. S. Villa-Verde, *Front. Endocrinol. (Lausanne).*, 2025, **16**, 1545421.
59 S. Sciacchitano, L. Lavra, A. Morgante, A. Ulivieri, F. Magi, G. P. De Francesco, C. Bellotti, L. B. Salehi and A. Ricci, *International Journal of Molecular Sciences 2018, Vol. 19, Page 379*, 2018, **19**, 379.
60 H. Tomizawa, Y. Yamada, M. Arima, Y. Miyabe, M. Fukuchi, H. Hikichi, R. C. N. Melo, T. Yamada and S. Ueki, *Biomolecules*, DOI:10.3390/BIOM12101385.
61 L. Yi, Y. Feng, D. Chen, Y. Jin and S. Zhang, *COPD*, 2023, **20**, 101–108.
62 M. Farhad, A. S. Rolig and W. L. Redmond, *Oncoimmunology*, 2018, **7**, e1434467.
63 T. Fukumori, N. Oka, Y. Takenaka, P. Nangia-Makker, E. Elsamman, T. Kasai, M. Shono, H. O. Kanayama, J. Ellerhorst, R. Lotan and A. Raz, *Cancer Res.*, 2006, **66**, 3114–3119.
64 National Cancer Institute Roundtable on Prostate Cancer: Future Research Directions1 | Cancer Research | American Association for Cancer Research, https://aacrjournals.org/cancerres/article/51/9/2498/497526/National-Cancer-Institute-Roundtable-on-Prostate, (accessed 8 March 2022).
65 Prostate cancer statistics | Cancer Research UK, https://www.cancerresearchuk.org/health-professional/cancer-statistics/statistics-by-cancer-type/prostate-cancer, (accessed 8 March 2022).
66 V. Balan, Y. Wang, P. Nangia-Makker, D. Kho, M. Bajaj, D. Smith, L. Heilbrun, A. Raz and E. Heath, *Oncotarget*, 2013, **4**, 542–549.
67 J. L. Araújo-Filho, M. R. Melo-Junior, E. I. C. Beltrão, L. R. A. de Lima, C. B. L. Antunes and L. B. de Carvalho, *Int. J. Clin. Exp. Pathol.*, 2013, **6**, 1861.
68 Prostate Cancer - UK National Screening Committee (UK NSC) - GOV.UK, https://view-health-screening-recommendations.service.gov.uk/prostate-cancer/, (accessed 8 March 2022).
69 What is thyroid cancer? | Cancer Research UK, https://www.cancerresearchuk.org/about-cancer/thyroid-cancer/about-thyroid-cancer, (accessed 24 September 2025).
70 B. S. Sumana, S. Shashidhar and A. S. Shivarudrappa, *J. Clin. Diagn. Res.*, 2015, **9**, EC07.
71 T. M. Okda, G. M. K. Atwa, A. F. Eldehn, N. Dahran, K. F. Alsharif and E. K. Elmahallawy, *Biomedicines*, 2022, **10**, 352.
72 J. Li, E. Vasilyeva and S. M. Wiseman, *Expert Rev. Anticancer Ther.*, 2019, **19**, 1017–1027.
73 E. N. Primo, M. J. Kogan, H. E. Verdejo, S. Bollo, M. D. Rubianes and G. A. Rivas, *ACS Appl. Mater. Interfaces*, 2018, **10**, 23501–23508.
74 A. K. Bi, V. Santhosh and K. Sigamani, *Cureus*, 2022, **14**, e28310.
75 A. R. Van Der Velde, L. Gullestad, T. Ueland, P. Aukrust, Y. Guo, A. Adourian, P. Muntendam, D. J. Van Veldhuisen and R. A. De Boer, *Circ. Heart Fail.*, 2013, **6**, 219–226.

76 Z. Tang, J. He, J. Chen, Y. Niu, Y. Zhao, Y. Zhang and C. Yu, *Biosens. Bioelectron.*, 2018, **101**, 253–259.
77 K. Hollingsworth, A. Di Maio, S. J. Richards, J. B. Vendeville, D. E. Wheatley, C. E. Council, T. Keenan, H. Ledru, H. Chidwick, K. Huang, F. Parmeggiani, A. Marchesi, W. Chai, R. McBerney, T. P. Kamiński, M. R. Balmforth, A. Tamasanu, J. D. Finnigan, C. Young, S. L. Warriner, M. E. Webb, M. A. Fascione, S. Flitsch, M. C. Galan, T. Feizi, M. I. Gibson, Y. Liu, W. B. Turnbull and B. Linclau, *Nature Communications* , 2024, **15**, 1–14.
78 Y. K. Park, B. Bold, W. K. Lee, M. H. Jeon, K. H. An, S. Y. Jeong and Y. K. Shim, *International Journal of Molecular Sciences 2011, Vol. 12, Pages 2946-2957*, 2011, **12**, 2946–2957.
79 M. C. Martos-Maldonado, I. Quesada-Soriano, L. García-Fuentes and A. Vargas-Berenguel, *Nanomaterials 2020, Vol. 10, Page 203*, 2020, **10**, 203.
80 D. Vrbata, M. Filipová, M. R. Tavares, J. Červený, M. Vlachová, M. Šírová, H. Pelantová, L. Petrásková, L. Bumba, R. Konefał, T. Etrych, V. Křen, P. Chytil and P. Bojarová, *J. Med. Chem.*, 2022, **65**, 3866–3878.
81 J. Jiménez-Barbero, B. Linclau, A. Ardá, N. C. Reichardt, M. Sollogoub, L. Unione and S. P. Vincent, *Chem. Soc. Rev.*, 2020, **49**, 3863–3888.
82 Y. Yu and M. Delbianco, *Chem. - Eur. J.*, 2020, **26**, 9814–9825.
83 C. Jordan, K. Siebold, P. Priegue, P. H. Seeberger and R. Gilmour, *J. Am. Chem. Soc.*, 2024, **146**, 15366–15375.
84 S. J. Richards, T. Keenan, J. B. Vendeville, D. E. Wheatley, H. Chidwick, D. Budhadev, C. E. Council, C. S. Webster, H. Ledru, A. N. Baker, M. Walker, M. C. Galan, B. Linclau, M. A. Fascione and M. I. Gibson, *Chem. Sci.*, 2021, **12**, 905–910.
85 M. Kurfiřt, M. Dračínský, L. Červenková Šťastná, P. Cuřínová, V. Hamala, M. Hovorková, P. Bojarová and J. Karban, *Chem. - Eur. J.*, 2021, **27**, 13040–13051.
86 T. Keenan, F. Parmeggiani, J. Malassis, C. Q. Fontenelle, J. B. Vendeville, W. Offen, P. Both, K. Huang, A. Marchesi, A. Heyam, C. Young, S. J. Charnock, G. J. Davies, B. Linclau, S. L. Flitsch and M. A. Fascione, *Cell Chem. Biol.*, 2020, **27**, 1199-1206.e5.
87 H. Yu, V. Thon, K. Lau, L. Cai, Y. Chen, S. Mu, Y. Li, P. G. Wang and X. Chen, *Chemical Communications*, 2010, **46**, 7507–7509.
88 P. G. Georgiou, A. N. Baker, S. J. Richards, A. Laezza, M. I. Gibson, M. Walker and M. I. Gibson, *J. Mater. Chem. B*, 2019, **8**, 136–145.
89 S. K. Arya, A. Chaubey and B. D. Malhotra, *Proc Indian Natn Sci Acad*, 2006, **72**, 249–266.
90 R. S. Sethi, *Biosens. Bioelectron.*, 1994, **9**, 243–264.
91 M. Wang, L. Jin, P. Hang-Mei Leung, F. Wang-Ngai Chow, X. Zhao, H. Chen, W. Pan, H. Liu and S. Li, *Front. Bioeng. Biotechnol.*, 2024, **12**, 1393789.
92 A. Syahir, K. Usui, K. Tomizaki, K. Kajikawa and H. Mihara, *Microarrays (Basel)*, 2015, **4**, 228–244.
93 T. N. L. Pham, S. H. Nguyen and M. T. Tran, *Heliyon*, 2024, **10**, e38371.
94 V. Ong, M. A. Mohamed, H. Ma, A. Al-Shami, S. Khazaee Nejad, F. Amirghasemi, A. Tabassum, M. J. Lee, A. Rohleder, C. Zhu, C. Tam, P. Nowlen and M. P. S. Mousavi, *Biosens. Bioelectron.*, 2025, **280**, 117386.
95 F. A. R. Mota, M. L. C. Passos, J. L. M. Santos and M. L. M. F. S. Saraiva, *Biosens. Bioelectron.*, 2024, **251**, 116095.
96 M. Pimpilova, *Discover Electrochemistry*, 2024, **1**, 1–20.
97 A. Ainla, M. P. S. Mousavi, M. N. Tsaloglou, J. Redston, J. G. Bell, M. T. Fernández-Abedul and G. M. Whitesides, *Anal. Chem.*, 2018, **90**, 6240–6246.
98 X. Shen, F. Ju, G. Li and L. Ma, *Sensors (Basel)*, DOI:10.3390/S20102781.

99 A. V. Cordova-Huaman, V. R. Jauja-Ccana and A. La Rosa-Toro, *Heliyon*, 2021, **7**, e06259.
100 K. Komori, M. Usui, Y. Sakai, al -, M. E. Meyerhoff and K.-H. Cha, *ECS Sensors Plus*, 2022, **1**, 031601.
101 C. M. A. Brett and A. M. Oliveira. Brett, *Electrochemistry : principles, methods, and applications*, Oxford University Press, Oxford ; New York, 1993.
102 A. J. Bard and L. R. Faulkner, *Electrochemical Methods: Fundamentals and Applications*, John Wiley & Sons, Inc., New York, NY, 2nd Edition., 2001.
103 M. Madadelahi, F. O. Romero-Soto, R. Kumar, U. B. Tlaxcala and M. J. Madou, *Biosens. Bioelectron.*, 2025, **272**, 117099.
104 F. Lisdat and D. Schäfer, *Anal. Bioanal. Chem.*, 2008, **391**, 1555–1567.
105 S. Wang, J. Zhang, O. Gharbi, V. Vivier, M. Gao and M. E. Orazem, *Nature Reviews Methods Primers*, 2021, **1**, 41.
106 J. Lazar, C. Schnelting, E. Slavcheva and U. Schnakenberg, *Anal. Chem.*, 2016, **88**, 682–687.
107 J. Liu, M. M. Chisti and X. Zeng, *Anal. Chem.*, 2017, **89**, 4013–4020.
108 M. E. Strong, J. R. Richards, M. Torres, C. M. Beck and J. T. La Belle, *Biosens. Bioelectron.*, 2021, **177**, 112949.
109 A. C. Lazanas and M. I. Prodromidis, *ACS Measurement Science Au*, 2023, **3**, 162–193.
110 Basics of EIS: Electrochemical Research-Impedance Gamry Instruments, https://www.gamry.com/application-notes/EIS/basics-of-electrochemical-impedance-spectroscopy/, (accessed 20 July 2022).
111 A. Bogomolova, E. Komarova, K. Reber, T. Gerasimov, O. Yavuz, S. Bhatt and M. Aldissi, *Anal. Chem.*, 2009, **81**, 3944–3949.
112 E. P. Randviir and C. E. Banks, *Anal. Methods*, 2013, **5**, 1098–1115.
113 EIS Data Plotting | Pine Research Instrumentation, https://pineresearch.com/support-article/eis-data-plotting/, (accessed 29 August 2025).
114 J. Huang, Z. Li, B. Y. Liaw and J. Zhang, *J. Power Sources*, 2016, **309**, 82–98.
115 D. D. MacDonald, *Electrochim. Acta*, 2006, **51**, 1376–1388.
116 S. Holm, T. Holm and Ø. G. Martinsen, *PLoS One*, 2021, **16**, e0248786.
117 V. V. Pototskaya and O. I. Gichan, *Electrochim. Acta*, 2017, **235**, 583–594.
118 Electrochemical Impedance Spectroscopy (EIS) Basics | Pine Research Instrumentation, https://pineresearch.com/support-article/eis-basics/, (accessed 29 August 2025).
119 A. Lasia, *Electrochemical Impedance Spectroscopy and its Applications*, Springer New York, New York, NY, 2014.
120 R. Saxena and S. Srivastava, *Sens. Actuators B Chem.*, 2019, **297**, 126780.
121 E. B. Bahadir and M. K. Sezgintürk, *Artif. Cells Nanomed. Biotechnol.*, 2014, **44**, 248–262.
122 H. Cesiulis, N. Tsyntsaru, A. Ramanavicius and G. Ragoisha, *NanoScience and Technology*, 2016, 3–42.
123 J.-G. Guan, Y.-Q. Miao and Q.-J. Zhang, *J. Biosci. Bioeng.*, 2004, **97**, 219–226.
124 J. D. Schrattenecker, R. Heer, E. Melnik, T. Maier, G. Fafilek and R. Hainberger, *Biosens. Bioelectron.*, 2019, **127**, 25–30.
125 Y. Wang, Z. Ye and Y. Ying, *Sensors 2012, Vol. 12, Pages 3449-3471*, 2012, **12**, 3449–3471.
126 H. A. Hussein, A. Kandeil, M. Gomaa, R. Mohamed El Nashar, I. M. El-Sherbiny and R. Y. A. Hassan, *ACS Sens.*, 2021, **6**, 4098–4107.
127 H. S. Magar, R. Y. A. Hassan and A. Mulchandani, *Sensors*, 2021, **21**, 6578.

128 J. Chen, B. Arianpour, K. Wang, S. Wang, J. Yin, Y. Zhang, E. Zhu and T. K. Hsiai, *Front. Mater.*, 2023, **10**, 1146045.
129 J. Sopoušek, J. Věžník, J. Houser, P. Skládal and K. Lacina, *Electrochim. Acta*, 2021, **388**, 138616.
130 V. Vogiazi, A. De La Cruz, W. R. Heineman, R. J. White and D. D. Dionysiou, *Anal. Chem.*, 2021, **93**, 812–819.
131 G. Gao, M. Pan and C. D. Vecitis, *J. Mater. Chem. A Mater.*, 2015, **3**, 7575–7582.
132 K. Lacina, J. Věžník, J. Sopoušek, Z. Farka, V. Lacinová and P. Skládal, *Bioelectrochemistry*, DOI:10.1016/J.BIOELECHEM.2022.108308.
133 M. C. Rodriguez, A. N. Kawde and J. Wang, *Chemical Communications*, 2005, **4267**, 4267–4269.
134 S. Kaur and I. Kaur, *Electroanalysis*, 2019, **31**, 2507–2517.
135 N. J. Agard, J. A. Prescher and C. R. Bertozzi, *J. Am. Chem. Soc.*, 2004, **126**, 15046–15047.
136 S. Fletcher and V. J. Black, *J. Phys. Chem. C*, 2016, **120**, 8014–8022.
137 P. Valverde, J.-B. Vendeville, K. Hollingsworth, A. P. Mattey, T. Keenan, H. Chidwick, H. Ledru, K. Huonnic, K. Huang, M. E. Light, N. Turner, J. Jiménez-Barbero, M. C. Galan, M. A. Fascione, S. Flitsch, W. B. Turnbull and B. Linclau, *Chem. Commun. (Cambridge, U. K.)*, 2020, **56**, 6408–6411.
138 T. Keenan, R. Mills, E. Pocock, D. Budhadev, F. Parmeggiani, S. Flitsch and M. Fascione, *Carbohydr. Res.*, 2019, **472**, 132–137.
139 L. Li, Y. Liu, W. Wang, J. Cheng, W. Zhao and P. Wang, *Carbohydr. Res.*, 2012, **355**, 35–39.
140 H. Yu, V. Thon, K. Lau, L. Cai, Y. Chen, S. Mu, Y. Li, P. G. Wang and X. Chen, *Chem. Commun. (Camb).*, 2010, **46**, 7507.
141 N. N. Elgrishi, K. J. Rountree, B. D. Mccarthy, E. S. Rountree, T. T. Eisenhart and J. L. Dempsey, *J. Chem. Educ.*, 2018, **95**, 197–206.
142 R. D. Crapnell and C. E. Banks, *ChemElectroChem*, 2024, **11**, e202400370.
143 G. Paimard, E. Ghasali and M. Baeza, *Chemosensors 2023, Vol. 11, Page 113*, 2023, **11**, 113.
144 Y. Xue, X. Li, H. Li and W. Zhang, *Nat. Commun.*, 2014, **5**, 1–9.
145 A. Bardea, E. Katz and I. Willner, *Electroanalysis*, 2000, **12**, 1097–1106.
146 J. H. Conway and N. J. A. Sloane, DOI:10.1007/978-1-4757-6568-7.
147 L. M. Fischer, M. Tenje, A. R. Heiskanen, N. Masuda, J. Castillo, A. Bentien, J. Émneus, M. H. Jakobsen and A. Boisen, *Microelectron. Eng.*, 2009, **86**, 1282–1285.
148 E. Kerr, R. Alexander, P. S. Francis, R. M. Guijt, G. J. Barbante and E. H. Doeven, *Front. Chem.*, 2021, **8**, 628483.
149 M. Zamani, C. M. Klapperich and A. L. Furst, *Lab Chip*, 2023, **23**, 1410.
150 Y. Xue, X. Li, H. Li and W. Zhang, *Nature Communications 2014 5:1*, 2014, **5**, 4348-.
151 Y. Ram, T. Yoetz-Kopelman, Y. Dror, A. Freeman and Y. Shacham-Diamand, *Electrochim. Acta*, 2016, **200**, 161–167.
152 M. M. Rahman, A. J. S. Ahammad, J. H. Jin, S. J. Ahn and J. J. Lee, *Sensors 2010, Vol. 10, Pages 4855-4886*, 2010, **10**, 4855–4886.
153 Y. Nakajima, Y. Sato and T. Konishi, *Chem. Pharm. Bull. (Tokyo).*, 2007, **55**, 1222–1226.
154 M. H. Cheah and P. Chernev, *Scientific Reports 2021 11:1*, 2021, **11**, 1–7.
155 X. Hua, H. L. Xia and Y. T. Long, *Chem. Sci.*, 2019, **10**, 6215–6219.
156 S. Vogt, Q. Su, C. Gutiérrez-Sánchez and G. Nöll, *Anal. Chem.*, 2016, **88**, 4383–4390.

157 G. Zhang, Y. Qiao, T. Xu, C. Zhang, Y. Zhang, L. Shi, S. Shuang and C. Dong, *Nanoscale*, 2015, **7**, 12666–12672.
158 S. Lee, W. J. Kim and M. Chung, *Analyst*, 2021, **146**, 5236–5244.
159 L. M. Doubova, M. Fabrizio, S. Daolio, A. Forlini, S. Rondinini and A. Vertova, *Russian Journal of Electrochemistry*, 2012, **48**, 351–363.
160 J. D. Schrattenecker, R. Heer, R. Hainberger and G. Fafilek, *Proceedings 2017, Vol. 1, Page 534*, 2017, **1**, 534.
161 R. L. McCreery, *Chem. Rev.*, 2008, **108**, 2646–2687.
162 K. Bandyopadhyay, S.-G. Liu, H. Liu and L. Echegoyen, *Chem. - Eur. J.*, 2000, **6**, 4385–4392.
163 M. F. Mousavi, M. Amiri, A. Noori and S. M. Khoshfetrat, *Electroanalysis*, 2017, **29**, 2818–2831.
164 M. A. Ali, K. Mondal, Y. Jiao, S. Oren, Z. Xu, A. Sharma and L. Dong, *ACS Appl. Mater. Interfaces*, 2016, **8**, 20570–20582.
165 S. M. Khoshfetrat, P. Seyed Dorraji, M. Shayan, F. Khatami and K. Omidfar, *Anal. Chem.*, 2022, **94**, 8005–8013.
166 R. Gesztelyi, J. Zsuga, A. Kemeny-Beke, B. Varga, B. Juhasz and A. Tosaki, *Arch. Hist. Exact Sci.*, 2012, **66**, 427–438.
167 T. von Mach, M. C. Carlsson, T. Straube, U. Nilsson, H. Leffler and R. Jacob, *Biochem. J.*, 2014, **457**, 107–115.
168 H. J. Issaq, Z. Xiao and T. D. Veenstra, *Chem. Rev. (Washington, DC, U. S.)*, 2007, **107**, 3601–3620.
169 J. Sopoušek, J. Věžník, J. Houser, P. Skládal and K. Lacina, *Electrochim. Acta*, 2021, **388**, 138616.
170 A. García-Miranda Ferrari, S. J. Rowley-Neale and C. E. Banks, *Talanta Open*, 2021, **3**, 100032.
171 S. Singh, J. Wang and S. Cinti, *ECS Sens. Plus*, 2022, **1**, 023401.
172 J. Wang, *Analytical Electrochemistry, Third Edition*, 2006, 1–250.
173 S. Malathi, I. Pakrudheen, S. N. Kalkura, T. J. Webster and S. Balasubramanian, *Sensors International*, 2022, **3**, 100169.
174 P. S. Adarakatti and S. K. Kempahanumakkagari, *SPR Electrochemistry*, 2018, **15**, 58–95.
175 A. Vilan and D. Cahen, *Chem. Rev.*, 2017, **117**, 4624–4666.
176 T. N. Huan, R. T. Jane, A. Benayad, L. Guetaz, P. D. Tran and V. Artero, *Energy Environ. Sci.*, 2016, **9**, 940–947.
177 M. J. Moehlenbrock and S. D. Minteer, in *Methods in Molecular Biology*, Humana Press Inc., 2017, vol. 1504, pp. 1–7.
178 H. Allen and O. Hill, *Pure and Applied Chemistry*, 1987, **59**, 743–748.
179 C. R. Ispas, G. Crivat and S. Andreescu, *Anal. Lett.*, 2012, **45**, 168–186.
180 N. Baig, A. Rana and A. N. Kawde, *Electroanalysis*, 2018, **30**, 2551–2574.
181 B. Feier, I. Fizesan, C. Mériadec, S. Ababou Girard, C. Cristea, R. Sandulescu and F. Geneste, *Journal of Electroanalytical Chemistry*, 2015, **744**, 1–7.
182 B. Feier, D. Floner, C. Cristea, E. Bodoki, R. Sandulescu and F. Geneste, *Talanta*, 2012, **98**, 152–156.
183 R. Nasraoui, D. Floner, C. Paul-Roth and F. Geneste, *Journal of Electroanalytical Chemistry*, 2010, **638**, 9–14.
184 N. D. J. Yates, M. A. Fascione and A. Parkin, *Chemistry - A European Journal*, 2018, **24**, 12164–12182.

185 D. Hetemi, V. Noël and J. Pinson, *Biosensors (Basel).*, 2020, **10**, 4.
186 L. V. Hai, S. Reisberg, A. Chevillot-Biraud, V. Noel, M. C. Pham and B. Piro, *Electrochim. Acta*, 2014, **140**, 49–58.
187 Z. Nasri and E. Shams, *Electrochim. Acta*, 2013, **112**, 640–647.
188 R. Wang and C. Xue, *Analytical Methods*, 2013, **5**, 5195–5200.
189 J. Vinther, J. Iruthayaraj, K. Gothelf, S. U. Pedersen and K. Daasbjerg, *Langmuir*, 2013, **29**, 5181–5189.
190 M. N. Hansen, E. Farjami, M. Kristiansen, L. Clima, S. U. Pedersen, K. Daasbjerg, E. E. Ferapontova and K. V. Gothelf, *Journal of Organic Chemistry*, 2010, **75**, 2474–2481.
191 T. Menanteau, M. Dias, E. Levillain, A. J. Downard and T. Breton, *Journal of Physical Chemistry C*, 2016, **120**, 4423–4429.
192 C. Combellas, F. Kanoufi, J. Pinson and F. I. Podvorica, *J. Am. Chem. Soc.*, 2008, **130**, 8576–8577.
193 S. Patil and A. Bugarin, *European J. Org. Chem.*, 2016, **2016**, 860–870.
194 C. A. Martius and P. Griess, *Journal of Inorganic and General Chemistry*, 1866, 132–137.
195 H. E. Winberg and D. D. Coffman, *J. Am. Chem. Soc.*, 1965, **87**, 2776–2777.
196 F. Marchesi, M. Turriziani, G. Tortorelli, G. Avvisati, F. Torino and L. De Vecchis, *Pharmacol. Res.*, 2007, **56**, 275–287.
197 D. B. Kimball and M. M. Haley, *Angew. Chem. Int. Ed.*, 2002, **41**, 3338–3351.
198 D. M. Khramov and C. W. Bielawski, *Chemical Communications*, 2005, 4958–4960.
199 D. M. Khramov and C. W. Bielawski, *Journal of Organic Chemistry*, 2007, **72**, 9407–9417.
200 S. Patil, K. White and A. Bugarin, *Tetrahedron Lett.*, 2014, **55**, 4826–4829.
201 F. W. Kimani and J. C. Jewett, *Angew. Chem. Int. Ed.*, 2015, **54**, 4051–4054.
202 J. He, F. W. Kimani and J. C. Jewett, *J. Am. Chem. Soc.*, 2015, **137**, 9764–9767.
203 J. He, F. W. Kimani and J. C. Jewett, *Synlett*, 2017, **28**, 1767–1770.
204 S. M. Jensen, F. W. Kimani and J. C. Jewett, *ChemBioChem*, 2016, **17**, 2216–2219.
205 L. E. Guzman, F. W. Kimani and J. C. Jewett, *ChemBioChem*, 2016, **17**, 2220–2222.
206 B. M. Cornali, F. W. Kimani and J. C. Jewett, *Org. Lett.*, 2016, **18**, 4948–4950.
207 M. Shadmehr, G. J. Davis, B. T. Mehari, S. M. Jensen and J. C. Jewett, *ChemBioChem*, 2018, **19**, 2550–2552.
208 A. N. Wijetunge, G. J. Davis, M. Shadmehr, J. A. Townsend, M. T. Marty and J. C. Jewett, *Bioconjug. Chem.*, 2021, **32**, 254–258.
209 L. E. Guzmán, A. N. Wijetunge, B. F. Riske, B. B. Massani, M. A. Riehle and J. C. Jewett, *J. Am. Chem. Soc.*, 2024, **146**, 8480–8485.
210 M. S. Singh, S. Chowdhury and S. Koley, *Tetrahedron*, 2016, **72**, 5257–5283.
211 G. Pratsch, T. Wallaschkowski and M. R. Heinrich, *Chemistry - A European Journal*, 2012, **18**, 11555–11559.
212 A. Kimani, *Triazabutadiene Chemistry in Organic Synthesis and Chemical Biology Item Type text; Electronic Dissertation*, The University of Arizona., 2016.
213 N. D. J. Yates, University of York, 2021.
214 N. D. J. Yates, N. E. Hatton, M. A. Fascione and A. Parkin, *ChemBioChem*, 2023, **24**, e202300313.
215 N. D. J. Yates, L. Hudson, O. Schwabe and A. Parkin, *Langmuir*, DOI:10.1021/ACS.LANGMUIR.4C04848.
216 S. P. Harrington and T. M. Devine, *J. Electrochem. Soc.*, 2008, **155**, C381.
217 M. A. MacDonald and H. A. Andreas, *Electrochim Acta*, 2014, **129**, 290–299.
218 R. Saxena and S. Srivastava, *Sens Actuators B Chem*, 2019, **297**, 126780.

219 S. C. Joycee, A. S. Raja, A. S. Amalraj and S. Rajendran, *Int. J. Corros. Scale Inhib*, 2021, **10**, 943–960.
220 A. Benedetto, M. Balog, P. Viel, F. Le Derf, M. Sallé and S. Palacin, *Electrochim. Acta*, 2008, **53**, 7117–7122.
221 A. L. Gui, G. Liu, M. Chockalingam, G. L. Saux, J. B. Harper and J. J. Gooding, *Electroanalysis*, 2010, **22**, 1283–1289.
222 G. Liu, T. Böcking and J. J. Gooding, *Journal of Electroanalytical Chemistry*, 2007, **600**, 335–344.
223 D. Chattopadhyay, *Resonance*, 2017, **22**, 79–87.
224 e. G. Perevalova, N. A. Simukova, T. V. Nikitina, P. D. Reshetov and A. N. Nesmeyanov, *Bulletin of the Academy of Sciences of the USSR Division of Chemical Science*, 1961, **10**, 67–71.
225 M. A. Morales and J. M. Halpern, *Bioconjug. Chem.*, 2018, **29**, 3231.
226 J. G. S. Moo, A. Ambrosi, A. Bonanni and M. Pumera, *Chem. Asian J.*, 2012, **7**, 759–770.
227 M. M. Lounasvuori, M. Rosillo-Lopez, C. G. Salzmann, D. J. Caruana and K. B. Holt, *Faraday Discuss.*, 2014, **172**, 293–310.
228 M. Sokołowska and W. Bal, *J. Inorg. Biochem.*, 2005, **99**, 1653–1660.
229 J. F. Masson, E. Gauda, B. Mizaikoff and C. Kranz, *Anal. Bioanal. Chem.*, 2008, **390**, 2067–2071.
230 J. K. Grady, N. D. Chasteen and D. C. Harris, *Anal. Biochem.*, 1988, **173**, 111–115.
231 C. K. Almlie, N. E. Larkey and S. M. Burrows, *Analytical Methods*, 2015, **7**, 7296–7310.
232 K. Bano, J. Zhang, A. M. Bond, P. R. Unwin and J. V. Macpherson, *Journal of Physical Chemistry C*, 2015, **119**, 12464–12472.
233 H. Adamson, A. M. Bond and A. Parkin, *Chemical Communications*, 2017, **53**, 9519–9533.
234 N. G. Baranska, B. Jones, M. R. Dowsett, C. Rhodes, D. M. Elton, J. Zhang, A. M. Bond, D. Gavaghan, H. O. Lloyd-Laney and A. Parkin, *ACS Measurement Science Au*, 2024, **4**, 418–431.
235 F. H. Pilz and P. Kielb, *BBA Advances*, 2023, **4**, 100095.
236 P. J. Delahay, Am, P. Delahay, T. P. Fehlner, J. Ulman, W. A. Nugent, J. K. Kochi, S. Fukuzumi and C. L. Wong, *Journal of Physical Chemistry*, 2002, **85**, 1731–1741.
237 A. M. Bond, N. W. Duffy, S. X. Guo, J. Zhang and D. Elton, *American Chemical Society*, 2005, preprint, DOI: 10.1021/ac053370k.
238 R. J. Schwall, A. M. Bond and D. E. Smith, *Anal. Chem.*, 1977, **49**, 1805–1812.
239 H. O. Lloyd-Laney, N. D. J. Yates, M. J. Robinson, A. R. Hewson, J. D. Firth, D. M. Elton, J. Zhang, A. M. Bond, A. Parkin and D. J. Gavaghan, *Anal. Chem.*, 2021, **93**, 2062–2071.
240 H. O. Lloyd-Laney, N. D. J. Yates, M. J. Robinson, A. R. Hewson, J. Branch, G. R. Hemsworth, A. M. Bond, A. Parkin and D. J. Gavaghan, *Journal of Electroanalytical Chemistry*, 2023, **935**, 117264.
241 J. T. Long and S. G. Weber, *Electroanalysis*, 1992, **4**, 429–437.
242 C. G. Bell, C. A. Anastassiou, D. O'Hare, K. H. Parker and J. H. Siggers, *Electrochim. Acta*, 2011, **56**, 7569–7579.
243 S. A. Brazill, S. E. Bender, N. E. Hebert, J. K. Cullison, E. W. Kristensen and W. G. Kuhr, *Journal of Electroanalytical Chemistry*, 2002, **531**, 119–132.
244 P. Singhal and W. G. Kuhr, *Anal. Chem.*, 1997, **69**, 3552–3557.
245 S. A. Brazill, P. Singhal and W. G. Kuhr, *Anal. Chem.*, 2000, **72**, 5542–5548.
246 P. Kumari and S. B. Adeloju, *Talanta*, 2019, **194**, 127–133.
247 M. Weatherill, University of York, 2024.

248 K. L. Rahn, U. Peramune, T. Zhang and R. K. Anand, *Annu. Rev. Anal. Chem. (Palo Alto Calif)*, 2023, **16**, 49–69.
249 V. Sanko and F. Kuralay, *Biosensors 2023, Vol. 13, Page 333*, 2023, **13**, 333.
250 S. Sarkar and S. Kundu, *Mater. Today Proc.*, DOI:10.1016/J.MATPR.2023.04.200.
251 L. Tang, J. Zhang, N. Oumata, N. Mignet, M. Sollogoub and Y. Zhang, *Eur. J. Med. Chem.*, 2025, **287**, 117315.
252 N. E. Hatton, J. Nabarro, N. D. J. Yates, A. Parkin, L. G. Wilson, C. G. Baumann and M. A. Fascione, *JACS Au*, 2024, **4**, 2122–2129.
253 N. Hansen, *ArXiv*, 2016, 1–39.
254 M. Clerx, M. Robinson, B. Lambert, C. L. Lei, S. Ghosh, G. R. Mirams and D. J. Gavaghan, *J. Open Res. Softw.*, 2019, **7**, 23.
255 L. Li, Y. Liu, W. Wang, J. Cheng, W. Zhao and P. Wang, *Carbohydr. Res.*, 2012, **355**, 35–39.
256 H. Brisset, A.-E. Navarro, F. Moggia, B. Jousselme, P. Blanchard and J. Roncali, *J. Electroanal. Chem.*, 2007, **603**, 149–154.